Optical Fibre Sensors with Surface-immobilised Fluoroionophores

By

Herbert Tze Cheung Foo

THE UNIVERSITY of ADELAIDE

A thesis submitted for the fulfilment of the

degree of Doctor of Philosophy

in the

Faculty of Science

School of Chemistry and Physics

July 2014

Declaration of Authorship

I certify that this work contains no material which has been accepted for the award of any other degree or diploma in any university or other tertiary institution and, to the best of my knowledge and belief, contains no material previously published or written by another person, except where due reference has been made in the text. In addition, I certify that no part of this work will, in the future, be used in a submission for any other degree or diploma in any university or other tertiary institution without the prior approval of the University of Adelaide and where applicable, any partner institution responsible for the joint-award of this degree.

I give consent to this copy of my thesis when deposited in the University Library, being made available for loan and photocopying, subject to the provisions of the Copyright Act 1968.

The author acknowledges that copyright of the published works contained within this thesis resides with the copyright holder(s) of those works.

I also give permission for the digital version of my thesis to be made available on the web, via the University's digital research repository, the library catalogue and also through web search engines, unless permission has been granted by the University to restrict access for a period of time.

Signed: _____

Date: _____

Table of contents

Abstract

Regular monitoring of the concentration of ionic nutrients such as Nitrate (N), Phosphate (P) and Potassium (K) ions in soils is necessary for agricultural management. Optical fibre dip sensors provide sensing platforms that have the potential to be small and flexible that can reach the root zone. This thesis contains studies towards the development of novel optical fibre soil nutrient sensors using suspended core fibres (SCFs) and Photoinduced Electron Transfer (PET) based fluoroionophores. SCFs provide long interaction path length that potentially increase the sensitivity and lower the detection limit. Furthermore it requires only nanoliters for analysis. PET fluoroionophores using 4-amino-1,8-naphthalimide as the common fluorophore can be integrated within a SCF to become optical fibre sensors in two ways. The first approach is to pre-mix the fluoroionophore with the analyte to be sensed; the second approach is to immobilise the fluoroionophore on the internal surface of SCF. Chapter 2 and 5 of this thesis has demonstrated both potential operating scenarios are feasible for cation sensing. Furthermore, both cation and anion sensing are feasible using the first approach.

Surface immobilisations of the fluoroionophores on the glass materials are critical for the development of the practical SCF sensors (second approach). In order to achieve this, it is first necessary to develop techniques for the characterisation of the functionalised surfaces. Chapter 3 and 4 of this thesis has demonstrated a versatile approach of using different glass model systems and surface analysis techniques such as X-ray photoelectron spectroscopy, Time of flight secondary ion mass spectrometry (ToF-SIMS), fluorescence imaging, spectroscopic ellipsometry, atomic force microscopy for measuring parameters such as the surface density of amine groups and sensor molecules, coating coverage, surface roughness and coating thickness that represent the surface chemistry of SCF. In addition, ToF-SIMS imaging is demonstrated to reveal that the lead ions distribution could be used as a marker of surface coverage of the coating. The application of using ToF-SIMS for relative coating thickness measurement on is also demonstrated in this thesis.

Publications during candidature

Journal publications:

Englich, F. V.; Foo, T. C.; Richardson, A. C.; Ebendorff-Heidepriem, H.; Sumby, C. J.; Monro, T. M., Photoinduced Electron Transfer Based Ion Sensing within an Optical Fiber. *Sensors-Basel*, **2011,** *11* (10), 9560-9572

Foo, H. T. C.; Ebendorff-Heidepriem, H.; Sumby, C. J.; Monro, T., Towards microstructured optical fibre sensors: surface analysis of silanised lead silicate glass. *Journal of Materials Chemistry C* **2013,** *1*, 6782-6789.

Conference papers:

Foo, T. C.; François, A.; Ebendorff-Heidepriem, H.; Sumby, C. J.; Monro, T. M., Comparison of Surface Functionalization Techniques on Silica and Soft Glasses for Optical Fibre Sensing Applications. In *Australian Conference on Optical Fibre Technology (ACOFT)*, Adelaide, Australia, 2009 (Accepted for oral presentation)

Englich, F. V.; Foo, T. C.; Ebendorff-Heidepriem, H.; Sumby, C. J.; Monro, T. In *Towards a microstructured optical fibre fluorescence sensor based on photoinduced electron transfer photobleaching*, Proceedings of the Australian Conference on Optics, Lasers and Spectroscopy and Australian Conference on Optical Fibre Technology in association with the International Workshop on Dissipative Solutions, Adelaide, Adelaide, 2009; pp 105-106 (Accepted for oral presentation)

Richardson, A. C; Foo, T. C; Englich, F. V; Ebendorff-Heidepriem, H; Sumby, C. J; Monro, T. M. *A microstructured optical fiber sensor for ion-sensing based on the photoinduced electron transfer effect*, Proceedings of the 3rd Asia Pacific Optical Sensors Conference (APOS 2012), 2012

Note that I officially changed my name from Tze Cheung Foo to Herbert Tze Cheung Foo in October 2013

Acknowledgements

This was certainly an enjoyable transdisciplinary research journey, where I have had the chance to work with and learn from scientists from various discipline areas such as glass chemistry, surface chemistry, organic chemistry, physical chemistry, optics and photonics. It is my pleasure to acknowledge everyone for their support and assistance to me throughout my degree of Doctor of Philosophy (PhD).

First of all, I would like to thank my supervisors Heike Ebendorff-Heidepriem, Chris Sumby and Tanya Monro. This is a great team with a glass scientist, a chemist and a physicist. Without their guidance and support, it would have been impossible to accomplish the research presented in this thesis. Thanks to all supervisors for editing this thesis.

I would like to acknowledge my collaborators Mai-Chi Nguyen, Andrew Richardson, Florian Englich and Alexandre François in the Institute of Photonics and Advanced Sensing (IPAS) for their important contributions to this research project.

I acknowledge the support from some of the surface scientists at Flinders University; they are Natalya Schmerl and Günther Andersson. A lot of the data presented in this thesis were measured by the well-maintained MIES-XPS instrument at Flinders University. They are acknowledged also for many useful discussions regarding surface analyses.

I also acknowledge the support from John Denman from Ian Wark Research Institute, who runs the ToF-SIMS instrument. John is also acknowledged for discussions regarding the complicated Tof-SIMS data analyses.

I would like to thank the technical support from Roger Moore, Peter Henry, Kevin Kuan and Alastair Dowler for fabricating all fibres and capillaries used in this research project.

To Stephen Warren-Smith, Erik Schartner and Matthew Henderson, thanks for many academic and non-academic discussions and advices, which helped me

enormously throughout my PhD. Thanks to them also for help with proof-reading this thesis.

To all my friends in the chemistry department and the Institute for Photonics and Advanced Sensing (IPAS), thanks for the support over years. It is certainly enjoyable to work with you guys.

I acknowledge the financial support from Micormet Pty Ltd and specifically to Jim Townsend, Terry Crawn and Paul Dalby, who provided their professional support and opinions throughout the whole research project.

On the personal side, I would like to thank my housemates Raymond, Edward and Yaying for making our home such a wonderful place to live. Finally and most importantly, I would like give a special thank to my sister Fiona, my mum Yin Fui and my dad Pit Yue for their love, support and encouragement to me over years. This thesis was accomplished during a personally difficult time. Without the support from friends and family, I could not imagine that I can complete this thesis.

Contributions

This transdisciplinary research project was supported by the Australian Research Council Linkage Grant Scheme and our industry partner, Micromet Pty Ltd, who sought to develop a solar-powered soil ionic nutrient probe that could be inserted within the root zone to continuously monitor concentrations of phosphate, nitrate and potassium (P, N, K) ions. The National Collaborative Research Infrastructure Strategy (NCRIS) has provided equipment used regularly in this project.

This research project was supervised by Heike Ebendorff-Heidepriem, Chris Sumby and Tanya Monro. I was responsible to the development of sensor molecules and surface functionalisation procedures for the suspended core fibres (SCFs); the Physics Research Fellows employed on the project were responsible for the development of the optical set-ups. The Physics Research Fellows were Florian Englich (2009 to 2011) and Andrew Richardson (2011 to 2012). Research assistant Mai-Chi Nguyen joined the project team in 2012 to perform additional optics experiments for this project.

The development of the project was regularly discussed with Paul Dalby, Jim Townsend and Terry Crawn from Micromet Pty Ltd. All academic aspects of this project related to this thesis were discussed at regular meetings with my supervisors Heike Ebendorff-Heidepriem, Chris Sumby and Tanya Monro.

Most of the experiments reported in this thesis were performed collaboratively. The following sections describe the specific contributions by me and my collaborators in each experiment reported in this thesis.

Organic synthesis of model fluorophores and fluoroionophores

I performed the synthesis and characterisation of model fluorophores and PET fluoroionophores for sodium and fluoride ions sensing. I also perform synthesis of the surface attachable fluorophores and fluoroionophores. Furthermore, I worked to synthesise a novel potassium-selective fluoroionophore. The attempted synthesis of a previously reported potassium-selective fluoroionophore (**He.2**) was performed by Peter Valente.

Characterisation of model fluoroionophores and fluorophores in SCFs and cuvette using the different optic setups

The optical set-up for the cuvette and SCFs measurements was developed initially by Florian Englich and subsequently byAndrew Richardson. Ion sensing experiments using a diode laser were performed collaboratively by Mai-Chi Nguyen, Andrew Richardson and Florian V. Englich, with my assistance for sample preparation. Codes for analysing the fluorescence spectra were written by Andrew Richardson, Mai-Chi Nguyen and modified by me using MATLAB (R2008a, The MathWorks, Natick, Massachusetts).

Glass Preform and slides fabrication

Glass perform and slides were fabricated by Heike Ebendorff-Heidepriem.

Suspended core fibres (SCFs) fabrication

Lead silicate (F2) SCFs and silica SCFs were fabricated by Roger Moore, Alastair Dowler and Erik Schartner.

Surface functionalisation experiment using capillary

I performed the surface functionalisation experiments using capillaries in collaboration with Alexandre Francois. The tellurite and ZBLAN glass were fabricated by Kevin Kuan. The lead silicate (F2), bismuth and tellurite glass capillaries were fabricated by Heike Ebendorff-Heidepriem and Roger Moore.

Surface characterisation of bare glass and functionalised glass slides

I performed the surface functionalisation experiments using silane reagents and surface attachable fluoroionophores.

I performed the XPS measurements with training and assistance from Natalya Schmerl and Günther Andersson, The Flinders University of South Australia. I performed the XPS data analyses.

The ToF-SIMS measurements were performed by John Denman from the Ian Wark Research Institute, the University of South Australia. I performed the Tof-SIMS data analyses.

Characterisation of the ion sensing function of SCFs functionalised with fluoroionophores

Functionalisation experiments on the silica SCFs for loss and fluorescence measurements were performed collaboratively by Ms Mai-Chi Nguyen and me. The sodium ions sensing experiments were performed primarily by Ms Mai-Chi Nguyen with my assistance in the solution preparation. The SEM images were captured by Erik Schartner. The functionalised SCF loss measurements were performed by Ms Mai-Chi Nguyen. The losses of uncoated silica SCFs were measured by Erik Schartner.

Experiments to identify methods for normalisation

The planning and the results of the normalisation experiments were discussed with Stephen Warren-Smith, Erik Schartner and Mai-Chi Nguyen. The optics experiments were performed predominantly by Mai-Chi Nguyen with my assistance for the solution preparation

List of Figures

List of Schemes

List of Tables

Abbreviations

AFM	**A**tomic **f**orce **m**icroscopy
APTES	3-**A**mino**p**ropyl**t**ri**e**thoxy**s**ilane
ATR-FTIR	**A**ttenuated **T**otal **R**eflectance- **F**ourier **T**ransform **I**nfra**r**ed
AUTES	11-**A**mino**u**ndecyl**t**ri**e**thoxy**s**ilane
CCD	**C**harge **C**oupled **D**evice
CDI	1,1-**C**arbonyl**d**iim**i**dazole
DBU	1,8-**D**iaza**b**icyclo[5.4.0]-**u**ndec-7-ene
DIPEA	N,N-**Di**iso**p**ropyl**e**thyl**a**mine
DMF	**Dim**ethyl**f**ormamide
EDC	1-**E**thyl-3-(3-**d**imethylaminopropyl) **c**arbodiimide
EDX	**E**nergy-**D**ispersive **X**-ray
FE	**F**luorescence **E**nhancement
F2	Lead silicate glass
HR	**H**igh **R**esolution
HRMS	**H**igh **R**esolution **M**ass **S**pectrometry
HRXPS	**H**igh **R**esolution **X**-ray **P**hotoelectron **S**pectroscopy
NMR	**N**uclear **M**agnetic **R**esonance
PC	**P**rinciple **C**omponent
PCA	**P**rinciple **C**omponent **A**nalysis
PCT	**P**hotoinduced **C**harge **T**ransfer
PET	**P**hotoinduced **E**lectron **T**ransfer

PMT	**P**hoto**m**ultiplier **T**ube
SCFs	**S**uspended-**C**ore **F**ibres
SE	**S**pectroscopic **E**llipsometry
SEM	**S**canning **E**lectron **M**icroscopy
THF	**T**etra**h**ydro**f**uran
TLC	**T**hin **L**ayer **C**hromatography
Tof-SIMS	**T**ime **O**f **F**light **S**econdary **I**on **M**ass **S**pectroscopy
NMP	**N**-**M**ethyl-2-**P**yrrolidone
NHS	**N**-**h**ydroxy**s**uccinimide
XPS	**X**-ray **P**hotoelectron **S**pectroscopy
+SIMS	Positive **S**econdary **I**on **M**ass **S**pectroscopy
-SIMS	Negative **S**econdary **I**on **M**ass **S**pectroscopy

Chapter 1

Introduction

1.1 Background and Motivation

The research described in this thesis was motivated by industry demands for a low cost soil nutrient ion sensor based on the deployment and sensing benefits provided by optical fibre technology. In the research supported by the Australian Research Council Linkage Scheme, our industry partner, Micromet Pty Ltd, sought to develop a solar-powered soil ionic nutrient probe that could be inserted within the root zone of a plant to continuously monitor the concentration of nitrate, phosphate and potassium (P, N, K) ions. The target dynamic range of the sensors for nitrate, phosphate and potassium were 2–50, 1–10 and 1–10 ppm respectively, which are found in the soil solution, the liquid phase of soil, under natural conditions [1].

The soil solution is the main source of ionic nutrients that terrestrial plants can absorb through their roots. Examples of the common ionic nutrients in soil solutions that are required by terrestrial plants are potassium (K^+), sodium (Na^+), calcium (Ca^{2+}), magnesium (Mg^{2+}), nitrate (NO_3^-) and phosphate (PO_4^{3-}) [2, 3]. The composition and concentration of the ionic nutrients in soil solutions are time and location specific, because they depend on many factors such as weather, ground water type, dissolution of fertilisers, and reactions between the solid soil, atmosphere and soil solution [4]. Monitoring the concentration and the composition of the ionic nutrients is important in agriculture because it has a strong link to the yield of an agricultural site [2]. In particular, ionic nutrient sensing in soil solutions is particularly important as a tool for site-specific crop management, which is also known as precision agriculture. This approach minimises the controllable parameters such as fertiliser dosage and water usage while increasing the yield of crop production [5]. Precise, real-time knowledge of the concentrations and compositions of the ionic nutrients in a soil solution enables the agronomist to control the dosage of the fertiliser and hence the yield of the site [5].

Traditionally, the sensing of ionic nutrients from soil solution requires soil sampling. The soil samples are extracted and then the solution samples are analysed by instruments such as inductively coupled plasma atomic emission spectrometry (ICP-AES) and ion chromatography in the laboratory [6-8]. This method does not provide in-situ data. In addition, it can be expensive and time consuming to perform for a large area and thus, only a few locations can be measured. As mentioned above, the concentration and composition of the ionic nutrients have location-specific profiles and therefore data gathered by this method are not representative. In addition, the soil sampling process is a destructive method, which damages the soil and the root structure of plants near the sampling site.

Ion-selective electrodes (ISEs) have been the major instrument for in-situ ionic nutrient detection in soil solution [9]. ISEs are an electrochemical sensor with a membrane, which is selective to the permeation of particular ions; therefore the current represents the concentration of specific ions [10]. Most of the modern ISE use specific organic ionophores mixed with polymer to form the membrane, which is selectively permeable to particular ions. The selectivity of the membrane is controlled by the ionophore, which acts as a shuttle that transfers ions from one side to the other [10]. The binding of the ions (Guests) to the ionophores (Hosts) can be controlled by the molecular design of the hosts [10, 11]. Many reviews have been published to summarise the current development in this area of research [10-12]. While ISEs provide a non-destructive and accurate way to perform ion sensing, it suffers from limitations such as signal drift over time, which needs regular recalibration [13]. This drifting is usually caused by electromagnetic field interference [14]. Furthermore ISEs are expensive to deploy over a large area.

In contrast, an optical fibre provides a sensing platform that has the potential to be small and flexible; therefore it can penetrate into the soil without digging or damaging the soil. In doing so, optical fibre sensors can reach the root zone, which is in the deep layer of the soil, and provide data on the in-situ ion concentration. This information is critical for agricultural management because it represents the ion concentration data at the plant absorption zone. In addition, optical measurements are less likely to be affected by electromagnetic field interference. The cost of fabrication for each optical fibre sensor is also relatively

low compared with an ISE electrode; therefore large number of sensors can be deployed over a large area. Furthermore they have the potential to make measurements that are localised in a small area such as stem or fruit of the plant. Mutiplexing of the sensing of different ions is also possible with a bundle of fibre.

1.1.1 Microstructured Optical Fibres

Microstructured optical fibres (MOFs) are a new class of optical fibre which has microscopic air holes within the fibre [15, 16]. Within MOFs light is guided inside the structure through total internal reflection or the photonic bandgap effect [15]. The analyte can be introduced into fibre by loading the sample to be sensed into the air holes where the interaction of the light guided by the fibre and the sample can be exploited along the full length of the fibre. Because of the long interaction path length, the detection limit and the sensitivity can be better than traditional optical fibre based chemical sensors, which use only the fibre tip for sensing [17]. Furthermore, sensing using MOFs requires only small volume (~ nanoliter range) analyte [18].

MOFs can have many different physical structures; certain structures such as exposed core fibre (Figure 1.1a) demonstrate the potential for instantaneous and/or distributive sensing, which is important for ion sensing over large areas [19, 20]. The most common MOFs being studied for sensing applications are suspended core fibres (SCFs) (Figure 1.1b), which have the glass core suspended by struts and surrounded by air holes [18]. SCFs have shown potential in fluorescence sensing for chemicals such as aluminium ions and hydrogen peroxide, as well as biologically important species such as enzymes and antibodies [18, 21-24]. In designing a soil nutrient sensor, SCFs were considered as a promising platform.

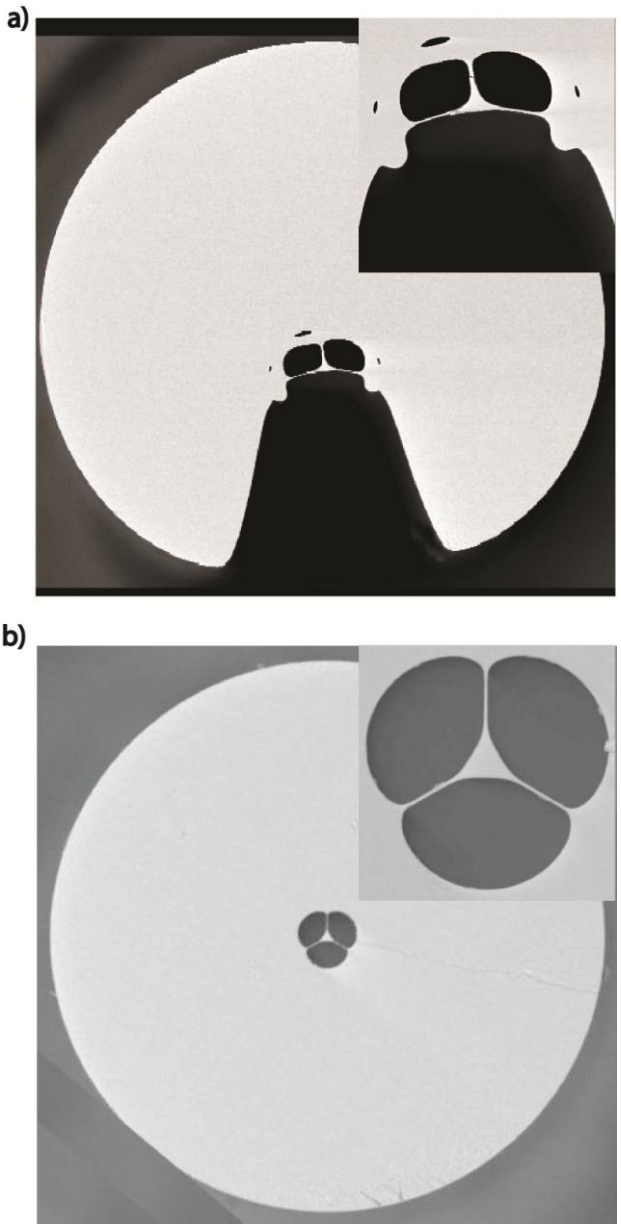

Figure 1.1: (a) Lead silicate (F2) exposed core fibre.[19] (b) Lead silicate (F2) suspended core fibre [24]. (Insets are close-up images of the suspended core structure)

1.1.2 Soil nutrients fibre sensors

To fabricate a soil nutrient ion sensor using SCFs, a fluorophore that is selective to the target ion is essential. Photoinduced electron transfer (PET) fluoroionophores are promising candidates that can provide a concentration-dependent emission signal that can be detected within the SCF. The change in the

emission intensity is captured by the SCF and transmited to the detector. The mechanism of detection is discussed in detail in Chapter 2. A PET fluoroionophore consists of a fluorophore, which emits a fluorescence signal in response to the binding of an ion, and a covalently linked ionophore, which selectively binds to the target ions. Details are discussed in Section 1.2.5. Many successful examples of PET fluoroionophores have been reported for the detection of a variety of cations and anions with remarkable selectivity [25]. Some examples of these PET fluoroionophores have been commercialised and applied in a medical device to measure cations such as protons (pH sensing), sodium, potassium and calcium in blood [26, 27]. PET fluoroionophores can be designed and engineered for specific ions, such that the same fluorophore can be attached to ionophores specific for different ions [28]. Therefore, the same optical components could in principle be shared by multiple sensors.

The main research question for this project was how to combine PET fluoroionophores and SCFs to perform ion sensing in soil solutions. There are two possible operating scenarios (A and B) for performing sensing with PET fluoroionophores and SCFs. In operating scenario A, shown in Figure 1.2a, the change of fluorescence intensity of the PET fluoroionophore is measured in a SCF by measuring the difference in emission intensity of the PET fluoroionophore before and after mixing with the analyte. The detailed mechanism of fluorescence sensing is discussed in Section 1.2.1. The analyte passes through the filter and is then mixed with the chosen PET fluoroionophore within a microfluidic chip. This chip enables efficient mixing in the nanolitre volume range [29]. Mixing is required before injection into the SCF to ensure the homogeneity of the solution. After mixing the solution is transferred through a capillary into the SCF. While this was proposed as an operating method in a commercial device, no microfluidic mixing was performed in this project. Instead, the fluoroionophores and analytes were pre-mixed and then filled into the SCFs. In this scenario the SCF is acting as the optical guidance and sensing platform to transmit the excitation light source and emitted light to and from the mixture of fluoroionophore and analyte.

In operating scenario B, shown in Figure 1.2b, the analyte is passed through the filter and then transferred through a capillary directly into a SCF that has PET fluoroionophores attached onto its internal surface. The analyte then reacts with

the surface attached PET fluoroionophores and the sensing measurements are performed. In terms of operation, this is simpler than operating scenario A because there is no pre-mixing required. Therefore, it is the preferable operating scenario. The rationale of surface attachment is discussed in Section 1.2.2.

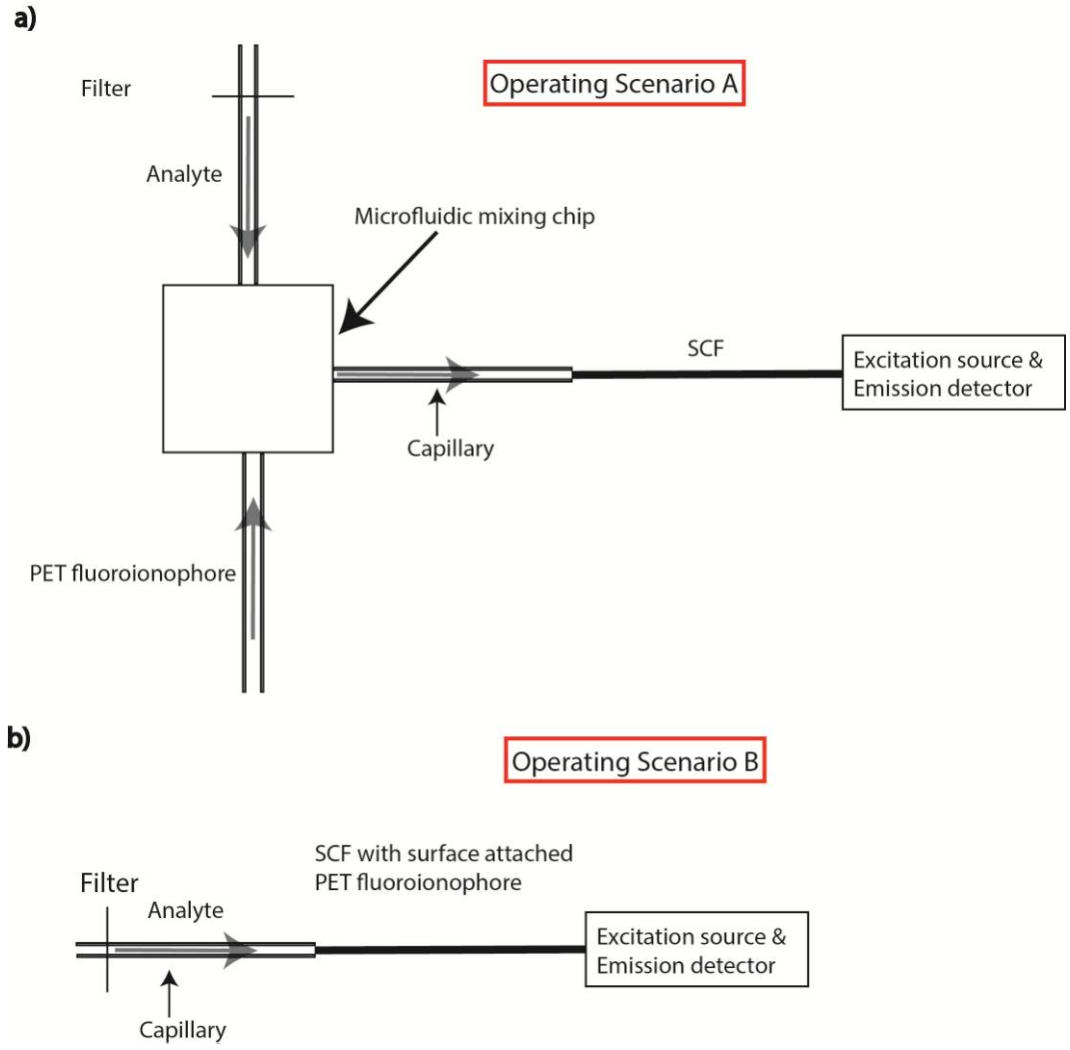

Figure 1.2: Two operating scenarios for ion sensing using SCFs and PET fluoroionophores. (a) a microfluidic chip and (b) a SCF with surface-attached PET fluoroionophores

In order to demonstrate a sensor using operating scenario B with the potential to be translated into practical devices, it is critical to be able to functionalise the surfaces in a reproducible manner. This requires a detailed understanding of the surface chemistry for the functionalised glass materials used to fabricate SCFs. Information such as surface roughness, coating coverage, coating thickness and surface density of the surface attached fluoroionophores are important parameter

for the sensor fabrication. It is necessary to have methodologies for analysing these parameters. These techniques are essential for optimising the surface functionalisation process to the internal surfaces of SCFs. In this project, different surface analysis methodologies were applied to gain greater understanding of the surface functionalisation chemistry for common SCF glass materials.

1.2 State-of-the-art

This project built on current technologies in the area of SCF sensing, fluoroionophore synthesis, surface functionalisation chemistry and surface analysis methodologies. The following sections provide some background and literature reviews for each area.

1.2.1 Fluorescence sensing mechanism with suspended core fibre

Figure 1.3a provides a schematic representation of the mechanism of fluorescence sensing within a SCF. Inside a SCF the excitation light source and the emitted light are guided through the glass core at the centre, which acts as a 'rail' for the light; part of the guided light is propagated in the air holes surrounding the core. After excitation of the fluorophore, photons are emitted from the fluorophore in all directions. A portion of the photons that are emitted within a particular acceptance angle can be captured and propagated in either the backward or forward directions along the core. The fraction of the light that is captured depends on the fibre geometry and refractive index contrast between the analyte and the glass material. In fluorescence spectroscopy using a cuvette, the emission intensity of a fluorophore is proportional to the excitation power, interaction path length and the percentage of the emitted photons captured by the detector. It is the same in the fluorescence spectroscopy using SCFs; however, the path length of a SCF is the whole length of a fibre.

Figure 1.3b shows the light power distribution of the light propagating along the core of the SCF. This waveguide structure enables the guided light to interact with the solution along the solution-filled length of the SCF. Thus, the SCF is acting similarly to a nanolitre scale cuvette but with an interaction path length equals to the length of the fibre. A typical path length of a cuvette is 10 mm, whereas the

typical fibre length is 200 mm. Therefore a SCF has a much longer path length than a typical cuvette.

For fluorescence spectroscopy it is important to prevent the excitation source from being detected in the instrument. Hence, most fluorometers have the detector locates perpendicularly to the excitation beam path [30, 31]. In addition, a fluorometer has monochromators and an optical filter to remove light from the excitation source [30, 31]. Unlike a fluorometer, the SCF sensor described in this thesis has the detector located in the same direction as the excitation source. As shown in Figure 1.3b, the emitted light propagates in both forward and backward direction, but the excitation source light mainly propagates in the forward direction, therefore most of the excitation source light is not detected. The dichroic mirror and the optical filter are also used in the SCF sensor to further remove the excitation source light. The detection of emitted light is not affected in the backward detection mode and therefore it is valid for the sensor to operate in this mode [32]. The optics setup of the SCF sensors is discussed in detail in Chapter 2.

The power fraction (PF) propagating outside the core depends on the refractive index contrast between the glass core and the media in the holes, and the details of the fibre geometry including the core size [18, 32-34]. Through modelling and experimental validation, Afshar *et. al* and Warren-Smith *et. al* [18, 32-34] have shown that the power of the light propagating outside the core increases as the core size of the SCF deceases. For suspended core fibre sensors, the power fraction (PF) outside the core is also proportional to the excitation power.

The percentage of the emitted photons captured into the core of a SCF is known as the fluorescence capturing fraction (FCF) and is dependent on the numerical aperture (NA) of the fibre. Equation 1 shows that the NA is dependent on the index contrast between the core and the analyte solution.

$$NA = \sin\theta_{max} = \sqrt{n_{core}^2 - n_{clad}^2} \qquad \text{(Equation 1)}$$

where θ_{max} is the acceptance angle of the fibre; n_{clad} is the refractive index of the analyte solution and n_{core} is the refractive index of the core of a SCF. A larger NA

results in a larger acceptance angle (Figure 1.4) and therefore the capture of more emitted photons. Since NA is dependent on the index contrast between the glass material and analyte, the choice of the glass material affects the fluorescence capturing capability of the sensor.

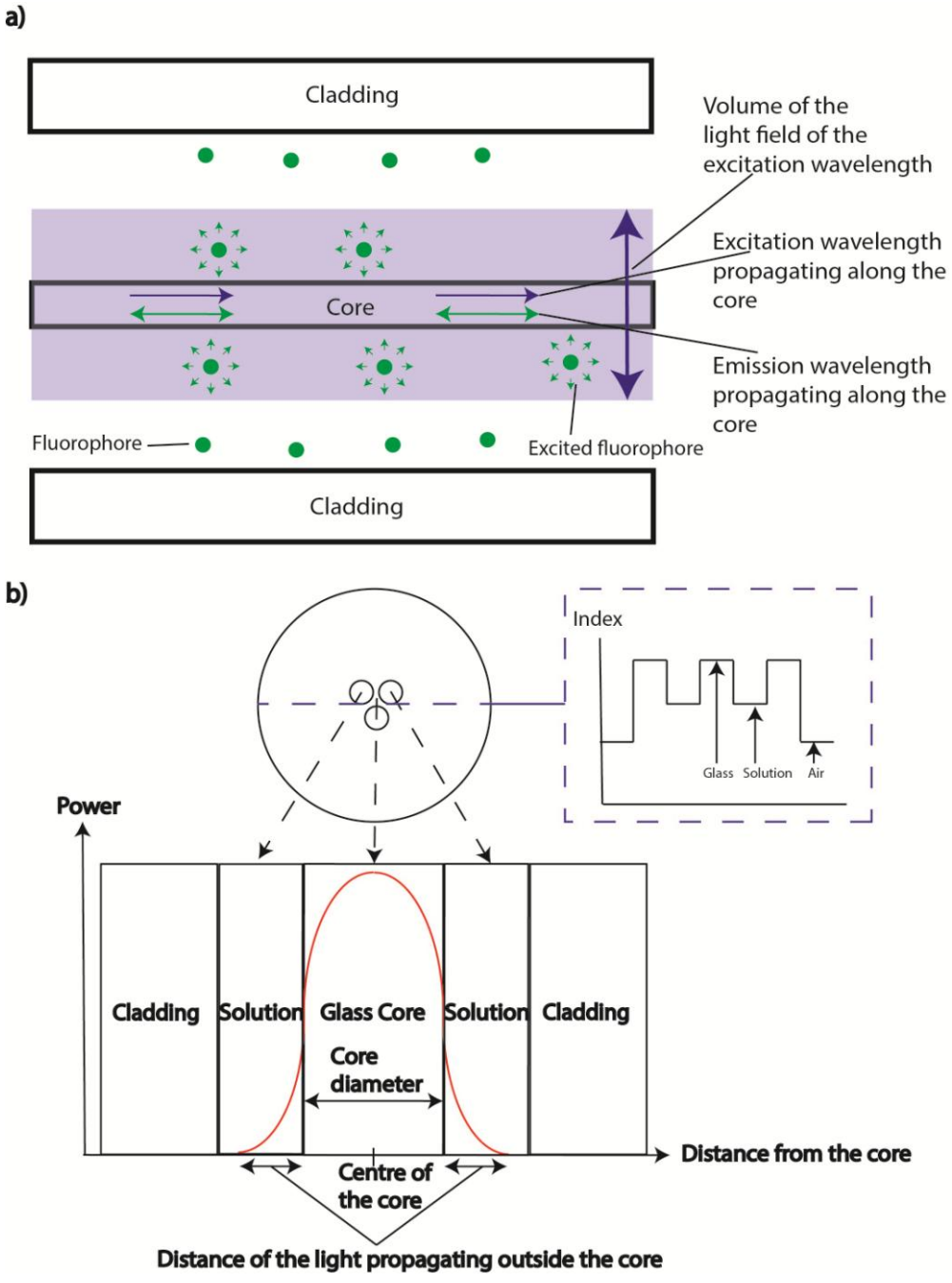

Figure 1.3: (a) Schematic diagram of the fluorescence sensing mechanism of a SCF with non-immobilised fluorophores. (b) Distribution of power within a SCF. The insert is the refractive index profile along the centre axis of a SCF

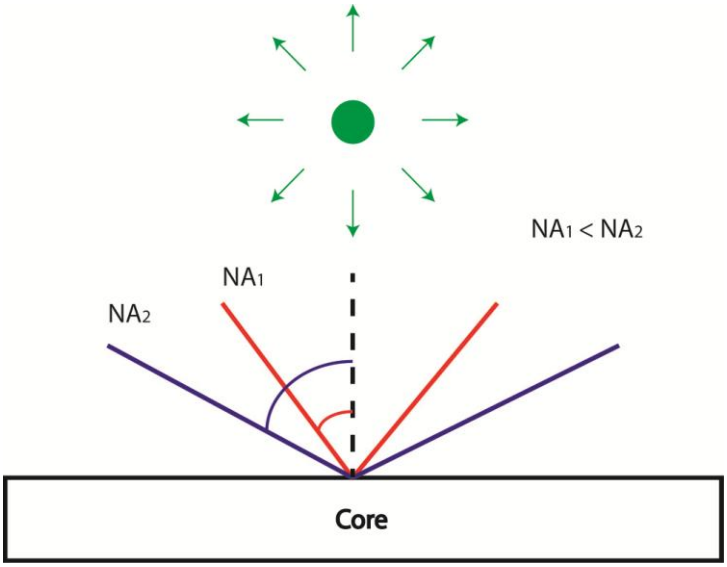

Figure 1.4: A pictorial representation of the acceptance angle with different fibre NAs. The larger the NA, the larger the acceptance angle, and the greater the proportion of photons captured by the fibre core.

1.2.2 Rationale for attaching fluorophores to the core surface

Operating scenario B requires no pre-mixing step and is therefore a preferable option from a practical perspective. For example, it is possible to have a device connected to multiple SCFs functionalised with different fluoroionophores for detection of different ions. Moreover, attaching the fluorophore to the glass core surface can theoretically improve the sensitivity and detection limit of the sensor. Figure 1.5 shows a schematic diagram of a SCF with fluorophores attached on the core surface. The intensity of the excitation light is a function of the distance from the core. The closer the fluorophore is to the core of the fibre, the greater excitation power it is exposed to. Similarly, the emitted photons are more efficiently captured when the fluorophore is near the core because the emitted photons have a higher chance to be captured before they are either scattered or absorbed by other particles.

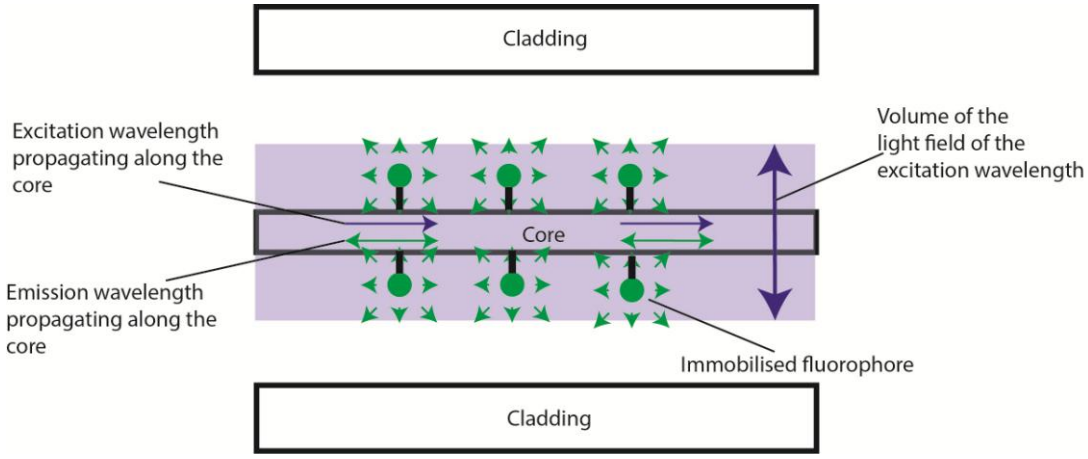

Figure 1.5: Schematic diagram of the fluorescence sensing mechanism in SCFs with immobilised fluorophores

1.2.3 Fabrication of suspended core fibres (SCFs)

A small core SCF is usually fabricated in two steps in order to obtain a sufficiently small core for use in sensing [35]. The first step is to fabricate a structured preform, which is a glass rod with a macroscopic internal structure. The second step is to draw the fibre from the preform. The resulting fibre has a microscopic internal structure, which has approximately the same geometrical cross-section as the preform. There are three common methods used to make a preform. The first method is by extrusion, whereby the glass billet is heated to a temperature close to the softening point and extruded through a die. The detailed procedure of fabrication of the SCFs by extrusion technique has been reported [16, 35]. However, this fabrication method is only applicable to 'soft glass' materials such as lead silicate, tellurite, bismuth and heavy metal fluoride glass, which have relatively low melting and softening points [16]. The second method to make a structured preform is to drill holes inside a glass rod; this operation is usually performed using an ultrasonic drilling machine [36]. However, this method is time consuming and the high surface roughness on the internal surface of the drilled holes can potentially increase the attenuation of the fibre [16]. The third method is to stack glass capillaries around a rod inside a tube; however this method is highly labour intensive and the reproducibility is highly dependent on the craftsmanship of the fabricator [16, 37]. The last two methods are theoretically possible for any glass types including silica. In this project the preforms for the

silica SCFs were fabricated using the drilling method, whereas the preforms for the lead silicates (F2) SCFs were fabricated by the extrusion method.

1.2.4 Attenuation of glass materials for suspended core fibre (SCF) fabrication

The attenuation spectrum of the glass material restricts the choice of fluorophore for the sensor fabrication; the optical fibre must be highly transparent both at the fluorophore's absorption and emission wavelengths.

Figure 1.6 shows the attenuation spectrum calculated from the internal transmission of bulk lead silicate (F2) glass from Schott and bulk silica glass (Suprasil 300) from Heraesus in the range of 400 nm to 1060 nm [38, 39]. The F2 glass shows lowest attenuation (greatest transmission) from 500 nm (UV-edge) to 1060 nm, whereas silica shows consistently low attenuation across this wavelength range. In terms of the attenuation within the visible-near infrared range silica glass is a better material than F2 because it provides less limitation in the choice of fluorophores. It is also noted that fluorophores excited at wavelengths close to the UV-edge are feasible and this will be further discussed in Chapter 2.

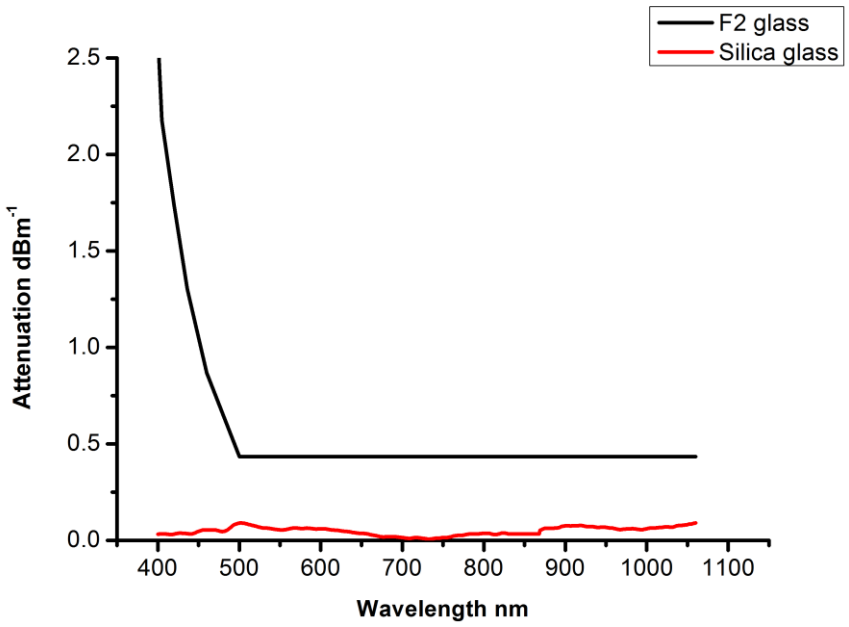

Figure 1.6: The attenuation spectra of bulk silica (Suprasil 300) (red line) and lead silicate (F2) glass (black line) for 10 mm lengths

1.2.5 Fluoroionophores

While the SCF can guide light, it does not provide any selective ion detection function intrinsically. Thus, to make an optical fibre into an ion sensor, it is necessary to have a molecular sensor (e.g. a fluoroionophore) that generates an optical signal when it reacts specifically with the targeted ion. A fluoroionophore consists of a fluorophore that is covalently linked to an ionophore which selectively binds to the target ion. When an ionophore binds to a specific ion, the fluorescence properties such as emission intensity or wavelength of the fluorophore are changed. Ideally, this change is proportional to the quantity of the target ions and thus the concentration of the target ions can be quantified. More information regarding the design and synthesis of cation and anion fluoroionophores can be found in the reviews written by Valeur *et.al* and Gunnlaugsson *et.al*. [25, 40] The latter in particular deals with the use of naphthalamide as an ion sensor and the reader is directed to this work for a comprehensive review of the area.

There are two main mechanisms by which an ionophore can alter the emission properties of a fluorophore through the binding of ions. These are photoinduced charge transfer (PCT) and photoinduced electron transfer (PET). Both mechanisms can be used for cations and anions sensing [28, 41, 42]. Each mechanism is described with the aid of selected examples in the following sections. The design concepts for PET and PCT sensors are different (Figure 1.7), with the main difference due to the presence of a spacer in the PET sensor between the ionophore and the fluorophore.

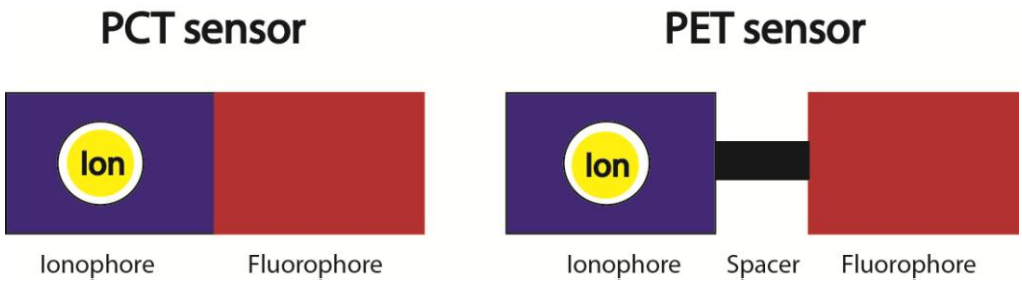

Figure 1.7: Molecular design concepts of PCT and PET fluoroionophores

1.2.5.1 Photoinduced charge transfer (PCT)

PCT is a light-induced intramolecular charge transfer process that changes the dipole moment of the fluorophore in the excited state. When the dipole moment is changed via the conjugated system, electrons are shifted from the electron donating group to the accepting group. The design approach for PCT fluoroionophores is to make either the donating group or the accepting group selective to the ion analyte under consideration (Figure 1.8a and b). Figure 1.8a shows the PCT mechanism for a PCT fluoroionophore where the electron donating group is part of the ionophore. In the absence of a cation, electrons donation from the secondary amine in the aza-crown ether to the accepting group (fluorophore) occurs; this process creates a particular dipole moment for the excited state. When the cation binds to the ionophore, it disturbs the charge transfer process and thus the excited state has higher potential energy relative to the unbound ionophore ($E_2 > E_1$) that causes blue shift of the absorption and emission spectra.

Figure 1.8b shows a PCT fluoroionophore where the electron accepting group is the ionophore. In this case, the electron donor is the tertiary amine nitrogen atom of the julolidyl ring and the acceptor is the carbonyl group. The excited state is stabilised when the ionophore binds to the cation and therefore the absorption and emission spectra undergo a red shift.

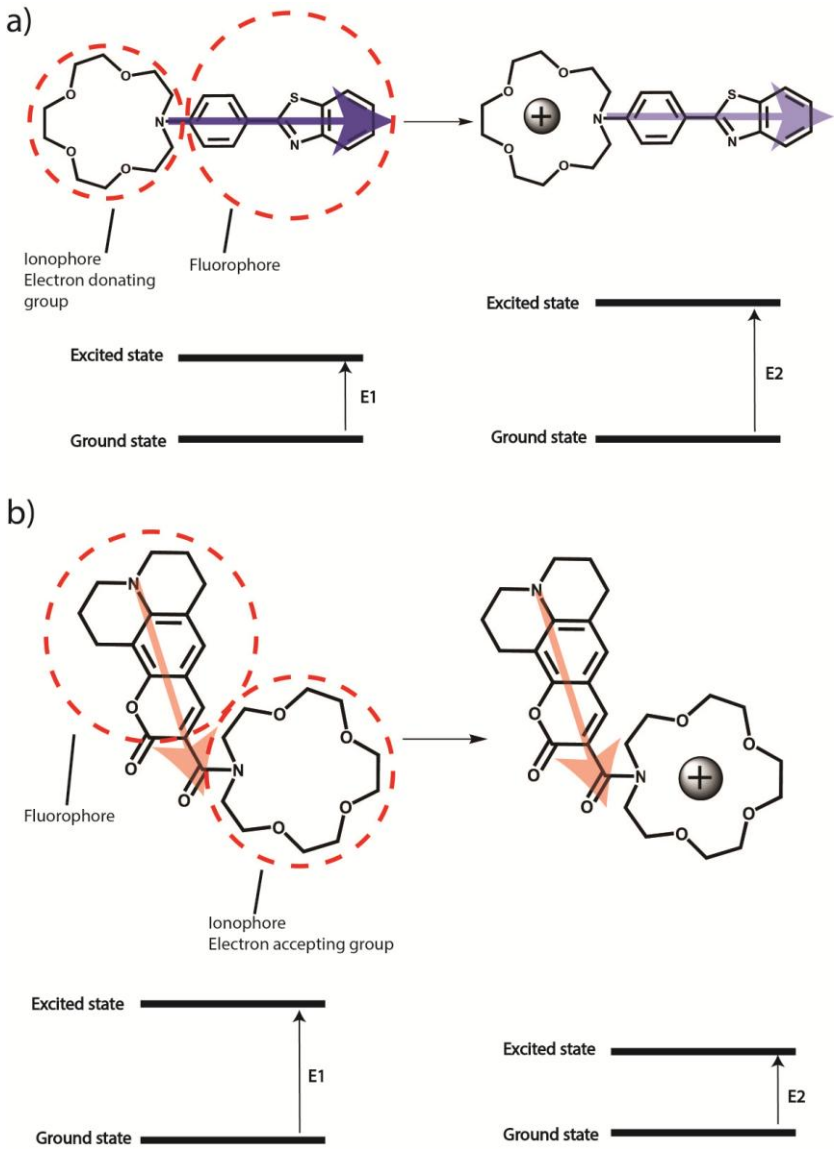

Figure 1.8: Schematic diagrams of PCT mechanisms. (a) The ionophore acts as the electron donating group or (b) the ionophore acts as the electron accepting group.

1.2.5.2 Photoinduced electron transfer (PET)

PET is a light-induced electron transfer process. The design approach is to link an ionophore to a fluorophore via a spacer moiety (Figure 1.7). The spacer is aliphatic and therefore the electron transfer between the ionophore and the fluorophore occurs through free space. This spacer prohibits any electronic interaction through the conjugated system; hence the absorption spectrum is independent of the ion interaction with the ionophore [25]. The ideal PET

fluoroionophore should only experience a change in quantum yield when it binds to the target ion.

The design of a PET fluoroionophore is based on thermodynamic calculations of the free energy of PET (ΔG_{PET}), which can be calculated from the redox potentials of the highest occupied molecular orbital (HOMO) of the independent fluorophore and the ionophore. It is noted that although both the fluorophore and the ionophore are parts of one molecule and therefore should have only one molecular orbital (MO), for the purposes of this calculation it is reasonable to consider them as two molecules with two separate MOs. The lower the ΔG_{PET}, the higher is the rate of PET. As the rate of emission is in competition with the PET process, the fluorophore is quenched when the PET rate is faster than the emission rate.

Figure 1.9a shows the PET mechanism for a cation sensor [43, 44]. In the excited state, the electron occupies the lowest unoccupied molecular orbital (LUMO) of the fluorophore. The first step of the PET quenching is the free space electron transfer from the HOMO of the unoccupied ionophore to the HOMO of the excited fluorophore. As a result the HOMO of the fluorophore is occupied and the excited electron from the LUMO cannot release its energy via fluorescence. In the second step, the excited electron in the LUMO of the fluorophore releases its energy via non-radiative decay to the environment. Thus, the fluorophore is quenched, or turned 'OFF'. When the ionophore binds to a cation, the potential energy of the HOMO of the ionophore decreases; therefore the rate of the PET process decreases. Quenching is no longer possible and the quantum yield and the emission intensity increases. The fluorophore is then turn 'ON'.

Figure 1.9b shows an example of anion sensing. Many anion PET fluoroionophores are OFF-ON sensors, so that fluorescence quenching occurs when the anion is bound. In the example shown in Figure 1.9b, Gunnlaugsson *et al.* suggests that fluorescence quenching is due to the electron donation from the anion that binds to the thiourea group by hydrogen bonds [25]. However, in general there is lack of a detailed explanation for the PET quenching mechanism in anion sensing [45].

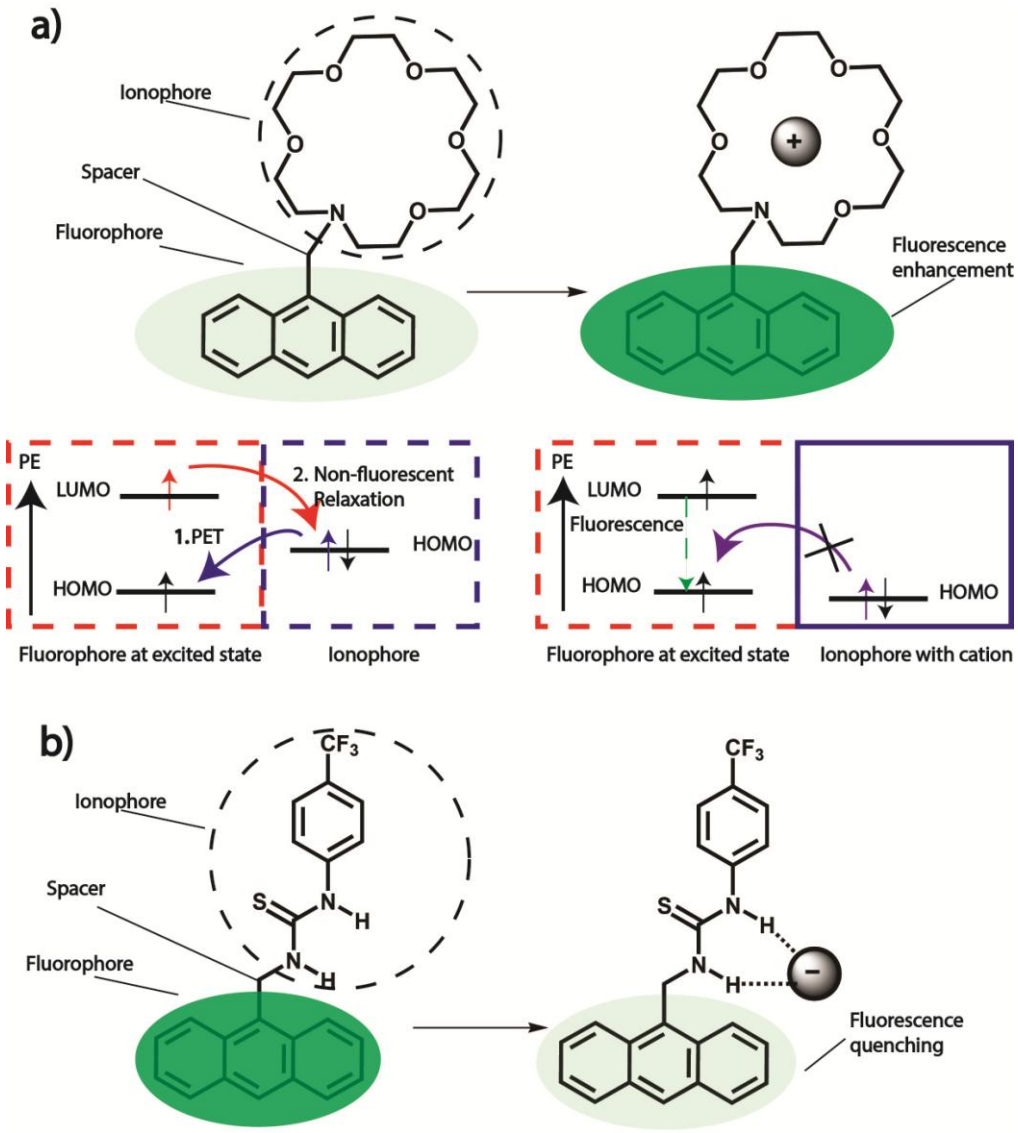

Figure 1.9: The PET mechanism for (a) cation and (b) anion detection

1.2.5.3 Choice of fluoroionophore for the suspended core fibre (SCF) ion sensor

In this project, we focused on using PET fluoroionophores in the SCF ion sensor for two reasons. The first is because 1,8-aminonaphthalimide containing PET sensors developed by He *et al*. showed promising results, including commercial examples for potassium, sodium and calcium ion sensing, which are the major components in soil solutions [26, 27, 46]. The second is that Gunnlaugsson *et al.* developed anion sensors for fluoride, acetate and hydrogen phosphate using the same 1,8-aminonaphthalimide fluorophore [47]. Thus both cation and anion sensing can be potentially achieved using the same or a very similar optical set-

up. The rationale of choosing this fluorophore is discussed in Chapter 2. The feasibility of using a particular PET fluoroionophore within a SCF depends on many factors, including the photostability of the fluorophore inside a SCF and the feasibility of attaching it onto a glass surface, which is discussed in Chapter 5.

1.2.6 Photobleaching of fluorophores

Photobleaching is the gradual decrease of emission intensity of the fluorophore after light exposure. This process not only diminishes the response of a sensor, it also introduces an extra variation in the emission signal that can cause errors in the measurement, and challenges in re-using the sensor. Photobleaching is not the same as fluorescence quenching, even though both processes diminish the emission intensity. Fluorescence quenching is caused by the change of the micro-environment of the fluorophore; while photobleaching is entirely a light induced phenomenon that occurs in conditions of intense light exposure such as when laser illumination is used.

There are two types of photobleaching, which are photophysical bleaching and photochemical bleaching. Figure 1.10 shows a schematic diagram of the excitation cycle and the photobleaching pathways [48-50]. In the normal excitation cycle the excited fluorophore relaxes to the singlet state and it either undergoes emission and then continues the cycle, or undergoes intersystem crossing (ISC) to the triplet state. From the triplet state, it can either relax back to the ground state by non-radiative pathways, or it can enter into a photophysical bleaching (D^+), which is likely to be a charged radical [48, 49]. The D^+ state usually has a long lifetime [48, 49]. From D^+, it can either slowly relax back to the ground state or it can react with other molecules such as singlet oxygen and chemically transform to other non-fluorescent photoproducts; this chemical transformation is referred as photochemical bleaching [48, 49]. Photochemical bleaching is irreversible [48, 49]. In contrast, photophysical bleaching is reversible. Anti-photobleaching reagents such as Trolox (6-hydroxy-2,5,7,8-tetramethylchroman-2-carboxylic acid) can shorten the regeneration time from D^+ to the ground state and thereby reduces the opportunity for the irreversible photochemical bleaching [51].

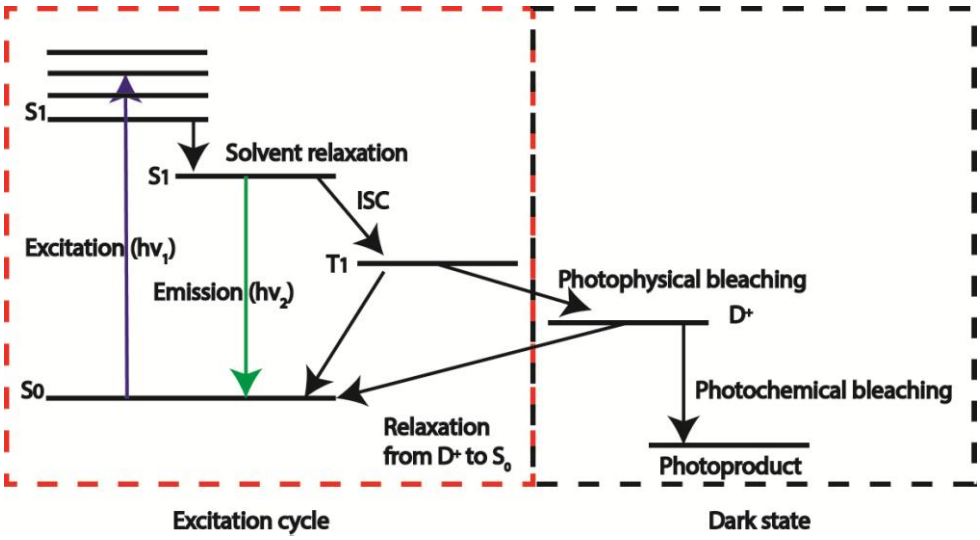

Figure 1.10: A simplified Jablonski diagram illustrating the normal excitation cycle and photobleaching possibilities

The photochemical bleaching rate is strongly dependent on the excitation intensity and the concentration of oxygen [52]. Fluorophores inside a SCF experience significantly stronger light intensities compared with that in a cuvette. Therefore, the photochemical bleaching rate of a fluorophore inside the SCF is higher compared with cuvette and this is an important consideration for the fluorophore choice [24].

1.2.7 Surface attachment strategies

Attachment of a fluoroionophore to the glass surface is a major consideration in this project. The first step in one glass functionalisation strategy is to introduce organic coatings onto the glass surface, in order to covalently attach sensor molecules. There are a number of ways to introduce organic functional group on the glass surface; silane coupling reagents and polyelectrolytes are two commonly used glass surface functionalisation reagents for SCFs [18, 21, 23, 53-56]. The attachment mechanisms of both reagents are described in the following sections.

Silane coupling reagents (Figure 1.11a) are silicon based molecules containing four substituents. Three of the substituents are hydrolysable groups (X), which are commonly halogens, hydroxyl groups, and methyl or ethyl ethers for glass attachment. The R group is an organic functional group that enables further covalent attachment of small organic molecules (e.g. fluoroionophores) or large

bioorganic molecules (e.g. proteins). The R group choice depends on what kind of functional groups are available in the counterpart molecules. Commonly available R groups are amine, carboxylate, epoxy, thiol and isocyanate. Figure 1.11b shows the simplified mechanism for silane coupling on the glass surface [57]. Before the attachment, at least one of the X group need to be hydrolysed to form a silanol group that undergoes a condensation reaction with a silanol group on the glass surface. The details of the silane reaction on the glass surface are discussed in Chapter 3C.

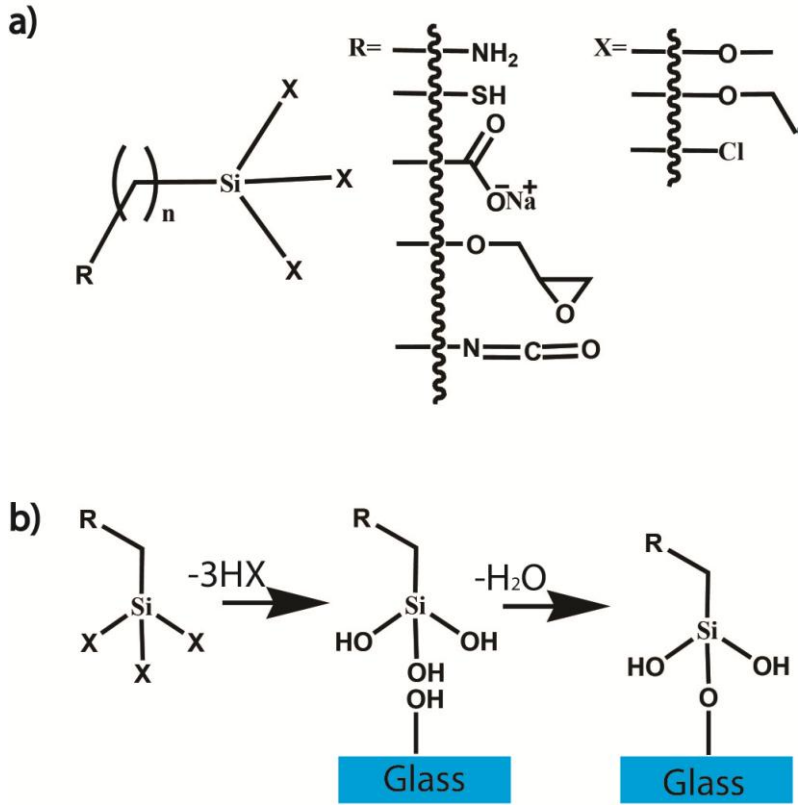

Figure 1.11: (a) General structures of silane reagents and (b) a simplified mechanism of silane condensation on a glass surface

Polyelectrolytes are charged polymers, which contain a variety of functional groups such as amines, carboxylates or sulfonates. Figure 1.12 shows the structure of common polyelectrolytes such as poly(allylamine) (PAH), poly(acrylic acid) (PAA) sodium salt and poly(sodium 4-styrenesulfonate) (PSS). Polyelectrolytes are deposited layer by layer, to form a polyelectrolyte multilayer film (PEM) that displays functional groups on the surface. The process of polyelectrolyte deposition on a glass surface is discussed in detail in Chapter 3. For glass coating,

the deposition usually commences with a positive polyelectrolytes followed by a negative polyelectrolytes and so on.

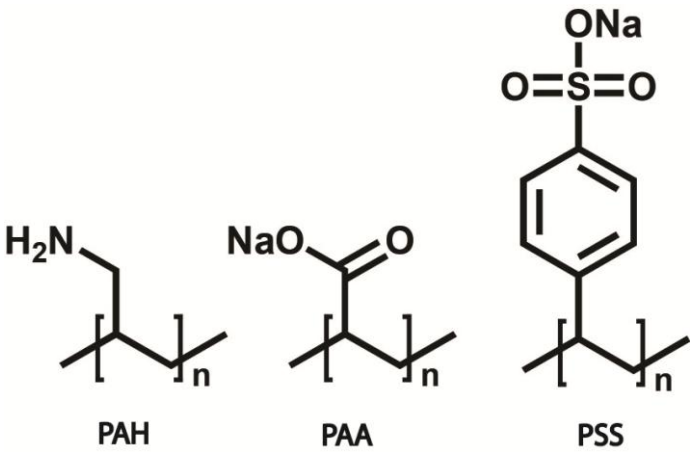

Figure 1.12: The structures of poly(allylamine) (PAH), poly(acrylic acid) (PAA) sodium salt and poly(sodium 4-styrenesulfonate) (PSS)

1.2.8 Surface analysis techniques

The key challenge in the surface functionalisation of glass materials in this project is to identify suitable surface analysis techniques. This is not a trivial task because the thickness of the functionalised layer is in the range of a few nanometres. The analysis techniques have to be surface sensitive in order to provide important information such as physical topography, thickness, chemical composition and description of the chemical bonding, and capable of analysing samples with particular geometric constraints (e.g. curved surfaces). Optimisation of the coating or attachment procedures is based on information obtained from the surface analysis. In addressing this challenge, it was noted that no single surface analysis technique can provide all the desired information about a surface and thus, different but complementary analysis techniques are required.

In this project, five surface analysis techniques were used to analyse the functionalised glass surface. They are fluorescence imaging, X-ray photoelectron spectroscopy (XPS), time of flight secondary ion mass spectrometry (ToF-SIMS), atomic force microscopy (AFM) and spectroscopic ellipsometry (SE). All of these techniques are commonly used in surface analysis for functionalised plastics, silicon wafers and glass materials [58-64]. Background of these surface analysis techniques are described in the following sections.

1.2.8.1 Fluorescence imaging

The fluorescence imager (Typhoon^{TM} imager) is a variable mode imager that can capture digital images of fluorescent and chemiluminescent samples. This instrument is widely used in biological science [65]. The instrument utilised in this project has three internal lasers with emission wavelengths of 488, 532 and 633 nm and a photomultiplier tube (PMT) detector. Unlike a spectrofluorometer where the emission spectrum is recorded after excitation, a Typhoon^{TM} imager records an image of the emission received by the PMT. Since the light received by the PMT includes some of the unwanted wavelengths such as the excitation light, a filter has to be used to ensure the light received is from the emission spectrum of the fluorophore. The intensity of the signal can be quantified by the associated instrument software. The advantage of using a Typhoon^{TM} imager over a spectrofluorometer is the ability to perform high throughput analysis on glass samples of different geometric constraints. Multiple glass slides can be loaded on the large imaging plate (43 cm x 35 cm) and analysed together. The Typhoon^{TM} imager also records spatial information regarding the coverage of the fluorophore. A disadvantage is that the Typhoon does not generate an emission spectrum and, thus, spectral shifts or variation in the full width at half maximum (FWHM) cannot be determined. In this project, this technique is used for determining the surface density of the fluorophores or fluoroionophores.

1.2.8.2 X-ray photoelectron spectroscopy (XPS)

X-ray photoelectron spectroscopy (XPS) is a type of electron spectroscopy that provides qualitative and quantitative information of all elements except for hydrogen and helium [66]. The sampling depth of XPS is approximately 10 nm and is therefore highly surface sensitive. XPS provides information on the surface elemental composition with typical errors less than 10% [66]. Moreover, it can provide information on the chemical environment of an element, such as oxidation state or the identity of atoms covalently bonded to the element under examination [66].

The principle of XPS is based on the Einstein equation for the photoelectric effect (Equation 2) that describes the phenomenon of electron emission from a solid, liquid or gas after absorbing energy from light. The higher the energy of the absorbed light, the more electrons are emitted from the material.

$$E_{kin} = E_B + hv + \varphi_{sp} \qquad \text{(Equation 2)}$$

In Equation 2, E_{kin} is the kinetic energy measured by the spectrometer, hv is the known energy from the X-ray source, and φ_{sp} is the spectrometer work function, which is a known parameter. Therefore, E_B, which is the binding energy of the electron in the atom, can be calculated. E_B is specific for each of element and its environment. Hence, the identity of the element and its bonding environment can be obtained from the measured spectrum. After subtraction of the background spectrum, the area of a particular peak is proportional to the relative quantity of each element, so that the atomic percentage can be calculated from the XPS spectrum. The sub-peaks, which provide information on the chemical bonding, can be identified by the deconvolution of the main peak. Figure 1.13 shows a schematic diagram of how an XPS measurement is conducted. In this project, this technique is used to determine the surface chemistry of the glass material, APTES coating and the surface attached fluoroionophores.

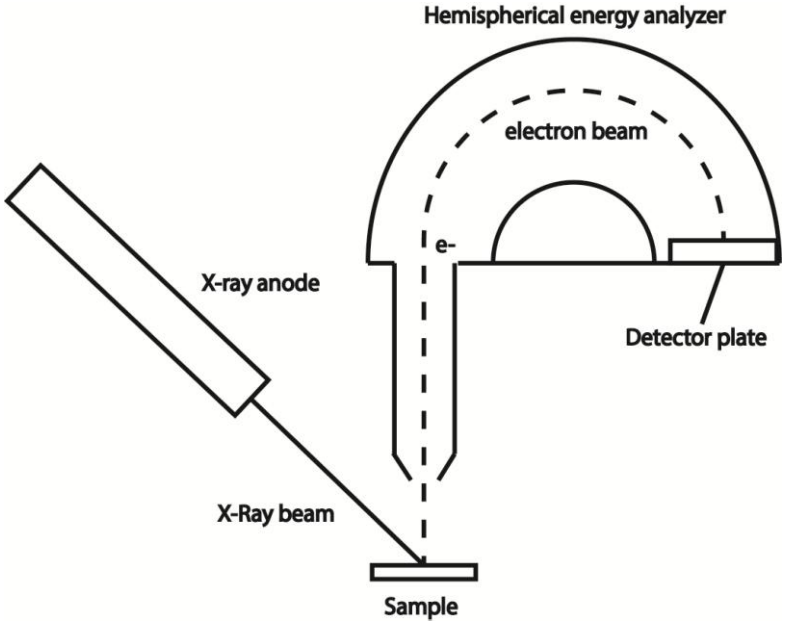

Figure 1.13: A schematic diagram of an XPS measurement

1.2.8.3 Time of flight secondary ion mass spectrometry (ToF-SIMS)

Figure 1.14 shows how time of flight secondary ion mass spectrometry (ToF-SIMS) data are collected. The surface of a sample is bombarded by a high energy ion beam (the primary ion beam/source). A large number of particles are emitted from the surface after the collision but only charged secondary ions can be detected by the time of flight (ToF) mass spectrometer. The secondary ions are accelerated to approximately the same kinetic energy by a fixed potential and then fly through a tube before they hit the detector. The flight time (T) for each ion is recorded. Based on Equation 3, given that the potential (V) and the tube length (L) are constant; the measured flight time (T) is proportional to the mass-to-charge (*m/z*) ratio.

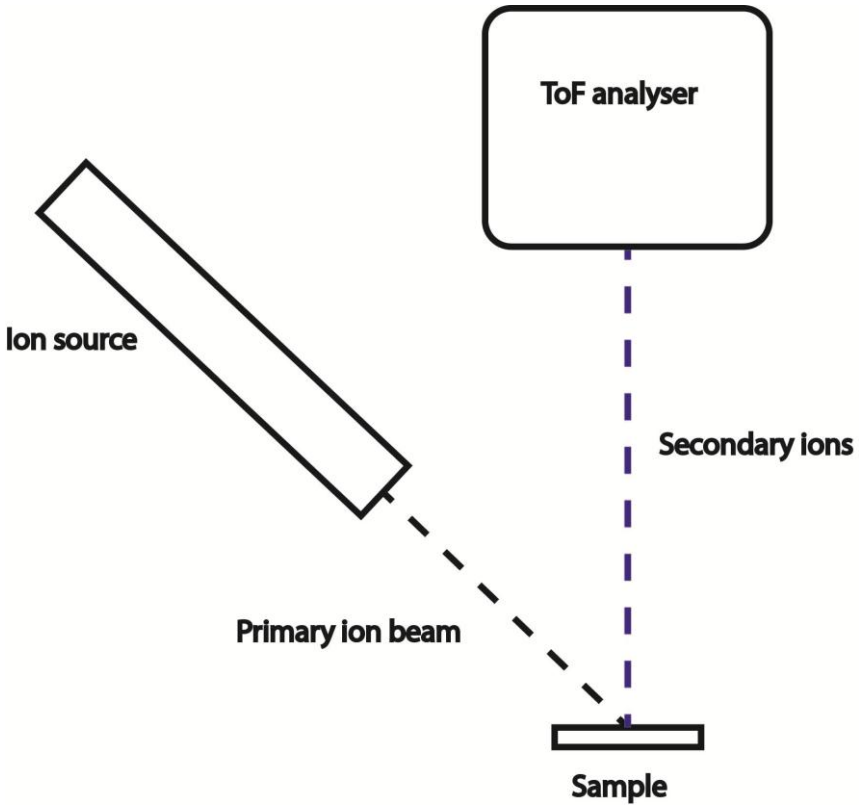

Figure 1.14: A schematic diagram of the ToF-SIMS measurement

$$T = L\left(\frac{m}{2zV}\right)^{\frac{1}{2}} \qquad \text{(Equation 3)}$$

The ToF mass spectrometer has a high mass resolution (m/Δm = 5000 –20000) and sensitivity. The high mass resolution makes ToF-SIMS good for analysing organic materials or coatings because ToF-SIMS generates a large number of molecular fragments with similar m/z, while the high sensitivity enables the detection of larger molecular fragments that are generated in smaller quantities.

The quantity of data generated by a ToF-SIMS analysis is enormous, the data is complex and the relative intensity of each peak is inter-related. Thus, the main challenge is how to interpret the data generated from ToF-SIMS. To extract data such as surface chemical composition, multivariate analysis (MVA) is required. Principal component analysis (PCA) is the most common MVA method for analysing ToF-SIMS data including imaging data obtained from ToF-SIMS [67]. PCA of ToF-SIMS data has been applied on many surfaces such as polymers, self-assembled monolayers and biological samples. The mathematical background of PCA is described in the following section. In addition to the above data, ToF-SIMS is able to perform imaging and depth profiling analyses. In this project, this technique is used to determine the surface chemistry of the glass material, APTES coating and the surface attached fluoroionophores. The imaging capability provides a surface chemical map that gives information about the coverage of the APTES coating and fluoroionophore. The depth profiling capability analyses the chemical composition as a function of depth, which provides a relative measurement of the thickness of the surface coating.

1.2.8.4 Principal component analysis (PCA) for ToF-SIMS data analysis

ToF-SIMS data are interrelated or non-orthogonal in mathematical terms, because it describes fragments that originate from the same surface. PCA is a multivariate analysis method suitable for solving this problem. The objective of PCA is to reduce the dimension of the data by describing only a small number of orthogonal factors/principal components (PC) that capture the largest amount of the variance within the multidimensional, but non-orthogonal data set [68]. PCA can be described as forming a new imaginary vector space by rotating the axis of the original 2D plot of the data, in order to capture the largest amount of variance. Figure 1.15 shows a schematic representation of PCA analysis where the red

square is an imaginary vector space that has two principal components (PC1 and PC2) that capture the largest amount of variance of the original data set.

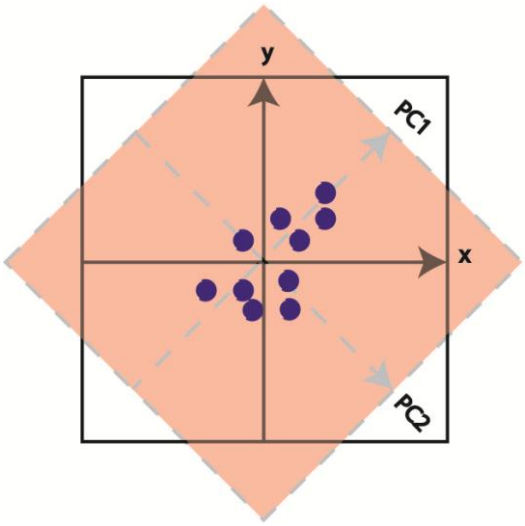

Figure 1.15: A schematic representation of PCA analysis

Mathematically, PCA is an eigenvector decomposition of the non-orthogonal data matrix [A] (Equation 4). The data matrix is decomposed into a number of single column matrices called eigenvectors with their associated eigenvalues.

$$[A]x_n = [\lambda_n]x_n \qquad \text{(Equation 4)}$$

In Equation 4, x_n is the *n*th eigenvector and λ_n is its associated eigenvalue. The total number of non-zero eigenvectors is N, which is the rank of the data matrix. These eigenvectors are optimised for describing the variance of the data vector space. More importantly, each eigenvector is orthogonal to each other, thus it is not interrelated as in the original data matrix. The value of the eigenvalue of each eigenvector represents the amount of variance captured by this eigenvector, where each eigenvector is a PC. The PCs are then arranged in descending order by their corresponding eigenvalue to form an eigenvector matrix [X] (Equation 5):

$$[X] = (x_1\, x_2\, x_3 \ldots\ldots x_N) \qquad \text{(Equation 5)}$$

where x_1 is the PC that captures the largest amount of variance. The percentage of variance captured by each eigenvector is calculated based on Equation 6:

$$\% \text{ of variance captured} = \frac{\lambda_n}{\text{Sum of all } \lambda_n} \times 100\% \qquad \text{(Equation 6)}$$

The data matrix [A] is transformed into a new orthogonal matrix [Z] that is called the score matrix, obtained by multiplying the eigenvectors (PCs) matrix [X] (Equation 7).

$$[Z] = [A][X] \qquad \text{(Equation 7)}$$

In summary, the data matrix [A] is decomposed into two matrices (Equation 8). Figure 1.16 shows the relationship and the composition of the data [A], score [Z] and transpose of eigenvectors/PCs [X] matrices. The scores [Z] matrix represents the relationship between samples in the PC vector space. From the scores 2D plot of the first two PCs, patterns or clusters of samples can be recognised. The eigenvectors [X] matrix is also known as the loading matrix and it represents the correlation between a variable from the original data matrix [A] to the scores of PCs. The loading matrix shows the magnitude and the directions of the measured variable contributing to the score.

$$[A] = [Z][X]^{-1} \qquad \text{(Equation 8)}$$

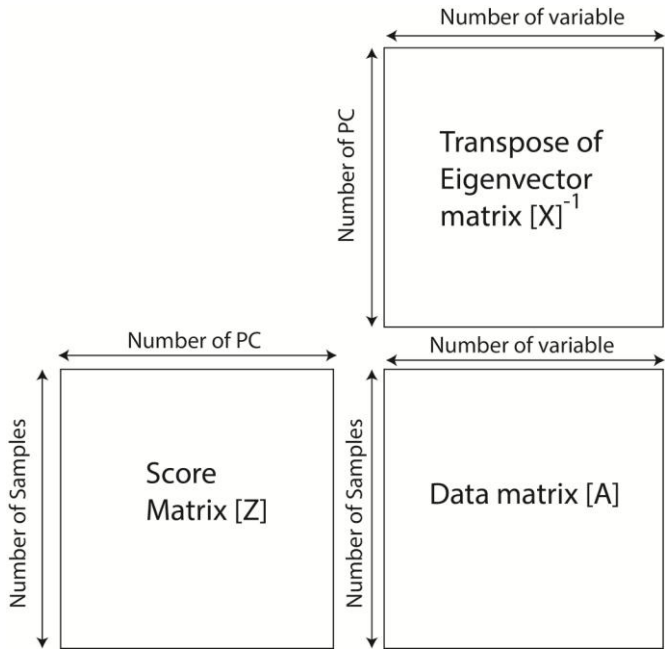

Figure 1.16: The relationship and the composition of the data [A], score [Z] and transpose of eigenvector/PC [X] matrices

Figure 1.17 shows a hypothetical example of a PCA. The score plot shows clear clustering of Group 1 and 2, which alternatively show similar positive or negative PC1 scores. The loading plot shows that variables d, e and f have a positive correlation to the PC1 score; whereas variable a, b and c have a negative correlation to the PC1 score. The conclusion of this analysis is that Group 1 and Group 2 are different and that Group 1 consists of variable d, e and f, whereas Group 2 consists of variable a, b and c.

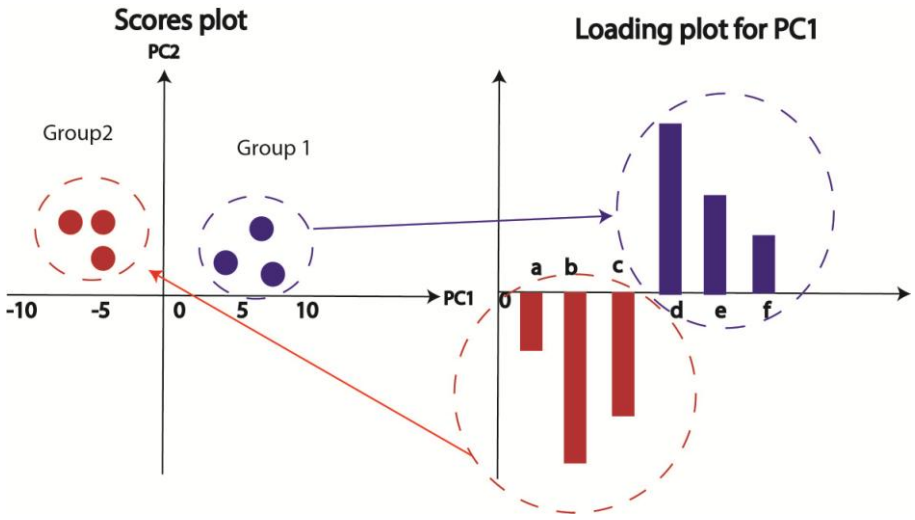

Figure 1.17: A hypothetical example of PCA

1.2.8.5 Atomic force microscopy (AFM)

AFM captures a topographic image on the nanometre scale. The main reason for using AFM in this project is to measure surface roughness. Figure 1.18 shows a schematic diagram of the operation of AFM. The probe (cantilever) has a sharp tip that interacts with the surface of the sample. The interaction is caused by the small attraction force between atoms. The movement of the cantilever causes deflection of the laser light allowing a topographic image of the surface to be captured. In this project, this technique is used to determine the surface roughness before and after the functionalisation process on silicon wafer, which was used as the model system of silica glass. Details are discussed in Chapter 3.

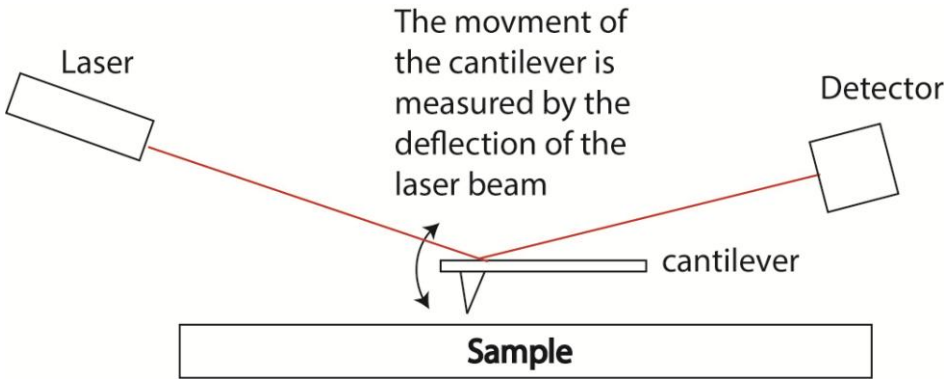

Figure 1.18: A schematic diagram of the AFM measurements

1.2.8.6 Spectroscopic ellipsometry (SE)

SE measures the change in the polarization of light from the reflection or transmission of a surface. The change in polarization is quantified by an amplitude ratio (ψ) and s phase difference (Δ). In the UV-Visible spectroscopic ellipsometry (VASE) ψ and Δ are recorded at each wavelength for each angle. As a result the instrument is able to measure film thicknesses, refractive indices, dielectric constants and absorption coefficients [69].

The data analysis is performed by a commercial software program that fits the data into a constructed optical model. In terms of analysing the thickness of a film on a substrate, the optical model requires the refractive indices for both film and substrate, and the thickness of the substrate. The only variable is the thickness of the film. The mean-squared-error (MSE), which is the measure of goodness of fit, is calculated for the fitting as a feedback parameter [70]. The program continuously changes the variable until it reaches the lowest MSE [69]. In this project, this technique is for determining the APTES coating thickness on silicon wafers, which infer as a model system of silica glass. Details are discussed in Chapter 3.

1.3 Research objectives

The objectives of this work presented in this thesis were to:

1. Demonstrate solution ion sensing by mixing PET fluoroionophores and the analytes in SCFs (operating scenario A).
2. Develop an understanding of surface functionalisation of silica and lead silicate glass materials for SCF sensor fabrication.
3. Develop analysis methodologies for the surface attached PET fluoroionophores on glass materials.
4. Demonstrate ion sensing for surface bound PET fluoroionophores within SCFs (operating scenario B).

1.4 Thesis structure

This thesis describes research on the development of a novel optical fibre ion sensor using SCFs as the optical platform and PET fluoroionophores as the molecular sensor. The fundamental aspects towards both operating scenario A and B have been described in Section 1.2. The flowchart below (Figure 1.19) illustrates the connection between the chapters and appendices in this thesis.

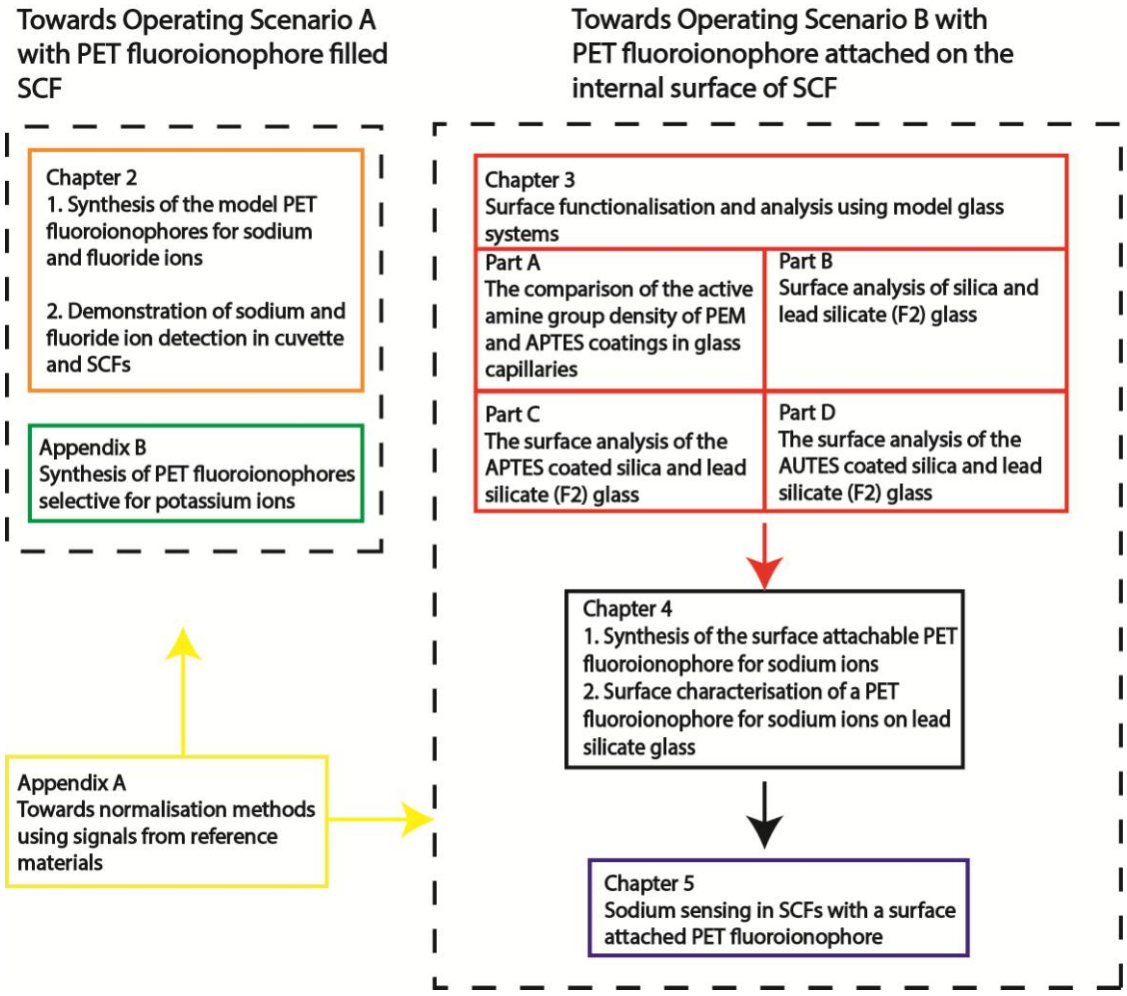

Figure 1.19: A flowchart showing the connection between the chapters and appendices in this thesis

Chapter 2 covers feasibility experiments based on two model fluoroionophores, which have either phenylaza-15-crown-5 as the ionophore for sodium or thiourea as the ionophore for fluoride. Both ionophores are covalently linked to 1,8-naphthalimide which acts as the fluorophore. This chapter commences with the synthesis of a 4-amino-1,8-naphthalimide derivative, which is the fluorophore

used throughout the project. This work is then followed by the synthesis and characterisation of the model fluoroionophores for sodium and fluoride ions. Sodium ions and fluoride ions detection are demonstrated in both cuvettes and SCFs. All experiments discussed in this chapter utilise the first operating scenario, requiring the PET fluoroionophore to be mixed with the analyte before the injection into the SCF.

In Chapter 3, the use of glass model systems such as silicon wafers, extruded slides, capillaries and unstructured fibres for studying the surface functionalisation of glass are discussed. This chapter is divided into four parts. Part A provides a comparison of the active amine group density following polyelectrolytes multilayer (PEM) and 3-aminopropyltriethoxysilane (APTES) functionalisation methods. The active amine groups were identified by covalent attachment to biotin, which was then labelled by quantum dot-tagged streptavidin. The experiments were performed in various capillaries with different glass materials. The pros and cons of PEM and APTES for this project are discussed. In Part B, the surface composition and the structure of the silica and lead silicate glasses are discussed based on the results of the elemental and high resolution XPS analysis. This information is important in understanding the glass substrate surface chemistry for surface functionalisation. In Part C, XPS was used to determine the chemical composition of APTES coatings on silica and lead silicate (F2) glass slides. AFM and SE were used to determine the surface roughness and thickness of the APTES coating on silica glass. Unstructured fibres coated with APTES were analysed using ToF-SIMS in order to provide complementary information about the surface chemistry of APTES on the silica and lead silicate glass substrates. The reproducibilities of APTES on silica and lead silicate (F2) glass are also discussed. Finally, in Part D the application of an alternative silane reagent, 11-aminoundecyltriethoxysilane (AUTES), is discussed. AUTES has the potential to provide improved coating reproducibility due to its longer aliphatic hydrocarbon chain (11 carbons) relative to APTES. XPS and AFM measurements were performed to determine the chemical composition and surface roughness of AUTES coated silica glass and silicon wafers.

In Chapter 4, the attachment chemistry of PET fluoroionophores on APTES-grafted F2 glass is reported. The PET fluoroionophore-APTES coatings of the

slides were analysed by fluorescence imaging, XPS, ToF-SIMS, ToF-SIMS imaging and ToF-SIMS depth profiling. Each analysis technique provided complementary information for semi-quantitative determinations of the surface density of the fluoroionophores, coating thickness and coverage of the PET fluoroionophores on APTES coating.

In Chapter 5, the feasibility of sodium sensing by surface attached PET fluoroionophore within silica SCFs was investigated. The technical challenges and sensing theory for PET fluoroionophore functionalised SCFs are also discussed.

Chapter 6 concludes the thesis and provides future research directions for the development of optical fibre ion sensors using SCFs as the optical platform with or without surface-attached PET fluoroionophores.

In Appendix A, attempts at using intrinsic Raman signals from the glass and an extrinsic reference from Qdots as the emission intensity standard for signal normalisation are discussed. Finally, in Appendix B the attempted syntheses of aminonaphthalimide based potassium-selective PET fluoroionophores are discussed.

1.5 Summary of all model compounds

As described in the previous sections, most of the experiments described in this thesis are based on model fluorophores and fluoroionophores. Figure 1.20 shows structures of all model compounds used in experiments discussed in this thesis.

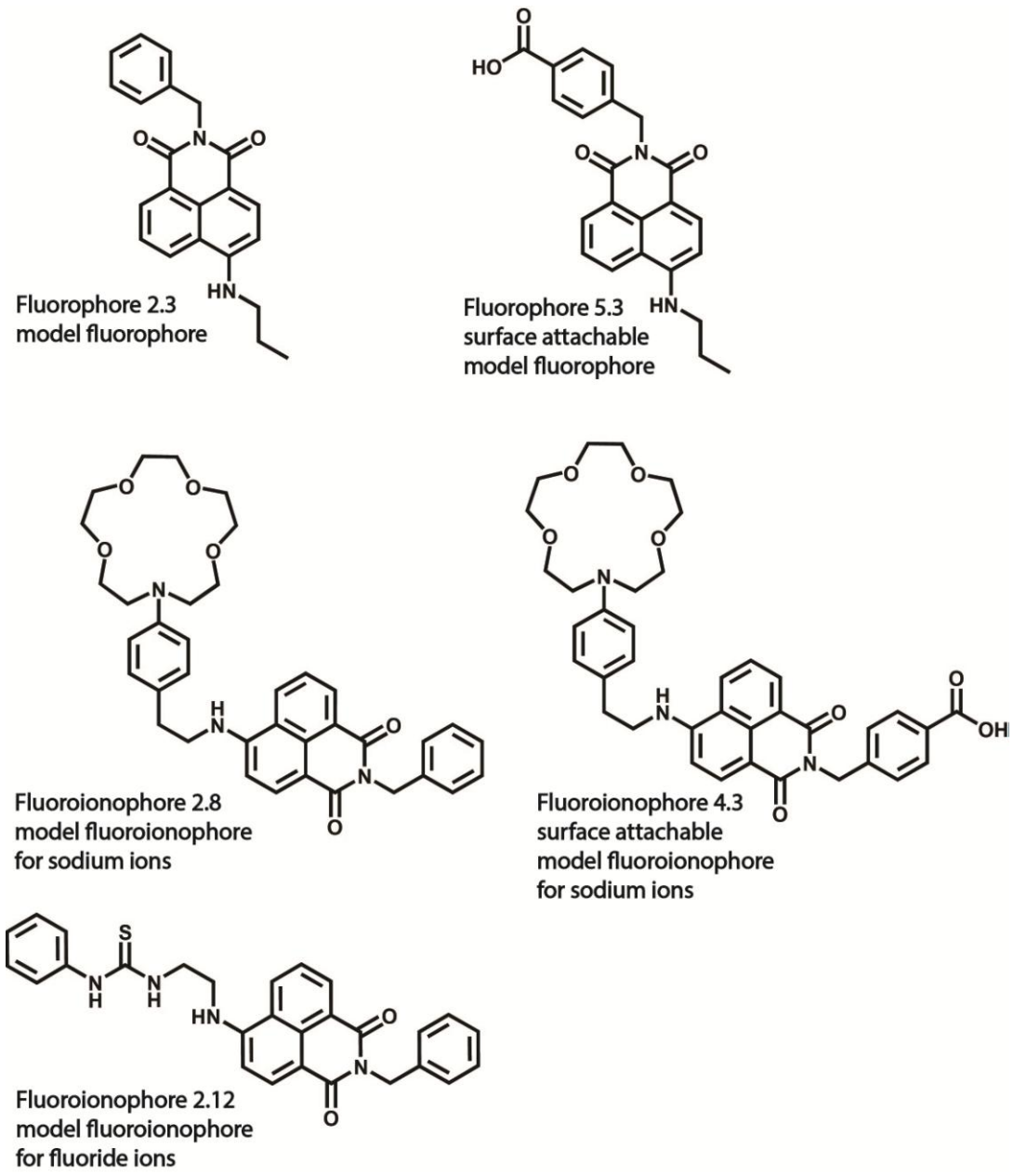

Figure 1.20: Summary of model fluorophores and model fluoroionophores used in experiments discussed in this thesis

1.6 References

1. Orlov, D.S., *Soil Chemistry*, ed. V.S. Kothekar. 1992, Brookfield: A.A. Balkema publisher.

2. Bohn, H.L., McNeal, B., and O'Connor, G., *Soil Chemistry*. 3rd ed. 2001, New York: John Wiley &Sons, Inc.

3. Smethurst, P.J., *Soil solution and other soil analyses as indicators of nutrient supply: a review.* Forest Ecology and Management, 2000. **138**(1-3): p. 397-411.

4. Filep, G., *Soil Chemistry Processes and Constituents*. 1999, Budapest: Akademiai Kiado.

5. Kim, H., Sudduth, K.A., and Hummel, J.W., *Soil macronutrient sensing for precision agriculture.* Journal of Environmental Monitoring, 2009. **11**: p. 1810-1824.

6. Dahlquist, R.L. and Knoll, J.W., *Inductively Coupled Plasma-Atomic Emission Spectrometry - Analysis of Biological-Materials and Soils for Major, Trace, and Ultra-Trace Elements.* Applied Spectroscopy, 1978. **32**(1): p. 1-29.

7. Fassel, V.A. and Kniseley, R.N., *Inductively Coupled Plasma - Optical Emission-Spectroscopy.* Analytical Chemistry, 1974. **46**(13): p. 1110-&.

8. Ouimette, D.G. and Coffey, M.D., *Quantitative-Analysis of Organic Phosphonates, Phosphonate, and Other Inorganic Anions in Plants and Soil by Using High-Performance Ion Chromatography.* Phytopathology, 1988. **78**(9): p. 1150-1155.

9. Kim, H.J., Hummel, J.W., Sudduth, K.A., and Motavalli, P.P., *Simultaneous analysis of soil macronutrients using ion-selective electrodes.* Soil Science Society of America Journal, 2007. **71**(6): p. 1867-1877.

10. Koryta, J., *Ion-Selective Electrodes.* Annual Review of Materials Science, 1986. **16**: p. 13-27.

11. Buhlmann, P. and Chen, L.D., *Ion-selective electrodes with ionophore-doped sensing membranes*. Supramolecular Chemistry: From Molecules to Nanomaterials. Vol. 5. 2012, New York: John Wiley & Sons, Ltd.

12. Bakker, E. and Meyerhoff, M.E., *Ionophore-based membrane electrodes: new analytical concepts and non-classical response mechanisms.* Analytica Chimica Acta, 2000. **416**(2): p. 121-137.

13. Zuliani, C. and Diamond, D., *Opportunities and challenges of using ion-selective electrodes in environmental monitoring and wearable sensors.* Electrochimica Acta, 2012. **84**: p. 29-34.

14. Dybko, A., *Errors in Chemical Sensor Measurements.* Sensors, 2001. **1**: p. 29-37.

15. Laegsgaard, J. and Bjarklev, A., *Microstructured optical fibers - Fundamentals and applications.* Journal of the American Ceramic Society, 2006. **89**(1): p. 2-12.

16. Monro, T.M. and Ebendorff-Heidepriem, H., *Progress in microstructured optical fibers.* Annual Review of Materials Research, 2006. **36**: p. 467-495.

17. Monro, T.M., Richardson, D.J., and Bennett, P.J., *Developing holey fibres for evanescent field devices.* Electronics Letters, 1999. **35**(14): p. 1188-1189.

18. Monro, T.M., Warren-Smith, S., Schartner, E.P., Francois, A., Heng, S., Ebendorff-Heidepriem, H., and Afshar, S., *Sensing with suspended-core optical fibers.* Optical Fiber Technology, 2010. **16**(6): p. 343-356.

19. Warren-Smith, S.C., Sinchenko, E., Stoddart, P.R., and Monro, T.M., *Distributed Fluorescence Sensing Using Exposed Core Microstructured Optical Fiber.* Ieee Photonics Technology Letters, 2010. **22**(18): p. 1385-1387.

20. Kostecki, R., Ebendorff-Heidepriem, H., Davis, C., McAdam, G., Warren-Smith, S.C., and Monro, T.M., *Silica exposed-core microstructured optical fibers.* Optical Materials Express, 2012. **2**(11): p. 1538-1547.

21. Ruan, Y., Foo, T.C., Warren-Smith, S., Hoffmann, P., Moore, R.C., Ebendorff-Heidepriem, H., and Monro, T.M., *Antibody immobilization within glass microstructured fibers: a route to sensitive and selective biosensors.* Optics Express, 2008. **16**(22): p. 18514-18523.

22. Warren-Smith, S.C., Nie, G., Schartner, E.P., Salamonsen, L.A., and Monro, T.M., *Enzyme activity assays within microstructured optical fibers enabled by automated alignment.* BIOMEDICAL OPTICS EXPRESS, 2012. **3**(12): p. 3304-3313.

23. Warren-Smith, S.C., Heng, S., Ebendorff-Heidepriem, H., Abell, A.D., and Monro, T.M., *Fluorescence-Based Aluminum Ion Sensing Using a Surface-Functionalized Microstructured Optical Fiber.* Langmuir, 2011. **27**(9): p. 5680-5685.

24. Schartner, E.P., *Hydrogen peroxide sensing with microstructured optical fibres*, in *School of Chemistry and Physics*. 2011, The University of Adelaide.

25. Gunnlaugsson, T., Glynn, M., Tocci, G.M., Kruger, P.E., and Pfeffer, F.M., *Anion recognition and sensing in organic and aqueous media using luminescent and colorimetric sensors.* Coordination Chemistry Reviews, 2006. **250**(23-24): p. 3094-3117.

26. He, H.R., Mortellaro, M.A., Leiner, M.J.P., Fraatz, R.J., and Tusa, J.K., *A fluorescent sensor with high selectivity and sensitivity for potassium in water.* Journal of the American Chemical Society, 2003. **125**(6): p. 1468-1469.

27. He, H.R., Mortellaro, M.A., Leiner, M.J.P., Young, S.T., Fraatz, R.J., and Tusa, J.K., *A fluorescent chemosensor for sodium based on photoinduced electron transfer.* Analytical Chemistry, 2003. **75**(3): p. 549-555.

28. de Silva, A.P., Moody, T.S., and Wright, G.D., *Fluorescent PET (Photoinduced Electron Transfer) sensors as potent analytical tools.* Analyst, 2009. **134**(12): p. 2385-2393.

29. Lee, C.Y., Chang, C.L., Wang, Y.N., and Fu, L.M., *Microfluidic Mixing: A Review.* International Journal of Molecular Sciences, 2011. **12**(5): p. 3263-3287.

30. Skoog, D.A., Holler, E.J., and Crouch, A.R., *Principles of Instrumental Analysis*. 6th ed. 2007, Canada: Brooks/Cole.

31. Lakowicz, J.R., *Principles of Fluorescence Spectroscopy*. 3rd ed. 2006, New York: Springer science+business Media, LLC.

32. Afshar, S., Warren-Smith, S., and Monro, T., *Enhancement of fluorescence-based sensing using microstructured optical fibres.* Optics Express, 2007. **15**(26): p. 17891-17901.

33. Afshar, S.V., Ruan, Y.L., Warren-Smith, S.C., and Monro, T.M., *Enhanced fluorescence sensing using microstructured optical fibers: a comparison of forward and backward collection modes.* Optics Letters, 2008. **33**(13): p. 1473-1475.

34. Warren-Smith, S.C., Afshar, V.S., and Monro, T.M., *Fluorescence-based sensing with optical nanowires: a generalized model and experimental validation.* Optics Express, 2010. **18**(9): p. 9474-9485.

35. Ebendorff-Heidepriem, H., Warren-Smith, S.C., and Monro, T.M., *Suspended nanowires: Fabrication, design and characterization of fibers with nanoscale cores.* Optics Express, 2009. **17**(4): p. 2646-2657.

36. Webb, A.S., Poletti, F., Richardson, D.J., and Sahu, J.K., *Suspended-core holey fiber for evanescent-field sensing.* Optical Engineering, 2007. **46**(1).

37. Dong, L., Thomas, B.K., and Fu, L.B., *Highly nonlinear silica suspended core fibers.* Optics Express, 2008. **16**(21): p. 16423-16430.

38. Heraeus, *Transmission calculator*. 2013.

39. Schott (2013) *Datasheet F2*.

40. Valeur, B. and Leray, I., *Design principles of fluorescent molecular sensors for cation recognition.* Coordination Chemistry Reviews, 2000. **205**: p. 3-40.

41. Wu, F.Y., Li, Z., Guo, L., Wang, X., Lin, M.H., Zhao, Y.F., and Jiang, Y.B., *A unique NH-spacer for N-benzamidothiourea based anion sensors. Substituent effect on anion sensing of the ICT dual fluorescent N-(p-dimethylaminobenzamido)-N '-arylthioureas.* Organic & Biomolecular Chemistry, 2006. **4**(4): p. 624-630.

42. Gunnlaugsson, T., Kruger, P.E., Lee, T.C., Parkesh, R., Pfeffer, F.M., and Hussey, G.M., *Dual responsive chemosensors for anions: the combination of fluorescent PET (photoinduced electron transfer) and colorimetric chemosensors in a single molecule.* Tetrahedron Letters, 2003. **44**(35): p. 6575-6578.

43. Waller, A., *Eelectron-transfer and complex formation in the excited state.* Pure and Applied Chemistry, 1968. **16**(115).

44. Bissell, R.A., De Silva, A.P., Gunaratne, H.Q.N., Lynch, P.L.M., Maguire, G.E.M., Mccoy, C.P., and Sandanayake, K.R.A.S., *Fluorescent Pet (Photoinduced Electron-Transfer) Sensors.* Photoinduced Electron Transfer V, 1993. **168**: p. 223-264.

45. Chen, J., Zhou, P., Li, G., T, C., and He, G., *Fluoride Anion Sensing Mechanism of 2-Ureido-4[1H]-pyrimidinone Quadruple Hydrogen-Bonded Supramolecular Assembly: Photoinduced Electron Transfer and Partial Configuration Change.* Journal of Physical Chemistry B, 2013. **117**: p. 5212-5221.

46. He, H.R. and Tusa, J.K., *Critical care analyzer with fluorescent optical chemosensors for blood analytes.* Journal of Materials Chemistry, 2005. **15**(27-28): p. 2640-2647.

47. Gunnlaugsson, T., Ali, H.D.P., Glynn, M., Kruger, P.E., Hussey, G.M., Pfeffer, F.M., dos Santos, C.M.G., and Tierney, J., *Fluorescent photoinduced electron transfer (PET) sensors for anions; From design to potential application.* Journal of Fluorescence, 2005. **15**(3): p. 287-299.

48. Schuster, J., Cichos, F., and von Borczyskowski, C., *Influence of self-trapped states on the fluorescence intermittency of single molecules.* Applied Physics Letters, 2005. **87**(5).

49. Zondervan, R., Kulzer, F., Orlinskii, S.B., and Orrit, M., *Photoblinking of rhodamine 6G in poly(vinyl alcohol): Radical dark state formed through the triplet.* Journal of Physical Chemistry A, 2003. **107**(35): p. 6770-6776.

50. Vogelsang, J., Cordes, T., Forthmann, C., Steinhauer, C., and Tinnefeld, P., *Controlling the fluorescence of ordinary oxazine dyes for single-molecule switching and superresolution microscopy.* Proceedings of the National Academy of Sciences of the United States of America, 2009. **106**(20): p. 8107-8112.

51. Cordes, T., Vogelsang, J., and Tinnefeld, P., *On the Mechanism of Trolox as Antiblinking and Antibleaching Reagent.* Journal of the American Chemical Society, 2009. **131**(14): p. 5018-+.

52. Widengren, J. and Rigler, R., *Mechanisms of photobleaching investigated by fluorescence correlation spectroscopy.* Bioimaging, 1996. **4**: p. 149-157.

53. Foo, T.C., François, A., Ebendorff-Heidepriem, H., Sumby, C.J., and Monro, T.M., *Comparison of Surface Functionalization Techniques on Silica and Soft Glasses for Optical Fibre Sensing Applications*, in *Australian Conference on Optical Fibre Technology (ACOFT)*. 2009: Adelaide, Australia.

54. Decher, G., *Fuzzy nanoassemblies: Toward layered polymeric multicomposites.* Science, 1997. **277**(5330): p. 1232-1237.

55. Debs, J.E., Ebendorff-Heidepriem, H., Quinton, J.S., and Monro, T.M., *A Fundamental Study Into the Surface Functionalization of Soft Glass Microstructured Optical Fibers via Silane Coupling Agents.* Journal of Lightwave Technology, 2009. **27**(5-8): p. 576-582.

56. Bhatia, S.K., Shriverlake, L.C., Prior, K.J., Georger, J.H., Calvert, J.M., Bredehorst, R., and Ligler, F.S., *Use of Thiol-Terminal Silanes and*

Heterobifunctional Crosslinkers for Immobilization of Antibodies on Silica Surfaces. Analytical Biochemistry, 1989. **178**(2): p. 408-413.

57. Hermanson, G.T., *Bioconjugate techniques*. 2nd ed. 2008, London.

58. Chatterjee, R., *Application of TOF-SIMS to monitor coating processes on biological and organic surfaces.* Applied Surface Science, 2004. **231**: p. 437-441.

59. Sodhi, R.N.S., *Time-of-flight secondary ion mass spectrometry (TOF-SIMS): versatility in chemical and imaging surface analysis.* Analyst, 2004. **129**(6): p. 483-487.

60. Lee, C.Y., Harbers, G.M., Grainger, D.W., Gamble, L.J., and Castner, D.G., *Fluorescence, XPS, and TOF-SIMS surface chemical state image analysis of DNA microarrays.* Journal of the American Chemical Society, 2007. **129**(30): p. 9429-9438.

61. Xing, Y.J., Dementev, N., and Borguet, E., *Chemical labeling for quantitative characterization of surface chemistry.* Current Opinion in Solid State & Materials Science, 2007. **11**(5-6): p. 86-91.

62. Cheng, F., Gamble, L.J., and Castner, D.G., *XPS, TOF-SIMS, NEXAFS, and SPR characterization of nitrilotriacetic acid-terminated self-assembled monolayers for controllable immobilization of proteins.* Analytical Chemistry, 2008. **80**(7): p. 2564-2573.

63. Libertino, S., Giannazzo, F., Aiello, V., Scandurra, A., Sinatra, F., Renis, M., and Fichera, M., *XPS and AFM characterization of the enzyme glucose oxidase immobilized on SiO2 surfaces.* Langmuir, 2008. **24**(5): p. 1965-1972.

64. Hoffmann, K., Mix, R., Friedrich, J.F., and Resch-Genger, U., *Spectroscopic characterization of plasma - Chemically functionalized and fluorophore-labeled polymer surfaces,* in *Reviews in fluorescence*, U. Resch-Genger, Editor. 2008, Springer: New York. p. 139-159.

65. McNamara, P., Lew, W., and Han, L., *Fluorescent imaging and analysis with Typhoon 8600.* Electrophoresis, 2001. **22**(5): p. 837-842.

66. Ratner, B.D. and Castner, D.G., *electron spectroscopy for chemical analysis*, in *Surface analysis*
The principal Techniques, J.C. Vickerman and I.S. Gilmore, Editors. 2009, Wiley: West Sussex.

67. Graham, D.J., Wagner, M.S., and Castner, D.G., *Information from complexity: Challenges of TOF-SIMS data interpretation.* Applied Surface Science, 2006. **252**(19): p. 6860-6868.

68. Lee, J. and Gilmore, I.S., *The application of multivariate data analysis techniques in surface analysis*, in *Surface analysis - The principal techniques*, J.C. Vickerman and I.S. Gilmore, Editors. 2009, Wiley: West Sussex.

69. Fujiwara, H., *Spectroscopic Ellipsometry: Principles and Applications*. 2007, Tokyo: Maruzen co Ltd.

70. *Guilde to using WVASE32^{TM} software for optical data analysis*. 1995, Nebraska: J. A. Woolam. Co. Inc.

Chapter 2

Demonstration of ions sensing using model photoinduced electron transfer (PET) fluoroionophores in suspended core fibres (SCFs)

2.1 Introduction

As described in Chapter 1, a photoinduced electron transfer **(**PET) fluoroionphore consist of two parts; the ionophore that serves to selectively capture the ion and the fluorophore emits a fluorescence signal. To fabricate a SCF sensor for any specific ion, the ionophore has to be selective to the target ions, whereas the fluorophore can be varied with respect to the optical components and system requirements. Basic requirements of the fluorophore component of the sensor are similar to requirements for a fluorophore for fluorescence imaging. The fluoroionophore needs to have a large Stokes' shift for an easy separation of the excitation wavelength, high photostability for stable emission intensity, and the absorption and emission spectrum should be within the transmission window of the optical fibre. In terms of the photostability, the requirement for fluorophores working in SCFs is more stringent because the light intensity within is much higher than that of the fluorescence imaging. In addition, the fluoroionophore should have a moiety for the surface attachment for the operating scenario B.

He *et al.* and Gunnlaugsson *et al.* have both reported successful examples of PET fluoroionophores (Figure 2.1) selective to sodium, potassium and fluoride ions [1-3]. All of these PET fluoroionophores use 4 amino-1,8-naphthalimide as the fluorophores. In these fluoroionophores the amine group in the 4-position of the naphthalimide acts as the electron donating group and the imide moiety acts as an electron withdrawing group; these give an internal charge transfer (ICT) excited state. This ICT excited state provides 4 amino-1,8-naphthalimide with a broad absorption and emission spectrum in the visible wavelength region. A PET

fluoroionophore for the sodium ions sensing (reported by He *et al.*) has the absorption and emission bands in water at 450 nm and 550 nm, which is within the transmission window of both lead silicate (F2) and silica glass. 4-Amino-1,8-naphthalimide derivatives are suitable to be used in a SCF ion sensor because they demonstrate good photostability as a laser dye and have a larger Stokes' shift (*ca.* 100 nm) than many common fluorophores such as Rhodamine 6G [4].

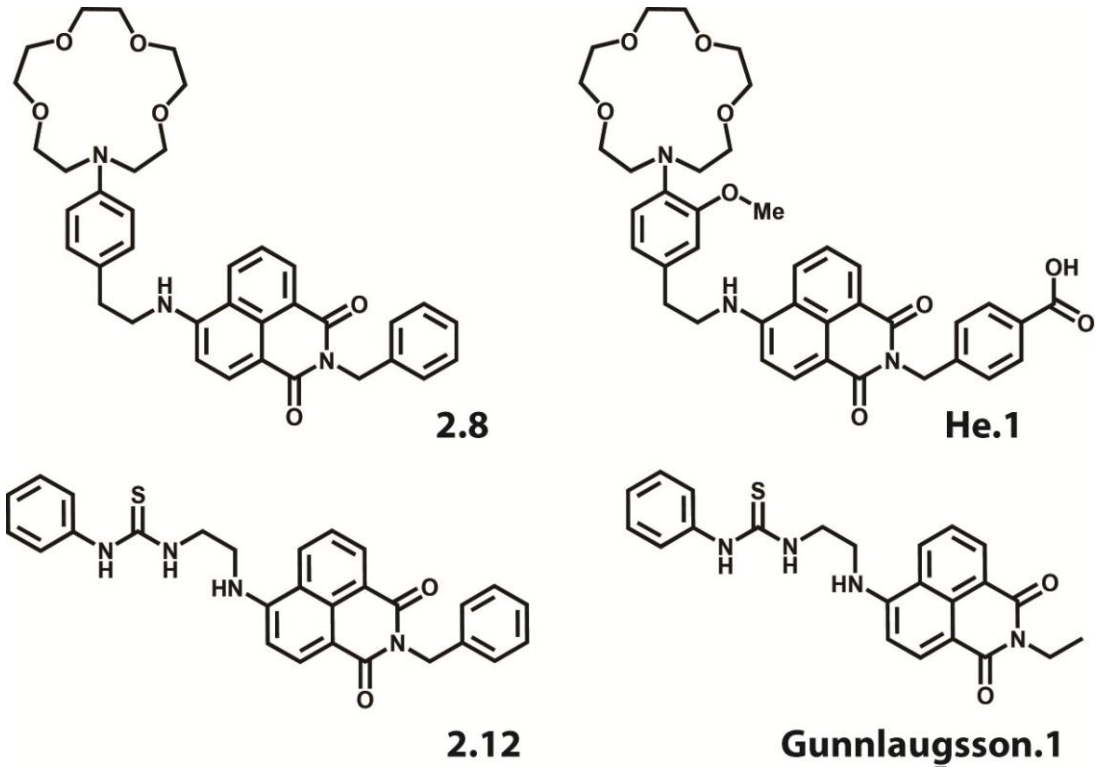

Figure 2.1: Structures of the model fluoroionophores for cations (**2.8**) and for anions (**2.12**) sensing in comparison to previously reported fluoroionophores for sodium (**He.1**) and fluoride ions (**Gunnlaugsson.1**)

The aims of this study are, firstly, to demonstrate the feasibility of ion concentration measurements using model PET fluoroionophores with 4-amino-1,8-naphthalimide as the fluorophores in SCF and, secondly, to compare the sensing performance characteristics, such as sensitivity and dynamic linear range of model PET fluoroionophores, in SCFs and cuvette.

Given that both cations and anions binding fluoroionophores have the same fluorophore unit, a model fluorophore *N*-benzyl-4-propylamine-1,8-naphthalimide (**2.3**) (shown in Scheme 2.1 at page 61) was synthesised first before the synthesis of the model fluoroionophores. The optical properties of model fluorophore **2.3** in

acetonitrile were examined in cuvette to ensure that the absorption and emission wavelengths are within the transmission window of both lead silicate (F2) glass and silica glass SCFs. The preliminary study on the photostability of fluorophore **2.3** was presented at the Australian Conference on Optical Fibre Technology (ACOFT) in 2009 [5].

To demonstrate cations and anions detection using PET fluoroionophores in SCFs, PET fluoroionophores (Figure 2.1), which are structurally similar to previously reported PET fluoroionophores for sodium ions (**He.1)** and fluoride ions (**Gunnlaugsson.1**, Figure 2.1), were synthesised and used in this study. These model fluorophores and fluoroionophores were not soluble in water and so, all experiments were performed in acetonitrile instead of water. The motivation for the modification of the sodium ions PET fluoroionophore **2.8** was to simplify the structure of the fluoroionophore, thereby reducing the synthetic steps and time required for synthesis. The trade-off in the simplification of the ionophore is a decrease in selectivity and binding constant for sodium. Furthermore, it was not necessary to attach the fluoroionophores to a surface in this particular study; therefore no carboxyl group was required. Synthesis of a derivative of fluoroionophore **2.8** that can be covalently attached on functionalised glass surfaces is discussed in Chapter 4.

A preliminary study of sodium ions sensing for fluoroionophore **2.8** in cuvette and SCFs was published in 2011 [6]. The focus of this Chapter is to describe in detail the feasibility of quantitative sodium ion concentration measurements using fluoroionophore **2.8** in SCFs.

The structure of fluoroionophore **2.12** is similar to a previously published anion sensor that can sense anions in acetonitrile [7]; the only difference is that the ethyl group attached to the imide nitrogen is replaced by a benzyl group. The motivation for this modification was to standardise the fluorophore structure (an *N*-benzyl-4-amino-1,8-naphthalimide) and hence the absorption and emission spectra of all PET sensors in this project. The choice of benzyl group is because it blocks the reactivity of imide for further reactions. The synthesis of a surface attachable PET fluoroionophore is discussed in Chapter 4. The advantage of using the same fluorophore is that the excitation laser, filters and dichroic mirror can be

shared in both experiments, which lowers the cost and the complexity of the experiments.

2.2 Experimental

2.2.1 Sample preparation and measurement procedures for using the spectrofluorometer

Fluoroionophore **2.8** and sodium perchlorate were dissolved in HPLC grade acetonitrile. The ionic strength was maintained with 100 mM tetraethylammonium perchlorate (NEt_4ClO_4), acting as an ionic buffer. Fluoroionophore **2.12** and tetraethylammonium fluoride hydrate were also dissolved in HPLC grade acetonitrile, but no ionic buffer was used in these experiments. The spectrofluorometer has a Xenon flash lamp as the excitation source and a photomultiplier tube (PMT) as the detector. The excitation wavelength was 470 nm. The excitation and emission slit width were set at 5 mm. All measurements were recorded at 25°C using 700 µL quartz cuvettes with an excitation path-length of 10 mm. PET fluoroionophores and target ions were pre-mixed and incubated at room temperature for at least 120 minutes before the spectra were recorded. Three fluorescence spectra were recorded per sample on a Varian Cary Eclipse spectrofluorometer. The data analysis method is described in Section 2.2.3.

Warning: Perchlorate salts are strong oxidising agents and are potentially explosive.

2.2.2 Experimental set-up for the fluorescence measurement with cuvettes and SCFs

Sensing experiments with the same pre-mixed solutions were performed in both cuvettes and F2 SCFs using the same excitation source and spectrometer. The aim of doing these experiments in parallel was to compare performance characteristics such as the linear dynamic range and sensitivity for each model fluoroionophore in cuvettes and in SCFs. The cuvette measurements were performed in PMMA cuvettes (2 mL) for fluoroionophore **2.8** and quartz cuvettes (700 µL) for

fluoroionophore **2.12**. Due to the continuous development, there were three generations of the experimental set-up for the SCFs fluorescence measurements. The key differences of the optical set-ups are summarised in Table 2.1.

Table 2.1: Summary of the key differences in all generations of the optical set-up described in this thesis

Generation	Laser	Manufacturer	Method of fluorescence detection	Fluorophore/ Fluoroionophore used in the setup	SCF material	Cuvette
1st	477 nm Argon ion	Melles Griot	Forward	**2.3**	F2	No
2nd	473 nm Diode	Crystal laser	Backward	**2.8** **2.12**	F2	Yes
3rd	473 nm Diode	Toptica	Backward	**2.8** **2.12** **4.3** (See Chapter 5) **5.3** (See Chapter 5)	F2/ silica	Yes

Figure 2.2 shows the first generation optical set-up. The main differences between the first generation set-up and the second and third generation set-ups were the laser type and the method of capturing the fluorescence signal. In terms of the laser, the argon ion laser has low beam-pointing stability compared with a diode laser; therefore a diode laser was used in the 2nd and 3rd generation optics set-ups. In terms of the method of fluorescence detection, a backward detection method has two advantages over a forward detection method. Firstly, the backward detection method allows one end of the SCF to be free for dipping into the solution, therefore no readjustment of optics needs to be performed after dipping. Secondly, Afshar *et al.* showed that the fluorescence capturing fraction (FCF) is sensitive to the length of SCF in the forward detection method, whereas after the saturation point the FCF of the backward detection method is not sensitive to the length of SCF [8, 9]. Both advantages improve the consistency of the fluorescence measurements.

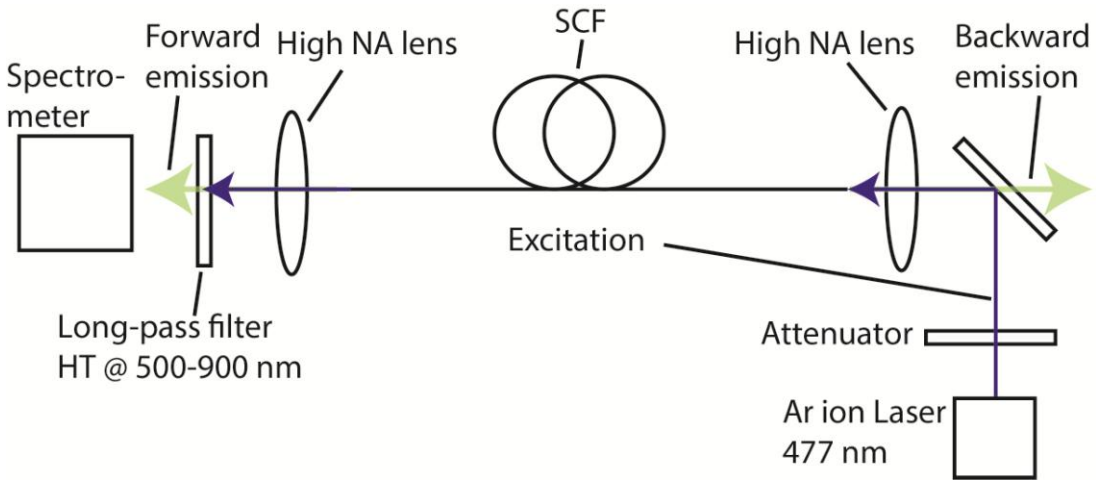

Figure 2.2: The 1st generation optics setup using an argon ion laser (477 nm) as the excitation source. The fluorescence was captured in the forward direction, which was not the same as other experiments described in this thesis

Figure 2.3a shows a schematic diagram of the second and third generation optical set-ups for the SCF sensing experiments. The key difference between the second and third generation optical set-up is the brand of the diode laser. The blue line shows the laser beam path and the green line is the back scatter beam path to the spectrometer. Figure 2.3b shows the second generation optical set-up for F2 SCF sensing experiment of fluoroionophore **2.8** in F2 SCF. The excitation source was a 473-nm diode laser (Crystal laser CL-473-025, continuous wave, TEM_{00}, linearly polarised, max output power 10 mW). The excitation beam was attenuated by a neutral-density (ND) filter to 0.1 mW. Note that in the preliminary experiments, the excitation beam was attenuated by a ND filter to 2.5 mW.

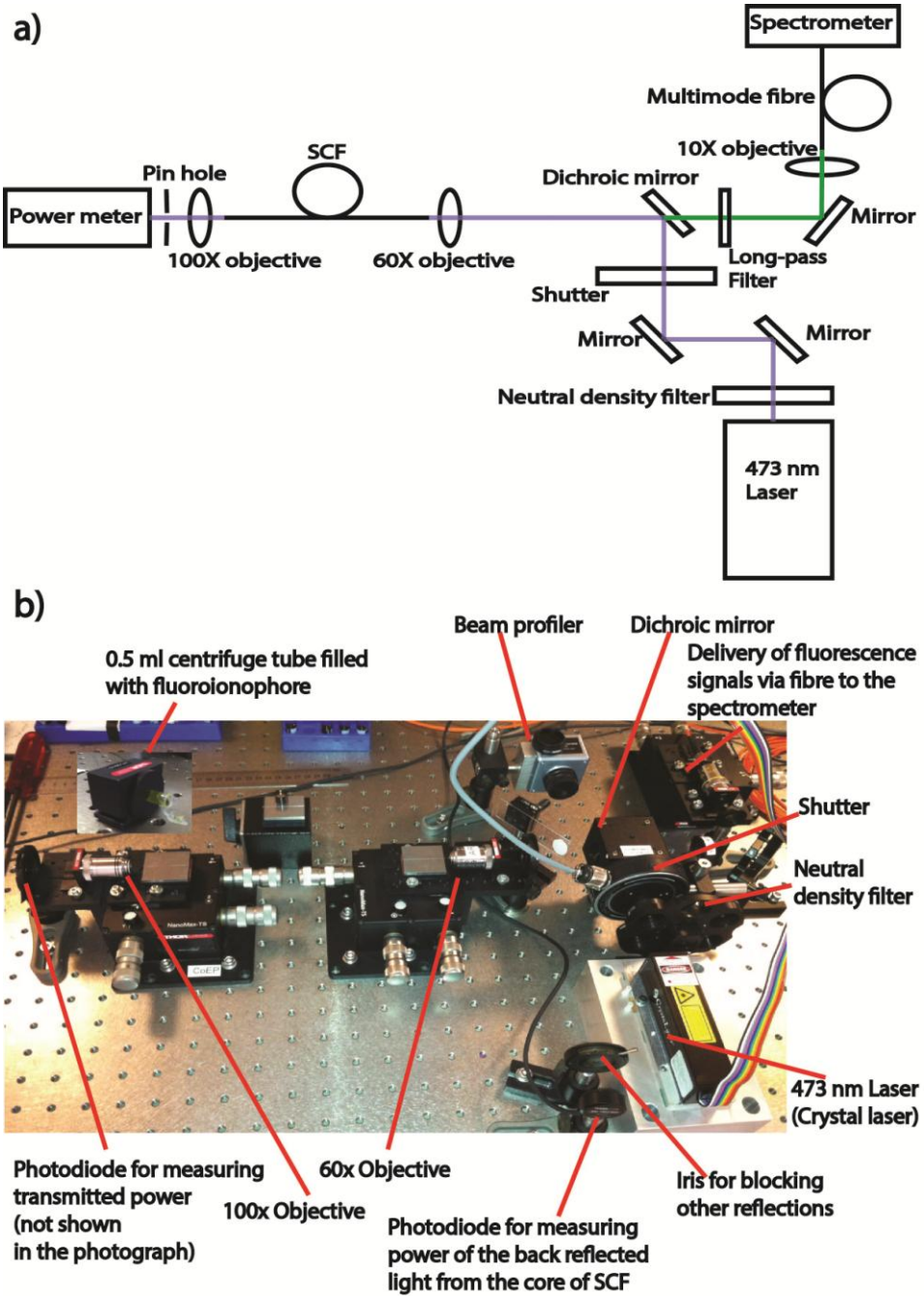

Figure 2.3 (a): A schematic diagram of the 2nd and 3rd generation optical set-ups for the SCF sensing experiments (without all laser quality monitoring equipment). (b) The optical set-up for the SCF sodium ions sensing experiments (2nd generation)

After the ND filter, the beam was free-space coupled, through a dichroic mirror (HR: 471 - 491 nm, edge-λ: 497 nm, HT: 503.3 - 900 nm), into a microscope objective (Edmund optics 60x, NA: 0.75). The excitation beam was aligned into the core of the right end of the SCF. The transmitted light was collected by a

second microscope objective (Edmund optics 100x, NA: 1.25) and focused onto the power meter. Both ends of the SCF were mounted onto two separate 3-axis nanometer stages (Thorlabs Model MAX316). For each measurement, the excitation beam was focused into the core of SCFs and then the coupled pump beam power was maximised using the nanometer stage to position the fibre end at the focus of the 60x objective. An iris that was placed in front of the power meter was used to block out residual transmitted cladding light. The backward-propagated fluorescence emission signal was collimated by the 60x objective and filtered by the dichroic mirror, and a long-pass filter (pass band: 504.7 - 900 nm) was used to block remaining excitation light. However, the long-pass filter was removed in the third generation set-up, since the dichroic mirror is enough to remove most of the pump light. The signal was then coupled via a microscope objective (Olympus 10x, NA: 0.25) into a multimode fibre (Thorlabs, core dia.: 400 µm, NA: 0.48), connected to an imaging spectrometer (Horiba Jobin Yvon iHR320) with a cooled 1024 x 256 pixel CCD camera. The spectrometer input slit width was 1 mm. An optical shutter synchronised with the data-acquisition time of the spectrometer was used to protect the fluoroionophore from the excitation beam between acquisitions of fluorescence spectra to minimise photobleaching. 10 spectra were acquired and each acquisition required 16 ms. The total acquisition time was 144 ms. Note that 8 spectra were acquired and each acquisition required 2.5 ms in the preliminary experiment [6] for fluoroionophore **2.8**. The total acquisition time was 17.5 ms.

For each experiment, a ~30 cm SCF with cleaved ends was used. An unfilled SCF was mounted on the nanometer fibre positioning stages and the optical coupling was optimised. Then, the 100x objective end of the SCF was removed from the nanometer stage and dipped into the analyte solution in a 500 µL tube. Holes in the SCF were filled with the analyte solution by capillary force for 5 minutes, only partially filling the length of the SCF. After filling the SCF with solution, the 100x objective end was secured back onto the nanometer stage. By partially filling the fibre holes, no analyte solution was able to evaporate at the 60x objective endface of the SCF. Evaporation of an analyte solution containing an inorganic salt or organic compound is undesirable as it causes crystallisation at the fibre endface and thus reduces coupling reproducibility and introduces

scattering loss. After the SCF was filled with solution for 5 mins, the measurement was performed immediately. Each filled SCF was used only once.

Figure 2.4a shows the third generation optical set-up for all of the F2 and silica SCFs sensing experiments for fluoroionophore **2.12**; this optical set-up was also used for the silica SCF sensing experiments for fluoroionophore **2.8.** The laser source was changed to a 473-nm diode laser (Toptica-ibeam-smart-473-S-10305, continuous wave, TEM_{00}, linearly polarised, maximum output power 100 mW), as it was found that the laser from Crystal Laser had unstable output power. In addition the beam profile quality was found to be poor (i.e. not at TEM_{00}). These two issues had introduced some measurement instability and therefore the Crystal Laser was replaced by another laser (Tropica). The excitation beam was attenuated by a ND filter to 0.01 mW for all measurements except the sodium sensing measurements, for which the excitation beam power was attenuated to 0.1 mW. The 60x objective that focuses light into the SCF was replaced by a 40x objective (Olympus), which gives higher coupling stability. The motivation for using the beam expander was to only use the centre part of the Gaussian beam in the experiment. However, from these experiments there was no evidence suggesting that it has a significant effect in improving the consistency of the measurements.

The cuvette experiments were performed in the cuvette holder (Ocean Optics) shown in Figure 2.4b. The excitation beam was attenuated by a ND filter to 1 mW and delivered to the curvette by an optical fibre. The emission was captured by another optical fibre perpendicular to the excitation light. The emission light was delivered to the spectrometer (Horiba) via this second optical fibre. Three fluorescence spectra were recorded per sample. The cuvette measurement of fluoroionophore **2.8** was performed using the diode laser in the 2nd generation optical set-up and PMMA cuvettes, while the cuvette measurements of fluoroionophore **2.12** were performed using a diode laser in the 3rd generation optical set-up and quartz cuvettes.

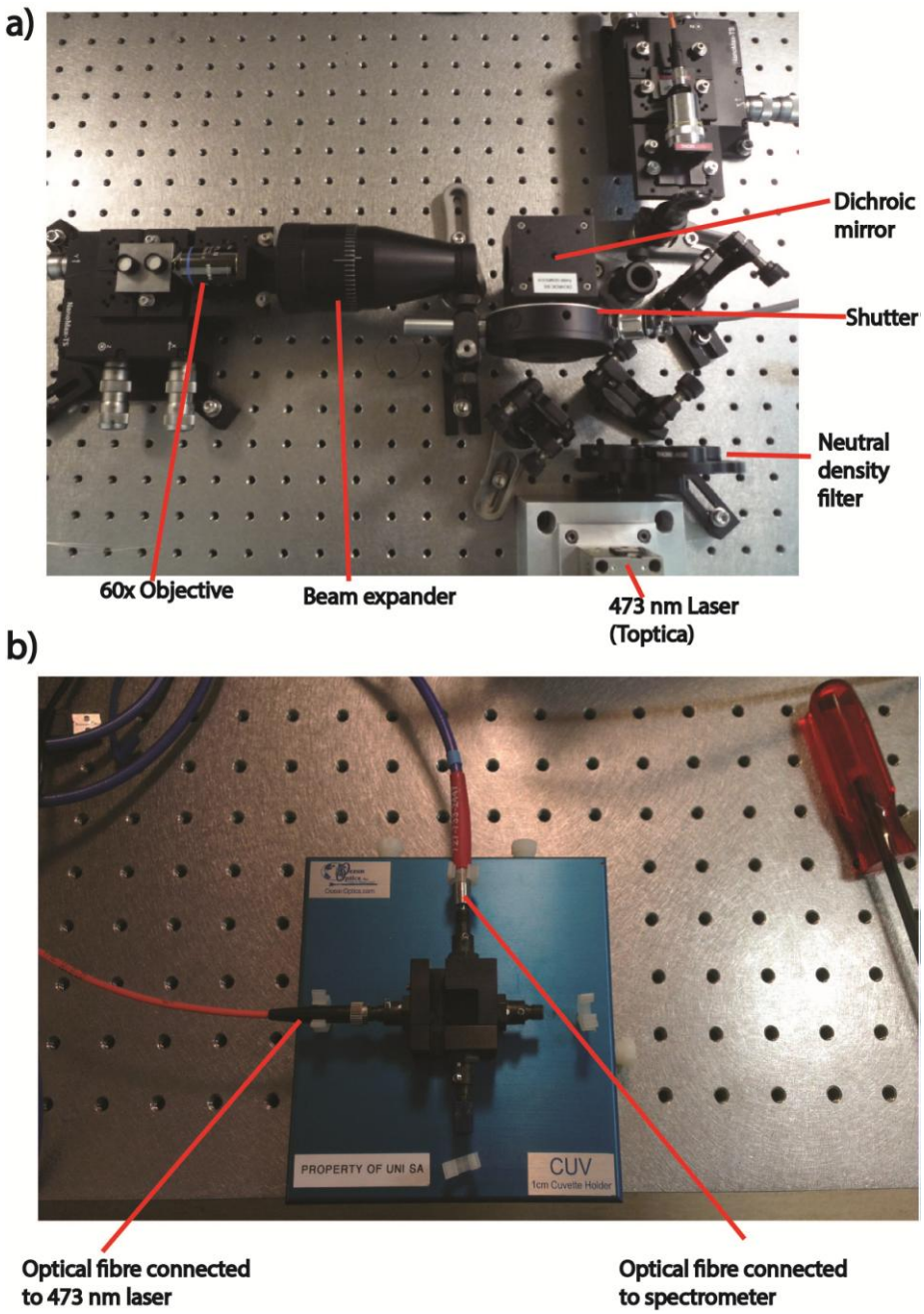

Figure 2.4 (a) The optical set-up for SCF fluoride sensing experiments (3rd generation). (b) The cuvette holder connected to the same excitation source and spectrometer as used in the SCF ions sensing experiments

2.2.3 Method of data analysis

10 emission spectra were recorded for each SCF sample and 3 spectra were recorded for each cuvette sample. Since the peak emission wavelength of the aminonaphthalimide is dependent on the spectral responses of the detector, the analysis based on the peak intensity is not a reliable way to perform data analysis. The shift of emission wavelength peak of different fluorophore is discussed in Section 2.3.10.

In this project, the average emission spectrum was calculated (Equation 2.1) and then the average emission spectrum was integrated to find integrated average emission intensity (I) (Equation 2.2). The calculation was performed using Microsoft Excel, Origin and Matlab 2008. It was noted that the numerical integrations performed by Origin or Matlab 2008 have less than 1% difference because of using different algorithms. The emission wavelength range of the integration of the emission spectrum of fluoroionophores at early stage of experiments in F2 SCF was 499 nm to 700 nm. However, the emission wavelength range of the integration was changed to 480 nm to 700 nm in later on experiments in F2 and silica SCFs. This change did not make much difference in the analysis because the emission intensity of both types of fluoroionophores is low from 480 nm to 499 nm. Furthermore, the results were normalised with the maximum integrated average emission spectrum (Equation 2.4) within the same experiment. The calculation of the standard deviation (SD) of the integrated average emission intensity was performed using Matlab 2008 (Equation 2.3)

$$\text{Average emission spectrum } (\bar{S}) = \frac{S_{1st} + \ldots . S_{nth}}{n} \qquad \text{(Equation 2.1)}$$

$$\text{Integrated emission intensity(I) for fluoroionophore } \mathbf{2.8} = \int_{499}^{700} i_{\lambda} \qquad \text{(Equation 2.2)}$$

$$\text{Integrated emission intensity(I) for fluoroionophore } \mathbf{2.12} = \int_{480}^{700} i_{\lambda}$$

i = emission wavelength at λ nm

$$\text{Standard deviation of integrated emission intensity } (SD_I) = \sqrt{\frac{\sum_{n=1}^{n} (I_{nth} - \bar{I})^2}{n}} \qquad \text{(Equation 2.3)}$$

$\bar{I}$ = Integrated mean emission intensity

Total number of SCF measurement (n) = 10 Total number of cuvette measurement (n) = 3

$$\text{Normalised average integrated emission intensity} = \frac{\bar{I}}{\text{Maximum } \bar{I}} \qquad \text{(Equation 2.4)}$$

2.2.3.1 Photobleaching analysis

As explained in Chapter 1 (Section 1.2.6), all organic fluorophores have the potential for photobleaching. It is important to ensure all measurements were not affected by this phenomenon. Photobleaching analyses were performed for each SCF measurement by normalising each integrated spectra to the first spectra recorded (Equation 2.5). The percentage shows the signal variation relative to the first scan. If there was photobleaching during the measurement time, the percentage would decrease progressively after each scan. 10 spectra were acquired and each acquisition required 16 ms. The total acquisition time was 144 ms. Note that 8 spectra were acquired and each acquisition required 2.5 ms in the preliminary experiment [6] for fluoroionophore **2.8**. The total acquisition time was 17.5 ms

$$\frac{I_n}{I_1} \times 100\% \qquad \text{(Equation 2.5)}$$

I_{1st} = integrated fluorescence intensity of 1st spectra

I_{nth} = integrated fluorescence intensity of n^{th} spectra

2.2.3.2 Sensor performance analysis

The calibration curve of the normalised fluorescence intensities and the ion concentrations is usually only linear in the low concentration range. This is because the fluorescence intensity of the fluoroionophores depends on the equilibrium for the formation of the ion-fluoroionophore complexes. Most of the fluoroionophores are complexed by ions when the ratio of ion to fluoroionophore concentration is high. Therefore the fluorescence intensity becomes insensitive to the increase in ion concentration. Hence, the overall trend of fluorescence intensities as a function of ion concentrations is usually fitted by a non-linear function. In this project, the exponential function (Equation 2.4) was used to fit the calibration curve. The linear portion of the calibration curve was fitted with a linear equation (Equation 2.3).

The definitions of the sensitivity and the dynamic linear range used in this project are shown in Figure 2.5. The sensitivity is the slope of the linear fit from the linear regression analysis of the linear portion of the calibration curve. The data included in the linear regression are the maximum range of ion concentrations that gives a high correction coefficient ($R^2 \geq 0.98$) and the data points included in the residual plot of the regression should show a random scattering pattern along the zero axis, which proves that there is no systematic trend apart from the linear model. The dynamic linear range is the difference between the limit of linearity (LoL) and the limit of quantification (LoQ) of the calibration curve.

The LoQ (Equation 2.10A and B) is the minimum concentration for which quantitative measurement is feasible. It is normally defined as 10 times the standard deviation (SD) of the blank signal [10]. In the case of using fluoroionophores for ions detection, the blank is the fluorescence intensity of the fluoroionophores without ions. After determining the linear fit of the calibration, the LoL (Equation 2.9) is defined as the concentration at which there is a 5% change of the derivative of the exponential fit (Equation 2.8) when compared to the last experimental data point(x1) in the linear fit.

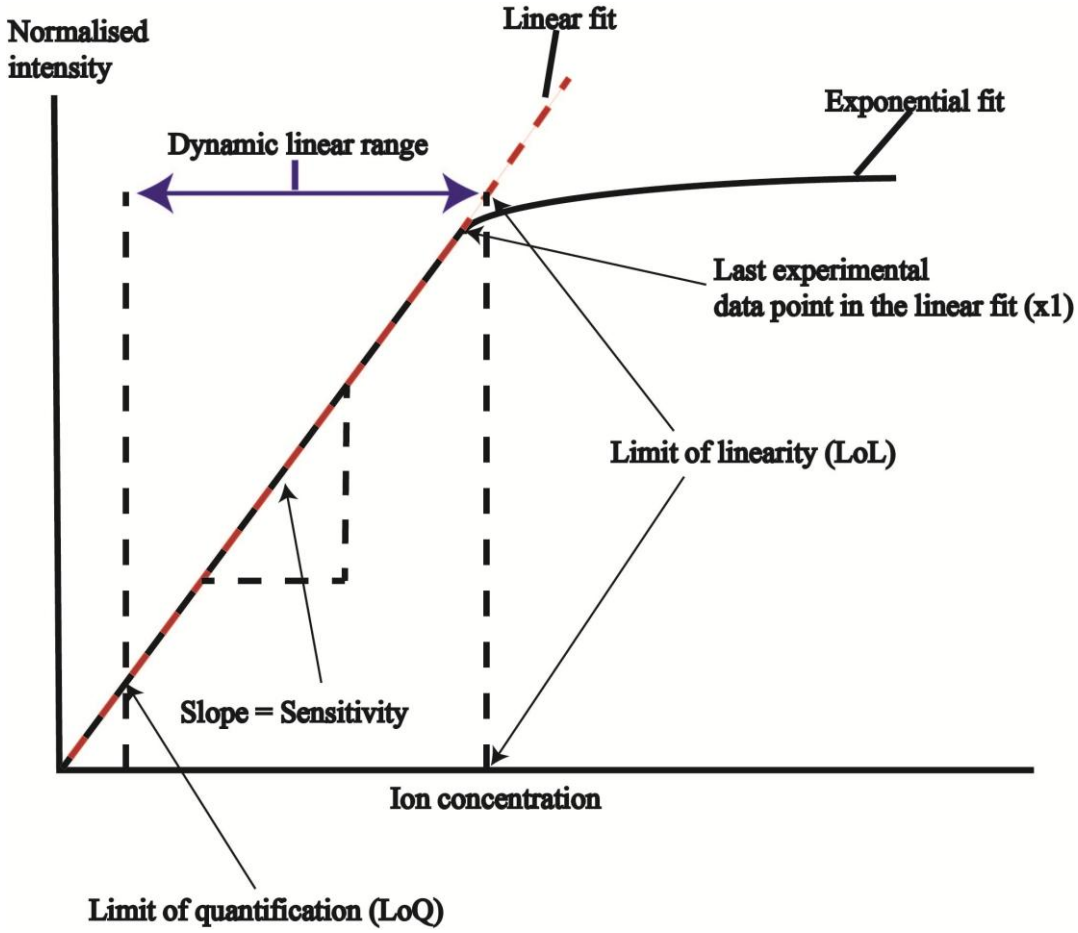

Figure 2.5: Definitions of the dynamic linear range and sensitivity [10]

Linear fit $y = mx + c$ (Equation 2.6)

Exponential fit $y = Ae^{\frac{x}{t}} + b$ (Equation 2.7)

Derivative of Exponential fit $\frac{dy}{dx} = \frac{A}{t} e^{\frac{x}{t}}$ A, x and t are constant (Equation 2.8)

LoL = 5% change of the derivative of the exponential fit compared to the last experimental data point in the linear fit (Equation 2.9)

LoL = (t)ln1.05 + x1

LoQ = Normalised integrated fluorescence intensity of the fluoroionophore **2.8** + 10 x SD of the Normalised integrated fluorescence intensity of the fluoroionophore **2.8** (Equation 2.10A)

LoQ = Normalised integrated fluorescence intensity of the fluoroionophore **2.12** - 10 x SD of the Normalised integrated fluorescence intensity of the fluoroionophore **2.12** (Equation 2.10B)

2.2.4 Synthesis of the model fluorophore (2.3) and fluoroionophores (2.8 and 2.12)

General procedures

All commercially available reagents were used without further purification. Thin layer chromatography was performed on MERCK aluminium-backed silica gel 60 F_{254} plates (20 x 20 cm, 0.25 mm thickness) and viewed using 254 nm UV light. Flash column chromatography was performed using Davisil silica gel 60 (particle size 0.040 - 0.063 mm) from Grace GmbH and Co. KG following the guidelines outlined in literature [11]. Microwave synthesis was performed in the CEM focused microwave^{TM} synthesis system (Discover@ SP) using a reaction tube and seal provided by CEM. Microwave irradiation started after 30 seconds pre-mixing. The microwave power was variable but the set point temperature was fixed.

^{1}H and ^{13}C NMR spectra were obtained using either a Varian Gemini 2000 Spectrometer (^{1}H: 300.13 MHz, ^{13}C: 75.48 MHz) or a Varian Inova Spectrometer

(^{1}H: 599.842 MHz, ^{13}C: 150.842 MHz). Chemical shift values were given on a δ scale quoted in parts per million (ppm), followed by the integration, multiplicity, coupling constant J and assignment. Spectra were recorded in chloroform-D from Cambridge Isotope Laboratories or dimethyl sulfoxide-d_6 (DMSO d_6) from Sigma Aldrich. ^{1}H NMR spectra recorded in $CDCl_3$ were referenced relative to the internal standard Me_4Si, $\delta_H = 0.0$, while for ^{13}C NMR spectra using $CDCl_3$ used $\delta_C = 77.23$ as an internal standard. ^{1}H NMR spectra recorded in dimethyl sulfoxide-d_6 (DMSO d_6) were referenced relative to the quintet of the DMSO d_6 as the internal reference, $\delta_H = 2.5$, while for ^{13}C NMR spectra using DMSO d_6 used $\delta_C = 39.51$ as an internal standard.

The following abbreviations for proton multiplicities were used: s, singlet; d, doublet; t, triplet; br, broad singlet. m, multiplet, indicated a broadened signal due to unresolved J value(s). ^{1}H and ^{13}C NMR signals of compound **2.3**, **2.6** and **2.8** were assigned by the combination of information from correlation spectroscopy (COSY), nuclear overhauser effect spectroscopy (NOESY), heteronuclear single quantum coherence (HSQC) and heteronuclear multiple bond correlation (HMBC) performed on the Varian Inova spectrometer (^{1}H: 599.842, ^{13}C: 150.842 MHz).

All infrared spectra were obtained using a Perkin Elmer Spectrum 100 UATR FT-IR spectrometer mounted with a diamond coated zinc selenide crystal. All electrospray ionization (ESI) mass spectra, except for compound **2.2**, were obtained using a Finnigan LCQ mass spectrometer. The electron impact (EI) mass spectrum of compound **2.2** was obtained on a Shimadzu GCMS-QP5050A mass spectrometer. Samples were all diluted with HPLC grade methanol. High resolution mass spectrometry (HRMS) were performed by the Adelaide Proteomics Centre at the University of Adelaide using a LTQ Orbitrap XL mass spectrometer from Thermo Fisher Scientific and by the Department of Chemistry of the University of Canterbury using a Bruker maXis 3G Ultra High Resolution Time of Flight (UHR-TOF) tandem mass spectrometer. All melting points were determined on a Gallenkamp variable heat melting point apparatus.

_N_-Benzyl-4-chloro-1,8-naphthalimide (2.2)

4-Chloro-1,8-naphthalic anhydride (2.00 g, 8.60 mmol) was stirred in 30 mL ethanol at 90°C for 20 minutes under a nitrogen atmosphere. Benzyl amine (950 µL, 8.70 mmol) was added into the reaction mixture and the resulting solution was heated at reflux for 66 hours. The crude product was collected by filtration, washed with ethanol and dried under vacuum. The crude product was recrystallised from ethanol to afford *N*-Benzyl-4-chloro-1,8-naphthalimide (**2.2**) as yellow crystals (1.84 g, 67%). m.p. 175 – 177°C (lit[12] m.p. 168.5 – 170.5°C) ; ^{1}H NMR (300 MHz, $CDCl_3$) d = 8.68 (d, *J* = 6.6 Hz, 1 H), 8.61 (d, *J* = 8.8 Hz, 1 H), 8.52 (d, *J* = 7.7 Hz, 1 H), 7.90 - 7.80 (m, 2 H), 7.58 - 7.49 (m, 2 H), 7.35 - 7.19 (m, 3H), 5.38 (s, 2 H); UATR FTIR (Diamond/ZnSe) υ/cm^{-1} 3065, 1916, 1698 and 1655; MS (EI, +ve mode) *m/z* 321 ([M-H]$^{+}$), 215, 187, 126, 91, 77, 65, 51.

_N_-benzyl-4-propylamine-1,8-naphthalimide (2.3)

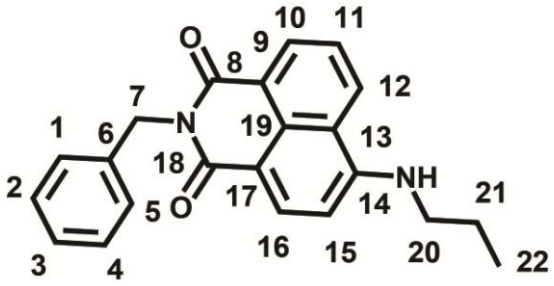

N-Benzyl-4-chloro-1,8-naphthalimide (1 g, 3.25 mmol) was dissolved in 1-methyl-2-pyrrolidone (NMP) (10 ml) at room temperature for 20 minutes. The mixture was heated to 105^{o}C and propylamine (550 µL) and *N*,*N*-diisopropylethyl amine (DIPEA) (1.4 mL) were added into the mixture, inducing a deep red colour change. The reaction mixture was stirred at 105^{o}C for 22 hours, cooled to room temperature, poured into water, and the aqueous layer extracted with dichloromethane (3 x 250 mL). The crude product was recrystallised from an ethyl acetate/hexane mixture to afford yellow powder of *N*-benzyl-4-propylamine-1,8-naphthalimide (**2.3**) (403 mg, 38%). m.p. 197- 200^{o}C δ_H (600 MHz, $CDCl_3$), 8.59 (1H, d, J= 7.1 Hz, H10), 8.48 (1H, d, J = 8.4 Hz, H17), 8.06 (1H, d, J = 8.3 Hz, H12), 7.61 (1H, t, J = 7.9 Hz, H11) 7.54 (2H, d, J = 7.5 Hz, H5/H1), 7.29 (2H, m, H4/H2), 7.21 (1H, t, J = 7.4 Hz, H3), 6.72(1H, d, J = 8.5 Hz, H15), 5.37

(2H, s, H7) , 5.24(br, NH), 3.38(2H, m H20) ,1.84 (2H, se, J = 7.3 Hz, H21), 1.11(3H, t, J = 7.4 Hz, H22). δ_c (150 MHz, $CDCl_3$), 164.691 (C8), 164.118 (C18), 149.492 (C14), 137.844 (C6), 134.720(C16), 131.313(C10), 129.9, 128.816(C1/C5), 128.327(C2/C4), 127.181 (C3), 125.768 (C12), 124.676 (C11), 123.194, 120.147(C13), 110.210(C17), 104,397 (C15), 45.440 (C20), 43.301 (C7), 22.259(C21), 11.619 (C22). MS(EI) *m/z* 344.3 ($M^{+\cdot}$+H, 25%), 343.3 (M^+, 100%), 223.5 (31%). UATR FTIR (Diamond/ZnSe) υ/cm^{-1} 3385, 1686, 1635, 1548. HRMS (ESI) *m/z* found 345.1604, $[C_{22}H_{20}N_2O_2 + H]^+$ required 345.1598.

4-Formyl-phenyl-15-crown-5 (2.5)

Phenyl-15-crown-5 (**2.4**) (1.98 g, 6.70 mmol) was dissolved in dimethylformamide (DMF) (33 mL), cooled to -4 °C, and phosphoryl chloride ($POCl_3$) (1.2 mL, 13.1 mmol) added to the mixture via precision syringe. The reaction mixture was stirred at *ca.* 0°C for 20 minutes, then at room temperature overnight before heating up to 60°C for 1 hour. After cooling to room temperature, the reaction mixture was poured into water (100 mL), the residue remaining in the flask was rinsed with water (40 mL) and the pH of the combined aqueous solutions was adjusted to pH 7 using saturated aqueous potassium carbonate solution. The aqueous solution was extracted with ethyl acetate (4 x 100 mL), the extracts dried with magnesium sulfate, the solvent removed under vacuum, and the resulting residue dried under high vacuum at ~50°C for 10 to 12 hours to afford 4-Nitroethylenyl-phenylaza-15-crown-5 (**2.6**) as a pale brown coloured solid (1.66 g, 78%). m.p. 87 – 89°C (lit[13] 87 – 88°C); ^{1}H NMR (300 MHz, $CDCl_3$) δ 9.73 (1H, s) 7.72 (2H, d, J = 9 Hz), 6.71 (2H, d, J = 9 Hz), 3.59 - 3.83 (20H, m); UATR FTIR (Diamond/ZnSe) υ/cm^{-1}, 2869, 2797, 2720, 2697, 1600, 1591, 1553 and 1524; MS (ESI, +ve mode) *m/z* 347.2 (17%), 346.1 ($[M+Na]^+$, 100%).

4-Nitroethylenyl-phenylaza-15-crown-5 (2.6)

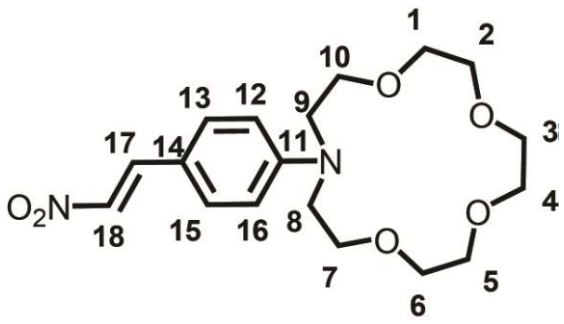

4-Formyl-phenyl-15-crown-5 (**2.5**) (1.66 g, 5.13 mmol) and ammonium acetate (4.06 g, 52.7 mmol) were stirred in glacial acetic acid (10 mL) and nitromethane (6.5 mL) at room temperature for 10 minutes before being heated at 65°C for 5 hours. After cooling, the reaction mixture was diluted with chloroform (20 mL), rinsed with water (3 x 50 mL) and the aqueous washings re-extracted with further chloroform (3 x 50 mL). The chlorinated extracts were combined, dried with magnesium sulfate and the solvent removed in vacuum. The crude product was dried under high vacuum overnight and then recrystallised from ethyl acetate/hexane (~1:3) to afford compound **5** as red needle-shaped crystals (1.20 g, 64 %). m.p. 131 - 133°C; ^{1}H NMR (600 MHz, $CDCl_3$) d = 7.95 (d, *J* = 13.5 Hz, 1 H, H18), 7.49 (d, *J* = 13.5 Hz, 1 H, H17), 7.40 (d, *J* = 8.8 Hz, 2 H, H13, H15), 6.68 (d, *J* = 8.8 Hz, 2 H, H12, H16), 3.81 – 3.60 (m, 20 H, CH_2 from aza-15-crown-5); ^{13}C NMR (151 MHz, $CDCl_3$) d = 151.25(C11), 140.34(C18), 132.34(C17), 131.81 (C13, C15), 117.55 (C14), 112.16 (C12, C16), 71.52, 70.53, 70.23, 68.40, 53.06 (5 x C from aza-15-crown-5); UATR FTIR (Diamond/ZnSe) υ/cm^{-1} 2866, 1593 and 1527; MS (ESI, +ve mode) *m/z* 390.1 (21%), 389 ($[M+Na]^+$, 100%); HRMS (ESI) *m/z* found 367.18672, $[C_{18}H_{26}N_2O_6 + H]^+$ required 367.18636.

4-Aminoethyl-phenylaza-15-crown-5 (**2.7**)

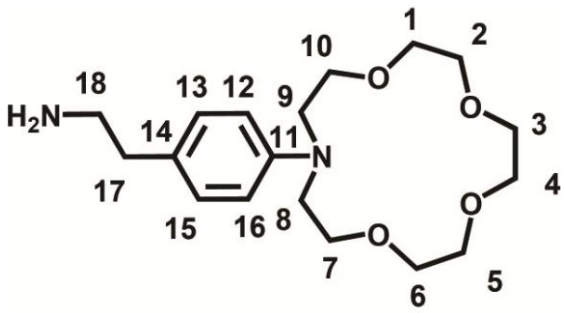

Lithium aluminium hydride (1.45 g, 38.2 mmol) was suspended in freshly distilled tetrahydrofuran (THF) (50 mL) at room temperature. 4-Nitroethylenyl-phenylaza-15-crown-5 (**2.6**) (699 mg, 1.91 mmol**)** was dissolved in THF (50 mL) and added dropwise to the reaction mixture. The reaction mixture was heated to reflux for 5 hours. The reaction was quenched by addition of potassium hydroxide solution (6 M, 47 mL). Further THF (47 mL) was added to the mixture, the slurry filtered and the solid pellet further washed with THF (4 x 25 mL). THF was not miscible with potassium hydroxide solution (6 M), therefore two phases were separated from the supernatant. THF was removed and the residue was redissolved in chloroform (50 mL). The chloroform solution was washed with water (2 x 50 mL) and the aqueous washings were combined with the potassium hydroxide solution separated from the supernatant. The combined basic aqueous solution was extracted with chloroform (2 x 50 mL). All chloroform solutions were then combined and dried with magnesium sulfate. The solvent was removed under vacuum to give **2.7** as orange-brown oil (580 mg, 90%). The product was used in the next step without further purification. ^{1}H NMR (600MHz, $CDCl_3$) d 7.03 (d, *J* = 8.2 Hz, 2 H, H13, H15), 6.61 (d, *J* = 8.8 Hz, 2 H, H12, H16), 3.80 - 3.51 (m, 30 H, H from aza-15-crown-5), 2.90 (t, *J* = 7.0 Hz, 2 H, H17), 2.63 (t, *J* = 7.0 Hz, 2 H, H18), 1.55 (br, NH_2); ^{13}C NMR (151 MHz, $CDCl_3$) d 146.30 (C11), 129.87 (C13, C15), 126.96 (C14), 111.72 (C12, C16), 71.55, 70.41, 68.93, 52.72 (5 x C from aza-15-crown-5 with one overlapping peak), 44.05 (C17) 39.15 (C18) ; UATR FTIR (Diamond/ZnSe) υ/cm^{-1} 2862, 1615 and 1518; MS (ESI, +ve mode) *m/z* 405.1 (20%), 361.2 ([M+Na]$^+$, 100%), 322.2 (24%); HRMS (ESI) *m/z* found 339.22785, [$C_{18}H_{30}N_2O_4$+H]$^+$ required 339.22783.

_N_-Benzyl-[4-(aza-15-crown-5)-phenylethylamino]-1,8-naphthalimide (2.8)

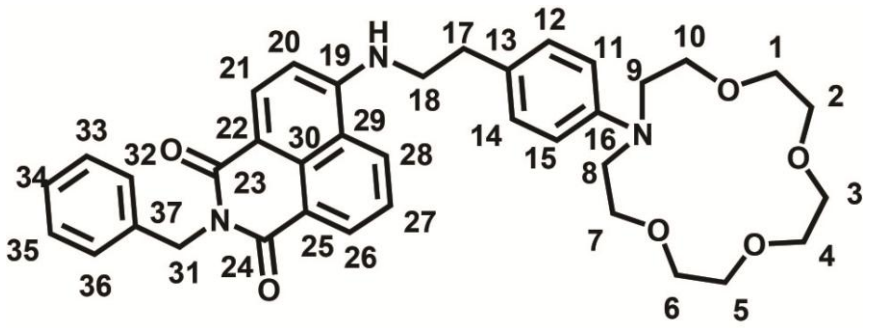

Compound **2.2** (199 mg, 0.618 mmol), **2.7** (418 mg, 1.24 mmol) and DIPEA (272 μL, 1.56 mmol) were dissolved in *N*-methyl-2-pyrrolidone (NMP) (18 mL) in a CEM ™ reaction tube. The tube was sealed and heated at 100°C under microwave irradiation for 4 hours and then at 130°C under microwave irradiation for 1 hour (the reaction progress was monitored by TLC at hourly intervals after the tube was cooled down to 60°C). The NMP was removed by distillation under reduced pressure at 50 - 60°C and the crude product was dried at ~50°C under high vacuum. Purification on silica gel with 1:1 ethyl acetate:chloroform eluate afforded fluoroionophore **2.8** as orange crystals (136 mg, 35%). m.p. 149 – 152°C; ^{1}H NMR (600 MHz, $CDCl_3$) d = 8.57 (d, *J* = 6.4 Hz, 1 H, H26), 8.48 (d, *J* = 8.2 Hz, 1 H, H21), 7.91 (d, *J* = 8.2 Hz, 1 H, H28), 7.57 (t, *J* = 7.9 Hz, 1H, H27), 7.35 (d, J = 7.0 Hz, 1H, H32, H36) 7.31 - 7.18 (m, 3 H, H33, H34, H35), 7.10 (d, *J* = 8.2 Hz, 2 H, H12, H14), 6.76 (d, *J* = 8.2 Hz, 1 H, H20), 6.65 (d, *J* = 8.2 Hz, 2 H, H11, H15), 5.36 (s, 2 H, H31 x 2), 5.31 (br. s., 1 H, NH), 3.81 - 3.54 (m, 22 H, CH_2 from aza-15-crown-5 and H18), 2.98 (t, *J* = 6.7 Hz, 2 H, H17 x 2); ^{13}C NMR (151 MHz, $CDCl_3$) d 164.92 (C22), 164.33 (C23, C24), 149.60 (C19), 146.89 (C16), 138.07 (C37), 134.94 (C21), 131.51 (C26), 130.12 (C30), 129.79 (C12, C14), 129.03 (C32 and C36), 128.54 (C33, C34 and C35), 127.39 (C33, C34 and C35), 126.17 (C28), 124.92 (C27), 124.86 (C19), 123.33 (C13), 120.54 (C29), 112.06 (C11, C15), 110.48 (C19), 104.76 (C20), 71.55, 70.43, 70.29, 68.81, 68.37, 52.75, 44.91 (C18 and 5 x CH_2 from aza-15-crown-5), 43.52 (C31), 33.89 (C17); UATR FTIR (Diamond/ZnSe) υ/cm^{-1} 3364, 2863, 1683, 1636, 1616, 1573, 1545 and 1518; MS (ESI, +ve mode) *m/z* 646.3 ([M+Na]$^{+}$, 100%), 643.2 (3 %), 624.2 (29%), 515.0 (30%), 415.9 (30%); HRMS (ESI) *m/z* found 624.30748, $[C_{37}H_{41}N_3O_6+H]^{+}$ required 624.30681.

N-Benzyl-4-bromo-1,8-naphthalimide (2.10)

Under a nitrogen atmosphere, 4-bromo-1,8-naphthalic anhydride (**2.9**) (1.01 g, 3.61 mmol) was stirred in 20 mL ethanol at 90°C. Benzylamine (380 µL, 3.48 mmol) was then added into the reaction mixture and the resulting solution was heated at reflux for 67 hours. The crude product was collected by filtration, washed with ethanol and dried under vacuum. The crude product was recrystallised from ethanol to afford *N*-benzyl-4-bromo-1,8-naphthalimide **2.10** (975 mg, 76%). m.p. 175 – 176°C (lit[14] m.p. 174.2 – 174.9°C); ^{1}H NMR (300 MHz, $CDCl_3$) δ 8.68 (dd, *J* = 1.10, 7.14 Hz, 1H), 8.58 (dd, *J* = 1.37, 8.52 Hz, 1H), 8.43 (d, *J* = 8.24 Hz, 1H), 8.04 (d, *J* = 8.24 Hz, 1H), 7.85 (dd, *J* = 7.42, 8.52 Hz, 1H), 7.46 - 7.58 (m, 2H), 7.15 - 7.36 (m, 3H), 5.38 (s, 2H); ^{13}C NMR (75 MHz,CDCl3) δ 163.7, 137.2, 133.5, 132.4, 131.6, 131.3, 130.7, 130.6, 129.2, 129.1, 128.7, 128.2, 127.8, 123.2, 122.3, 43.9; UATR FTIR (Diamond/ZnSe) υ/cm^{-1} 3062, 2971, 1695, 1654, 1615, 1588, 1570, 1506, 1495.

N-Benzyl-4-(2-aminoethylamino)-1,8-naphthalimide (2.11)

N-Benzyl-4-bromo-1,8-naphthalimide (**2.10**) (300 mg, 0.82 mmol) was stirred in ethylenediamine (10 mL, 150 mmol) at 80°C for 12 hrs. The solvent was removed by reduced pressure distillation at ~60°C. The residue was dissolved in chloroform (100 mL) and washed with saturated potassium bicarbonate solution (100 mL). The chloroform solution was washed with water (50 mL x 2) and dried with magnesium sulfate. The solvent was removed under vacuum. The product was obtained as an orange yellow solid (247 mg, 88%), which used in the next step without further purification. m.p. 167°C (lit[15] 239 – 240°C) ; ^{1}H NMR (300 MHz, CDCl3) δ 8.59 (dd, *J* = 1.10, 7.14 Hz, 1H), 8.48 (d, *J* = 8.24 Hz, 1H), 8.16 (dd, *J* = 0.82, 8.52 Hz, 1H), 7.61 (dd, *J* = 7.42, 8.52 Hz, 1H), 7.49 - 7.57 (m, 2H), 7.16 - 7.36 (m, 3H), 6.71 (d, *J* = 8.52 Hz, 1H), 6.17 (br. s.), 5.37 (s, 2H), 3.41 (td, *J* = 4.84, 6.52 Hz, 2H), 3.18 (dd, *J* = 4.81, 6.73 Hz, 2H); ^{13}C NMR (75 MHz, CDCl3) δ 150.0, 138.1, 134.9, 131.5, 130.1, 129.1, 128.5, 127.4, 126.5, 124.9, 123.2, 120.6, 110.3, 104.7, 45.0, 43.5, 40.3, 0.2; MS (ESI, +ve mode) *m/z* 712.9 ($2M^+$-2H, 100%), 714 ($2M^+$-H, 43%), 346.2 (M^+, 18%); HRMS (ESI) *m/z* found 346.155, $[C_{21}H_{20}N_3O_2+H]^+$ required 346.155; UATR FTIR (Diamond/ZnSe) υ/cm^{-1} 3335, 3287, 1678, 1628, 1572, 1551, 1497

N-Benzyl-4-(2-phenylthioureaethylamino)-1,8-naphthalimide (2.12)

N-Benzyl-4-(2-aminoethylamino)-1,8-naphthalimide (**2.11**) (101 mg, 0.29 mmol) and phenyl isothiocyanate (70 μL, 0.58 mmol) were stirred in anhydrous chloroform (10 mL) under a nitrogen atmosphere at room temperature for 18 hrs. The precipitate was filtered off and washed with chloroform (10 mL x 2). The product, an orange-yellow solid, was dried overnight (78 mg, 54%). m.p. 209°C (lit[15] 297 – 298°C); ^{1}H NMR (300 MHz, DMSO-d_6) δ 9.66 - 9.77 (m, 1H), 8.72 (d, *J* = 7.97 Hz, 1H), 8.46 (d, *J* = 6.87 Hz, 1H), 8.28 (d, *J* = 8.52 Hz, 1H), 7.97 (br. s., 2H), 7.65 - 7.79 (m, 2H), 7.08 - 7.38 (m, 10H), 6.99 (d, *J* = 8.79 Hz, 1H), 5.22 (s, 2H), 3.85 (d, *J* = 5.49 Hz, 2H), 3.63 (d, *J* = 5.49 Hz, 2H); ^{13}C NMR (75 MHz, DMSO-d_6) δ 180.5, 163.8, 163.0, 151.0, 137.9, 134.5, 129.5, 128.9, 128.3, 127.5, 126.9, 124.6, 123.6, 121.8, 120.2, 107.7; MS (ESI, +ve mode) *m/z* 503.2 (M^++ Na, 100%), 504.2 (34%); UATR FTIR (Diamond/ZnSe) υ/cm^{-1} 3240, 1737, 1676, 1634, 1615, 1586, 1541, 1509.

2.3 Results and discussion

2.3.1 Synthesis of N-benzyl-4-propylamine-1,8-naphthalimide (2.3)

Scheme 2.1 shows the synthesis of N-benzyl-4-propylamine-1,8-naphthalimide (**2.3**) utilised in this research. Benzylamine was coupled with 4-chloro-1,8-naphthalic anhydride to give N-benzyl-4-chloro-1,8-naphthalimide. The 4-chloro moiety was then substituted by propylamine via an aromatic nucleophilic substitution reaction; the overall yield was 25%. A ^{1}H NMR spectrum of fluorophore **2.3** shows diagnostic signals from the propyl group from 1.11 – 3.38 ppm, the amine group at 5.24 ppm and benzyl group at 5.37 ppm. The high resolution mass spectrometry (HRMS) of fluorophore **2.3** shows the mass matches the theoretical value.

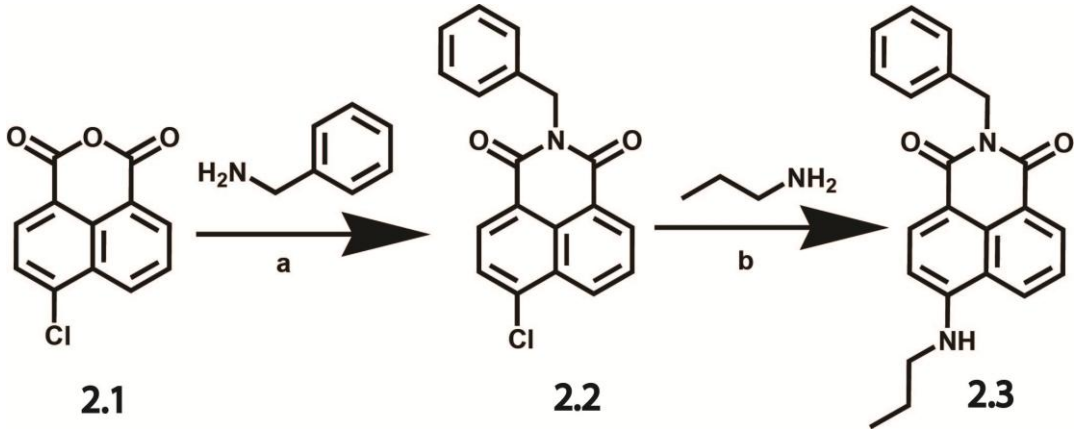

Scheme 2.1: Synthesis of model fluorophore (**2.3**). (a) Ethanol, 90°C, 66 hours, 67% (b) DIPEA, NMP, 105°C, 22 hours, 38%

2.3.2 Characterisation of fluorophore 2.3 in cuvettes and SCFs

The measurements of the molar extinction coefficient and fluorescence emission maxima of fluorophore **2.3** were performed in acetonitrile as this is a solvent which will dissolve both the PET fluoroionophore derivatives of **2.3** and the target ions as their perchlorate or tetraethylammonium salts. Figure 2.6a shows the spectrum of fluorophore **2.3**, plotted as molar extinction coefficient versus wavelength; the peak absorption wavelength of **2.3** is 435 nm and the molar extinction coefficient is 15506 $M^{-1}cm^{-1}$. However, as 435 nm is close to the UV edge of the transmission window for F2 glass, the excitation wavelength for the SCF experiments was chosen to be 473 nm [16]. This was done firstly because this is a wavelength from a commercially available diode laser, and a laser was the preferred light source in this project as it is easier to focus into the core of the SCF. Secondly, the F2 glass demonstrates lower attenuation at 473 nm, which was described in Chapter 1. Finally, excitation at 435 nm demonstrated a photodarkening effect in the SCF during preliminary experiments. The photodarkening effect decreases the transmission of the excitation light in the SCF as a function of time, which is undesirable for a SCF sensor. Figure 2.6b shows the emission spectrum of fluorophore **2.3** excited at 470 nm, measured by a Cary spectrofluorometer. The peak emission was 520 nm.

The excitation wavelength used in this project was 473 nm, except for the preliminary photobleaching experiment, which used an Argon ion laser at 477 nm. Equation 2.8 shows the dependence of the emission intensity (I(*l*)) on the molar

extinction coefficient (ε), given that the excitation intensity (I_o), concentration (c) of the fluorophore, path length of the cuvette/SCFs, quantum efficiency (Φ) and the instrumental factor (k) are constant.

$$I(l) = I_o k \Phi \varepsilon l c \qquad \text{(Equation 2.11)}$$

The molar extinction coefficient of fluorophore **2.3** at 473 nm is 5466 $M^{-1}cm^{-1}$, which is 35% of the maximum molar extinction coefficient at 435 nm. Therefore, the emission intensity of the fluorophore excited at 473 nm is only 35% of the excitation at 435 nm. The ions sensing function of the PET fluoroionophores is not affected as long as the change of fluorescence intensity is detectable.

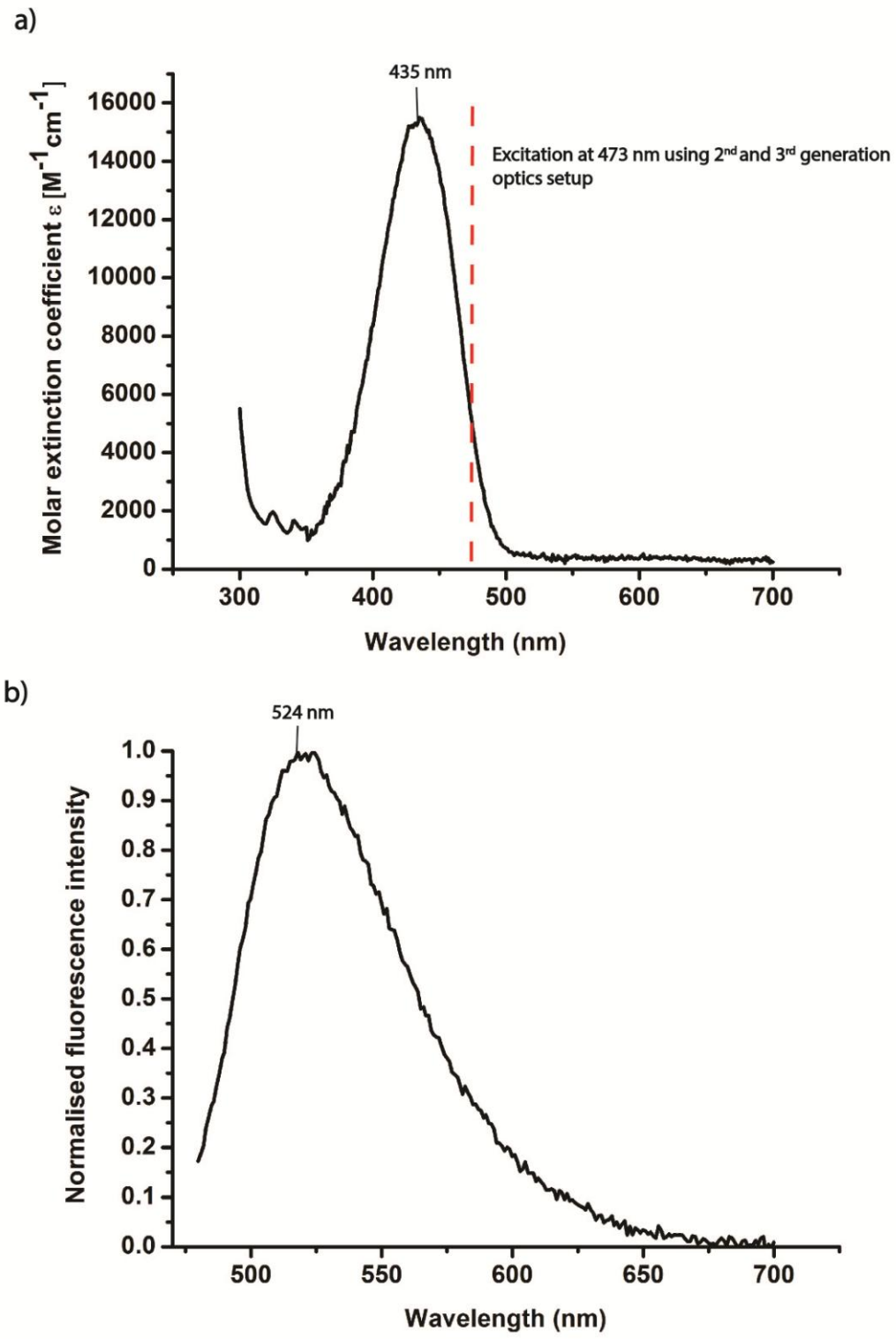

Figure 2.6: (a) The spectrum of fluorophore **2.3**, plotted as the molar extinction coefficient (ε) $M^{-1}cm^{-1}$ versus wavelength in CH_3CN (I = 0.1 M). The peak absorption wavelength is at 435 nm. (b) The normalised emission spectrum of fluorophore **2.3** (1.8 μM) in CH_3CN (I = 0.1 M) measured by a Cary spectrofluorometer. The peak emission wavelength is at 524 nm

After determining the excitation wavelength for the sensing experiment, the next step was to determine the photostability of fluorophore **2.3** when used within a SCF. This experiment was performed using the 1st generation optical set-up with an argon ion laser at 477 nm as the excitation source. This work was presented at the Australian Conference on Optical Fibre Technology (ACOFT) in 2009 [5]. As described in Chapter 1, photobleaching is dependent on the concentration of singlet oxygen and the excitation power. Figure 2.7 shows, as expected, that the higher the laser power, the higher the photobleaching rate. Since the photobleaching experiments for Rhodamine B and fluorophore **2.3** were not performed in the same solvent, the amount of singlet oxygen could be different. Thus, it is not fair to compare their relative photostability. The result of this preliminary experiment shows that the photobleaching of fluorophore **2.3** can be minimised by lowering the excitation laser power to 0.03 mW. This observation suggests that fluorophore **2.3** is suitable in SCF sensing as long as the power is kept below 0.03 mW. Therefore, in the later experiments described in this thesis, the laser power was kept at 0.01 mW or 0.001 mW.

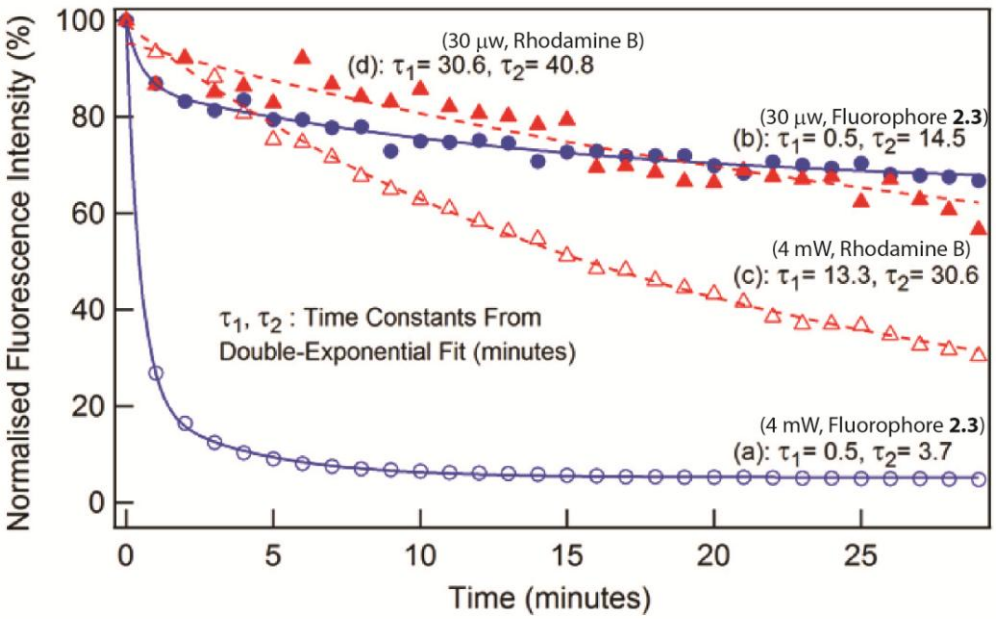

Figure 2.7: Photobleaching of fluorophore **2.3** in ethanol (blue) and Rhodamine B in dichloromethane (red) within SCFs. Fluorophore **2.3** excited with (a) 4 mW and (b) 30 µW laser output powers at 477 nm. Rhodamine B excited with 4 mW (c) and (d) 0.03 mW laser output powers at 532 nm [5].

2.3.3 Synthesis of model PET fluoroionophore 2.8 for cations sensing

Scheme 2.2 shows the synthesis of **2.8**. A commercially available ionophore, *N*-phenyl aza-15-crown-5 (**2.4**), was utilized which, using established literature procedures, can be linked to the photostable naphthalimide fluorophore through an ethyl spacer [2, 17]. Thus, **2.8** possesses a similar structure to the PET sensor reported by He *et al*., but for synthetic simplicity (16% overall yield, 4 linear steps) the methyl ether moiety ortho to the aza-15-crown-5 and the carboxyl moiety for surface or polymer attachment were omitted [2].

The ^{1}H NMR spectrum of fluoroionophore **2.8** shows a characteristic singlet from the benzyl proton (5.36 ppm) on the fluorophore side and the triplet from the aliphatic chain next to the amine group. The ratio between these two signals is 1:1, which indicates that the coupling of the ionophore and fluorophore was successful. Furthermore, HRMS of fluoroionophore **2.8** shows the mass matches the theoretical value.

Simple aza-crowns bind to alkali cations with binding constants in the molar range [18]; typically log K ~2 dm^3 mol^{-1} in aqueous conditions and ~3 dm^3 mol^{-1} in methanol [19-21]. These binding constants can be enhanced by providing additional donors such as a methoxy group on the aromatic ring [18], however the focus in this study was to demonstrate a proof-of-concept. The selectivity of the ionophore is important for the development of SCF sensors and is further discussed in Appendix B.

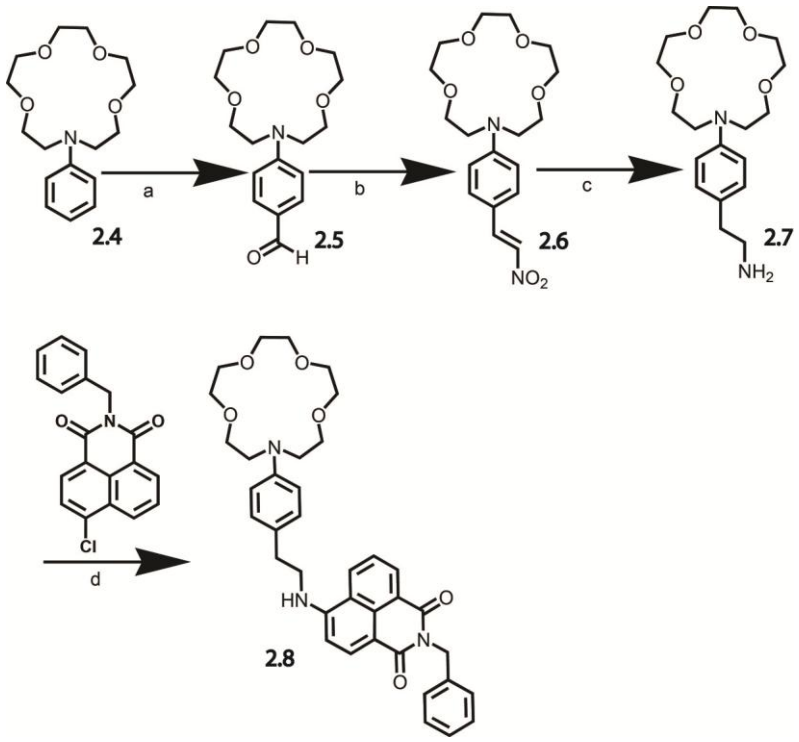

Scheme 2.2: The synthesis of the model PET-fluoroionophore for cations sensing (**2.8**): (a) $POCl_3$, DMF, 60°C, 78%. (b) AcOH, CH_3NO_2, NH_4OAc, 65°C, 64%. (c) $LiAlH_4$, THF, 80°C, 90% (crude product). (d) NMP, DIPEA, microwave, 100 - 130°C, 35%

The ionophore of fluoroionophore **2.8** is phenyl aza-15-crown-5, which binds to sodium, potassium, calcium, barium and ammonium ions [22-24]. Sodium ion was selected to be the ion used to demonstrate the cations sensing in SCFs. Sodium perchlorate was dissolved in acetonitrile with tetraethylammonium perchlorate (NEt_4ClO_4) acting as an ionic buffer. Tetraethylammonium salts were used as a component of the ionic buffer because the tetraethylammonium ion is too large to be accommodated into the 1-aza-crown-5-ether ionophore and hence does not compete for the binding site with sodium. In the sensing experiment, the concentration of tetraethylammonium ions was at least 5 times higher than the maximum sodium ion concentration; therefore the percentage change of the ionic strength of the solution due to the addition of sodium ions was minimised.

2.3.4 Synthesis of model PET fluoroionophore for anions sensing (2.12)

Scheme 2.3 shows the synthetic route used to prepare fluoroionophore **2.12**. Benzylamine was coupled to 4-bromo-1,8-naphthalic anhydride to form *N*-benzyl-4-bromo-1,8-naphthalimide. The 4-bromo moiety was then substituted in an aromatic nucleophilic substitution reaction by ethylenediamine to give **2.11**. The amine group of **2.11** was finally coupled to phenyl isothiocyanate to form thiourea **2.12** and the ionophore. The overall yield from **2.9** to **2.12** was 36%. The synthesis of **2.12** was also recently reported by Tolpygin *et al* with some modification of the conditions used and the resulting yields (Scheme 2.4) [15].

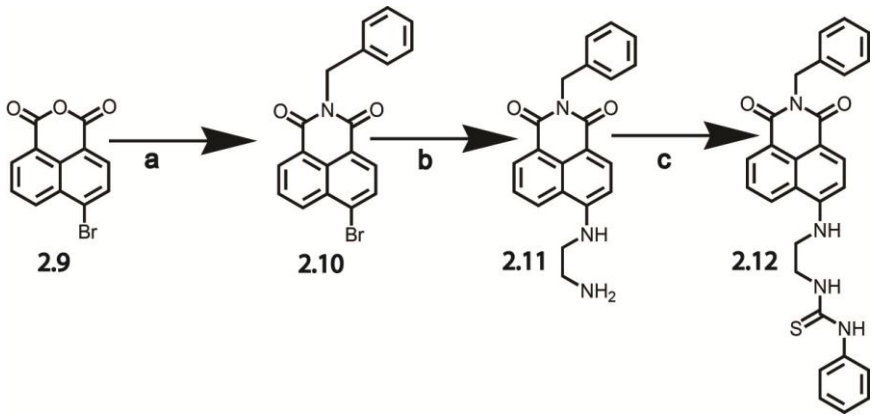

Scheme 2.3: Synthesis of model anions sensing PET fluoroionophore (**2.12**): (a) Benzylamine, ethanol, 90°C, 67 hrs, 76%. (b) ethylenediamine (neat), 80°C, 12 hrs, 88%. (c) phenyl isothiocyanate, anhydrous chloroform, room temperature, 18 hrs, 54%

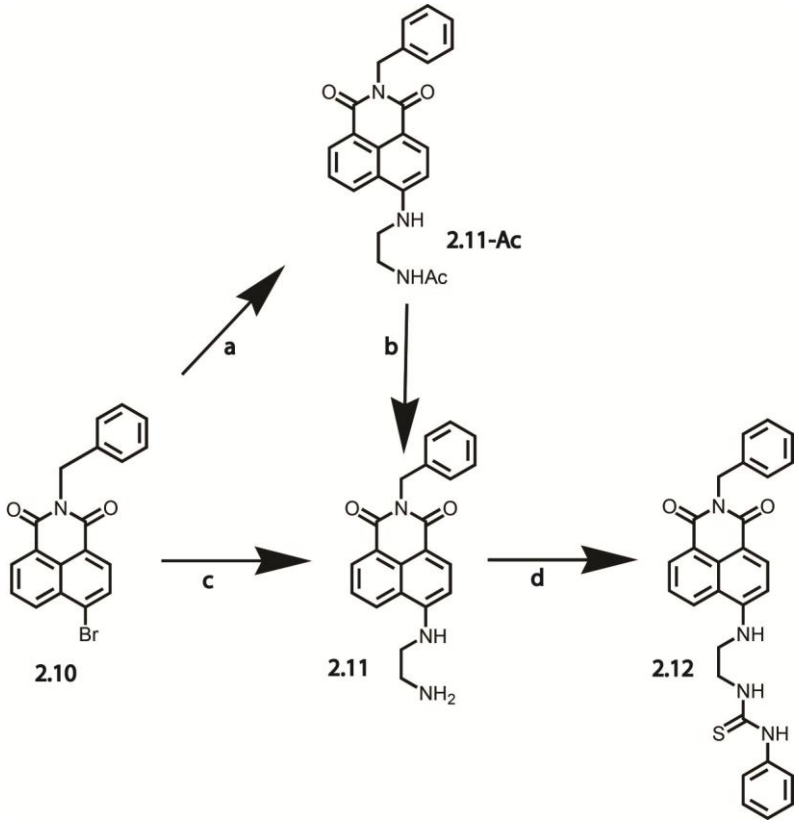

Scheme 2.4: Synthesis of fluoroionophore **2.12** using procedure reported by Tolpygin *et al* (a) ethanol, N-(2-amino-ethyl)acetamide, 20 hrs, reflux, 60%. (b) HBr (46%), 2-propanol, 2 hrs, reflux. 75% (c) ethylenediamine, ethanol, 20 hrs, reflux, 62%. (d) phenyl isothiocyanate, benzene, 5 hrs, reflux 83%

2.3.5 Characterisation of fluoroionophores 2.8 and 2.12 in cuvettes

Both model PET fluoroionophores are slight structural modifications of literature compounds. As a consequence of the changes to the structures, the functionality of **2.8** and **2.12** was validated before the SCF experiments.

As expected for **2.8**, Figure 2.8 shows that the intensity of the excitation and emission spectra both increase with the increasing concentration of sodium ions. The concentration of fluoroionophore **2.8** was kept constant at 0.02 mM during the experiment. No significant shift in the wavelength of the excitation or emission spectra occurs as the concentration of sodium ions increased, showing that **2.8** does not exhibit photoinduced charge transfer (PCT) and is therefore operating via a PET mechanism [25].

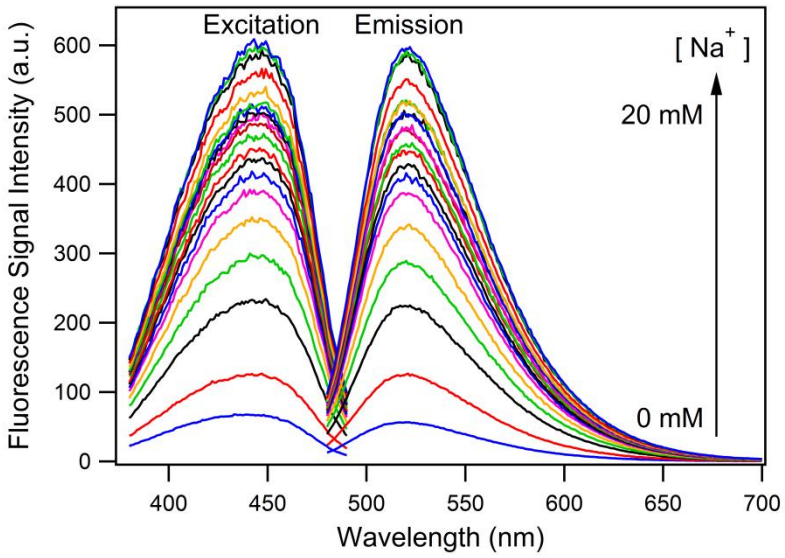

Figure 2.8: Excitation and emission spectra of fluoroionophore **2.8** in acetonitrile ($[NEt_4ClO_4]$ = 100 mM) with sodium ion concentrations ranging from 0 - 20 mM (100 mole equivalent) and a constant concentration of fluoroionophore **2.8** (0.02 mM). The excitation (left) and emission (right) spectra were recorded at fixed emission and excitation wavelengths of 520 nm and 440 nm, respectively

Figure 2.9a shows the normalised average integrated fluorescence intensity with respect to increasing sodium ion concentrations from 0 to 451 ppm. Due to the relatively weak affinity of the aza-15-crown-5 ionophore for sodium ions, [18] a clear saturation point cannot be identified even when sodium reaches 1000 mole equivalence (451 ppm). As described in Chapter 1, the anion PET sensing mechanism is opposite to that observed for PET cations sensors. PET anions sensors show a decrease in fluorescence intensity when it binds to anions. Figure 2.10a shows fluorescence quenching of fluoroionophore **2.12** with increasing concentration of fluoride ions from 0 to 23 ppm. The concentration of fluoroionophore **2.12** was kept constant at 0.02 mM during the experiment. A saturation point at 18 ppm is identified. This suggests the fluoride ion has strong binding to the fluoroionophore **2.12**. Figure 2.9b and 2.10b show linear calibration plots of the normalised average integrated fluorescence intensity of the fluoroionophore with sodium ion concentrations ranging from 0 to 23 ppm (Figure 2.6b) and fluoride ions ranging from 0 to 18 ppm (Figure 2.6b). The

regression coefficients (R^2) of both plots are 0.98, which suggests the experimental data points fit well on the regression line. The insets in Figure 2.6b and 2.7b are the residue plots of the linear calibration plot in these figures. The residue plots show that the data points are randomly distributed along the centre line; therefore linear regression is a suitable model.

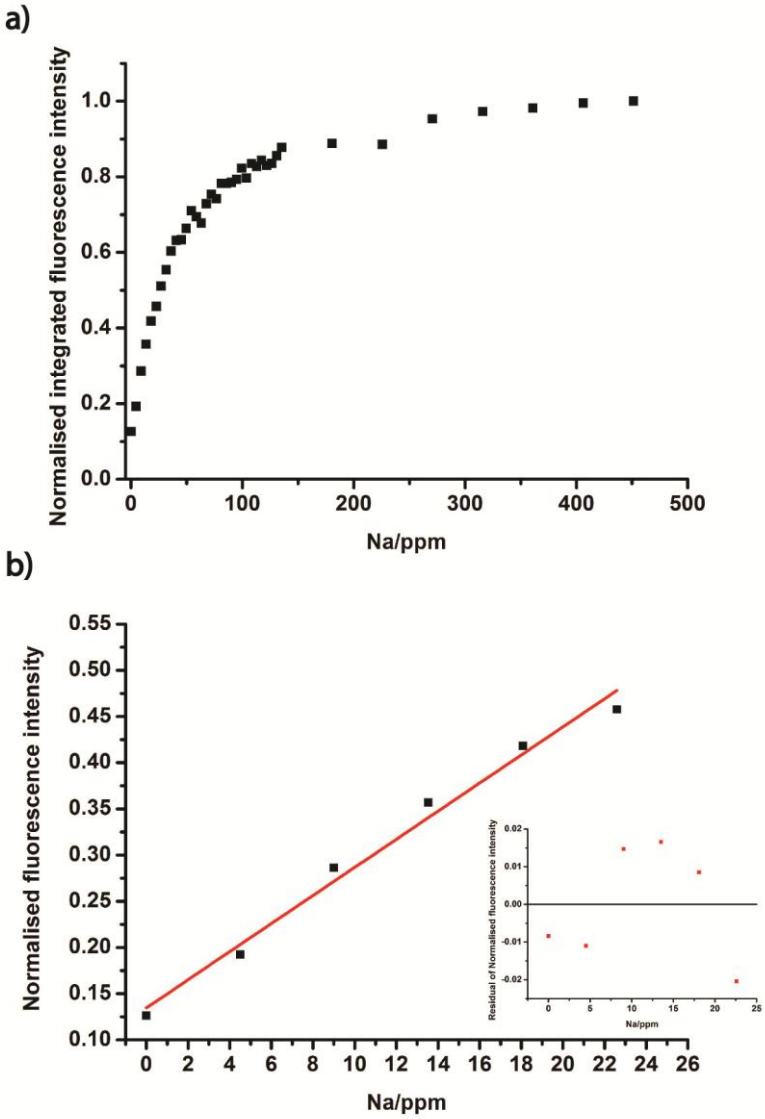

Figure 2.9: (a) Normalised average integrated fluorescence intensity for fluoroionophore **2.8** with different concentrations of sodium ions from 0 – 451 ppm (1000 mole equivalent) in CH_3CN (Ionic strength =100 mM). (b) linear regression for fluoroionophore **2.8** with different concentrations of sodium ions from 0 – 23 ppm (50 mole equivalent). The inset shows the residue plot of the linear regression.The R^2 of the regression is 0.98. The concentration of fluoroionophore **2.8** was 0.02 mM

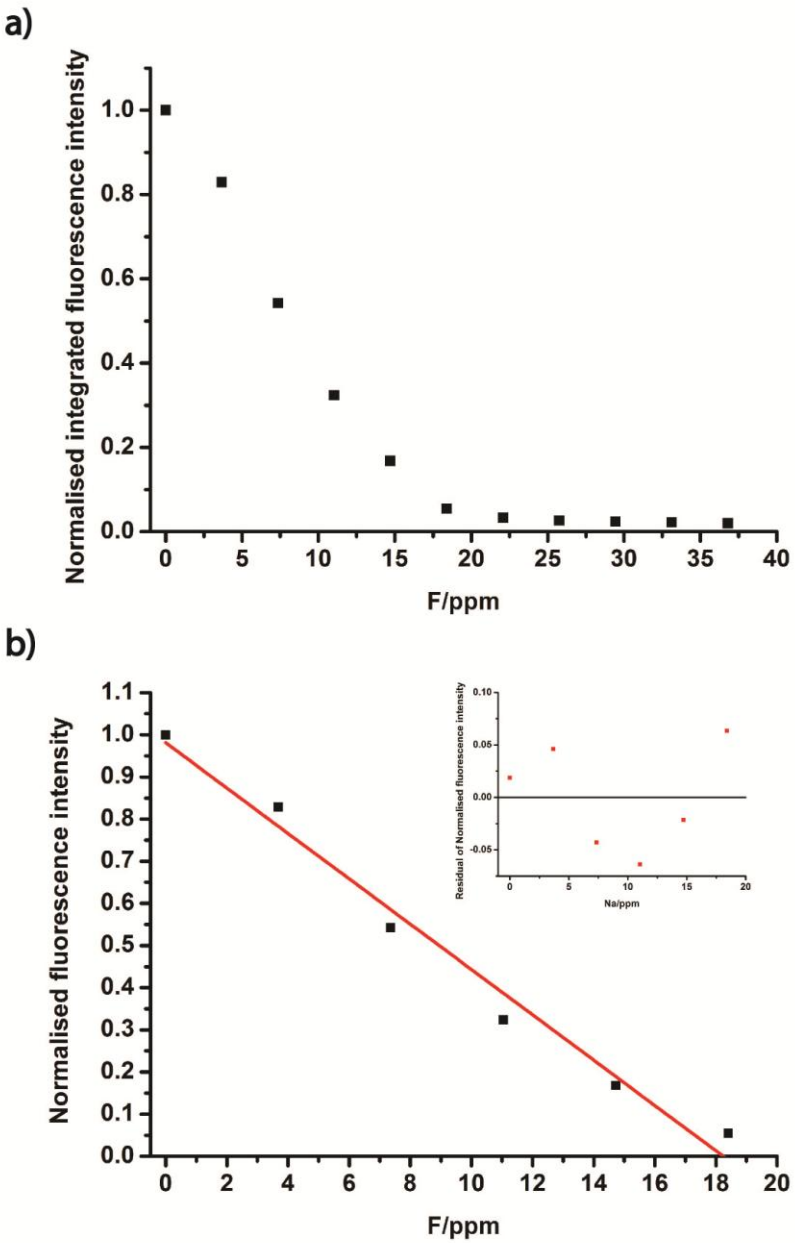

Figure 2.10: (a) Normalised average integrated fluorescence intensity for fluoroionophore **2.12** with different concentrations of fluoride ions from 0 – 37 ppm (97 mole equivalent) (b) Linear regression for fluoroionophore **2.12** with different concentrations of fluoride ions from 0 – 18 ppm (47 mole equivalent). The inset shows the residue plot of the linear regression. The R^2 of the regression is 0.98. The concentration of fluoroionophore **2.12** was 0.02 mM

2.3.6 Preliminary experiments of sodium ions sensing in SCFs

After the validation of the functionality of fluoroionophore **2.8** using the Cary spectrofluorometer, preliminary experiments were performed to demonstrate the feasibility of performing sodium ions detection in solution using F2 SCFs. This preliminary work was published in 2011 and presented at the Third Asia Pacific Optical Sensors Conference 2012 [26].

The 2nd generation optical set-up and fibre filling method are described in Section 2.2.2 [6]. Figure 2.11a shows the fluorescence enhancement of data sets A, B, C and D acquired at different times. The concentrations of fluoroionophore **2.8** in A and B are 0.402 mM, which is 51 times higher than C and D (0.0079 mM). However, the concentration ratio of sodium to fluoroionophore **2.8** was kept constant at 100:1. Fluorescence enhancement was observed in all data sets. The percentage fluorescence enhancement of data sets A to D are summarised in Table 2.2.

Table 2.2: Percentage fluorescence enhancement of data sets A to D

Data set	% fluorescence enhancement	Fluoroionophore **2.8** concentration/mM	Sodium ion concentration/ppm
A	36.4	0.402	925
B	21.4	0.402	925
C	4.1	0.0079	18.4
D	12.2	0.0079	18.4

All data sets show fluorescence enhancement, which indicates sodium ions sensing using fluoroionophore **2.8** in SCF is feasible. However, the percentage enhancement is inconsistent even for data sets with the same concentration of fluoroionophore **2.8**. This is attributed to unstable laser power and coupling. In this preliminary experiment, the percentage fluorescence enhancement in data sets C and D are less than that of A and B even when the fluoroionophore to sodium ion ratio was equal. This is possibly either because of the physisorption of the fluoroionophore on the core of the F2 SCF, or because of the leaching of sodium or potassium ions from the F2 glass, which is further discussed in Chapter 3B

[27]. The physisorption of the fluoroionophores on F2 glass surfaces is explored in detail in Chapter 4.

The leaching of sodium or potassium ions from glass increases the fluorescence intensity of the blank samples (Figure 2.11a), therefore the percentage enhancement decreases. Physisorption of the fluoroionophores also leads to an increase in the fluorescence intensity because the ionophores can interact with sodium ions and potassium ions on the glass surface. This interaction increases the fluorescence intensity of the fluoroionophores. Figure 2.11b shows the photobleaching rate of fluoroionophore **2.8 (**0.0079 mM) with 1.2 s exposure time. The fluorescence intensity decays to 60 – 70% of its original value. Photobleaching was significant in these preliminary experiments but was minimised later on as discussed in the next section.

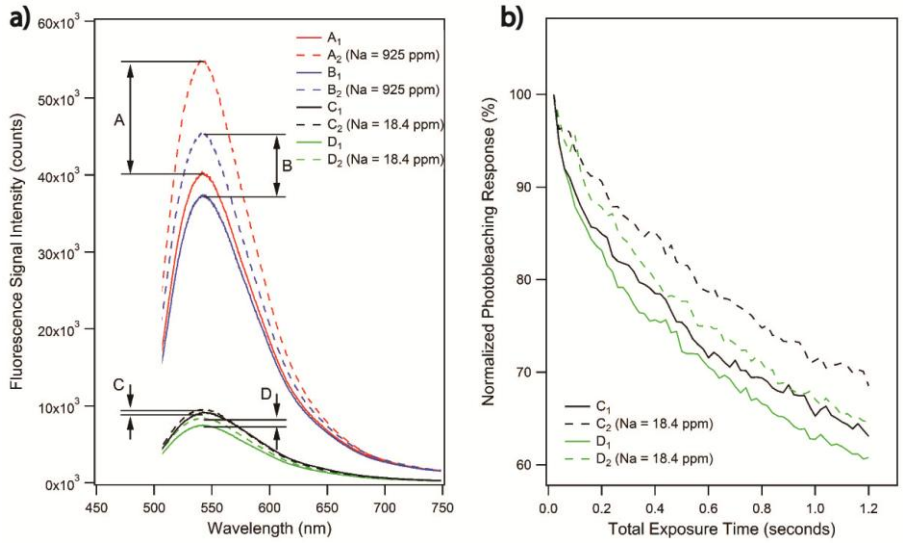

Figure 2.11: (a) Fluorescence spectra of the fluoroionophore **2.8** in F2 SCFs. A_1 and B_1 (Solid line) are spectra of fluoroionophore **2.8** (0.402 mM)(blank) and A_2 and B_2 (dashed line) are spectra of fluoroionophore **2.8**(0.402 mM) with 40.2 mM (925 ppm) sodium ions. C_1 and D_1 are spectra of fluoroionophore **2.8** (0.402 mM) (blank) and C_2 and D_2 are spectra of fluoroionophore **2.8** (0.0079 mM) with 0.799 mM (18.4 ppm) sodium ions. (b) Photobleaching response of trial C and D. C_1 and D_1 show the normalised photobleaching response of fluoroionophore **2.8** in SCFs. C_2 and D_2 show the normalised photobleaching response of fluoroionophore **2.8** with 18.4 ppm sodium ions.

2.3.7 Results of sodium ions sensing experiments in cuvettes and SCFs

Sodium sensing experiments using the 2nd generation optical set-up were undertaken in F2 SCFs in the concentration range 0 – 92 ppm (4 mM), while the concentration of fluoroionophore **2.8** was fixed at 0.02 mM. Cuvette measurements were performed with an optical set-up that is similar to the setup for measurements in SCFs, but the nanostage and lens for the SCF experiments were replaced by the cuvette holder as shown in Figure 2.2d. This can therefore provide a comparison of the performance of fluoroionophore **2.8** in a cuvette (bulk) and within SCFs.

As described in Chapter 1, photobleaching is a common problem for any fluorescence measurements in SCFs, as it leads to the reduction of fluorescence intensity and hence introduces reproducibility issues. Figures 2.I a–h (Chapter 2 Appendix) show the photobleaching analyses of experiments for fluoroionophore **2.8** in F2 SCFs. Apart from Figure 2.Ic showing approximately a 3% decrease, which could also be due to coupling variation, other measurements show no evidence of photobleaching within the measurement time used in these experiments. The photobleaching of fluoroionophore **2.8** was minimised by using a much lower excitation beam power with a longer exposure time. The excitation power in the preliminary experiments, discussed in Section 2.3.6, was 2.5 mW and total exposure time of a full measurement of one sample was 17.5 ms. In contrast, the maximum excitation power of the sensing experiments of fluoroionophore **2.8** and **2.12** discussed in subsequent sections was 0.1 mW and the total exposure time was 144 ms.

Figure 2.12 shows the normalised average integrated fluorescence intensity of fluoroionophore **2.8** for sodium ion concentrations in the range 0 – 92 ppm. The red line is obtained from the cuvette measurements and the black line from the F2 SCF measurements. Both show the same trend with increasing concentration of sodium ions. However, the normalised fluorescence intensity of fluoroionophore **2.8** without sodium ions in the SCF is much higher than that in the cuvette. This is possibly due to the physisorption of fluoroionophores on the core or leaching of sodium or potassium ions. Both reasons could contribute to the increase of the fluorescent intensity. Furthermore, the data from the SCF measurements show

greater fluctuation compared with the cuvette measurements. This is possibly a consequence of power fluctuations due to laser instabilities observed in the 2nd generation optical set-up. The fluctuation of the emission intensity is possibly due to the inconsistent leaching of the sodium and potassium or the physiorption of fluoroionophores **2.8** on the surface.

Although the data fluctuate due to the technical issues, this result suggests quantitative measurement of sodium ion concentration is possible in SCFs. Figure 2.VIIa (Chapter 2 Appendix) shows a calibration curve generated from the linear regression of data from 0 ppm to 9.2 ppm sodium ions. The regression coefficient is only 0.74 because of the fluctuation in emission intensity, but it still suggests the feasibility of quantitative measurements following further development.

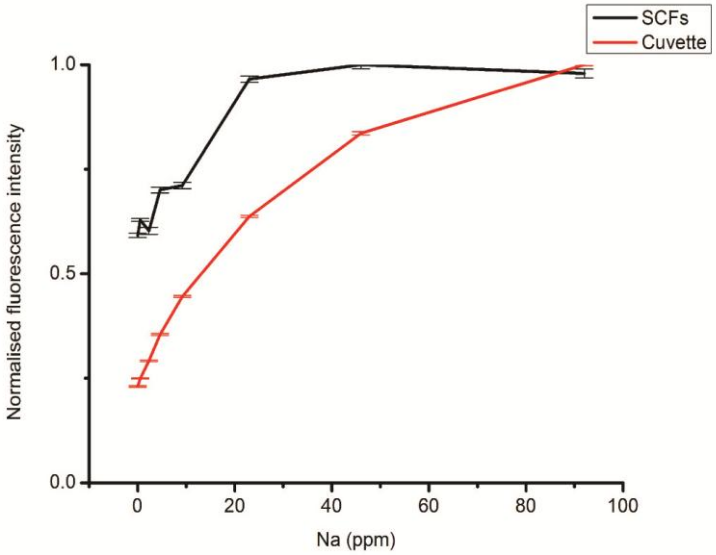

Figure 2.12: Normalised average integrated fluorescence intensity for fluoroionophore **2.8** (0.02 mM) with sodium ion concentrations in the range 0 – 92 ppm (200 mole equivalent)

2.3.8 Anions sensing experiments in SCFs

As well as the fluoride ion sensing, chloride; acetate and dihydrogenphosphate ion sensing experiments were also performed in cuvette and F2 and silica SCFs. Chloride, acetate and dihydrogenphosphate ions should not cause fluorescence quenching based on the literature [28]. Note that the experiments using F2 SCFs

were performed using the 2nd generation optical set-up, while the experiments using cuvette and silica SCFs were performed with the 3rd generation optical set-up.

As for the sensing experiments for fluoroionophore **2.8**, photobleaching analyses were performed for all the measurements with fluoroionophore **2.12** (Figures 2.II – VII in Chapter 2 Appendix). No evidence of photobleaching was found, which indicates that the measurement procedure was optimised for 4-amino-naphthalimide-based fluoroionophores.

Figure 2.13 shows the normalised average integrated fluorescence intensity as a function of the concentrations (0 – 33.7 ppm) of fluoride ions. It shows that the general trends of the F2 SCF measurements are similar to the cuvette measurements, where the normalised fluorescence intensity decreases with an increase in fluoride ion concentration. However, there is an increase in fluorescence intensity in silica SCF when fluoroionophores bind to fluoride ions. The 0 ppm point was repeated but the fluorescence intensity is still lower than that of the samples with the fluoride ion concentration up to 26.3 ppm. Therefore, it is not an experimental error. After the increase in fluorescence intensity from 0 ppm to 5 ppm fluoride ions, the intensity decreases with an increase in the fluoride ion concentration.

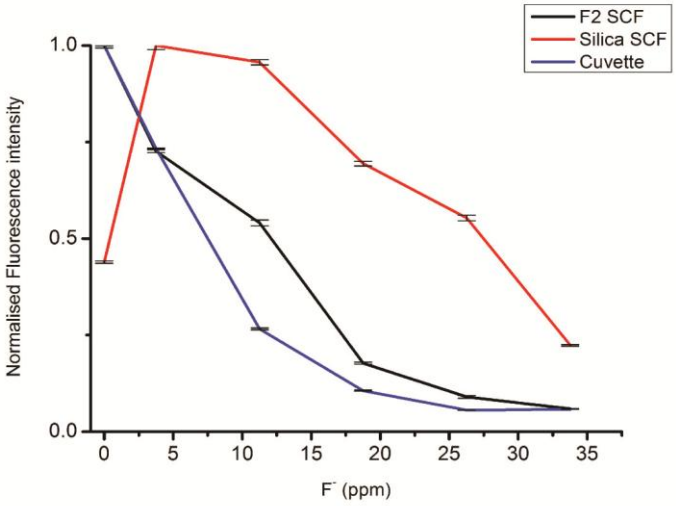

Figure 2.13: Normalised average integrated fluorescence intensity for fluoroionophore **2.12** (0.02 mM) with fluoride (F^-) ion concentrations in the range 0 – 33.7 ppm (88.7 mole equivalent)

This result suggests that there is another mechanism controlling the detected fluorescence intensity in SCFs. The difference observed between F2 and silica SCFs is possibly due to the difference in the surface charge of these glass materials, which then causes a different affinity for the fluoroionophore-fluoride complex towards the surface of the SCF. The affinity of charged particles for a material's surface is called electroosmatic flow. Different glass materials demonstrate different electroosmatic flows. Silica and silicate glass usually have an overall negative charge which is attributed to $Si\text{-}O^-$ groups on the surface. F2 is a silicate glass which contains sodium and potassium ions. These ions can be leached from the surface which creates higher negative charge at the surface compared to silica glass. This surface charge affects the fluorescence capturing efficiency by changing the distance between the fluoroionophore-fluoride complex and the surface of the core of the SCF. The evidence supporting enhanced surface negative charge for F2 glass is discussed in Chapter 3B.

Figure 2.14 describes the possible scenarios for the fluoroionophore **2.12** - fluoride complexes on F2 and silica glass surface. Both silanol and negative $Si\text{-}O^-$ exist on F2 and silica glass surfaces. The fluoride ion could be attracted via hydrogen bonding with silanol groups, whereas repulsion can occur between fluoride ions and the negative $Si\text{-}O^-$ groups on the glass surface. The overall balance between both interactions determines the overall distance between the fluoroionophore-fluoride complexes and the surface of the core. On a silica surface, the quantity of silanol groups is higher than negative $Si\text{-}O^-$ groups; therefore the chance of the fluoroionophore **2.12**-fluoride complexes being closer to the surface is higher than that of fluoroionophore **2.12** alone (Figure 2.13a). In contrast, an F2 surface (Figure 2.13b) has more negative charges, which create greater repulsion and reduce the chance of fluoroionophore **2.12**- fluoride complexes being held closer to the glass surface. The proximity of the fluoroionophores and the surface of the SCF core are highly correlated to the detected fluorescence intensity because the closer the complexes are to the core the higher the fluorescence capturing efficiency. This concept is discussed in Chapter 1 Section 1.2.

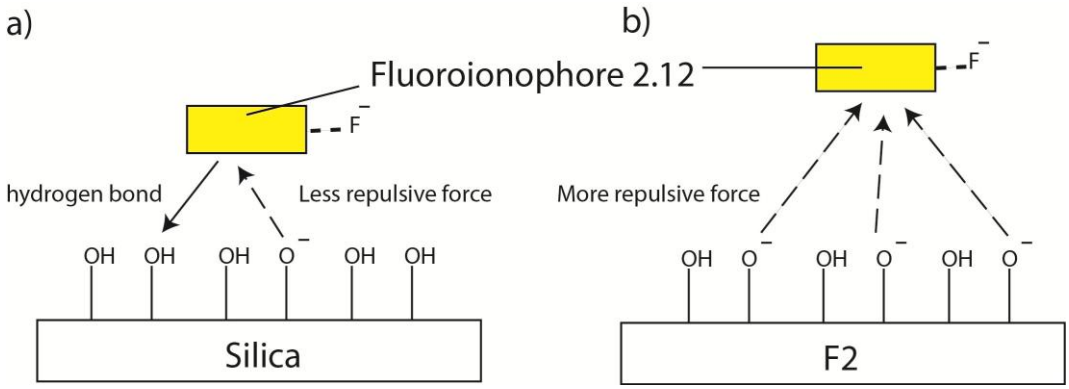

Figure 2.14: Possible explanations for the fluoroionophore **2.12** - fluoride complex positioning on (a) silica glass surface and (b) F2 glass surface

As also shown in figure 2.13, the trends for the normalised fluorescence intensity of fluoroionophore **2.12** and fluoride ions in F2 SCFs and cuvettes are similar. This similarity is higher than that of the trend for the normalised fluorescence intensity of fluoroionophore **2.8** and sodium ions in F2 SCFs and cuvettes, as shown in Figure 2.13. This suggests fluoroionophore **2.12** is insensitivity to the leaching of sodium and potassium compared with fluoroionophore **2.8.** It is firstly because fluoroionophore **2.12** is designed to be anions fluoroionophores; secondly, this leaching creates negatively charged surfaces that fluoroionophore **2.12**-fluoride complexes are being repelled from F2 glass surfaces regardless to the polarity of the solvent.

Figure 2.15 shows the normalised average integrated fluorescence intensity of fluoroionophore **2.12** as a function of chloride ion concentration. Apart from an 8% increase after the addition of 7 ppm chloride ions, the cuvette measurement of fluoroionophore **2.12** emission intensity is independent of chloride ion concentration. The normalised fluorescence intensity of chloride sensing in silica SCFs also shows no dependence on chloride ion concentration (0 – 62.7 ppm). The results for chloride ions sensing in SCFs is consistent with the cuvette measurements and corresponding data in the literature [7].

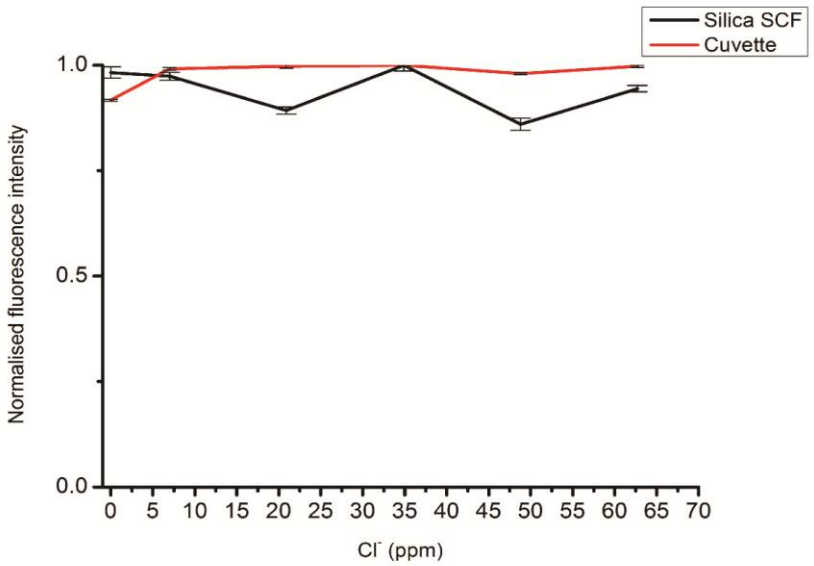

Figure 2.15: Normalised average integrated fluorescence intensity for fluoroionophore **2.12** (0.02 mM) with chloride (Cl^-) ions in the concentration range 0 – 62.7 ppm (88.4 mole equivalent)

Figure 2.16 shows that the normalised average integrated fluorescence intensity is also independent of acetate ion concentrations (0 – 117.3 ppm) and that acetate ions sensing in silica SCFs is also consistent with the cuvette experiments. Figure 2.16 shows the results of dihydrogen phosphate ions sensing experiments in F2 SCFs, silica SCFs and cuvettes. It shows a fluorescence enhancement in cuvette as a function of dihydrogen phosphate ion concentrations (0 – 171 ppm). The result is not consistent with observations for the structurally related PET fluoroionophore reported in the literature [7]. This is possibly due to the modification of the structure relative to the PET fluoroionophore reported in the literature. The fluorescence enhancement is also found in silica SCFs as a function of dihydrogen phosphate ion concentrations. The results in cuvettes and SCFs are mostly consistent except for the measured data point at 133 ppm. However, the results in F2 SCFs show fluorescence quenching, which is opposite to the observations in cuvette and in silica SCFs. This experiment was repeated and the second measurement also showed fluorescence quenching. One possible reason for this observation is that dihydrogen phosphate reacts with the F2 glass surface and releases some anionic species which can cause fluorescence quenching.

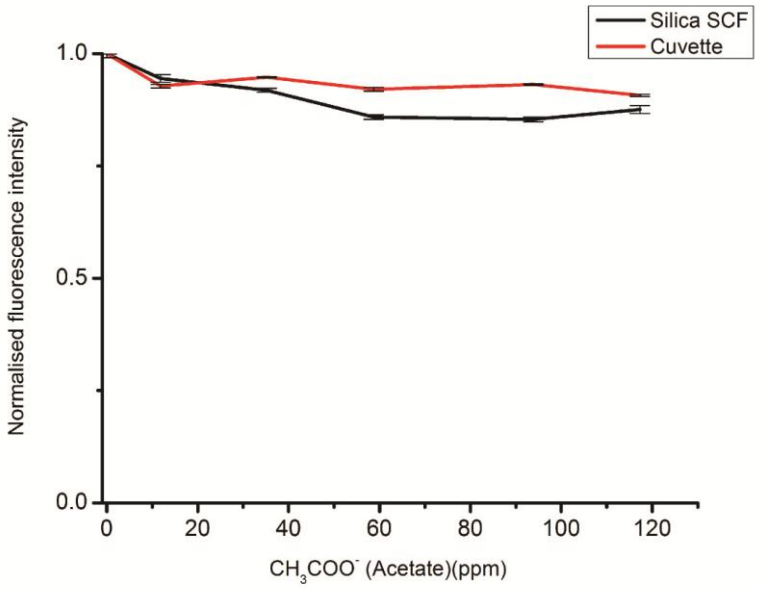

Figure 2.16: Normalised average integrated fluorescence intensity for fluoroionophore **2.12** (0.02 mM) with acetate ions (CH_3COO^-) in the concentration range 0 – 117.3 ppm (99.4 mol equivalent)

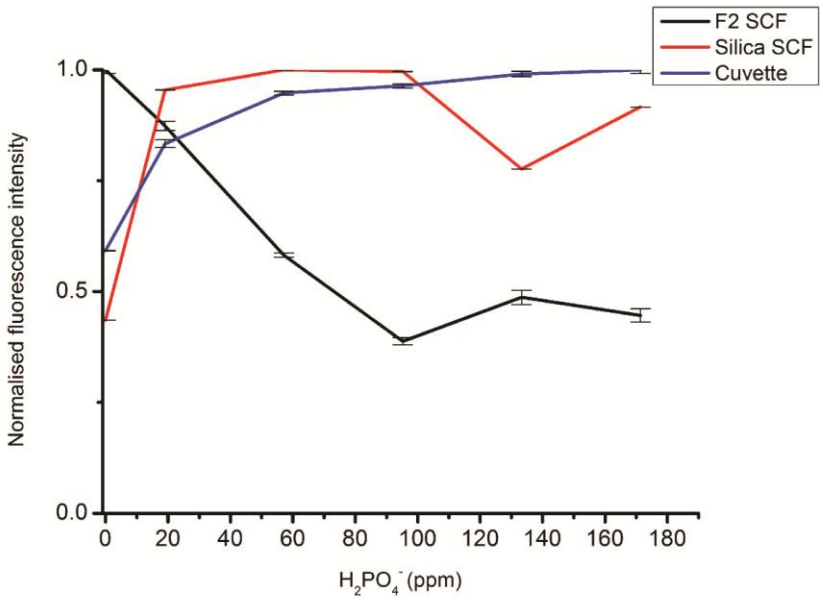

Figure 2.17: Normalised average integrated fluorescence intensity for fluoroionophore **2.12** (0.02 mM) with dihydrogen phosphate ($H_2PO_4^-$) ions in the concentration range 0 – 171 ppm (88.2 mole equivalent)

In summary, only an increase in fluoride ion concentration leads to a decrease in fluorescence intensity in cuvette measurements. The fluorescence intensity has no

dependency on the concentrations of chloride and acetate ions. Rather unexpectedly, dihydrogen phosphate ions show fluorescence enhancement with increased concentration. The trends of the cuvette and silica SCF measurements for fluoride, chloride, acetate and dihydrogen phosphate ions are highly similar. The trend of the cuvette and F2 SCF measurements for fluoride ions are also similar but show opposing results for dihydrogen phosphate ions. These results suggest that the quantitative measurement of a fluoride ion concentration is feasible in SCFs. Figure IXa in Chapter 2 Appendix shows a calibration curve generated from the linear regression of data from 0 ppm to 19 ppm fluoride ions. The regression coefficient is 0.92.

2.3.9 Comparison of cations and anions sensing performance for fluoroionophores in cuvettes and F2 SCFs

As described in Chapter 1, because of the longer interaction path length, the sensing performance characteristics, such as sensitivity and detection limit, for a PET fluoroionophores within SCFs are expected to be better than cuvettes measurements using the same optical set-up, provided that the loss of the SCF is low [29]. Since the detection limits of both PET fluoroionophores were not deemed to be a primary parameter for soil sensor development, as long as the sensor is working at the concentration range specified in Chapter 1, no experiments were undertaken to explore these limits. The dynamic linear range of a sensor is also an important parameter, however, there is no information regarding the expected performance of the dynamic linear range in SCFs.

The dynamic linear range and sensitivity of fluoroionophore **2.8** and **2.12** in cuvette and F2 SCFs are shown in Table 2.3. Fluoroionophore **2.8** shows a smaller dynamic range in SCFs compared to cuvettes measurements, whereas fluoroionophore **2.12** shows the same dynamic linear range in SCFs and cuvettes. The shortened dynamic range may be either due to the leaching of the sodium ions from the F2 glass or physisorption of fluoroionophores on the core of the SCF. The difference in the dynamic linear range suggests that the glass material can interfere with the sensor performance for in SCFs that use PET fluoroionophores to generate a signal. The sensitivity of fluoroionophore **2.8** in cuvette is significantly higher than SCF, which is also likely due to interferences from the glass material. The difference in the sensitivity of fluoroionophore **2.12** is

insignificant, most likely because the glass material does not interfere the binding of the fluoroionophore to anions. For anions sensing, F2 SCFs have a similar sensitivity and linear dynamic range compared to cuvettes. However, for cations sensing, F2 SCFs show lower sensitivity and a shorter dynamic range compared to cuvettes because of the interference from the glass material.

Table 2.3: Comparison of the sensitivity and the linear dynamic range of fluoroionophores **2.8** and **2.12** in cuvette and F2 SCFs

	Fluoroionophore **2.8** (Sodium ions)		Fluoroionophore **2.12** (Fluoride ions)	
	Cuvette	F2 SCF	Cuvette	F2 SCF
Sensitivity	0.023±0.001	0.013±0.004	-0.048±0.008	-0.041±0.005
Dynamic range/ppm	8	7	19	19

2.3.10 Emission wavelength maxima for the aminonaphthalimide fluorophores

In this project, the fluorescence emission spectra of all the fluorophores and fluoroionophores were measured using spectrometers from Varian and Horiba. Figure 2.18a shows the normalised emission spectrum of fluoroionophore **2.8** for cuvette measurements using both spectrometers. As can be seen, there is a 16 nm difference in the peak wavelength for the spectra of fluoroionophore **2.8**. Figure 2.18b and c show that the emission spectra of both Lucifer yellow (LY) and Rhodamine 6G (R6G), which also show differences in peak emission wavelength and full width half maximum (FWHM). The peak wavelength difference is 6 nm, and the FWHM difference is 3 nm for R6G. Measurements on LY show that the peak wavelength difference is 23 nm, and the FWHM difference is 10 nm. The difference in peak emission wavelength and FWHM are due to the different, instrument-specific responses of the spectrometers [30]. The instrument-specific response is expected, particularly with two spectrometers using different types of detector PMT (Varian Cary) versus CCD (Horiba). The emission spectrum of R6G has a smaller FWHM compared to LY and fluoroionophore **2.8** and hence it

was less affected by the difference in the instrument specific response of both spectrometers. No correction based on the spectral response was performed in this project because the cuvette and SCFs measurements were both performed with the Horiba spectrometer. The Cary spectrometer was used only for validating the PET fluoroionophores performance after the synthesis.

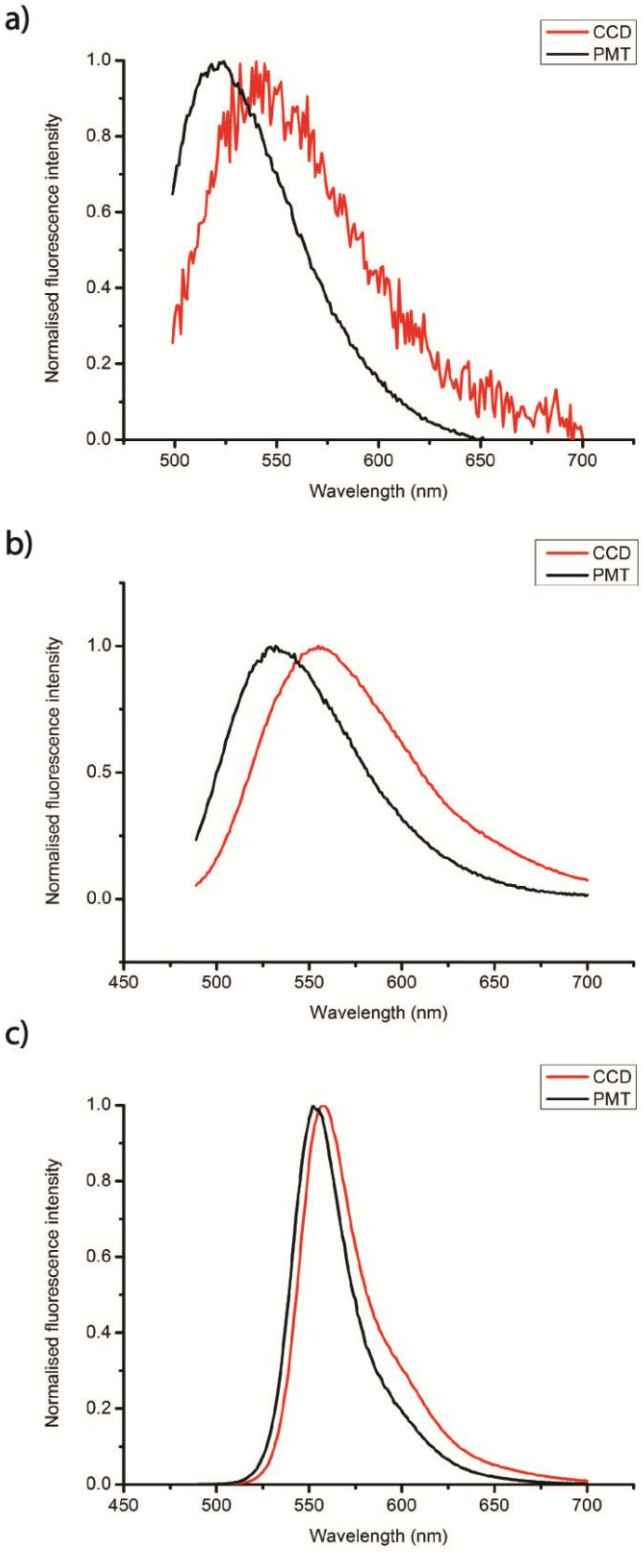

Figure 2.18: Normalised emission spectra of (a) fluoroionophore **2.8** in acetonitrile (0.02 mM, I = 0.1 M), (b) Lucifer Yellow dipotassium salt in water and (c) Rhodamine 6G in ethanol excited at 473 nm

2.4 Conclusions

The capacity to measure cation and anion concentrations in acetonitrile was demonstrated in SCFs for the first time. The SCFs were filled with model 4 amino-1,8-naphthalimide based PET fluoroionophores (Operating Scenario A). Quantitative measurements were demonstrated for sodium ions (0 – 9.2 ppm) and fluoride ions (0 – 19 ppm) ions. After excitation power and exposure time optimisation, no photobleaching occurred within the measurement time used. This demonstrates the possibility of using 4-amino-1,8-naphthalimide-based PET fluoroionophores without photobleaching in SCFs, which has much higher light intensity compared with cuvettes.

The sensitivity and dynamic linear range of the PET fluoroionophore **2.12** for fluoride showed no significant difference in either configuration. For cations sensing, SCFs showed a lower sensitivity and shorter dynamic range compared with cuvette because of interference from the glass material. This result suggests that the glass material is possibly interfering with the binding between target ions and fluoroionophores. Furthermore, the sensitivity and dynamic range are also affected by the attenuation of the SCFs. This is possibly the reason for lower sensitivity and shorter dynamic range of the cations sensing using SCFs.

2.5 References

1. Gunnlaugsson, T., Glynn, M., Tocci, G.M., Kruger, P.E., and Pfeffer, F.M., *Anion recognition and sensing in organic and aqueous media using luminescent and colorimetric sensors.* Coordination Chemistry Reviews, 2006. **250**(23-24): p. 3094-3117.

2. He, H.R., Mortellaro, M.A., Leiner, M.J.P., Young, S.T., Fraatz, R.J., and Tusa, J.K., *A fluorescent chemosensor for sodium based on photoinduced electron transfer.* Analytical Chemistry, 2003. **75**(3): p. 549-555.

3. He, H.R., Mortellaro, M.A., Leiner, M.J.P., Fraatz, R.J., and Tusa, J.K., *A fluorescent sensor with high selectivity and sensitivity for potassium in water.* Journal of the American Chemical Society, 2003. **125**(6): p. 1468-1469.

4. Martin, E., Weigand, R., and Pardo, A., *Solvent dependence of the inhibition of intramolecular charge-transfer in N-substituted 1,8-naphthalimide derivatives as dye lasers.* Journal of Luminescence, 1996. **68**(2-4): p. 157-164.

5. Englich, F.V., Foo, T.C., Ebendorff-Heidepriem, H., Sumby, C.J., and Monro, T., *Towards a microstructured optical fibre fluorescence sensor based on photoinduced electron transfer photobleaching*, in *Proceedings of the Australasian Conference on Optics, Lasers and Spectroscopy and Australian Conference on Optical Fibre Technology in association with the International Workshop on Dissipative Solitons*. 2009: Adelaide. p. 105-106.

6. Englich, F.V., Foo, T.C., Richardson, A.C., Ebendorff-Heidepriem, H., Sumby, C.J., and Monro, T.M., *Photoinduced Electron Transfer Based Ion Sensing within an Optical Fiber.* Sensors, 2011. **11**(10): p. 9560-9572.

7. Gunnlaugsson, T., Kruger, P.E., Lee, T.C., Parkesh, R., Pfeffer, F.M., and Hussey, G.M., *Dual responsive chemosensors for anions: the combination of fluorescent PET (photoinduced electron transfer) and colorimetric chemosensors in a single molecule.* Tetrahedron Letters, 2003. **44**(35): p. 6575-6578.

8. Schartner, E.P., *Hydrogen peroxide sensing with microstructured optical fibres*, in *School of Chemistry and Physics*. 2011, The University of Adelaide.

9. Afshar, S.V., Ruan, Y.L., Warren-Smith, S.C., and Monro, T.M., *Enhanced fluorescence sensing using microstructured optical fibers: a comparison of forward and backward collection modes.* Optics Letters, 2008. **33**(13): p. 1473-1475.

10. Skoog, D.A., Holler, E.J., and Crouch, A.R., *Principles of Instrumental Analysis*. 6th ed. 2007, Canada: Brooks/Cole.

11. J. Leonard, N.L., G. Procter, *Advanced practical organic chemistry*. 2nd ed. 1998: CRC Press
Taylor &Francis group.

12. Hisashi, S., *Naphthalic acid derivatives*, E.P. Office, Editor. 1964, Mitsubishi Chemical Industries Co. Ltd.

13. Dix, J.P. and Vogtle, F., *Ligand Structure and Complexation .50. Ion-Selective Crown Ether Dyes.* Chemische Berichte-Recueil, 1980. **113**(2): p. 457-470.

14. Wang, Y.C., Zhang, Y., Yi, X.H., and Qin, W., *Design and Synthesis of Some 1,8-Naphthalimides as Fluorescence Probes for Transition Metal Ions.* Asian Journal of Chemistry, 2012. **24**(1): p. 323-326.

15. Tolpygin, I.E., Shepelenko, E.N., Revinskii, Y.V., Dubonosov, A.D., Bren, V.A., and Minkin, V.I., *New chemosensor systems of the benzo-[de]Isoquinoline-1,3-Dione Series.* Chemistry of Heterocyclic Compounds, 2012. **48**(9): p. 1325-1331.

16. Schott *Schott optical glass data sheet*.

17. Callan, J.F., de Silva, A.P., and Magri, D.C., *Luminescent sensors and switches in the early 21st century.* Tetrahedron, 2005. **61**(36): p. 8551-8588.

18. Ioannidis, M., Gentleman, A.S., Ho, L., Lincoln, S.F., and Sumby, C.J., *Complexation and structural studies of a sulfonamide aza-15-crown-5 derivative.* Inorganic Chemistry Communications, 2010. **13**(5): p. 593-598.

19. Minta, A. and Tsien, R.Y., *Fluorescent Indicators for Cytosolic Sodium.* Journal of Biological Chemistry, 1989. **264**(32): p. 19449-19457.

20. Schultz, R.A., Dishong, D.M., and Gokel, G.W., *Crown-Cation Complex Effects .17. Lariat Ethers .4. Chain-Length and Ring Size Effects in Macrocyclic Polyethers Having Neutral Donor Groups on Flexible Arms.* Journal of the American Chemical Society, 1982. **104**(2): p. 625-626.

21. Schultz, R.A., White, B.D., Dishong, D.M., Arnold, K.A., and Gokel, G.W., *12-Membered, 15-Membered, and 18-Membered-Ring Nitrogen-Pivot Lariat Ethers - Syntheses, Properties, and Sodium and Ammonium Cation Binding-Properties.* Journal of the American Chemical Society, 1985. **107**(23): p. 6659-6668.

22. Liu, Y., Han, B.H., Inoue, Y., and Ouchi, M., *Complexation thermodynamics of crown ethers. 6. Calorimetric titration of cation complexation with some azacrown ethers.* Journal of Organic Chemistry, 1998. **63**(7): p. 2144-2147.

23. Alfimov, M.V., et al., *Structure and ion-complexing properties of an aza-15-crown-5 ether dye: synthesis, crystallography, NMR spectroscopy, spectrophotometry and potentiometry.* Journal of the Chemical Society-Perkin Transactions 2, 1997(11): p. 2249-2256.

24. Khayatian, G. and Karoonian, F.S., *Conductance and thermodynamic study of the complexation of ammonium ion with different crown ethers in binary nonaqueous solvents.* Journal of the Chinese Chemical Society, 2008. **55**(2): p. 377-384.

25. Valeur, B. and Leray, I., *Design principles of fluorescent molecular sensors for cation recognition.* Coordination Chemistry Reviews, 2000. **205**: p. 3-40.

26. Richardson, A.C., Foo, T.C., Englich, F.V., Ebendorff-Heidepriem, H., Sumby, C.J., and Monro, T.M., *A Microstructured Optical Fiber Sensor for Ion-Sensing Based on the Photoinduced Electron Transfer Effect*, in *Third Asia Pacific Optical Sensors Conference*. 2012.

27. Smets, B.M.J. and Tholen, M.G.W., *Leaching of Glasses with Molar Composition 20na2o.10ro.Xal2o3.(70-X)Sio2.* Journal of the American Ceramic Society, 1984. **67**(4): p. 281-284.

28. Duke, R.M. and Gunnlaugsson, T., *Selective fluorescent PET sensing of fluoride (F(-))using naphthalimide-thiourea and -urea conjugates.* Tetrahedron Letters, 2007. **48**(45): p. 8043-8047.

29. Monro, T.M., Warren-Smith, S., Schartner, E.P., Francois, A., Heng, S., Ebendorff-Heidepriem, H., and Afshar, S., *Sensing with suspended-core optical fibers.* Optical Fiber Technology, 2010. **16**(6): p. 343-356.

30. Cory, R.M., Miller, M.P., McKnight, D.M., Guerard, J.J., and Miller, P.L., *Effect of instrument-specific response on the analysis of fulvic acid fluorescence spectra.* Limnology and Oceanography-Methods, 2010. **8**: p. 67-78.

Chapter 2 Appendix: Supplementary information

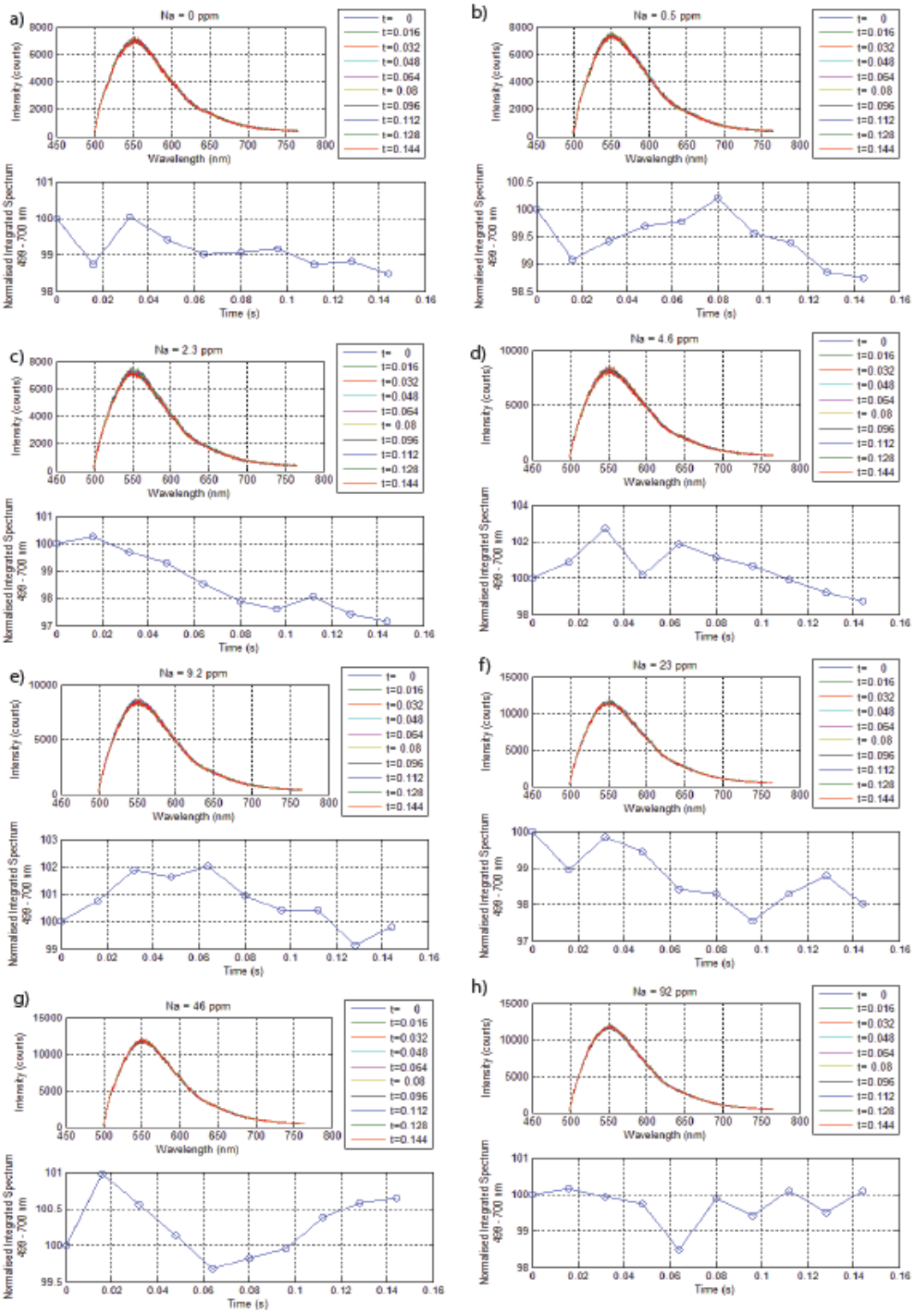

Figure 2.I a-h: Fluorescence spectra of fluoroionophore **2.8** (0.02 mM) acquired from 2nd generation optical set-up and photobleaching analysis for F2 SCFs with (a) 0 ppm of sodium ions, (b) 0.5 ppm, (c) 2.3 ppm, (d) 4.6 ppm , (e) 9.2 ppm, (f) 23 ppm, (g) 46 ppm and (h) 92 ppm

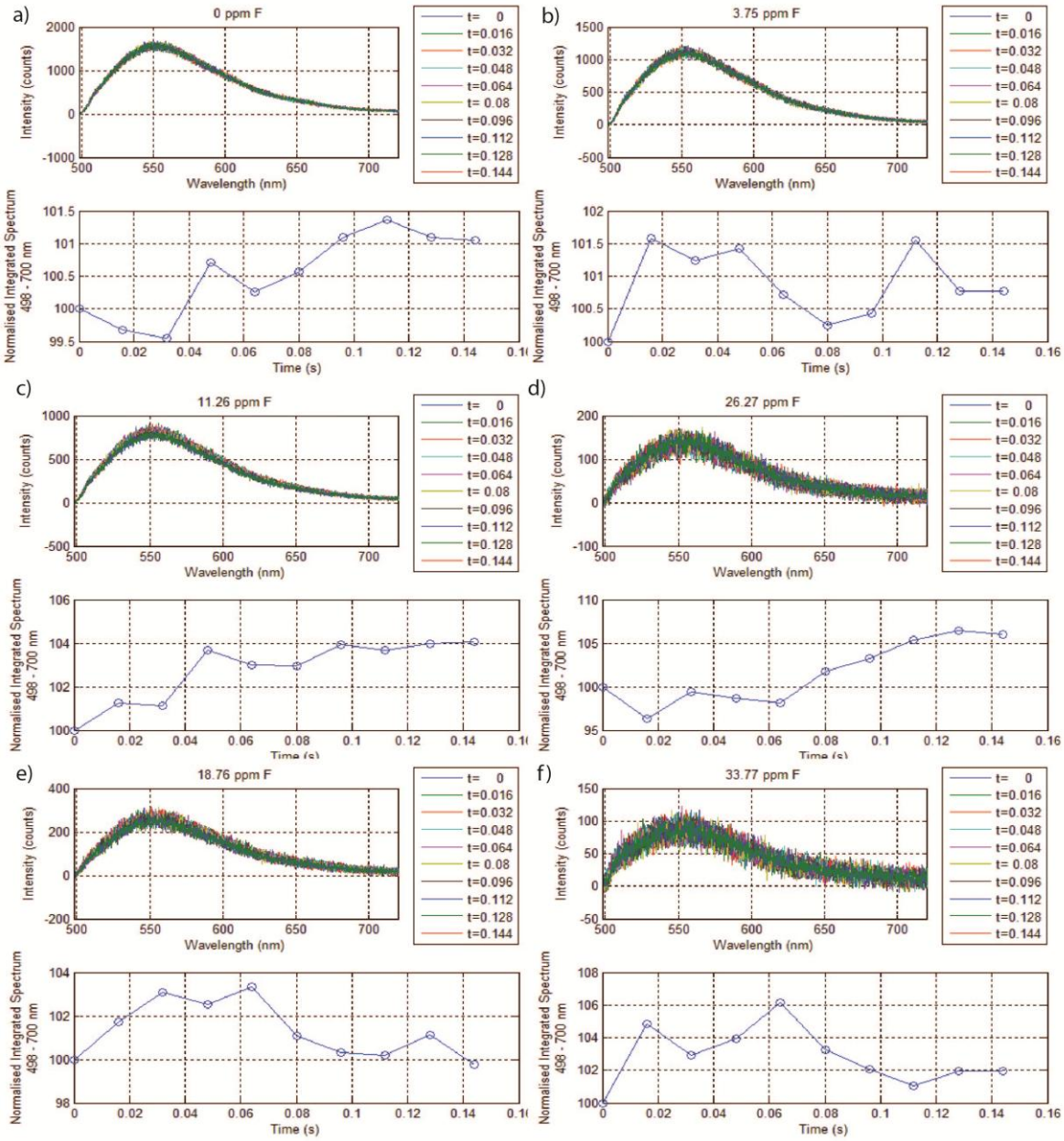

Figure 2.II: Fluorescence spectra of fluoroionophore **2.12** (0.02 mM) and photobleaching analysis for empty and filled F2 SCFs with (a) 0 ppm of fluoride ions, (b) 3.75 ppm, (c) 11.26 ppm, (d) 18.76 ppm, (e) 26.27 ppm, (f) 33.77 ppm

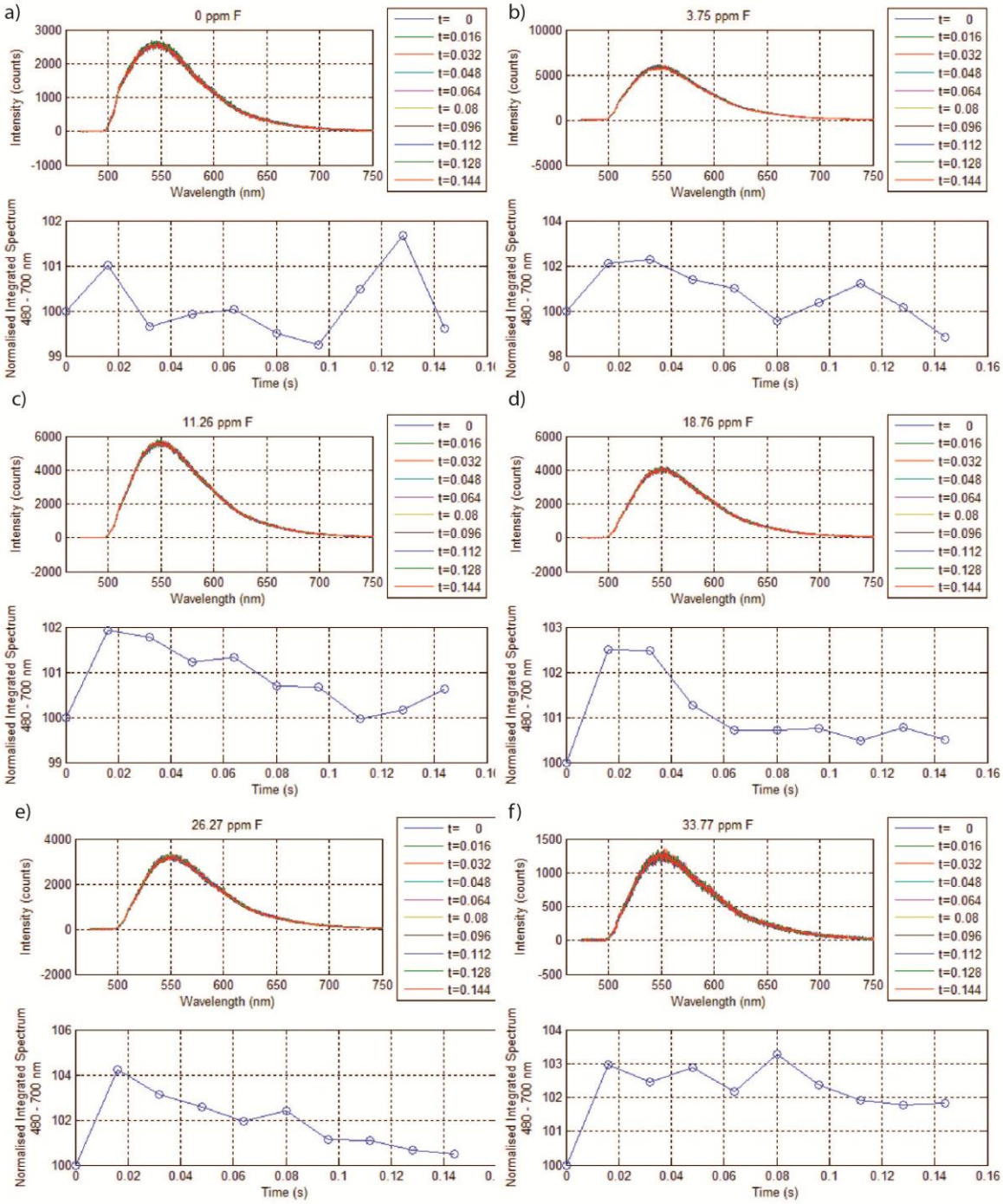

Figure 2.III: Fluorescence spectra of fluoroionophore **2.12** and photobleaching analysis for empty and filled silica SCFs with (a) 0 ppm of fluoride ions, (b) 3.75 ppm, (c) 11.26 ppm, (d) 18.76 ppm, (e) 26.27 ppm, (f) 33.77 ppm

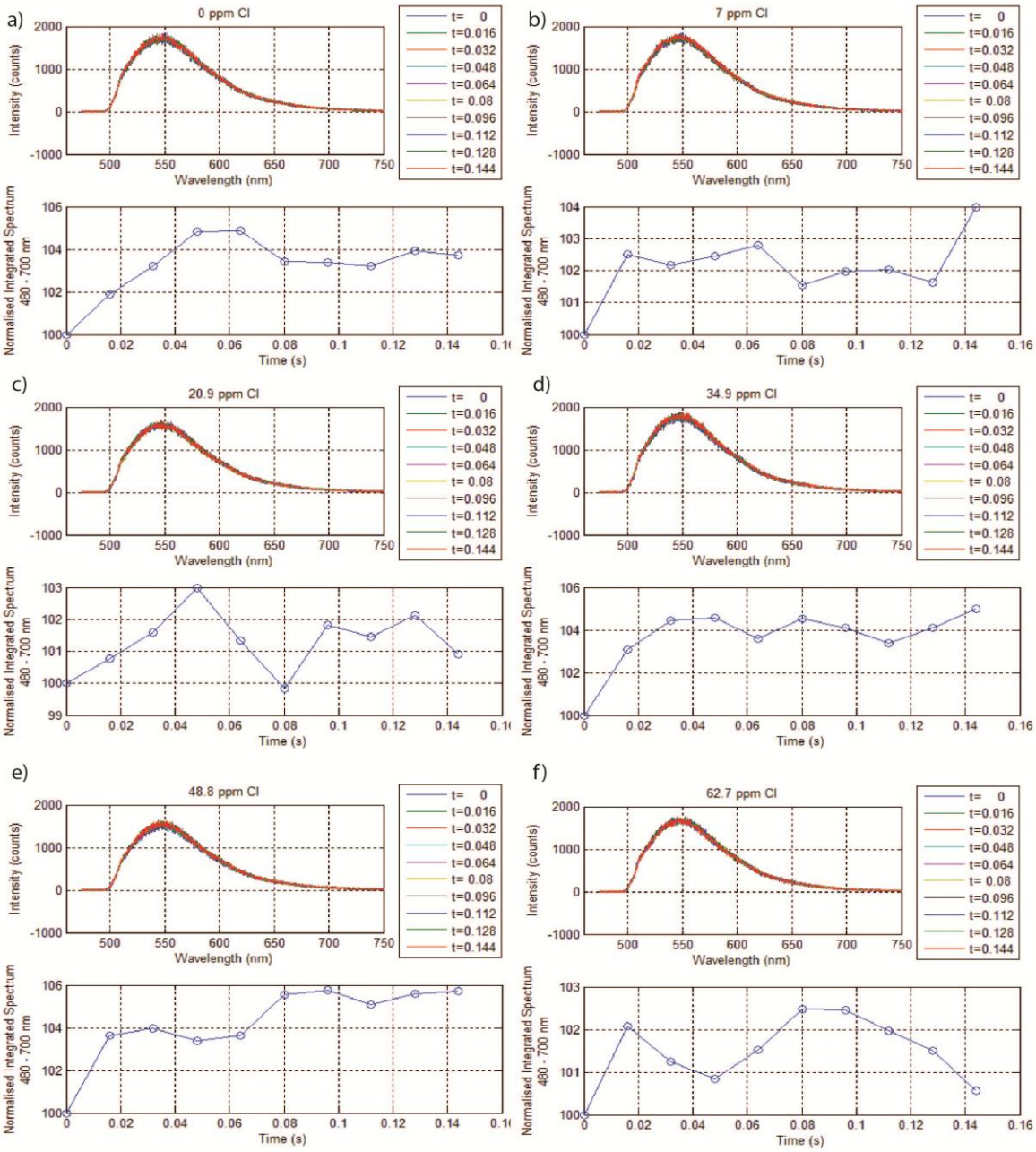

Figure 2.IV: Fluorescence spectra of fluoroionophore **2.12** and photobleaching analysis for empty and filled silica SCFs with (a) 0 ppm of chloride ions, (b) 7 ppm, (c) 20.9 ppm, (d) 34.9 ppm, (e) 48.8 ppm, (f) 62.7 ppm

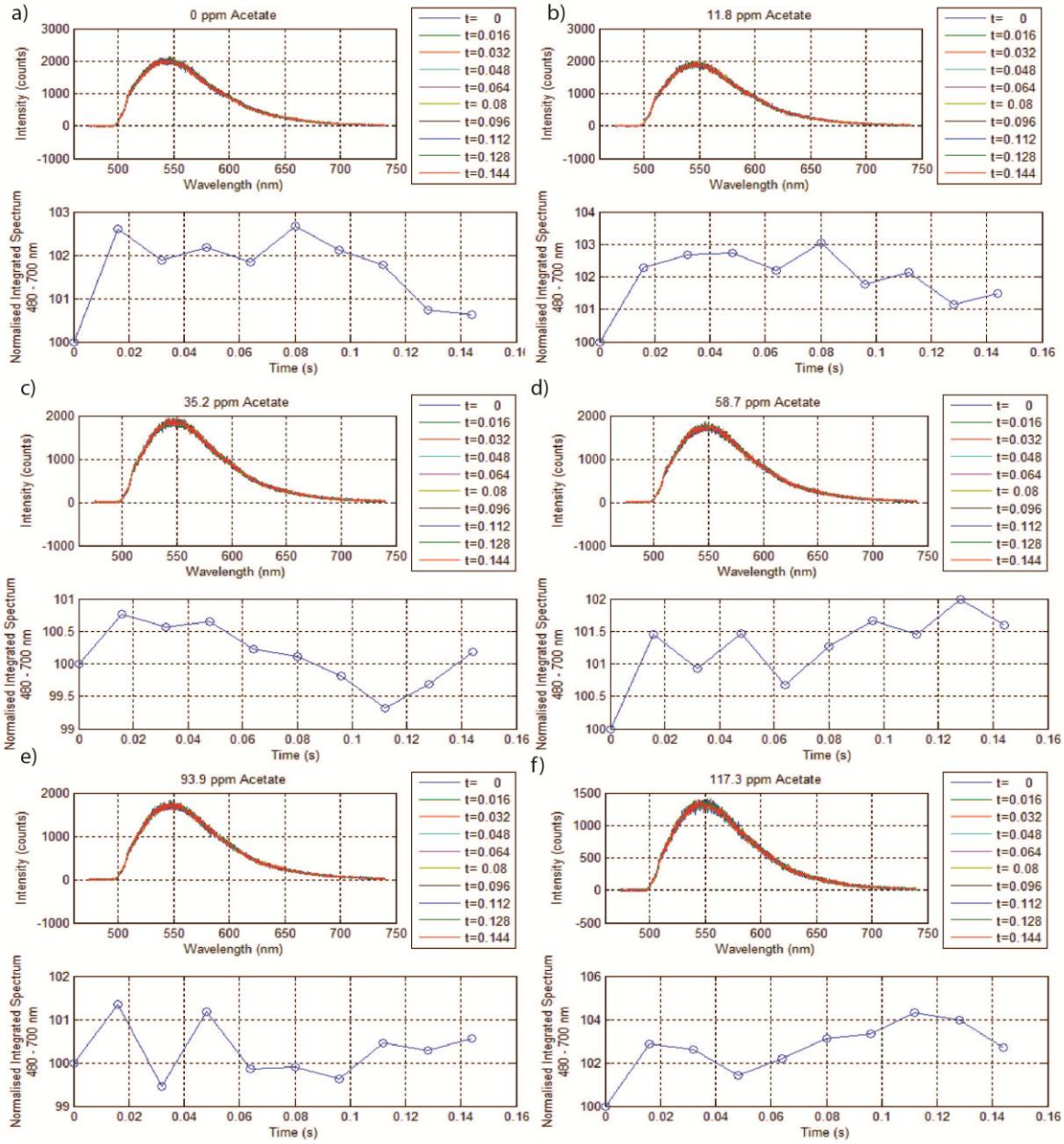

Figure 2.V: Fluorescence spectra of fluoroionophore **2.12** and photobleaching analysis for empty and filled silica SCFs with (a) 0 ppm of acetate ions, (b) 11.8 ppm, (c) 35.2 ppm, (d) 58.7 ppm, (e) 93.9 ppm, (f) 117.3 ppm

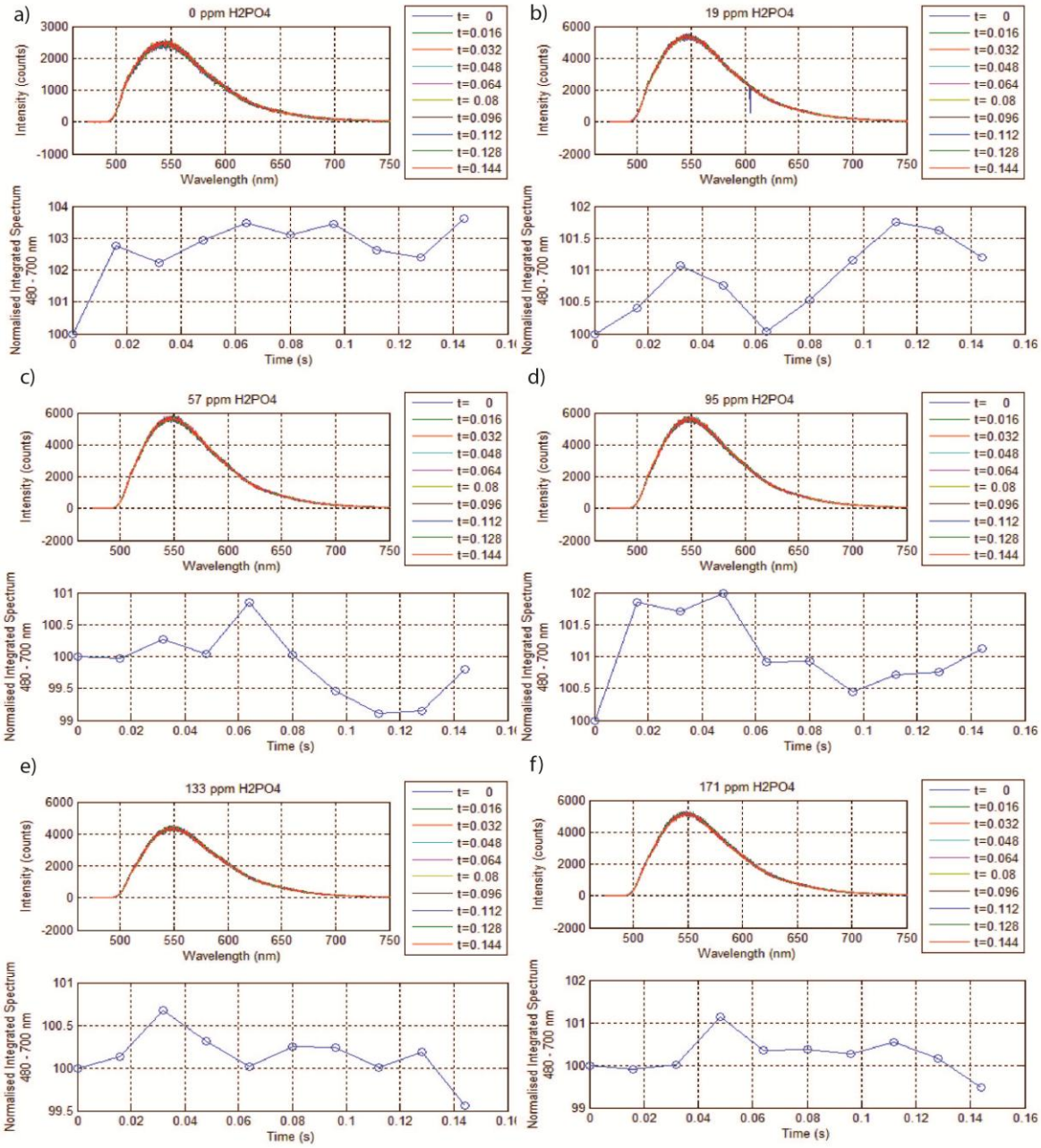

Figure 2.VI: Fluorescence spectra of fluoroionophore **2.12** and photobleaching analysis for empty and filled silica SCFs with (a) 0 ppm of dihydrogen phosphate ions, (b) 19 ppm, (c) 57 ppm, (d) 95 ppm, (e) 133 ppm, (f) 171 ppm

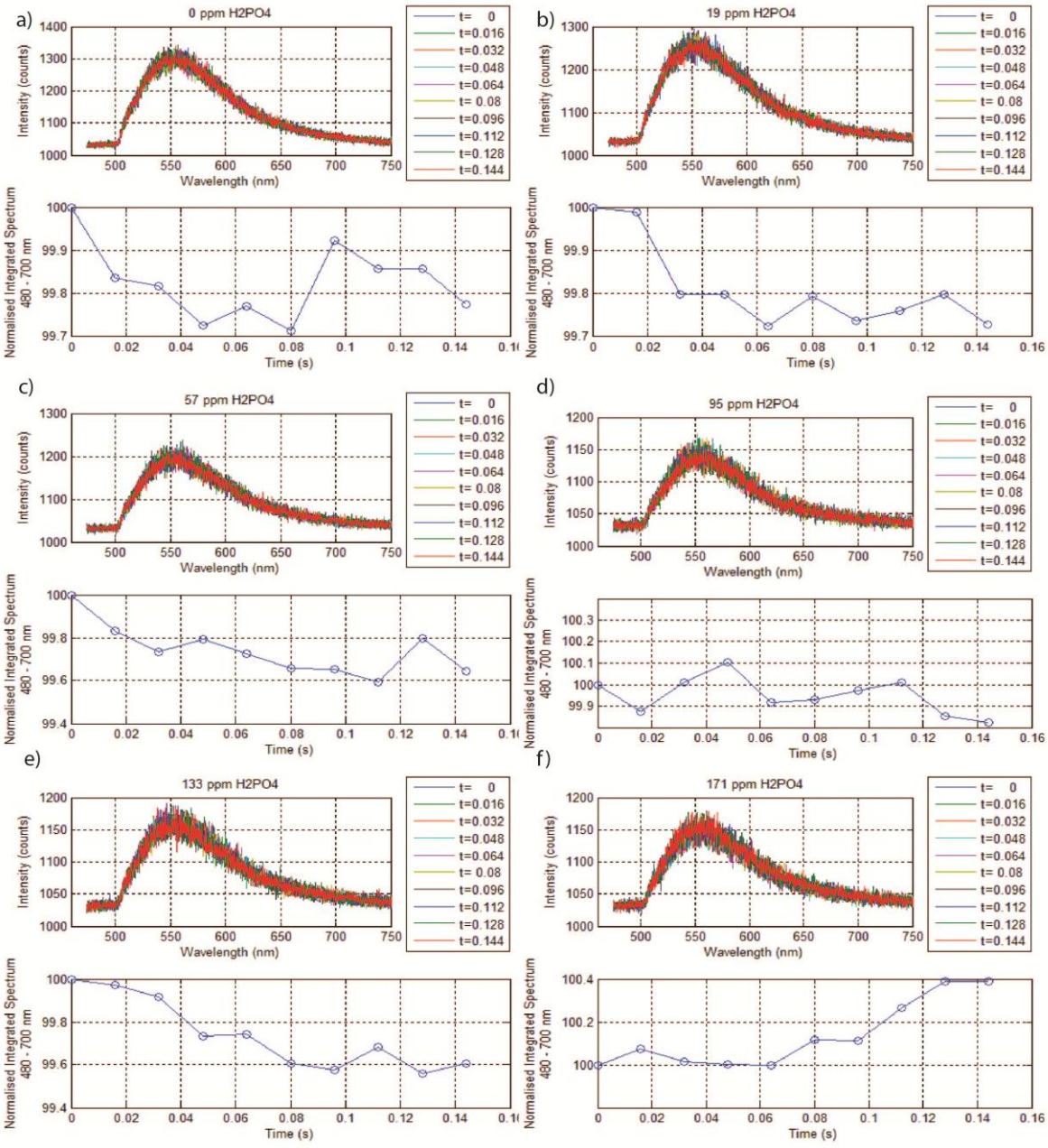

Figure 2.VII: Fluorescence spectra of fluoroionophore **2.12** and photobleaching analysis for empty and filled F2 SCFs with (a) 0 ppm dihydrogen phosphate ions, (b) 19 ppm, (c) 57 ppm, (d) 95 ppm, (e) 133 ppm, (f) 171 ppm

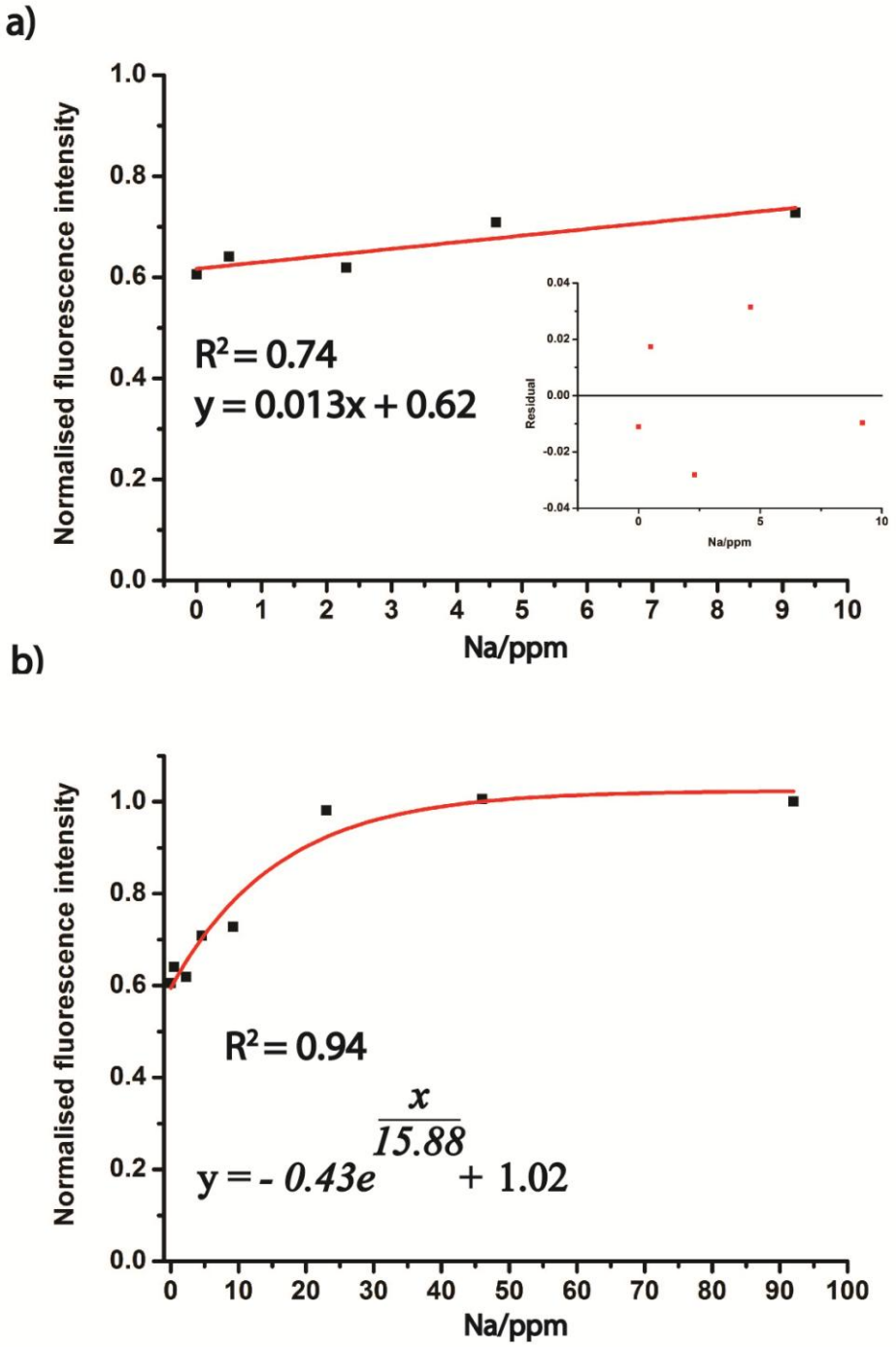

Figure 2.VIII: (a) Linear regression of the normalised fluorescence intensity of fluoroionophore **2.8** as a function of sodium ion concentrations from 0 – 9.2 ppm in F2 SCFs. The insert is the residual plot of the linear regression. (b) Exponential regression of the normalised fluorescence intensity of fluoroionophore **2.8** as a function of sodium ion concentrations from 0 – 92 ppm in F2 SCF. The insert is the residual plot of the exponential regression

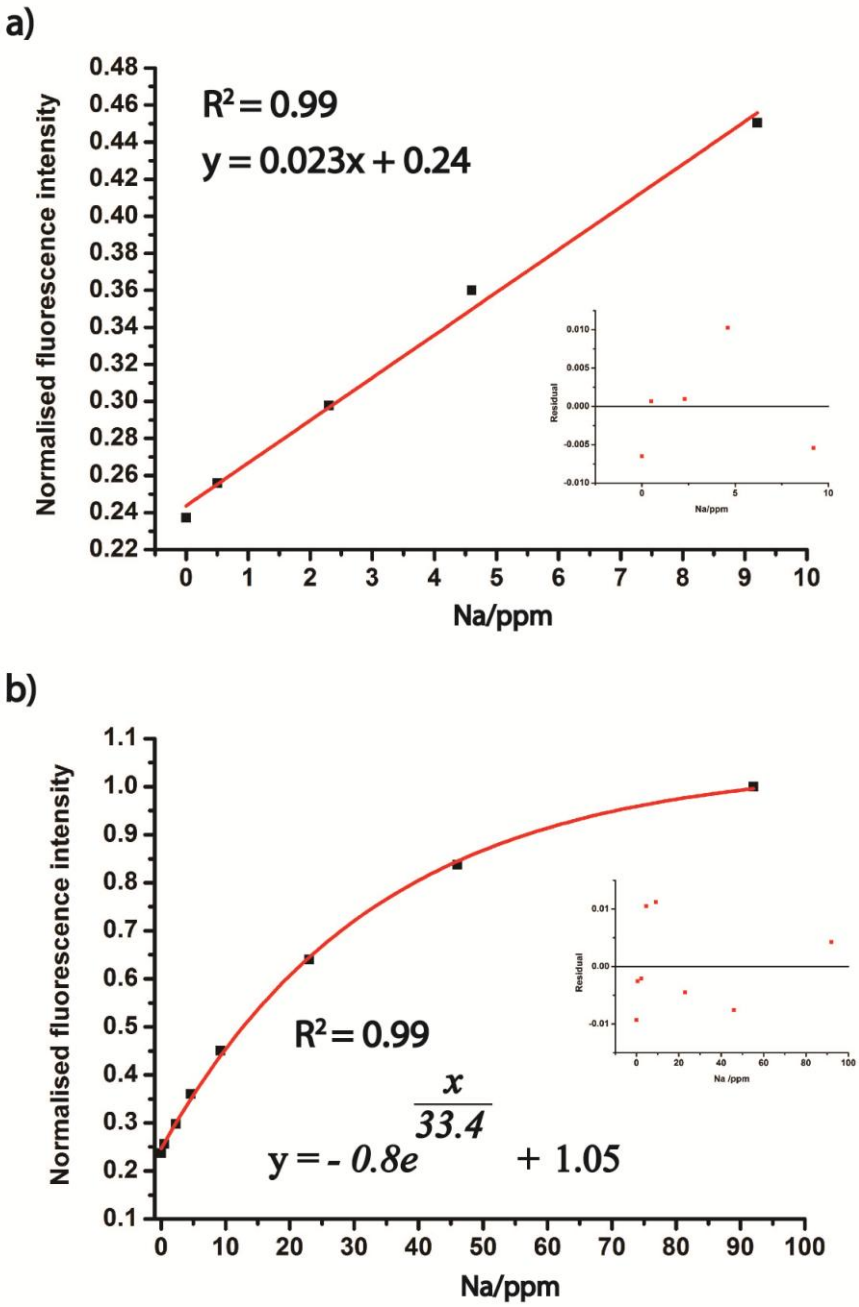

Figure 2.IX (a) Linear regression of the normalised average integrated fluorescence intensity of fluoroionophore **2.8** as a function of sodium ion concentrations from 0 – 9.2 ppm in cuvettes. The insert is the residual plot of the linear regression. (b) Exponential regression of the normalised average integrated fluorescence intensity of fluoroionophore **2.8** as a function of sodium ion concentrations from 0 – 92 ppm in cuvette. The insert is the residual plot of the exponential regression

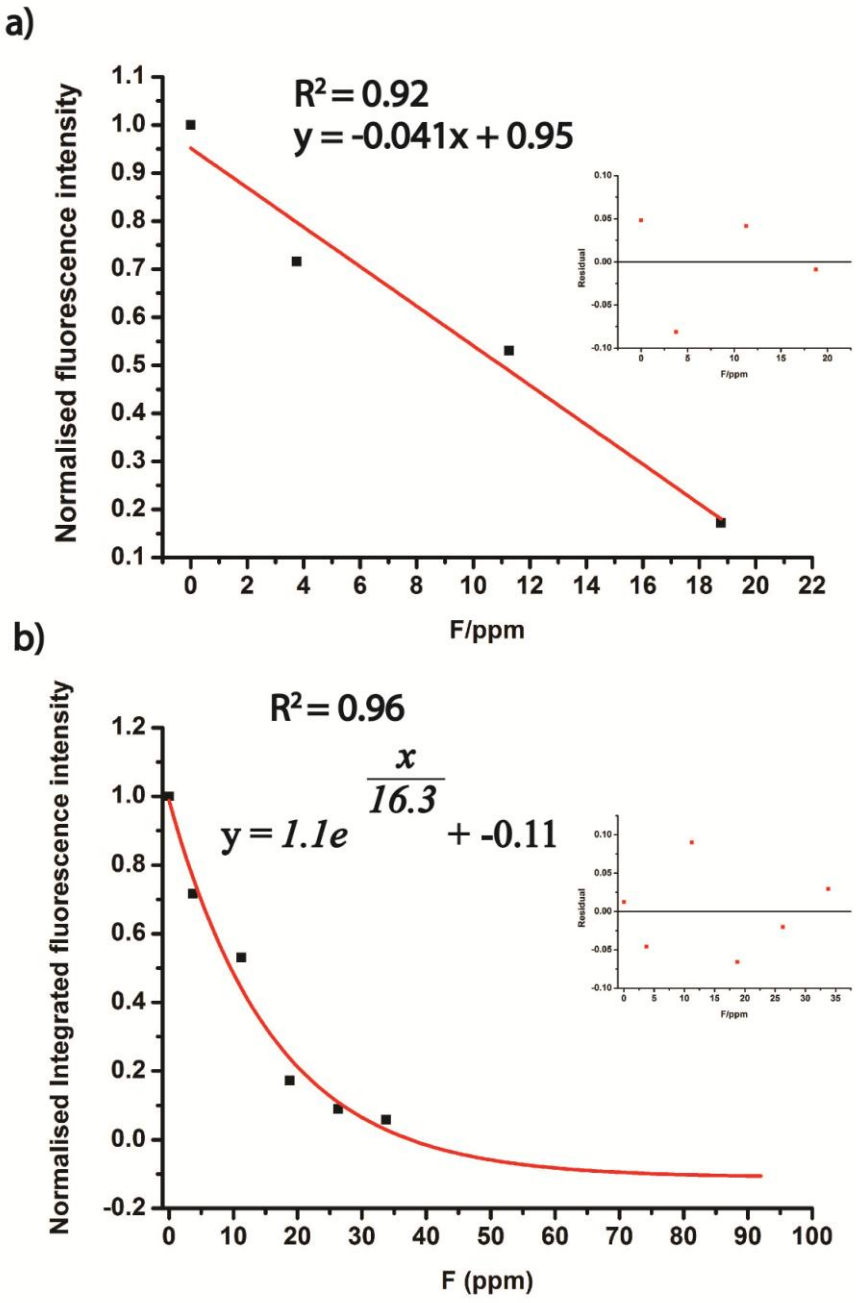

Figure 2.X: (a) Linear regression of the normalised average integrated fluorescence intensity of fluoroionophore **2.8** as a function of fluoride ion concentrations from 0 – 19 ppm in F2 SCFs. The insert is the residual plot of the linear regression. (b) Exponential regression of the normalised average integrated fluorescence intensity of fluoroionophore **2.12** as a function of fluoride ion concentrations from 0 – 92 ppm in F2 SCF. The insert is the residual plot of the exponential regression

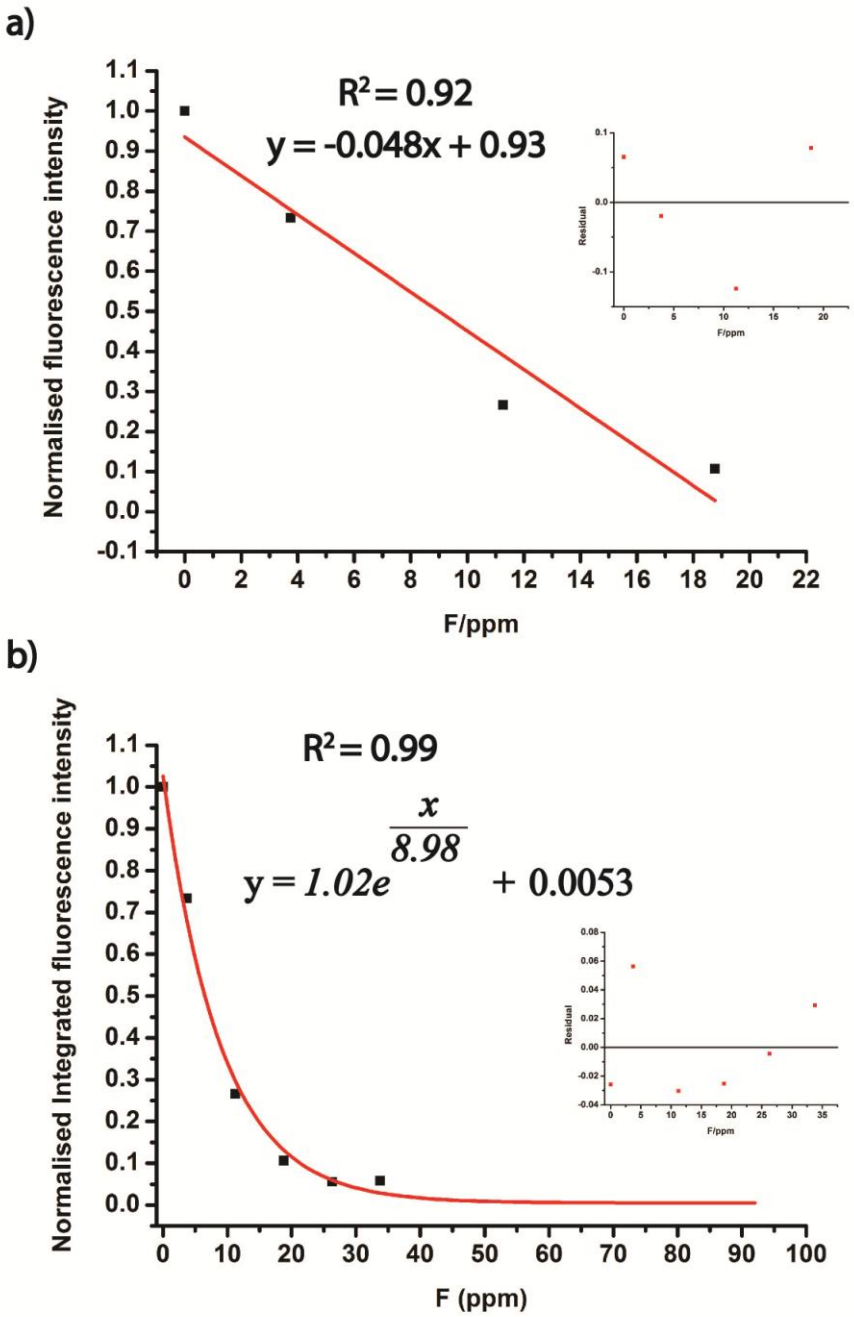

Figure 2.XI: (a) Linear regression of the normalised average integrated fluorescence intensity of fluoroionophore **2.12** as a function of fluoride ion concentrations from 0 – 34 ppm in cuvette. The insert is the residual plot of the linear regression. (b) Exponential regression of the normalised fluorescence intensity of fluoroionophore **2.12** as a function of fluoride ions concentrations from 0 – 34 ppm in cuvette. The insert is the residual plot of the exponential regression

Chapter 3

Studies of the surface functionalisation of SCFs using model glass systems

3.1 Background

As described in Chapter 1, the attachment of PET fluoroionophores to the internal surface of SCFs is the key step in operating scenario B. Silane and polyelectrolyte multilayer (PEM) functionalisation processes, which have been demonstrated to be two feasible methods for optical material functionalisation, were described Chapter 1. To enable further development of these processes it is important to understand the nature of the surface chemistry inside suspended core fibres (SCFs), in order to have a better control of the functionalisation procedure. However, it is challenging to perform surface analysis on the internal surface of SCFs because of the geometrical restriction associated with the micron-scale internal holes. Since the direct surface measurements are not possible within SCFs, the surface functionalisation study needs to be performed on model glass samples that have comparable surface conditions. Table 3A.1 summarises a range of model glass surfaces used in this project.

There are three major parameters to consider when selecting which model sample to use. The first is the glass composition; ideally it is the same as the composition of the glass to be used for the SCFs, which for the purposes of this PhD project were either lead silicate or silica glass. It is noted that most of the publications regarding optical material functionalisation focus on silica glass or silicon wafers [1-6]. There is a corrresponding lack of knowledge regarding functionalisation of soft glass materials such as lead silicate glass used within this project. The second factor is the surface chemistry of the glass platform. The surface chemistry is closely related to the glass surface composition, which is not necessarily the same as the bulk composition. Different surface treatments, such as different polishing methods can change the glass surface composition [7]. The third factor is the accessibility of surface analysis techniques. In Chapter 1, the basic approach and role of five surface analysis techniques such as fluorescence imaging, atomic

force microscopy (AFM), X-ray photoelectron spectroscopy (XPS), spectroscopic ellipsometry (SE) and time of flight secondary ion mass spectrometry (ToF-SIMS) used in this project were described. Physical parameters of the model system such as sample size and back-surface reflection determine which surface analysis technique is most feasible to use. Table 3.A.1 also summarises the techniques that are feasible for a particular model system.

Flat slides approximately 10 mm x 10 mm x 1 mm are the most versatile model sample geometry. This size and geometry confers minimum difficulty for loading the sample into/onto all the surface analysis instruments used in this project. In contrast, small model samples such as unstructured fibres with approximately 150 μm diameter introduce difficulty in XPS analysis, as it is difficult to acquire only the fibre signal without having the signal from the sample holder.

Flat glass slides can be analysed using ToF-SIMS, AFM, XPS, fluorescence imaging but not with ellipsometry. Transparent samples introduce back-reflection that decreases the accuracy of the analysis [8]. Other method such as roughening the back surface of the glass slide to minimise the back reflection is possible but it is difficult to protect the surface of the other side [8]. Silicon wafers are a suitable model system for all five surface analysis techniques because they are not transparent to visible light and have an amorphous native oxide layer. This oxide layer has the same composition as silica glass [9].

Capillaries have the same surface chemistry as SCFs, however, the geometrical restriction of a capillary is the same as SCFs, therefore techniques requiring direct sampling of the surface such as Tof-SIMS, AFM, XPS are not possible. The only feasible analysis method is fluorescence imaging though the thin glass wall.

In general, the best model glass system for mimicking internal surfaces of SCFs is the one which has the closest match to the internal surface chemical compositions of SCFs and is accessible to the widest range of surface analysis techniques.

Table 3A.1: The summary of the model glass surfaces used in this project

Model system	**Surface analyses performed in this project**	**Glass materials**	**Surface finish**
Internal surface of glass capillaries	Fluorescence imaging	Silica glass Lead silicate Tellurite Bismuth ZBLAN	Fire polished
Unstructured optical fibres, including typical circular fibres or ribbon shape fibres	Fluorescence imaging ToF-SIMS AFM	Silica glass Lead silicate glass Tellurite Bismuth ZBLAN	Fire polished
Commercial glass slides	Fluorescence imaging ToF-SIMS XPS AFM	Silica glass	Mechanically polished
Extruded glass slides	Fluorescence imaging ToF-SIMS XPS AFM	Lead silicate glass	Fire polished
Silicon wafers	Fluorescence imaging ToF-SIMS XPS SE AFM	Silica layer on top of silicon crystalline material	Mechanically polished

In the strategy explored in this PhD project, the functionalisation of a glass material consists of two steps. The first step is to introduce the foundation coating with functional groups, which can be established by coating the glass surface with either PEM or silane reagents. The second step is to covalently attach the fluorophore or fluoroionophore onto the glass surface, which has been functionalised with PEM or silane.

There are three major measurable parameters of a glass coating that are closely related to performances of a SCF sensor. The reproducibility of a coating determines the reproducibility of a SCFs sensor prepared via this two-step coupling strategy.

1. Density of surface attached molecules and surface functional groups (mol mm^{-2})

   The density of surface functional groups introduced in the first step has a strong correlation to a surface density of attached molecules in the second step [10]. XPS and ToF-SIMS are able to measure both the density of the surface attached molecules and surface functional groups [10]. If the attached molecules are fluorescent, fluorescence spectroscopy is able to measure the density of the attached molecules.
2. Thickness of the coating

   The thicker the coating, the weaker the excitation energy for the fluorophore or fluoroionophore, because it is further away from the peak of the evanescent field. However, if the refractive index of the coating is comparable to the glass material of the SCF, the coating thickness only increases the core size of a SCF. Hence, the coating thickness does not have significant effect on the SCF sensor performances. The thickness of the coating can be measured using a spectroscopic ellipsometry (SE).
3. Surface roughness

   This parameter is closely related to the scattering loss of SCFs. The higher the surface roughness, the higher the scattering loss experienced by the guided modes [11]. The surface roughness of APTES coated model systems such as silicon wafers, bare fibres and exposed core fibres can be measured using an atomic force microscopy (AFM) [2, 12].

This chapter is divided into four parts; Part A describes a comparative study of the surface density of 'active' amine functional groups on PEM and APTES coated fused silica, lead silicate (F2), bismuth, tellurite and ZBLAN capillaries. For this project, PEMs cannot be used as the functionalisation method because common polyelectrolytes contain large quantity of ions such as sodium, chloride and proton, which can interfere with the PET fluoroionophore [13]. However it is still scientifically valuable to compare the surface amine group densities of silane reagents and PEMs coated glass surface. This information can provide guidance for surface attachment of selective PET fluoroionophores, which cannot bind to ions from the PEM layer. This study demonstrates not only the functionalisation of silica and lead silicate glass types, but also the feasibility of the surface functionalisation of other soft glass types such as tellurite, bismuth and ZBLAN. These glasses were not used in this project, but have potential application in other projects requiring near to mid infrared wavelength transparency. From the perspective this project, this study provides information of the surface density of the amine functional groups provided by 3-aminopropyltriethoxysilane (APTES) for surface attachments of fluoroionophores.

Part B describes comprehensive surface analysis of silica and lead silicate glass using XPS. The aim of this study was to validate the glass XPS analysis methodology by comparing experimental and literature data of binding energies of each chemical bonding type on silica glass and lead silicate (F2) glass surfaces. In addition, the surface composition of the F2 glass measured by XPS was compared with the bulk composition measured by energy dispersive X-ray analysis (EDX) to understand the difference between these two compositions. Finally, the relative quantity of the silanol groups were compared for silica and F2 glass to understand the reactivity of the glass surface to 3-aminopropyltriethoxysilane (APTES).

Part C describes comprehensive XPS, ToF-SIMS, AFM and SE analyses of the APTES coatings on silica and lead silicate glass slides as well as silicon wafers. These analyses provided information regarding the chemical composition, thickness and surface roughness of the APTES coating. This information allowed the characteristics of the surface coating to be understood and the surface functionalisation procedure to be optimised.

Part D outlines XPS and AFM analyses of 11-aminoundecyltriethoxysilane (AUTES) coated silica glass slides. AUTES has an amine group attached at the end of a long aliphatic hydrocarbon chain (11 carbons), which restricts the vertical polymerisation of the AUTES coating and can reduce the variability of coating [14]. Therefore, AUTES has the potential to improve reproducibility and homogeneity on glass surfaces [14]. XPA and AFM analyses provided information regarding chemical composition and roughness of AUTES coated slides; thereby allowing the feasibility of using an AUTES coating on glass surfaces for this project to be determined.

3A: Comparison of the surface functional group densities of polyelectrolyte multilayer (PEM) and (3-aminopropyl)triethoxysilane (APTES) coatings on glass surfaces

3A.1 Introduction

Most of the previous glass functionalisation studies were based on silica, silicon wafer or borosilicate glass materials [2, 3, 15, 16]. There has been lack of study towards surface functionalisation on lead silicate, tellurite, fluoride glass materials. In this study, oxide glass capillaries made from fused silica, lead silicate, bismuth and tellurite glass were functionalised with PEM and APTES respectively. In addition, capillaries made from ZBLAN, a type of fluoride glass, were also functionalised with APTES. The glass capillaries were fabricated using the same procedures as for SCFs, which were described in Chapter 1. In principle, the internal surface of a capillary is chemically equivalent to the internal surface of a suspended-core fibre (SCF) because it has experienced the same heat treatment processes.

This study focuses on the functionalisation process without acid pre-treatment to increase the surface hydroxyl group density as suggested from previous literature. The acid pre-treatment is not applicable to F2, tellurite, bismuth and ZBLAN glass because it etches those glasses and changes the surface roughness [17-20]. Hence, no pre-treatment was performed in order to provide a direct comparison study.

After the APTES or PEM functionalisation, biotin was then attached to the functionalised surface via an amide coupling reaction. Biotin is not fluorescent; therefore the detection of the biotin is estimated using quantum dot (Qdot) tagged streptavidin. The avidin-biotin interaction has been widely used in bioconjugation reactions [21] as it has the strongest reported non-covalent interaction (10^{-15} M), and the association is fast and independent of the temperature, pH and solvent used [22].

The first objective of this study is to demonstrate the feasibility of the surface functionalisation of silica, lead silicate (F2), tellurite, bismuth and ZBLAN glass surfaces; to compare surface densities of ‘active’ amine functional groups of

APTES and PEM coated glass types listed above. Another objective of the study is to measure the surface density of the 'active' amine functional groups provided by 3-aminopropyltriethoxysilane (APTES) on silica and F2 glass for surface attachment of fluoroionophores. These data were used for estimating the quantity of fluoroionophores attachable on a surface. This work was presented in Australian Conference on Optical Fibre Technology (ACOFT) in 2009, which also included the results of 3-mercaptopropyltrimethoxysilane (MTS) coating [23].

3A.2 Experimental

3A.2.1 Preparation of capillaries

Fused silica capillaries (PEEKsil™) were obtained from SGE analytical science. The outer diameter of the silica capillaries was 410 μm and the inner diameter was 322 μm. The polymer outer coating was removed using a flame, and the capillary cut into ~ 8 cm pieces. The polymer coating had to be removed before functionalisation because the coating would be dissolved by solvents such as toluene, potentially transferring the dissolved polymer into the capillary and then coat the internal surface. The wall thickness of silica capillaries was 44 μm and it is consistent for all the experiments.

Table 3A.2 summarises the glass compositions of the glass billets fabricated into capillaries [24-26]. Glass billets were first extruded to form a tube preform and then the preform was drawn into a capillary. The preform tubes for the capillaries were extruded with an 8 mm inner diameter and 10 mm outer diameter. Following this step, these tubes were drawn into capillaries using a fibre drawing tower.

Table 3A.2 summarises the inner and outer diameter of in-house fabricated F2, bismuth, tellurite and ZBLAN capillaries. It shows that the innear and outer diameters of the in-house fabricated capillaries are not consistent. Although the variation of the inner diameter affected the flow rate of reagents into the capillary during the coating steps, it should not affect the kinetics of the surface functionalisation reactions as the reaction solution was stationary within the capillaries (apart from the washing step(s)).

Table 3A.2: Glass compositions and sources of the soft glass capillaries

Glass type	Composition	Source	Averaged Inner diameter/μm	Averaged outer diameter/ μm
F2	$71SiO_2$- 19PbO-$5Na_2O$ - $5K_2O$	Schott Glass Co	183 ± 24	232 ± 26
Bismuth	$43Bi_2O_3$ - 57(B_2O_3, SiO_2 and other oxides)	Asahi Glass Co	200 ± 4	240 ± 6
Tellurite	$73TeO_2$-20ZnO-$5Na_2O$-$2La_2O_3$	In house fabrication	194 ± 31	232 ± 41
ZBLAN	$53ZrF_4$-$20BaF_2$-$4LaF_3$-$3AlF_3$-20NaF	In house fabrication	89 ± 20	246 ± 3

3A.2.2 Surface functionalisation of capillaries

Table 3.A.3 shows all the steps of surface functionalisation procedures using APTES and PEM. Poly(allylamine) (PAH) and poly(sodium 4-styrenesulfonate) (PSS) were alternatively deposited using the layer-by-layer (LbL) method, starting and ending with a PAH layer [27]. 1-Ethyl-3-(3-dimethylaminopropyl) carbodiimide hydrochloride (EDC) (0.1M), *N*-hydroxysuccinimide (NHS) (0.025 M) were used to couple the biotin-D (0.2mM) to both the amine groups of APTES layer and the last PAH layer. This coupling reaction was performed in water. Since streptavidin can bind on the APTES or PEM coated surface non-specifically, a blocking reagent, Bovine Serum Albumin (BSA) (10%) in phosphate buffer saline (PBS) solution was deposited onto the surface. The PBS solution used in this project is diluted from tablets provided by Sigma Aldrich; the composition is NaCl (150 mM), Na_2HPO_3 (3 mM) and KH_2PO_4 (1.05 mM). The resulting pH is 7.2 to 7.6. After BSA deposition, a Qdot labelled streptavidin PBS solution (λ_{em} = 780 nm) was flowed through the capillaries [21].

Table 3A.3: Outline of the surface functionalisation procedure

APTES	PEM
1. 2% v/v APTES in anhydrous toluene incubation for 4 hours 2. Rinsed with PBS 15 – 30 mins 3. Amide coupling of biotin using EDC (0.1M) and NHS (0.025 M) in water 4. BSA (10%) deposition 5. Qdot-labelled streptavidin (1 μM) attachment	1. Poly(allylamine hydrochloride) (PAH) (1 mg mL^{-1}in 1M NaCl solution) incubation for 15 – 30 mins 2. Rinsed with PBS 15 – 30 mins 3. Poly(sodium-4-styrenesulfonate) (PSS) (1 mg ml^{-1} in 1M NaCl solution) incubation for 15 – 30 mins 4. Rinsed with PBS 15 – 30 mins 5. PAH incubation for 15 – 30 mins 6. Rinsed with PBS 15 – 30 mins 7. Amide coupling of biotin using EDC (0.1M) and NHS (0.025 M) in water 8. BSA (10%) deposition 9. Qdot-labelled streptavidin (1 μM) attachment

The fluorescence intensities for individual samples were determined using a Typhoon Trio Variable Mode Imager (Amsterdam Bioscience) with each pixel size equals to 50 x 50 μm. The pixel size for the measurement of ZBLAN coatings was 100 x 100 μm. The larger pixel size measurement requires less scanning time but less data points were acquired. Despite this, the averaged intensities per unit area of this experiment were still comparable to other experiments formed with smaller pixel size. The excitation wavelength of all measurements was 532 nm and no filter was used. The emission wavelength of the Qdot-labelled streptavidin is 780 nm.

3A.2.3 The method of data analysis

The fluorescence emission data from the capillaries were analysed using ImagineQuant® (Molecular Dynamic) and OriginPro 2008® (OriginLab). Using the program, 100 data points were obtained from a single column sampling grid on each capillary. Figure 3.A.1 shows images of functionalised ZBLAN capillaries and calibration capillaries to demonstrate the sampling method in data analysis. The fluorescence intensity of each capillary was calculated by subtracting the averaged maximum intensity with the averaged minimum intensity. The instrumental error was calculated from one standard deviation (1SD) of the area outside the capillary but within the sampling grid shown in Figure 3A.1. Calibration curves were obtained using capillaries of the same glass material filled with a known concentration of Qdot labelled streptavidin solution. The calibration curve correlates the fluorescence intensity and the quantity of the Qdot labelled streptavidin. Since the internal diameter of each capillary was measured, the surface density of Qdot labelled streptavidin can be calculated. The assumption of using this calibration curve is that the attachment of streptavidin to biotin does not affect the optical properties such as quantum yield and molar extinction of the Qdot. This was deemed reasonable as unlike organic fluorophores, no reported data suggested that the the attachment affects the optical properties of Qdots. Challenges of using comparable calibration curves for organic fluorophores are discussed in Chapter 4.

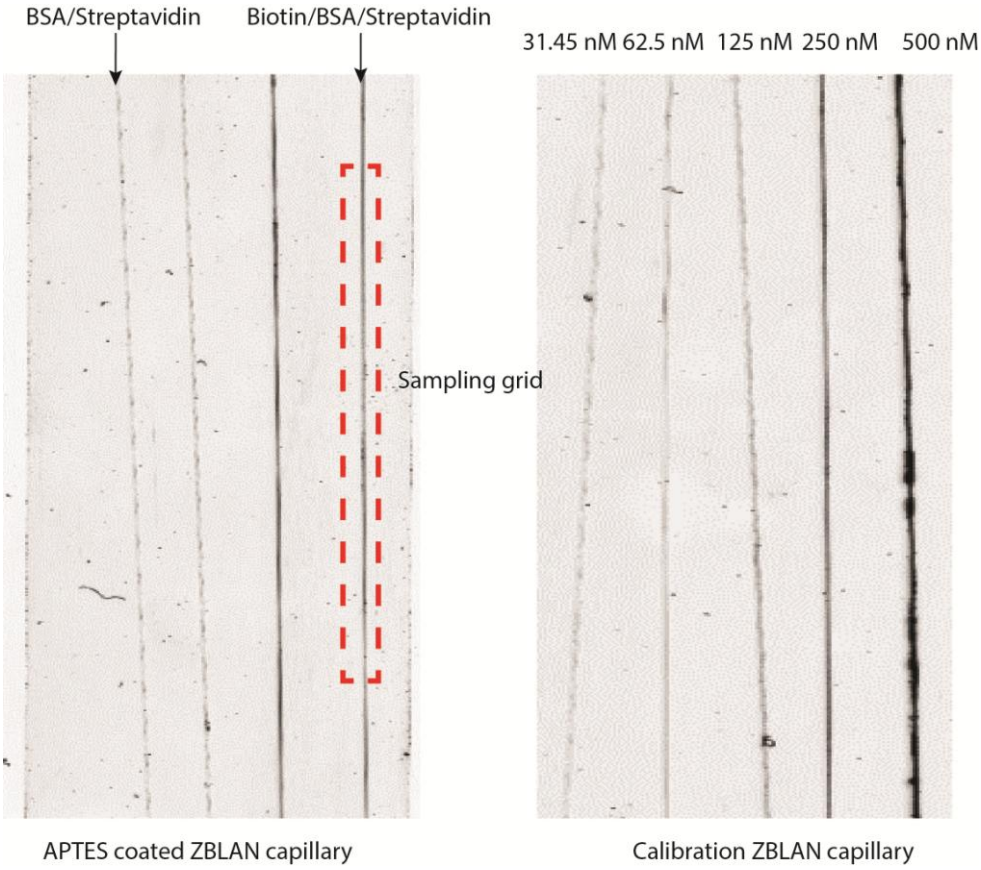

Figure 3A.1: Examples of the fluorescence images acquired on the typhoon imager. This fluorescence image shows functionalised capilliaries and calibration ZBLAN capillaries without functionalisation. The intensity of the colour represents the emission intensity. The concentrations of the Qdot-labelled streptavidin in the ZBLAN samples for calibration are shown on the top of the image

3A.3 Results and discussion

Biotin was covalently coupled on amine groups from the APTES or PAH coated glass surface. Figure 3A.2 shows a schematic representation of the two surfaces studied. Both initial coating processes introduce amine functionality to the glass surface, which can be coupled to the carboxyl group of biotin via standard peptide coupling reagents such as EDC and NHS. Coupling reagents are necessary for facilitating amide coupling reaction at room temperature [28].

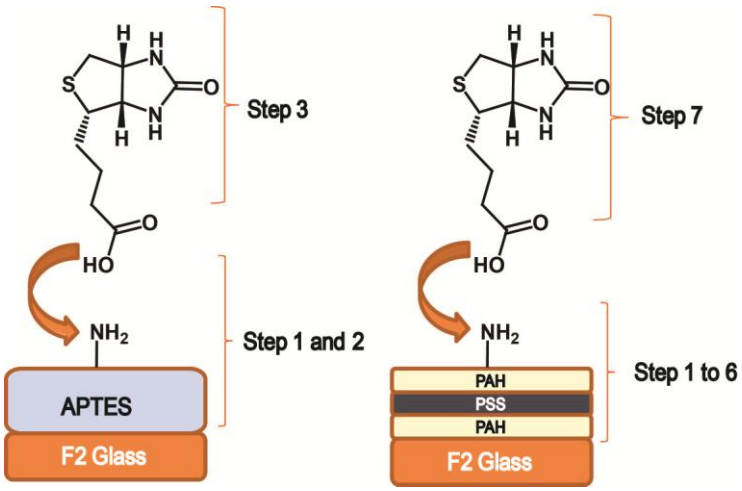

Figure 3A.2: A schematic diagram of the surface functionalisation of biotin on APTES and PEM coated F2 glass surfaces

The Qdot-labelled streptavidin adsorption on APTES and PEM coated surface is non-specific to the existence of biotin, therefore a blocking reagent is required to minimise this non-specific interaction [29]. BSA is a common blocking reagent used in immunoassays; its role is to block the non-specific binding of proteins on the functionalised surfaces.

Figure 3A.3a shows a schematic representation of the specific interaction of Qdot-labelled streptavidin with biotin using BSA as the blocking reagent. It is important to note that BSA cannot fully block the non-specific interaction of streptavidin to the surface. Figure 3A.4b shows possible modes of non-specific binding of streptavidin in the negative controls, which have no biotin attached. The streptavidin conjugate can bind to the BSA and to amine groups on the surface within the 'gaps' between BSA. These are non-specific interactions, the effect of which was measured in the negative control experiments. After subtracting fluorescence intensity of the corresponding negative control from the fluorescence intensity of the samples with biotin, BSA and Qdot labelled streptavidin, the density of the specific biotin-streptavidin interaction was calculated.

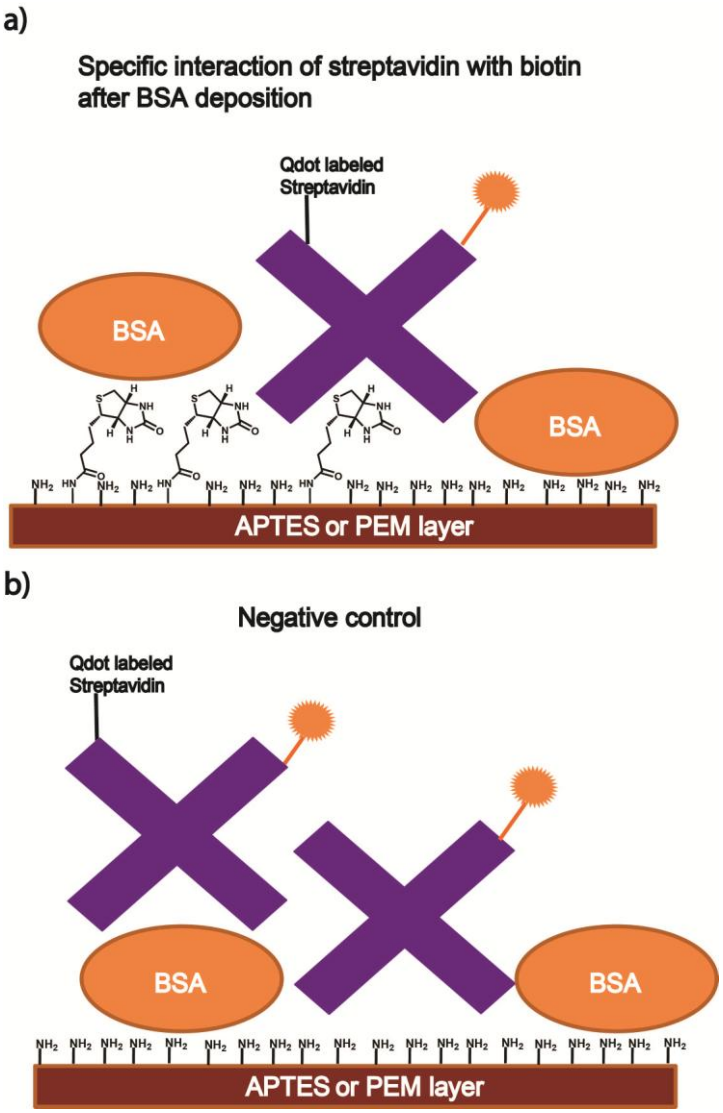

Figure 3A.3: Pictorial representations of the (a) specific biotin-streptavidin interaction after BSA deposition and (b) possible non-specific streptavidin interactions on the surfaces of the negative control

Figure 3A.4a shows the density of surface-bound streptavidin measured for the different glass types investigated. The samples labelled 'Process A' and 'C' are negative controls for APTES and PEM coatings, which show the non-specific interactions between the streptavidins and the blocking reagent (BSA) on top of the APTES and PEM coating as described in Figure 3A.3b.

Figure 3A.4b shows the molar surface density of the NH-Biotin-streptavidin on the PEM and APTES coating after subtracting the corresponding negative control. The results show that not just silica and lead silicate glass, for which surface functionalisation were demonstrated before, but other glass types such as tellurite,

bismuth and ZBLAN glass can be functionalised by both APTES and PEM. This result is the first report of surface functionalisation of these glass types.

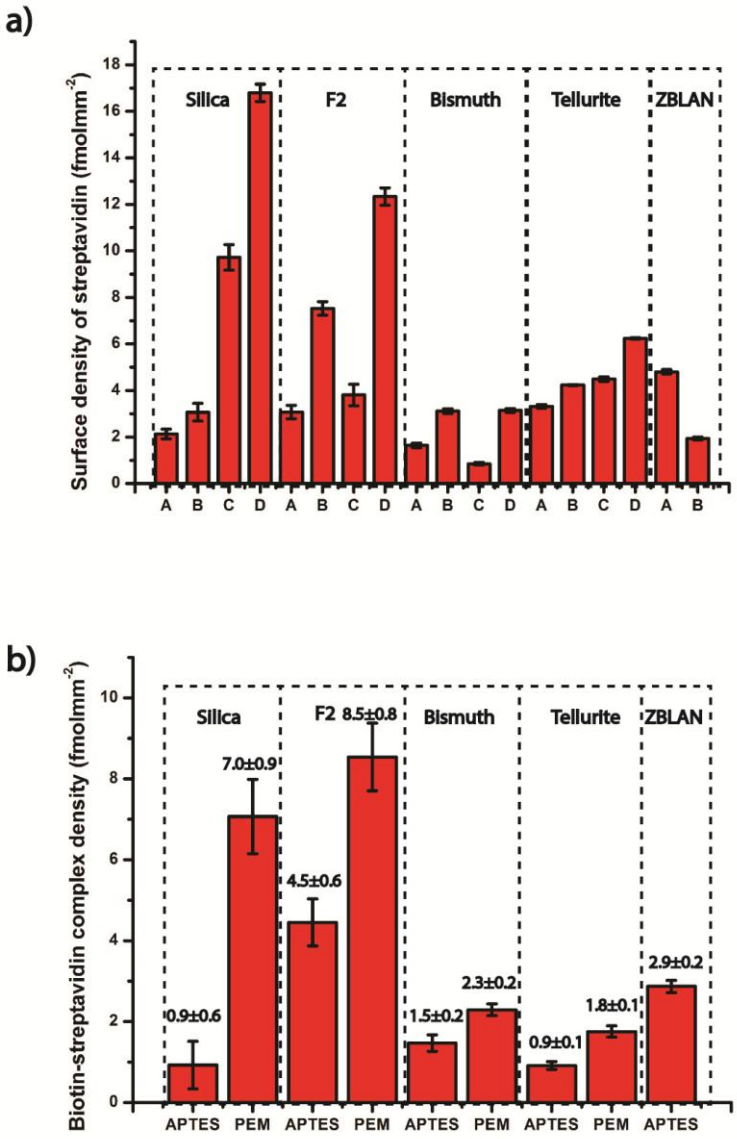

Figure 3A.4: (a) The densities of streptavidin molecules (fmol mm^{-2}) on APTES and PEM coated silica (Si), lead silicate (F2), tellurite, bismuth and ZBLAN glass surfaces, along with negative controls (A and C). A = APTES/BSA /streptavidin, B = APTES/BSA/biotin/streptavidin, C = PEM/BSA /streptavidin and D = PEM/BSA/biotin/streptavidin. (b) The densities of biotin-streptavidin complexes on APTES and PEM coated silica (Si), lead silicate (F2), tellurite bismuth and ZBLAN glass surface. The error bar is 1 standard deviation of the instrumental error

Figure 3A.5 shows the relationship between surface amine, surface bound biotin and streptavidin. As can be seen from this figure, the molar quantity of the surface amine groups covalently attached to biotin, that are in turn non-covalently attached to streptavidin (NH-biotin-streptavidin) is a subset of the molar quantity of the surface amine groups covalently attached to biotin (NH-biotin). Both NH-biotin-streptavidin and NH-biotin represent a subset of the total number of active amine groups available on the glass surface, because the streptavidin moieties do not bind to all biotin groups on the surface. Similarly, not all amines available on the surface are covalently bound by biotin. In this section, the biotin molecules that are capable of non-covalently binding to streptavidin and the amine that is capable of covalently binding the biotin are described as ‘active’. These 'active' amino groups are available for subsequent elaboration to give surface tethered sensor moieties.

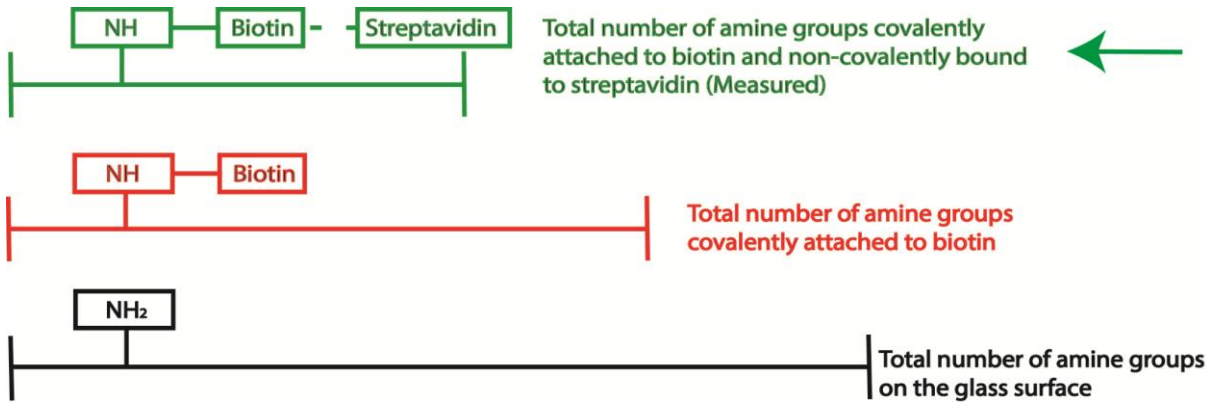

Figure 3A.5: The relationship between surface amine groups (NH_2), surface amine bound biotin (NH-Biotin) and surface amine bound biotin-streptavidin complexes (NH-Biotin-streptavidin)

Note that the orientation of the amine group on the surface does not affect the covalent attachment to biotin since biotin is a relatively small molecule (0.2 kDa) and the carboxyl group of the biotin is appended at the end of an aliphatic hydrocarbon chain.

The results shown in Figure 3A.4 also suggest that a PEM coating enabled a significantly higher density of NH-biotin-streptavidin conjugates compared to the APTES coating on all oxide glass substrates. Possible reasons for this are described in the following. The first possible reason is that PEM coatings offer a

higher number of total surface amine groups (including active and inactive groups) compared to APTES due to different bonding to the surface. Attachment of PEM to the surface is based on electrostatic interactions, unlike silane grafting on a surface, which requires condensation reactions to occur with the surface hydroxyl groups from the glass and with the ethoxy group on the grafted APTES (covalent bonding). Therefore the binding of PEM is independent of the molar surface density of hydroxyl groups on the surface. The second reason is that PEM coatings may have a higher quantity of active amine groups that were not buried in the coating. Previous studies have shown that APTES molecules grafted onto a surface can have different orientations, i.e. they can be inverted so that only the silanol groups are pointing out and the amine is buried in the coating [3, 4]. Furthermore, it is possible that the amine group density of APTES coating on a surface is not as controllable as PEM, which was deposited with a layer-by-layer (LbL) method. In this case the top layer will always be PAH, which guarantees the availability of amine groups.

The surface density of the amine groups for APTES functionalised silica and F2 glass surface are of particular interest, because APTES is the major functionalisation reagent in this project. The surface density of the NH-Biotin-streptavidin represent the minimum 'active' surface amine group density on the APTES coating on F2, which is 4.5 ± 0.6 fmol mm^{-2}. This is the first reported APTES 'active' surface amine group density for F2 glass.

Moon *et al.* reported the absolute surface amine group density of APTES on fused silica glass slides, which also have had no acid pre-treatment [30]. Their measurement is based on measuring the absorption of the immobilised 4-nitrobenzaldehyde via UV-Vis absorption spectroscopy [30]. They found the amine group density is 2.5 pmol mm^{-2}, whereas the amine group surface density of APTES coated silica capillary in this study is 0.9 ± 0.6 fmol mm^{-2}, which is 1000 times lower than the literature value. This large difference is mainly due to the fact that the analysis using biotin- streptavidin is focusing on the 'active' amine groups on the top surface of the APTES coating, whereas previous quantification method reported by Moon *et. al.* used the absorption of nitrobenzaldehyde to quantify the amine group density on the APTES coating,

which may include amine groups that are not located on the top surface of coating.

The advantage of using the biotin-streptavidin interaction to quantify the density of amine groups on the surface is that the streptavidin can only bind to active biotin molecules which are available on the surface of the coating. Streptavidin is a large molecule (60 kDa), which is less likely to penetrate into the coating and bind to 'inactive' biotin compared to small organic fluorophores.

In addition, the steric barrier introduced by BSA reduces the specific binding of streptavidin. The thickness of a monolayer BSA coating on APTES coated oxide layer of silicon is 1.2–1.4 nm [31], whereas, the maximum height of the biotin attached on the surface is less than 1 nm. This is estimated by counting the number of atom in the vertical axis (one carbon atom is ~ 0.1 nm). The BSA is thicker than the maximum height of biotin (Figure 3A.6). While BSA blocks the non-specific binding of the streptavidin on the amine groups on the surface, it also creates a steric barrier that inhibits the biotin-streptavidin interaction. The diameter of streptavidin is 11 nm [32], therefore the specific biotin-streptavidin interaction can only occur in a 'gap' of at least 11 nm distance between BSA molecules (Figure 3A.6). This steric barrier does not affect the relative comparison of the 'active' surface amine group density, but it reduces the binding of the streptavidin. It is noted that some literature [33] assumed that after BSA coating, the surface attached biotin is located on top of the BSA, however, it is highly dependent on the length of the linker. Based on the thickness of the BSA monolayer, the linker needs to be over 1 nm long to ensure the attached biotin is located on top of the BSA monolayer. BSA was originally believed not to create a steric barrier when the experiment described in this chapter was performed in 2009; however the measurement of the thickness of the BSA monolayer on silica was reported in 2010 [31].

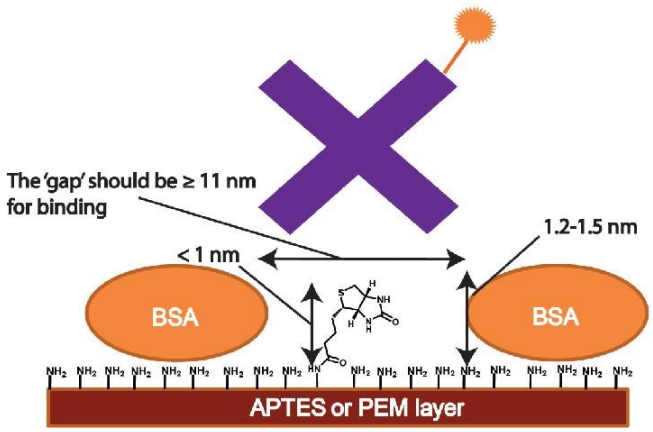

Figure 3A.6: Pictorial representation of the blocking mechanism of BSA in the biotin-streptavidin interaction used in this study

Figure 3A.7 compares the densities of NH-biotin-streptavidin on APTES coated capillaries. The surface densities of NH-biotin-streptavidin on APTES coated capillaries in descending order are as follows:

F2 > ZBLAN > bismuth > fused silica ~ tellurite.

The APTES surface density ultimately depends on the quantity of hydroxyl groups on the glass surface. The lower the quantity of surface hydroxyl groups on the glass, the lower the number of APTES molecules that are grafted onto the surface. The low quantity of surface hydroxyl groups also increases the chance of cross-linking between APTES molecules not directly grafted to the glass surface. Ultimately, the cross-linking between APTES can lead to a more random orientation of the APTES molecules, which increases the number of amine groups buried in the coating. Both reasons can contribute to the measured density of the NH-biotin-streptavidin on APTES coated glass.

The density of NH-biotin-streptavidin complexes on the APTES coating of F2 was significantly higher than that of fused silica, tellurite, bismuth and ZBLAN. The comparatively lower quantity of the hydroxyl groups on the fused silica surface was potentially related to the capillary drawing temperature, which can be estimated using temperature-viscosity-curves. The fused silica capillary was drawn at ~ 1850°C, which is much higher than the temperature required for F2 (~700°C), bismuth (~520°C), tellurite (390°C) and ZBLAN (310°C) [34]. The dehydroxylation temperature of silica is ~600°C and thus the silica drawing

temperature is ~ 1250°C above this temperature [35]. Although, the drawing temperature of F2 was above the dehydroxylation temperature as well, the drawing temperature was much lower compared to silica, therefore the quantity of hydroxyl groups remaining on the surface after drawing is likely to be higher compared to silica because of the slower dehydroxylation process. Furthermore, the rate of dehydroxylation is also depending on the composition of the glass as well. It is possibly showing that F2, bismuth, tellurite and ZBLAN glass have low rates of dehydroxylation at their drawing temperature.

Notably, Figure 3A.7 also shows that ZBLAN glass has relatively more hydroxyl groups available compared to tellurite and bismuth glasses and fused silica glass with no pre-treatment. This is a strong evidence that moisture from the air can react with the internal surface of ZBLAN glass capillaries, thereby hydrolysing Zr-F to form Zr-OH [20, 36].

In addition, silica glass pre-treatment with piranha solution (a mixture of H_2SO_4 and H_2O_2) or other acids can clean the glass surface and protonate the Si-O bonds on the surface before functionalisation. It was reported from literature that acid pre-treatment can increase the number of silanol groups on silica based glass [37]. However, it is known that strong acids can etch F2, bismuth and tellurite glasses; therefore it is not feasible to pre-treat those glasses with acid [38]. In order to have equivalent comparison, no pre-treatment was performed on any of the capillaries.

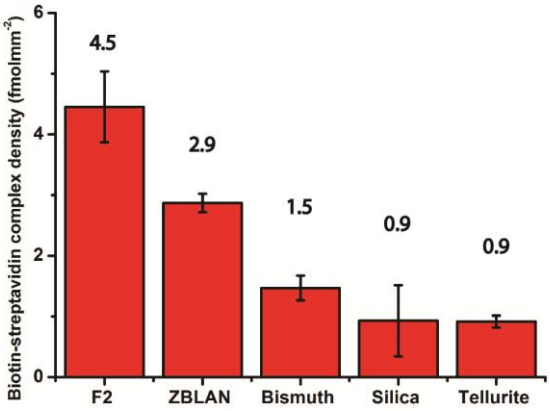

Figure 3A.7: Surface amine bound biotin-streptavidin complex (NH-biotin-streptavidin) density on the APTES coated F2, ZBLAN, bismuth, silica and tellurite glass

Figure 3A.8a shows the density of NH-biotin-streptavidin on 3 layers of PEM coating of F2, silica bismuth and tellurite glass surfaces. The results show that the differences in NH-biotin-streptavidin densities between F2 (predominantly silica) and silica glass substrates are not statistically significant. However, silica and F2 glass exhibit significantly higher NH-biotin-streptavidin densities compared to bismuth and tellurite glass, which is attributed to the higher quantity of PEM deposited on the glass surface. The PEM deposition is governed by the surface charge density of the glass material; the higher the surface charge density the more is PEM deposited on the glass surface. Figure 3.A.8b shows the differences of the electronegativity (Pauling scale) of Si-O, Bi-O and Te-O bonds [39]. NH-biotin-streptavidin complex density and electronegativity differences of the glass bonds display a similar trend which suggests that the differences in the quantity of PEM deposited on a surface correlates to the difference in polarity of the major glass components' bonds and thus the difference in the surface charge density on the glass materials.

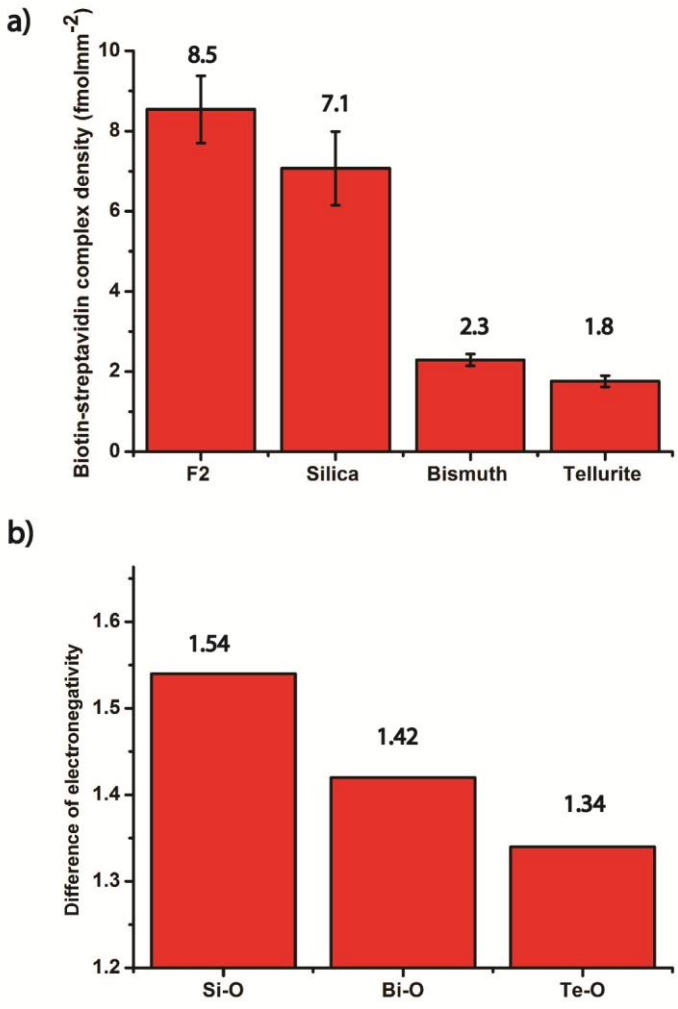

Figure 3A.8: (a) The densities of surface amine bound biotin-streptavidin complexes (NH-biotin-streptavidin) on PEM coated F2, silica, bismuth and tellurite glass. (b) The electronegativity (Pauling scale) differences for Si-O, Bi-O and Te-O bonds

3A.5 Conclusions

The results indicated PEM and APTES functionalisation can be performed on F2, silica, tellurite, bismuth glass surfaces. It also showed that APTES functionalisation is feasible on ZBLAN glass. This work is also the first demonstration of tellurite, bismuth and ZBLAN glass functionalisation, which suggests the possibility of using those glass materials for near to mid infrared sensing applications.

This study also indicated that PEM coatings on glass substrates provide more active amine groups on the surface compared to APTES on all of the different oxide glass surfaces, which have had no acid pre-treatment. Therefore, it is a better choice for a surface functionalisation strategy if surface density of the sensor molecules is important and the sensor molecules are not sensitive to the ions existing in the coating.

This study showed that the minimum 'active' amine group surface densities of the APTES coated on silica and F2 glass capillary are 0.9 ± 0.6 and 4.5 ± 0.6 $fmolmm^{-2}$ respectively. This is the minimum amine group surface density, as the majority of amine groups were buried inside the coating. Also, not all biotins were able to bind to the Qdot labelled streptavidin because of the wrong orientation or being covered by the BSA.

3A.6 References

1. Mendelsohn, J.D., Barrett, C.J., Chan, V.V., Pal, A.J., Mayes, A.M., and Rubner, M.F., *Fabrication of microporous thin films from polyelectrolyte multilayers.* Langmuir, 2000. **16**(11): p. 5017-5023.

2. Howarter, J.A. and Youngblood, J.P., *Optimization of silica silanization by 3-aminopropyltriethoxysilane.* Langmuir, 2006. **22**(26): p. 11142-11147.

3. Kim, J.Y., Seidler, P., Wan, L.S., and Fill, C., *Formation, structure, and reactivity of amino-terminated organic films on silicon substrates.* Journal of Colloid and Interface Science, 2009. **329**(1): p. 114-119.

4. Acres, R.G., Ellis, A.V., Alvino, J., Lenahan, C.E., Khodakov, D.A., Metha, G.F., and Andersson, G.G., *Molecular Structure of 3-Aminopropyltriethoxysilane Layers Formed on Silanol-Terminated Silicon Surfaces.* Journal of Physical Chemistry C, 2012. **116**(10): p. 6289-6297.

5. Zhu, M.J., Lerum, M.Z., and Chen, W., *How To Prepare Reproducible, Homogeneous, and Hydrolytically Stable Aminosilane-Derived Layers on Silica.* Langmuir, 2012. **28**(1): p. 416-423.

6. Losche, M., Schmitt, J., Decher, G., Bouwman, W.G., and Kjaer, K., *Detailed structure of molecularly thin polyelectrolyte multilayer films on solid substrates as revealed by neutron reflectometry.* Macromolecules, 1998. **31**(25): p. 8893-8906.

7. Mellott, N.P., Brantley, S.L., Hamilton, J.P., and Pantano, C.G., *Evaluation of surface preparation methods for glass.* Surface and Interface Analysis, 2001. **31**(5): p. 362-368.

8. Hayton, D.J. and Jenkin, T.E., *On the frustration of back-surface reflection fromtransparent substrates in ellipsometry.* Measurement Science and Technology, 2004. **15**.

9. Morita, M., Ohmi, T., Hasegawa, E., Kawakami, M., and Ohwada, M., *Growth of Native Oxide on a Silicon Surface.* Journal of Applied Physics, 1990. **68**(3): p. 1272-1281.

10. Xing, Y.J., Dementev, N., and Borguet, E., *Chemical labeling for quantitative characterization of surface chemistry.* Current Opinion in Solid State & Materials Science, 2007. **11**(5-6): p. 86-91.

11. Birks, T.A., et al., *The fundamental limits to the attenuation of hollow-core photonic crystal fibres.* 2005 7th International Conference on Transparent Optical Networks, Vol 1, Proceedings, 2005: p. 107-110.

12. Kostecki, R., Ebendorff-Heidepriem, H., Davis, C., McAdam, G., Warren-Smith, S.C., and Monro, T.M., *Silica exposed-core microstructured optical fibers.* Optical Materials Express, 2012. **2**(11): p. 1538-1547.

13. de Silva, A.P., Moody, T.S., and Wright, G.D., *Fluorescent PET (Photoinduced Electron Transfer) sensors as potent analytical tools.* Analyst, 2009. **134**(12): p. 2385-2393.

14. Seitz, O., Fernandes, P.G., Tian, R.H., Karnik, N., Wen, H.C., Stiegler, H., Chapman, R.A., Vogel, E.M., and Chabal, Y.J., *Control and stability of self-assembled monolayers under biosensing conditions.* Journal of Materials Chemistry, 2011. **21**(12): p. 4384-4392.

15. Metwalli, E., Haines, D., Becker, O., Conzone, S., and Pantano, C.G., *Surface characterizations of mono-, di-, and tri-aminosilane treated glass substrates.* Journal of Colloid and Interface Science, 2006. **298**(2): p. 825-831.

16. Wang, W. and Vaughn, M.W., *Morphology and amine accessibility of (3-aminopropyl) triethoxysilane films on glass surfaces.* Scanning, 2008. **30**(2): p. 65-77.

17. Cras, J.J., Rowe-Taitt, C.A., Nivens, D.A., and Ligler, F.S., *Comparison of chemical cleaning methods of glass in preparation for silanization.* Biosensors & Bioelectronics, 1999. **14**: p. 683-688.

18. Rahimi, R.A., Sadrnezhaad, S.K., and Raisali, G., *Chemical durability of lead silicate glass in HNO3, HCl and H2SO4 aqueous acid solutions.* Journal of Non-Crystalline Solids, 2009. **355**(3): p. 169-174.

19. Wang, J., Prasad, S., Kiang, K., Pattnaik, R.K., Toulouse, J., and Jain, H., *Source of optical loss in tellurite glass fibers.* Journal of Non-Crystalline Solids, 2006. **352**(6-7): p. 510-513.

20. Parker, J.M., *Fluoride Glasses.* Annual Review of Materials Science, 1989. **19**: p. 21-41.

21. Hermanson, G.T., *Bioconjugate techniques*. 2nd ed. 2008, London.

22. Diamandis, E.P. and Christopoulos, T.K., *The Biotin (Strept)Avidin System - Principles and Applications in Biotechnology.* Clinical Chemistry, 1991. **37**(5): p. 625-636.

23. Foo, T.C., François, A., Ebendorff-Heidepriem, H., Sumby, C.J., and Monro, T.M., *Comparison of Surface Functionalization Techniques on Silica and Soft Glasses for Optical Fibre Sensing Applications*, in *Australian Conference on Optical Fibre Technology (ACOFT)*. 2009: Adelaide, Australia.

24. Long, X.C. and Brueck, S.R.J., *Composition dependence of the photoinduced refractive-index change in lead silicate glasses.* Optics Letters, 1999. **24**(16): p. 1136-1138.

25. Oermann, M.R., Ebendorff-Heidepriem, H., Li, Y.H., Foo, T.C., and Monro, T.M., *Index matching between passive and active tellurite glasses for use in microstructured fiber lasers: Erbium doped lanthanum-tellurite glass.* Optics Express, 2009. **17**(18): p. 15578-15584.

26. Boyd, K., Ebendorff-Heidepriem, H., Monro, T.M., and Munch, J., *Surface tension and viscosity measurement of optical glasses using a scanning CO2 laser.* Optical Materials Express, 2012. **2**(8): p. 1101-1110.

27. Decher, G., *Fuzzy nanoassemblies: Toward layered polymeric multicomposites.* Science, 1997. **277**(5330): p. 1232-1237.

28. Valeur, E. and Bradley, M., *Amide bond formation: beyond the myth of coupling reagents.* Chemical Society Reviews, 2009. **38**(2): p. 606-631.

29. Ostuni, E., Yan, L., and Whitesides, G.M., *The interaction of proteins and cells with self-assembled monolayers of alkanethiolates on gold and silver.* Colloids and Surfaces B-Biointerfaces, 1999. **15**(1): p. 3-30.

30. Moon, J.H., Kim, J.H., Kim, K., Kang, T.H., Kim, B., Kim, C.H., Hahn, J.H., and Park, J.W., *Absolute surface density of the amine group of the aminosilylated thin layers: Ultraviolet-visible spectroscopy, second harmonic generation, and synchrotron-radiation photoelectron spectroscopy study*. Langmuir, 1997. **13**(16): p. 4305-4310.

31. Ron, I., Sepunaru, L., Itzhakov, S., Belenkova, T., Friedman, N., Pecht, I., Sheves, M., and Cahen, D., *Proteins as Electronic Materials: Electron Transport through Solid-State Protein Monolayer Junctions.* Journal of the American Chemical Society, 2010. **132**(12): p. 4131-4140.

32. Neish, C.S., Martin, I.L., Henderson, R.M., and Edwardson, J.M., *Direct visualization of ligand-protein interactions using atomic force microscopy*. British Journal of Pharmacology, 2002. **135**(8): p. 1943-1950.

33. Lahav, M., Vaskevich, A., and Rubinstein, I., *Biological sensing using transmission surface plasmon resonance spectroscopy.* Langmuir, 2004. **20**(18): p. 7365-7367.

34. Ebendorff-Heidepriem, H., *Unpublished data* 2013, Institute for Photonics and Advanced Sensing.

35. Wright, B.W., Peaden, P.A., Lee, M.L., and Booth, G.M., *Determination of Surface Hydroxyl Concentration on Glass and Fused-Silica Capillary Columns.* Chromatographia, 1982. **15**(9): p. 584-586.

36. Pantano, C.G. and Brow, R.K., *Hydrolysis Reactions at the Surface of Fluorozirconate Glass.* Journal of the American Ceramic Society, 1988. **71**(7): p. 577-581.

37. Verne, E., Vitale-Brovarone, C., Bui, E., Bianchi, C.L., and Boccaccini, A.R., *Surface functionalization of bioactive glasses.* Journal of Biomedical Materials Research Part A, 2009. **90A**(4): p. 981-992.

38. Bertoncello, R., Milanese, L., Bouquillon, A., Dran, J.C., Mille, B., and Salomon, J., *Leaching of lead silicate glasses in acid environment: compositional and structural changes.* Applied Physics a-Materials Science & Processing, 2004. **79**(2): p. 193-198.

39. Allred, A.L., *Electronegativity values from thermochemical data* Journal of Inorganic Nuclear Chemistry, 1961. **17**.

3B. Surface chemistry of silica and lead silicate (F2) glass

3B.1 Introduction

Silica glass and lead silicate (F2) glass are the two glass materials used for suspended core fibre (SCF) fabrication. As discussed in Chapter 1, the grafting chemistry of 3-aminopropyltriethoxysilane (APTES) is strongly correlated to the surface chemistry of glass substrates, i.e. the surface composition and, in particular, the quantity of silanol groups [1]. As described in Chapter 1, X-ray photoelectron spectroscopy **(**XPS) is a powerful technique that can provide information of surface compositions and chemical bonding of the glass substrates and the coating.

The first aim of this part of the project is to validate the glass XPS analysis methodology, by comparing the experimental and literature data of the binding energy of each type of chemical bonds for the silica [2, 3] and lead silicate (F2) glass surfaces. Although, there have been no reports on the XPS analysis of F2 glass, XPS analyses of a similar composition of lead silicate glass were reported by Wang *et al*. and Dalby *et al*. [4, 5]. In addition to validating the XPS analysis methodology, the surface composition of F2 glass measured by XPS is compared with the bulk composition measured by Energy dispersive X-ray (EDX) analysis to understand the difference between these two compositions. Finally, the relative quantity of silanol groups is compared for silica and F2 glass slides, to understand the differences in the reactivity of surfaces of F2 and silica glass with APTES.

3B.2 Experimental

3B.2.1 Preparation of silica glass slides

Silica slides (10 x10 x 1 mm) were obtained from SPI® supplies. Silica slides were submersed in Piranha solution (H_2O_2: H_2SO_4 = 3:7) for 30 minutes and then washed with water (2 x ~ 4 ml), followed by another 20 minutes sonication. Piranha solution is a common washing reagent that can remove hydrocarbon impurities on surface and increase the quantity of silanol groups on surface [6]. The slides were dried under vacuum at room temperature overnight.

3B.2.2 Preparation of lead silicate (F2) glass slides

A lead silicate (F2 glass from Schott Co.) glass billet was extruded through a stainless steel extrusion die with rectangular orifice at high temperature (585 °C) to form a flat ribbon with 2 mm x 10 mm cross-section. The ribbon was cut into ~ 10 mm x 10 mm slide sections using a diamond knife. A general description of the extrusion procedure was described in Chapter 1. Slides were cleaned firstly in detergent (~25% Decon90 solution) for 20 minutes in an ultrasonic bath, and then rinsed with deionized water thoroughly, followed by another 20 minutes ultrasonic cleaning in HPLC grade methanol. This cleaning procedure was also used for the cleaning of fibre preforms before SCFs fabrication. All slides were dried under vacuum overnight.

3B.2.3 X-ray photoelectron spectroscopy (XPS) measurements

XPS measurements were performed in an ultra high vacuum apparatus built by SPECS (Berlin, Germany). All the measurements were performed using a non-monochromatic Mg Kα X-ray source and hemispherical Phoibo 100 energy analyser from SPECS. Surface charge compensation was performed by electron flood gun SPECS FG20 at 1 eV and 5 μA. The optimisation of the voltage and current for the electron flood gun was performed on both silica and F2 glass slides. In the optimisation process, the voltage was kept constant at 1 eV and the current was adjusted until it gave the lowest full width at half maximum (FWHM) for the high resolution (HR) oxygen peak. This charge compensation setting was used for all the glass samples.

The binding energy of each element was calibrated by the adventitious carbon peak (C-H = 284.8 eV) [7]. The aperture spot diameter was 2 mm and three spots were measured for each slide. At each sampling spot, a survey spectrum with passing energy 40 eV with 0.5 eV energy step was collected. HRXPS was also performed at each spot, the passing energy of HRXPS was 10 eV with 0.05 eV energy step. The dwell time of all spectra was 0.1 s. High resolution spectra of C 1s, N 1s, Si 2p, O 2p, Na 1s and Pb 4f were collected.

3B.2.4 XPS data analysis

XPS data fitting was performed using Casa®XPS. A Shirley background was selected to model the background signal [8]. A Shirley background is one of the most common background modeling methods for XPS; it assumes an S-shape background for each peak, and the background is proportional to the area of the peak after the background subtraction [9]. It is an iterative calculation starting from the low and high end of the binding energy of the peak defined by the user [9].

The relative sensitivity factors (RSFs) for the X-ray source at 54.7° to the detector for C, N, O, Si, Pb and Na are 0.296, 0.477, 0.711, 0.339, 8.329 and 1.685 [7]. These values were used to calculate the atomic percentage of each element from the HR spectra. A convolution of Gaussian (70%) and Lorentzian (30%) peaks were used to fit individual peaks.

Peak fitting constraints were introduced in the deconvolution of the HR spectra of each element. All synthetic components within each HR spectrum were constrained to have the same full width at half maximum (FWHM). Putting constraints on the FWHM in XPS spectra deconvolution is a common practice and has been reported previously [4, 10].

The lead 4f and silicon 2p peaks are known to be doublets due to the spin-orbit coupling (or j – j coupling) [7]. For silicon, the 2p peak was separated into $2p_{3/2}$ and $2p_{1/2}$. The binding energy difference between $2p_{3/2}$ and $2p_{1/2}$ was constrained at 0.6 eV [4]. The intensity of the Si $2p_{1/2}$ peak is constrained at 50% of the Si $2p_{3/2}$ peak. For lead, the 4f peak was deconvoluted into $4f_{7/2}$ and $4f_{5/2}$. The binding energy difference between $4f_{7/2}$ and $4f_{5/2}$ was constrained at 4.86 eV. The intensity of the $4f_{5/2}$ was constrained at 75% of the area of $4f_{7/2}$ [4, 7]. For oxygen, carbon and sodium no additional constrains were introduced in the deconvolution of the HR spectra. The average binding energy and average percentage contribution was calculated for 9 analysis spots over three samples. The error of the average binding energy and average percentage contribution was 1 standard deviation (SD) of the mean of 9 analysis spots.

3B.3 Results and discussion

3B.3.1 Elemental analysis of the surface of silica glass

Silica glass slides analysed were cleaned with Piranha solution (H_2O_2: H_2SO_4 = 3:7) in order to remove hydrocarbon contaminants from the surface. Furthermore, the Piranha solution protonates non-bridging oxygen atoms to increase the quantity of silanol groups on the surface. In the survey spectrum of silica glass (Figure 3.B.1) only carbon, silicon and oxygen are found. Note that only the shaded peaks are relevant to the elemental analysis [11]. The remaining peaks are either from Auger electrons (KLL) of carbon and oxygen or 2s electrons from oxygen.

The results of this analysis are in agreement with the composition of silica glass, which is only composed of silicon dioxide (SiO_2). The carbon on the silica glass surface originates from the adventitious hydrocarbons that were either not removed upon washing or were picked up prior to the analysis.

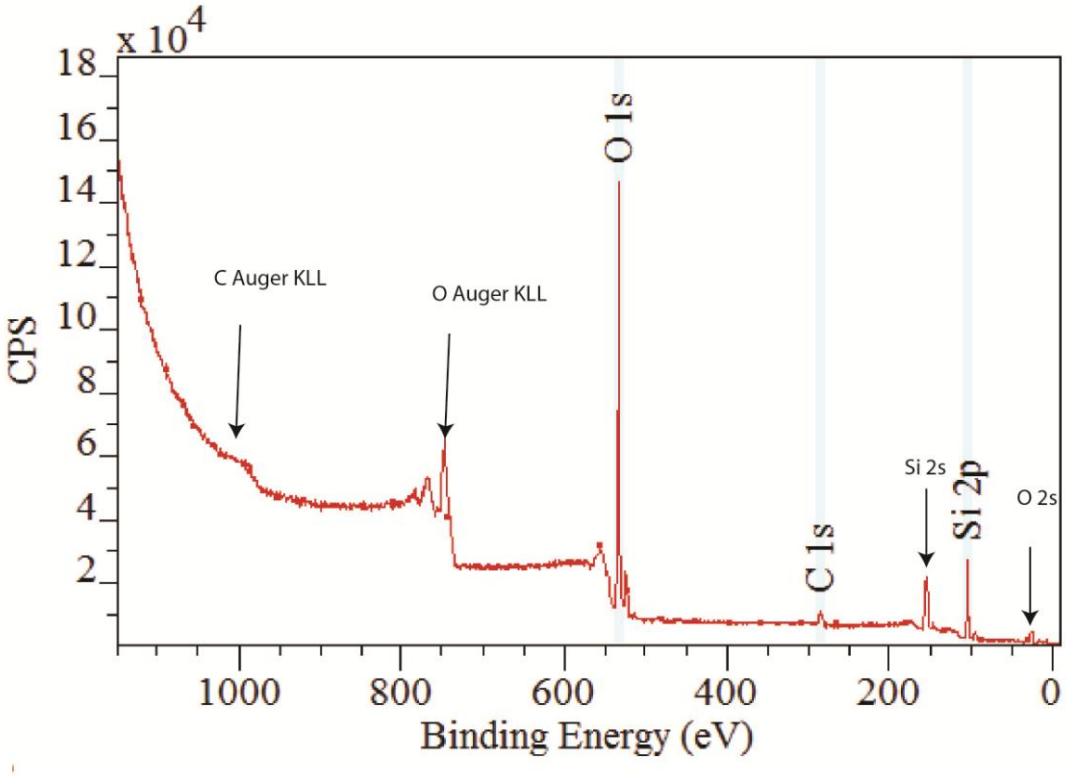

Figure 3B.1: A survey spectrum of a silica glass slide

HRXPS spectra for each element detected on the surface were collected for the quantification. This is more accurate than quantification using just the survey spectrum since the background signal of each individual element is modelled with more data. Table 3B.1 shows the average atomic percentage (at%) of each element. It is noted that the Si/O ratio is 0.43, which is lower than the expected value (0.5). It indicates that the atomic percentage of oxygen is higher than expected. The extra oxygen may be attributed to chemisorbed and/or physisorbed water, as well as oxygen containing adventitious carbons [12].

Table 3B.1: Average atomic percentages of all elements on the surface of silica glass slides

	Average at%
Si	28.5 ± 0.4
O	66.2 ± 0.9
C	5.3 ± 1.2

3B.3.2 Oxygen HRXPS spectra of silica glass

Figure 3B.2 shows the HRXPS spectrum of oxygen 1s for one spot on a silica glass slide. The peak can be separated into three components corresponding to three different types of oxygen atoms with different binding energies commonly found on silica glass surfaces. Conventionally, the oxygen atoms in silica glass are described as bridging oxygen (BO), which are oxygen atoms in the Si-O-Si bond, and non-bridging oxygen (NBO), which are oxygen atoms bonded to silicon or metal ion (M) impurities (Si-O-M) (Figure 3.B.3). The metal ion impurities (≥ 1 ppm) which typically exist in silica are aluminium, calcium, sodium and lithium [13]. Silanol/hydroxyl groups also exist on the surface of the silica glass, which arises from the chemisorption of water. It is expected that all three forms are observed for the samples. Scheme 3B.1 and 3B.2 show two mechanisms of chemisorption of water. Scheme 3B.1 shows a water molecule participating in a nucleophilic substitution (SN_2) reaction that breaks a siloxane bond to form two silanol groups. This mechanism can occur when the siloxane bond is strained. The strain is owing to either the thermal stress or bonding stress (three members ring) in the system [14]. Scheme 3B.2 shows another mechanism of silanol formation

on glass surfaces. Acidic solutions (such as Piranha) protonate NBOs and form silanol groups [15].

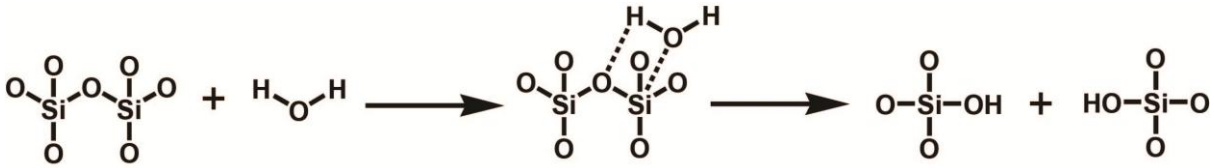

Scheme 3B.1: The mechanism of formation of silanol groups from bridging oxygen (BO)

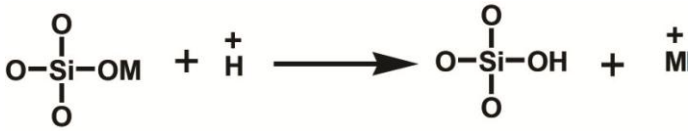

Scheme 3B.2: The mechanism of formation of silanol groups from non-bridging oxygen (NBO)

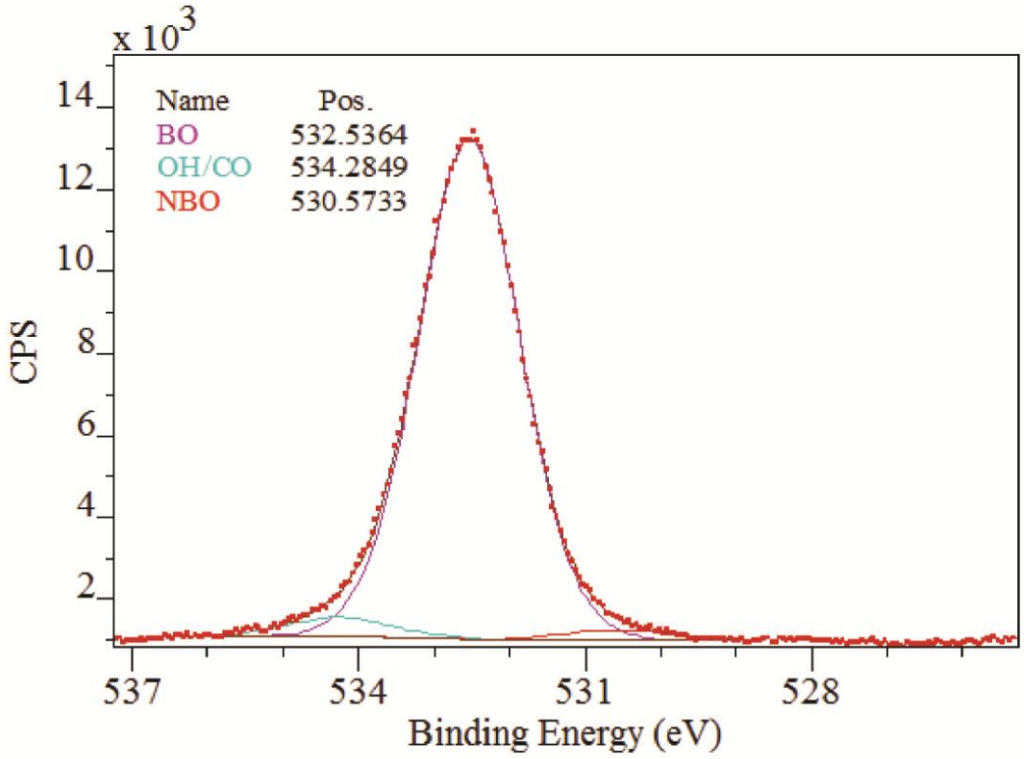

Figure 3B.2: A HRXPS spectrum of O 1s for a silica glass slide

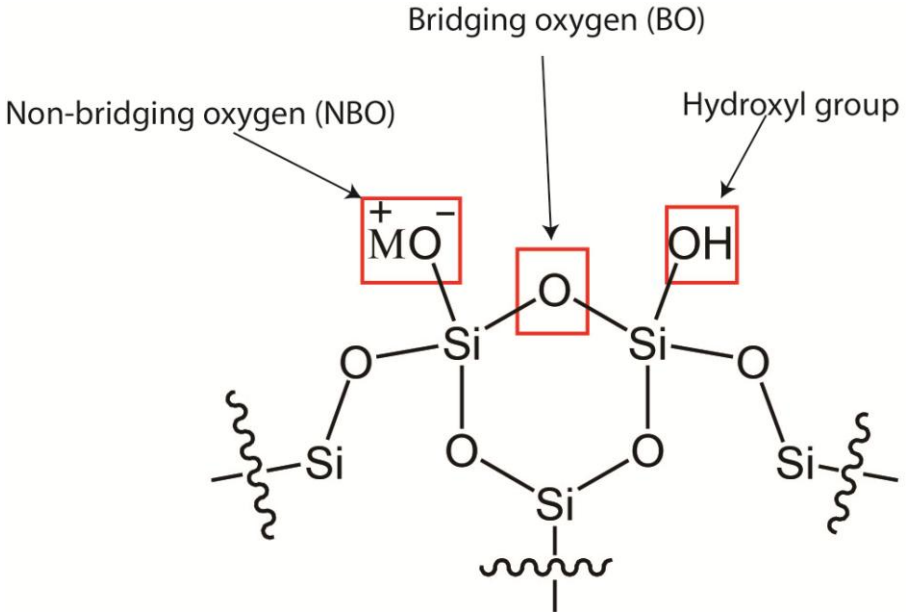

Figure 3B.3: Bridging oxygen (BO) atoms, non-bridging oxygen (NBO) atoms and hydroxyl groups (silanol groups) in the structure of silica glass

Table 3B.2 shows the average binding energies and the average percentages of BO, NBO and OH/CO. The measured binding energies of BO, NBO and OH/CO from the HRXPS spectra are consistent with literature values [2, 3]. As expected, the bridging oxygen was found to be the major oxygen component, as this is a part of the siloxane in the glass network. Similarly, NBOs comprise only a limited amount of the glass surface, since all the silica glass slides were washed with Piranha solution, and thereby Si-O^- groups on surface were converted into silanol groups (Si-OH). Thus the minor NBO component likely originates from the impurities in the glass, which is part of the Si-O-M bulk structure. In XPS the silanol (Si-OH) and carbonyl groups (C=O) have similar chemical shifts [16]. The carbonyl groups arise possibly from the adventitious hydrocarbons attached to the surface after the Piranha solution wash. The contribution from the adventitious hydrocarbon can be calculated and is discussed in the section below.

Table 3B.2: Average binding energies and average percentage contributions of NBO, BO and OH/CO on silica glass slides

	Binding energy/eV (measured value)	Binding energy/eV (literature)[2, 3, 10]	Percentage contribution (measured)
Non-bridging oxygen (NBO)	530.6 ± 0.1	530.2	2.5 ± 0.3
Bridging oxygen (BO)	532.6 ± 0.1	532.8	93.2 ± 0.6
Hydroxyl/carbonyl (OH/CO)	534.2 ± 0.1	534	4.3 ± 0.4

3B.3.3 Silicon HRXPS spectra of silica glass

Figure 3.II (Chapter 3 Appendix) shows the HR spectra of silicon for the silica slides. The peak of silicon was separated into two peaks (Si $2p_{3/2}$ and Si $2p_{1/2}$), which belong to a doublet of silicon 2p. Table 3B.3 shows that the average binding energies of Si $2p_{3/2}$ and Si $2p_{1/2}$ from the Si 2p HR were consistent with the literature values [2, 17].

Table 3B.3: Average binding energies of silicon $2p_{3/2}$ and $2p_{1/2}$ on silica glass slides

	Binding energy/eV (measured value)	Binding energy /eV (literature) [2]
Si $2p_{3/2}$	103.4 ± 0.1	103.5
Si $2p_{1/2}$	104 ± 0.1	104.1

3B.3.4 The elemental analysis of lead silicate (F2) glass

F2 is a silicate glass which is composed of four components; the bulk composition is 71 mol% SiO_2, 19 mol% PbO, 5 mol% Na_2O and 5 mol% K_2O [18]. Figure 3B.4 shows the survey spectrum of F2 glass slides, which shows the existence of silicon, lead, carbon, oxygen, potassium and sodium on the slide surface. Note that only the shaded peaks are relevant to the elemental analysis. The rest of the

peaks are either from Auger electrons (KLL) of carbon, oxygen and sodium, or 5d electron from lead [11].

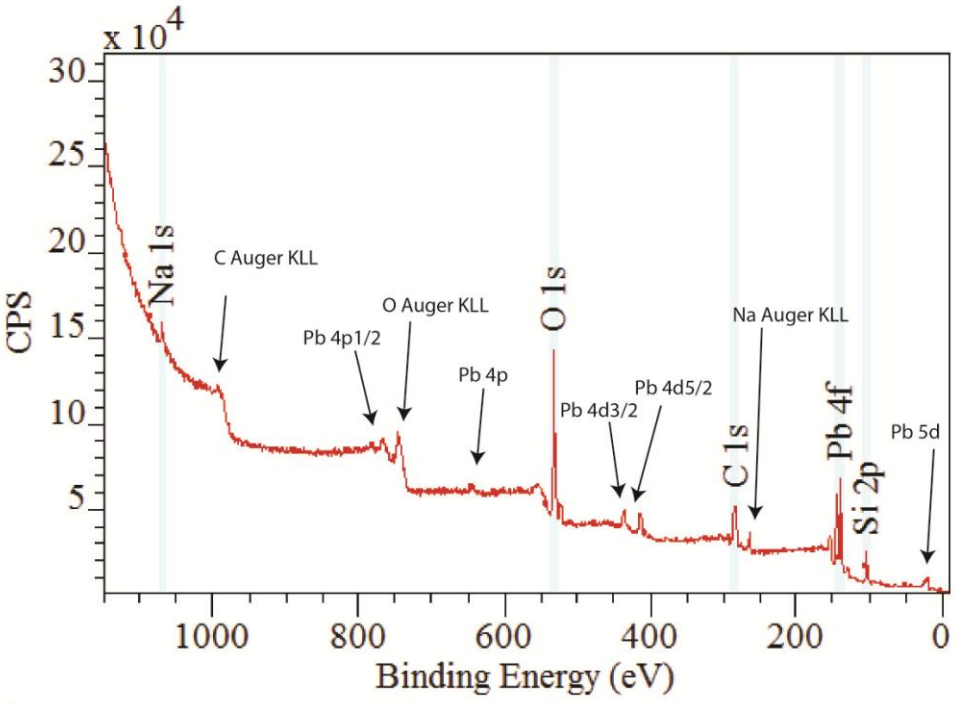

Figure 3B.4: The survey spectrum for a F2 glass slide

Figure 3B.5 shows the average atomic percentage of each element in F2 measured from energy dispersive X-ray analysis EDX [19] and XPS. EDX analyses confirms the existence of all the elements (O, Si, Pb, K and Na) reported in the literature as constituents of F2 glass [18]. The XPS survey spectrum shows that silicon, sodium, lead and oxygen were found in each sample, but in quite different proportions from the bulk glass measurements. From the XPS spectra, potassium was not observed in a significant quantity, which is discussed below. Furthermore, carbon is observed in all samples and one sample shows the existence of nitrogen on the slide surface; both likely occur due to physisorption of adventitious organic contaminants. Carbon and nitrogen atomic percentages are not reported in the EDX data showing in Figure 3B.5 because the EDX samples were coated with a graphite layer to provide conductivity. As a consequence, the atomic percentages of other elements in the EDX analysis are likely to be elevated. Figure 3B.7 shown below is a better comparison of the surface and bulk content of F2 glass.

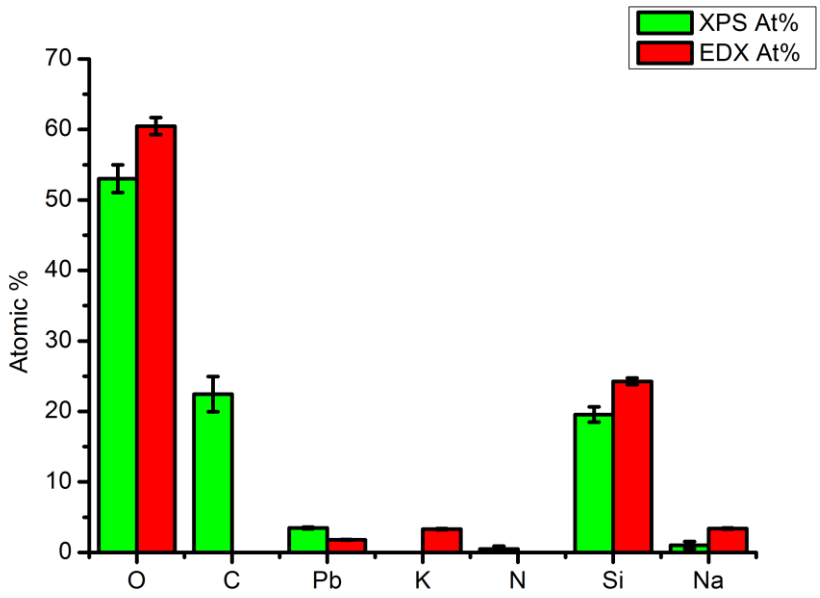

Figure 3B.5: Average atomic percentages of oxygen, carbon, lead, nitrogen, silicon, sodium and potassium measured by XPS and EDX respectively

Figure 3B.6 shows the survey scan in the range 240-320 eV, which indicates that potassium was also present on the surface. However, it is almost in the background noise floor since it is next to the high intensity carbon peak and therefore potassium is not included in the quantification.

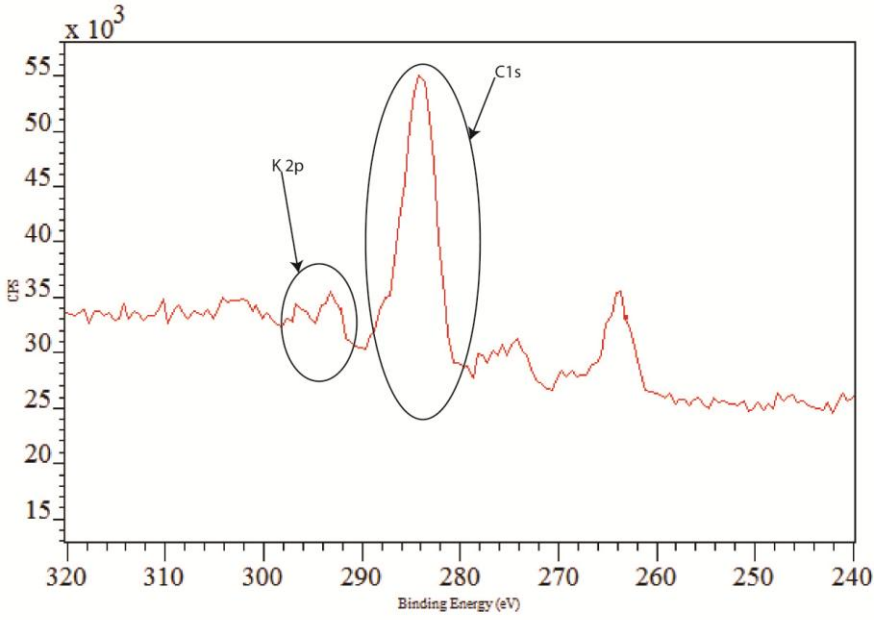

Figure 3B.6: A survey spectrum of a F2 glass slide in the range 240-320 eV

The sampling depth of XPS is ~ 3 to 10 nm, whereas EDX has micron scale sampling depths [20]. Thus, the measurements by EDX indicate the bulk composition of the glass, whereas the XPS data reveal the composition at the surface of the glass. Figure 3B.7 shows the atomic percentage of silicon, oxygen, lead and sodium measured by XPS and EDX, noting that this atomic percentage data is not the same as the data shown in Figure 3B.5. In Figure 3B.7, only silicon, oxygen, lead and sodium were included in the calculation. Figure 3B.7 shows that the oxygen atomic percentage on surface is higher than that of the bulk, whereas the lead and sodium atomic percentage on surface is lower than that of the bulk. This indicates that the sodium and lead were leached during the washing procedure (using detergent, water and methanol) used for the F2 slides [21]. It is possibly introducing greater negative charge to the surface because the leached ions are positively charged.

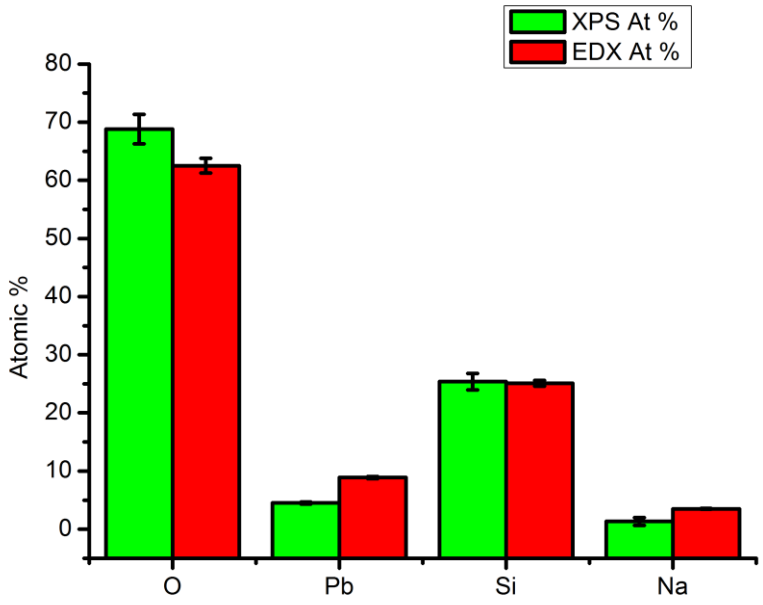

Figure 3B.7: Atomic percentages of oxygen, lead, silicon and sodium measured by EDX and XPS

3B.3.5 Oxygen HRXPS spectra for F2 glass

In the same manner as for the silica glass in Section 3B.3.2, A peak from a HRXPS spectrum of oxygen (Figure 3B.10) for F2 glass samples was separated into three components. These are bridging oxygen (BO), non-bridging oxygen (NBO) and hydroxyl/carbonyl (OH/CO). The hydroxyl groups component

represents the silanol groups on the surface, as in the silica glass. Comparing to the symmetrical oxygen HR spectrum of silica glass, the F2 oxygen HR spectrum is obviously asymmetric. This is due to the larger amount of NBO in the lead silicate glass compared to silica glass. Previous XPS studies of lead silicate glass also reported an asymmetric spectrum for oxygen [4, 5]. Table 3B.4 summarises the average binding energies and average percentages of BO, NBO and OH/CO from our experimental data from F2 glass slides and from literature data for lead silicate glass (20% PbO – 80% SiO_2) reported by Wang *et al.*[5] These results demonstrate that the measured values of F2 BO and NBO are consistent with the literature (Table 3B.4).

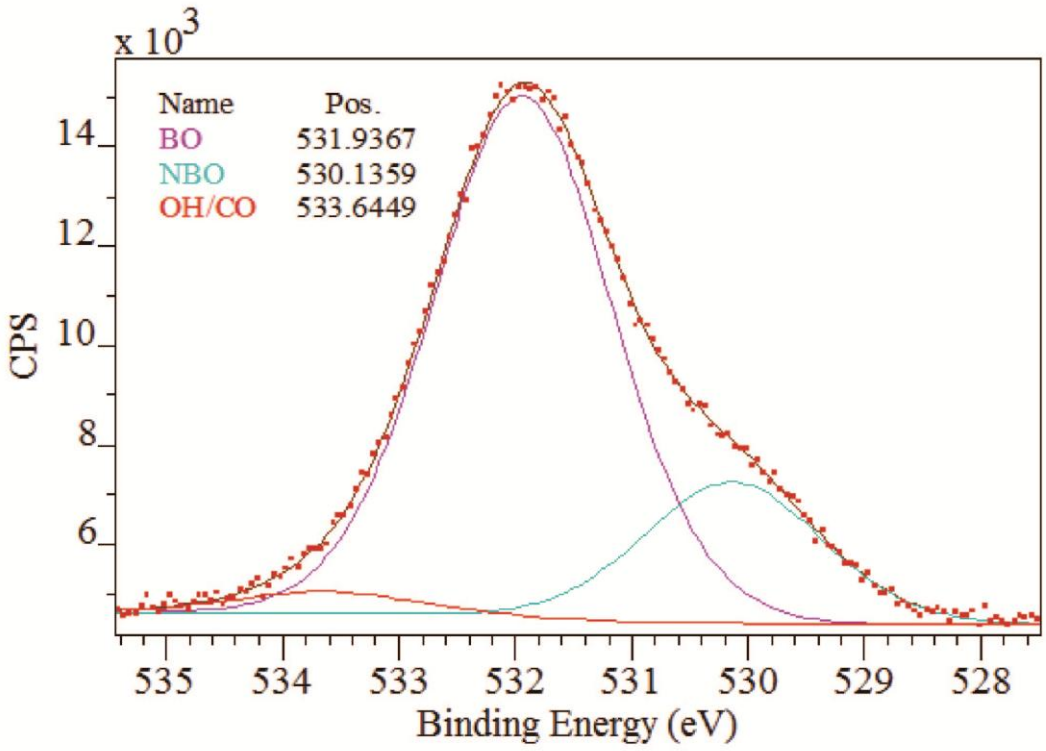

Figure 3B.8: A HRXPS spectrum of O 1s for a F2 glass slide

Table 3B.4: Average binding energies and average percentage contributions of NBO, BO on F2 glass slides

	Binding energy (measured)/eV	Binding energy (literature)[5]/eV	Percentage contribution (measured)
Non-bridging oxygen (NBO)	530.2 ± 0.1	530.1	19.6 ± 1
Bridging oxygen (BO)	532.0 ± 0.1	531.9	77.5 ± 0.9
Hydroxyl/carbonyl (OH/CO)	533.7 ± 0.2	N/A	2.9 ± 0.7

3B.3.6 Comparison of the silanol percentage for silica and lead silicate slides

Table 3B.5 shows the average binding energy of the hydroxyl/carbonyl group on the silica and lead silicate glass surfaces. After deconvolution, the OH/CO binding energy in F2 glass is 0.5 eV lower than that of silica glass. The binding energies of the BO and NBO peaks of F2 glass are also lower than that in silica glass. This is due to the difference in the electron distributions surrounding oxygen for F2 and silica glass. The lower binding energy indicates that the oxygen atoms in F2 have more charge.

Table 3B.5: Average binding energies and average percentage contribution of the OH/CO group on silica and F2 glass surfaces

	Binding energy on Silica (Measured)/eV	Percentage contribution (measured)	Binding energy on F2 (Measured)/eV	Percentage contribution (measured)
Hydroxyl/carbonyl (OH/CO)	534.2 ± 0.1	4.3 ± 0.4	533.7 ± 0.2	2.9 ± 0.7

As described before, the HRXPS O 1s signal contains contributions from Si-OH on the glass surface, and C=O, which possibly arises from adventitious hydrocarbons. While they have very similar chemical shifts, it is possible to subtract the contribution from carbonyl groups using Equation 1 [16].

$$OH_{\%} = OH / CO_{\%} - \frac{(C_{at\%})(CO_{\%})}{O_{at\%}} \quad \text{(Equation 1)}$$

$OH_{\%}$ = % of silanol in O 1s HR spectrum

$OH/CO_{\%}$= % of silanol and carbonyl in O 1s HR spectrum

$CO_{\%}$=% of CO in C 1s HR spectrum

$C_{at\%}$= atomic % of carbon

$O_{at\%}$=atomic % of oxygen

Figure 3B.11 shows the average silanol percentage in O 1s HRXPS for F2 and silica glass slides. There is no statistical difference between the silanol percentages for the two glass types. It is noted that the silica glass had been washed by Piranha solution in order to increase the density of silanol groups while the F2 glass had not been treated with Piranha solution or acid (because it is known that the acid can damage the lead silicate glass surface) [22]. This analysis indicates that F2 may provide similar density of silanol groups despite F2 having a lower atomic percentage of silicon. This phenomenon is possibly because the number of silanol groups depends on the number of NBOs. Lead silicate glass has more NBOs and thereby can provide more precursors for silanols than silica glass. Hence, even without the acid wash, the silicate glass can achieve a similar density of silanol groups compared with silica glass. The formation of silanol groups on the F2 glass surfaces is due to water chemisorption.

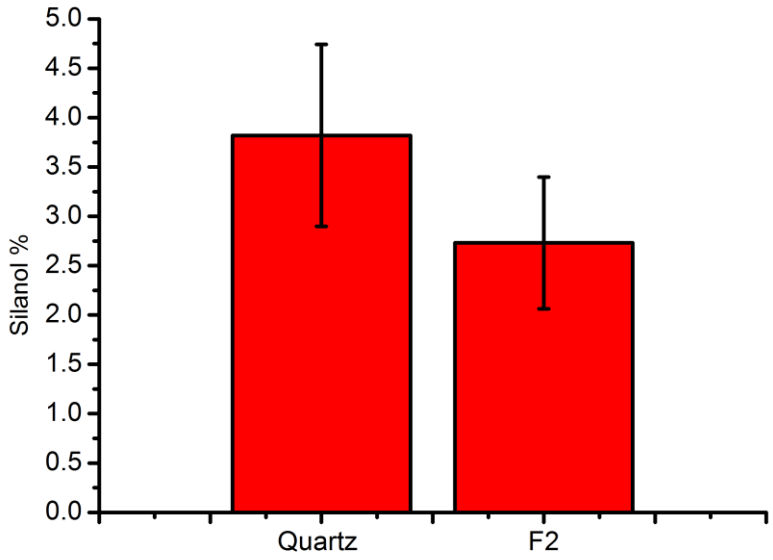

Figure 3B.9: Average silanol (Si-OH) percentages in the O 1s HRXPS spectra for silica and F2 glass slides

3B.3.7 Lead (Pb), silicon (Si) and sodium (Na) HRXPS spectra of F2 glass

Peaks from a HRXPS spectrum (Figure 3.I in Chapter 3 Appendix) of the Pb 4f peak of F2 slides was separated into two peaks (Pb $4f_{7/2}$ and Pb $4f_{5/2}$). Table 3.B.6 shows that the average binding energies of the Pb $4f_{7/2}$ and Pb $4f_{5/2}$ on the F2 glass slides surfaces are close to the literature values [5]. The binding energy of the lead $4f_{7/2}$ of crystalline lead oxide is 137.9 eV, which is lower than that of the Pb $4f_{7/2}$ found in F2 or other lead silicate glass [23]. This difference is suggesting that the lead in the glass system is more positive than that in the crystalline lead oxide [24]. Wang *et al*. and Dalby *et al.* both showed that the polarizability of Pb in lead silicate glass is concentration dependent; the lead oxide is the glass modifier instead of glass former when the concentration of lead oxide is less than 40 mol% [4, 5]. The lead oxide becomes the glass former when the PbO is above 40 mol% and the binding energy is closer to that in crystalline lead oxide because the covalent character of PbO is higher. As F2 glass has only 19 mol% PbO, the lead oxide in F2 glass is the glass modifier.

The ionic nature of lead in F2 glass suggests that lead ions can be washed off by aqueous solutions and explains why the lead composition on the surface is lower

than that in the bulk composition. Furthermore, Wang *et al.* also found that X-ray irradiation can cause reduction of lead during XPS measurement [24]. However, in this work only one oxidation state for Pb 4f was found and there is no evidence for lead oxide reduction to metallic lead during the measurement.

A peak from a HRXPS spectrum of silicon on F2 glass (Figure 3.III in Chapter 3 Appendix) was separated into two peaks (Si $2p_{3/2}$ and Si $2p_{1/2}$). The measured binding energies are the same as the literature value reported by Wang *et al*. [5]. Table 3B.6 shows that the average binding energies of Si $2p_{3/2}$ and Si $2p_{1/2}$ are lower on F2 glass slides compared with that on silica glass slides. These results suggest that the electron density on the silicon in F2 glass is higher than that of the silica glass [5]. This is because the F2 glass has more silicon attached to NBOs that have higher charge density.

Only one peak is fitted on the HRXPS sodium spectrum (Figure 3.IV in Chapter 3 Appendix). Table 3B.6 shows the comparison of the average binding energy of the Na 1s in F2 glass and the literature reported Na 1s binding energy of sodium silicate glass. The Na 1s binding energy in F2 is 1.9 eV lower than that of sodium silicate glass and is 3.3 eV lower than that of the Na 1s binding energy of crystalline sodium oxide [10], which is 1072.5 eV [25]. One of the possible reasons of the sodium binding energy being lower than that of the crystalline sodium oxide is that the sodium atom in lead silicate glass binds to an oxygen atom, that in turn binds to a lead atom, which has higher electronegativities than sodium, i.e. the electronegativity of sodium is 0.93, lead is 2.33 and oxygen is 3.44.

Table 3B.6: Average measured and literature binding energies of lead, silicon and sodium of lead silicate glass

	Binding energy (Measured)/eV	Binding energy (literature) /eV
Pb $4f_{7/2}$	138.6 ± 0.1	138.9 [5]
Pb $4f_{5/2}$	143.5 ± 0.1	143.8 [5]
Si $2p_{3/2}$	102.5 ± 0.1	102.6 [5]
Si $2p_{1/2}$	103.1 ± 0.1	103.2 [5]
Na 1s	1069.2 ± 0.3	1071.1 [26]

3B.4 Conclusions

This study showed that the experimental data of the average binding energy of each chemical bonding type for silica and lead silicate (F2) glass surfaces are consistent with literature data. These observations validated the X-ray photoelectron spectroscopy (XPS) analysis methodology of this project. The experimental and analysis parameters established here are used in the following sections.

Furthermore the F2 glass surface composition measured by XPS was found to be different to the bulk composition measured by energy dispersive X-ray (EDX) analysis. The atomic percentage of sodium and lead in the surface composition was less than that of the bulk composition, because of the leaching of those ions in the washing step. This potentially introduces greater negative charge to the surface because the leached ions are positively charged.

Finally, no statistical difference was found between the percentage contributions of silanol groups on Piranha washed silica and native F2 glass surfaces, which suggests the density of binding sites for 3-aminopropyltriethoxysilane (APTES) on F2 and Piranha washed silica glass surfaces are the same.

3B.5 References

1. Vandenberg, E.T., Bertilsson, L., Liedberg, B., Uvdal, K., Erlandsson, R., Elwing, H., and Lundstrom, I., *Structure of 3-Aminopropyl Triethoxy Silane on Silicon-Oxide.* Journal of Colloid and Interface Science, 1991. **147**(1): p. 103-118.

2. Zakaznova-Herzog, V.P., Nesbitt, H.W., Bancroft, G.M., and Tse, J.S., *High resolution core and valence band XPS spectra of non-conductor pyroxenes.* Surface Science, 2006. **600**(16): p. 3175-3186.

3. Kaupp, S., Bubert, H., Baur, L., Nelson, G., and Watzig, H., *Unexpected surface chemistry in capillaries for electrophoresis.* Journal of Chromatography A, 2000. **894**(1-2): p. 73-77.

4. Dalby, K.N., Nesbitt, H.W., Zakaznova-Herzog, V.P., and King, P.L., *Resolution of bridging oxygen signals from O 1s spectra of silicate glasses using XPS: Implications for O and Si speciation.* Geochimica Et Cosmochimica Acta, 2007. **71**(17): p. 4297-4313.

5. Wang, P.W. and Zhang, L.P., *Structural role of lead in lead silicate glasses derived from XPS spectra.* Journal of Non-Crystalline Solids, 1996. **194**(1-2): p. 129-134.

6. Cras, J.J., Rowe-Taitt, C.A., Nivens, D.A., and Ligler, F.S., *Comparison of chemical cleaning methods of glass in preparation for silanization.* Biosensors & Bioelectronics, 1999. **14**: p. 683-688.

7. Moulder, J.F., Stickle, W.F., Sobol, P.E., and Bomben, K.D., *Handbook of X-ray Photoelectron Spectroscopy*, ed. J. Chastain and J. Roger C. King. 1995, Minnesota: Physical Electronics, Inc.

8. Shirley, D.A., *High-Resolution X-Ray Photoemission Spectrum of Valence Bands of Gold.* Physical Review B, 1972. **5**(12): p. 4709-&.

9. Heide, P., *X-ray Photoelectron Spectroscopy: An introduction to Principles and Practices*. 2012, Hoboken: John Wiley & Sons.

10. Nesbitt, H.W., Bancroft, G.M., Henderson, G.S., Ho, R., Dalby, K.N., Huang, Y., and Yan, Z., *Bridging, non-bridging and free (O2-) oxygen in Na2O-SiO2 glasses: An X-ray Photoelectron Spectroscopic (XPS) and Nuclear Magnetic Resonance (NMR) study*. Journal of Non-Crystalline Solids, 2011. **357**(1): p. 170-180.

11. Fairley, N., *CasaXPS Manual 2.3.15 Introduction to XPS and AES*. 2009: Casa Software Ltd.

12. Miller, D.J., Biesinger, M.C., and McIntyre, N.S., *Interactions of CO2 and CO at fractional atmosphere pressures with iron and iron oxide surfaces: one possible mechanism for surface contamination?* Surface and Interface Analysis, 2002. **33**(4): p. 299-305.

13. Heraeus, *Quartz Glass for Optics Data and Properties*. 2013.

14. Michalske, T.A. and Freiman, S.W., *A Molecular Interpretation of Stress-Corrosion in Silica.* Nature, 1982. **295**(5849): p. 511-512.

15. Tilocca, A. and Cormack, A.N., *Modeling the Water-Bioglass Interface by Ab Initio Molecular Dynamics Simulations.* Acs Applied Materials & Interfaces, 2009. **1**(6): p. 1324-1333.

16. McCafferty, E. and Wightman, J.P., *Determination of the concentration of surface hydroxyl groups on metal oxide films by a quantitative XPS method.* Surface and Interface Analysis, 1998. **26**(8): p. 549-564.

17. Gross, T., Ramm, M., Sonntag, H., Unger, W., Weijers, H.M., and Adem, E.H., *An Xps Analysis of Different Sio2 Modifications Employing a C 1s as Well as an Au 4f7/2 Static Charge Reference.* Surface and Interface Analysis, 1992. **18**(1): p. 59-64.

18. Boyd, K., Ebendorff-Heidepriem, H., Monro, T.M., and Munch, J., *Surface tension and viscosity measurement of optical glasses using a scanning CO2 laser.* Optical Materials Express, 2012. **2**(8): p. 1101-1110.

19. Ebendorff-Heidepriem, H., *Unpublished data from the Energy dispersive X-ray analysis (EDX) measurement on Lead silicate (F2)*. 2013, Institute for Photonics and Advanced Sensing.

20. Ratner, B.D. and Castner, D.G., *electron spectroscopy for chemical analysis*, in *Surface analysis The principal Techniques*, J.C. Vickerman and I.S. Gilmore, Editors. 2009, Wiley: West Sussex.

21. Sun, Y.Z., *Mechanism of Water Corrosion of Boron-Lead Glasses.* Journal of Non-Crystalline Solids, 1982. **52**(1-3): p. 413-425.

22. Rahimi, R.A., Sadrnezhaad, S.K., and Raisali, G., *Chemical durability of lead silicate glass in HNO3, HCl and H2SO4 aqueous acid solutions.* Journal of Non-Crystalline Solids, 2009. **355**(3): p. 169-174.

23. Kim, K.S., Oleary, T.J., and Winograd, N., *X-Ray Photoelectron Spectra of Lead Oxides.* Analytical Chemistry, 1973. **45**(13): p. 2214-2218.

24. Wang, P.W., Zhang, L.P., Lu, L., Lemone, D.V., and Kinser, D.L., *Surface Modification of Lead Silicate Glass under X-Ray-Irradiation.* Applied Surface Science, 1995. **84**(1): p. 75-83.

25. Barrie, A. and Street, F.J., *An auger and X-ray photoelectron spectroscopic study of sodium metal and sodium oxide.* Journal of Electron Spectroscopy and Related Phenomena,, 1975. **7**: p. 1-31.

26. Mekki, A., Holland, D., McConville, C.F., and Salim, M., *An XPS study of iron sodium silicate glass surfaces.* Journal of Non-Crystalline Solids, 1996. **208**(3): p. 267-276.

3C. Surface characterisations of 3-aminopropyltriethoxysilane (APTES) coated silica and lead silicate (F2) glass

3C.1 Introduction

3-Aminopropyltriethoxysilane (APTES) is one of the most commonly used aminosilane reagents for covalently attaching amine functional groups onto glass materials. As discussed in Chapter 3A, this is the first coating step to introduce the desired functional groups on the internal surface of suspended core fibres (SCFs). The basic mechanism of the grafting begins with hydrolysis of at least one ethoxy group from the APTES molecule to form a silanol group followed by a condensation reaction of the silanol group with the glass substrate [1]. However, a condensation reaction between the silanol groups on the glass surface and the silane is not the only way of binding of silane molecules on a surface. It is known that the silane can bind in at least 8 different ways (Figure 3C.1) to the glass surface [2, 3]. APTES can bind to the surface via covalent bonds, electrostatic interactions or hydrogen bonds. Furthermore, electrostatic interactions and hydrogen bonding allow for multiple orientations of the APTES molecules on the surface.

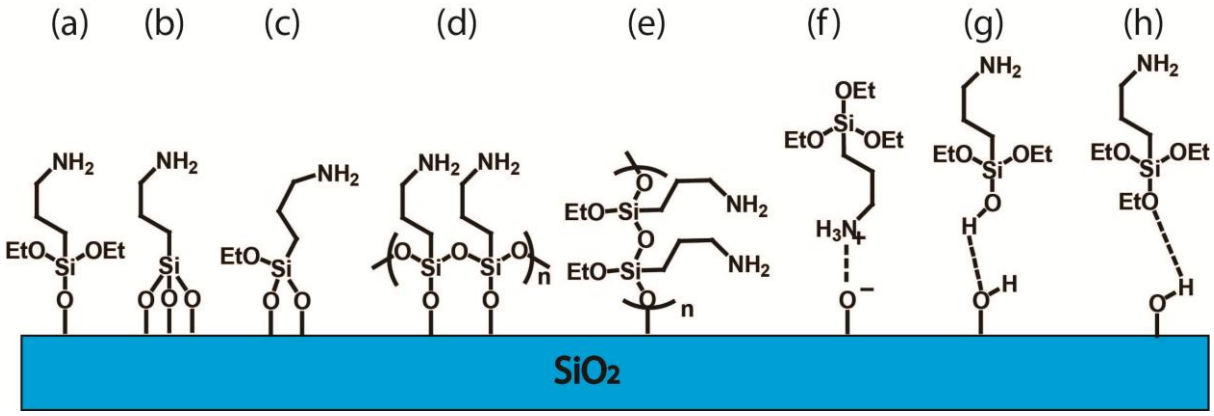

Figure 3C.1: Possible modes of binding for APTES molecules on a glass surface: (a) a single covalent bond, (b) three covalent bonds, (c) two covalent bonds, (d) horizontal polymerisation, (e) vertical polymerisation (f) inverted orientation with electrostatic interactions, (g) hydrogen bonding between silanol groups of the APTES molecule and the glass surface, and (h) hydrogen bonds between ethoxy groups from the APTES molecule and the silanol groups on the glass surface [2-4]

In addition, APTES molecules can polymerise horizontally or vertically. An APTES multilayer is formed by the combination of the vertically polymerised APTES and physiosorbed APTES molecules. The physiosorptions of APTES on the surface are via Van der Waals force, hydrogen bonds or electrostatic interactions to the covalently attached APTES molecules (Figure 3C.2). The structure of the multilayer APTES coating is highly irregular and complex, and the formation of either monolayer and multilayer APTES coatings is dependent on many experimental factors such as the type of solvent [5], water concentration in the solvent, laboratory humidity [3], temperature [6, 7], incubation time [4], APTES concentration and curing procedure used [8]. The dependence on many experimental factors is known to impact the reproducibility and consistency of the APTES coating procedure [3, 9].

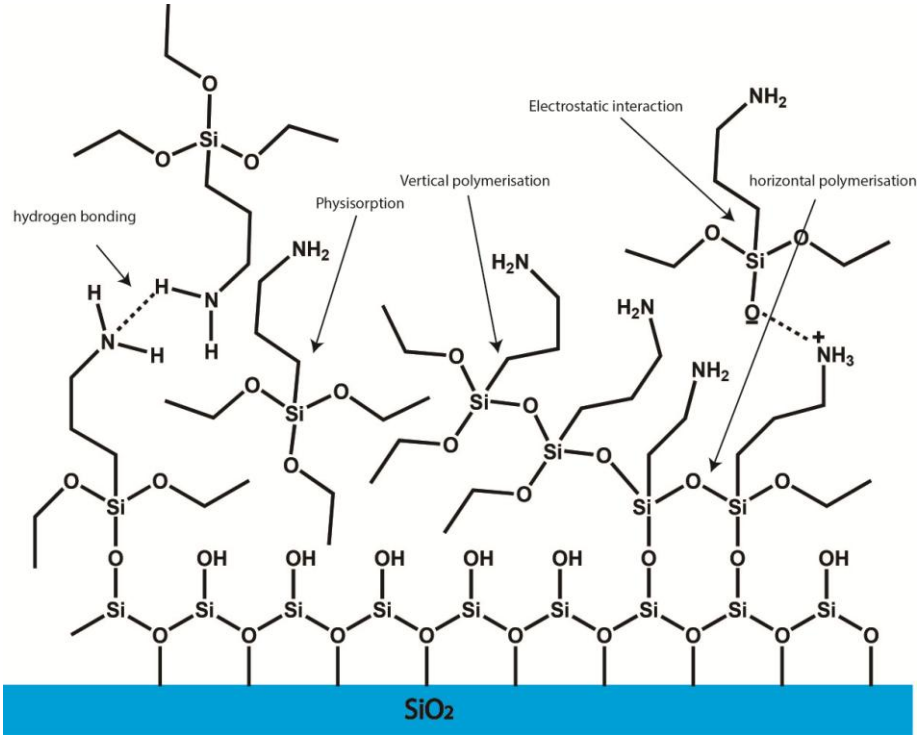

Figure 3C.2: Possible interactions of APTES molecules in a multilayer coating [2, 3]

Although, APTES coating of silicon wafers and silica glass slides have been extensively studied, it is necessary to demonstrate and characterise the coatings for use in this project, given that the APTES coating procedure is sensitive to many experimental factors [1, 4, 7, 10]. Little appears to be known regarding the surface chemistry of APTES coatings on lead silicate glass (F2). The aim of this

study is to establish an understanding of the surface chemistry, roughness and thickness of the APTES coatings on silica and lead silicate (F2) glass using 5% w/w APTES solution in anhydrous toluene, which is a common solvent for APTES coating chemistry [1-3], at 0.5 and 5 hours incubation time. According to the study by Kim *et al*, APTES in toluene is more stable and provides layers with more active amine groups for further attachment compared with layers deposited from aqueous solvents [4].

Solution coating procedures are feasible in SCFs. The solution is filled into holes of SCFs by capillary action, or by positive pressure created in a filling chamber [11, 12]. The fibre filling procedure is discussed in Chapter 5.

Another aim of this study is to quantify the variation of the thickness, roughness and the quantity of the amine functional groups for the APTES coating procedure. This is because any variations in the APTES coating on the glass have a direct impact on the surface attachment of fluoroionophores and subsequently on the sensor performance.

The studies were performed on silica and F2 glass slides, silicon wafers and unstructured F2 fibres as the model systems. To understand the surface composition and chemical bonding of the APTES layer, silica and F2 glass slides with APTES coatings were analysed using X-ray photoelectron spectroscopy (XPS). APTES coated silicon wafers were analysed by atomic force microscopy (AFM) and spectroscopic ellipsometery (SE), in order to determine the surface roughness and the coating thickness.

Other than F2 glass slides, the APTES coating procedure was also validated on unstructured (bare) F2 glass fibre surfaces. In terms of the glass surface chemistry these fibres are the most similar model system to the internal surface of F2 SCFs as they have been through the same extrusion and drawing process as structured fibres, while circumventing the challenge of performing XPS analysis inside SCFs. Time of flight secondary ion mass spectrometry (ToF-SIMS) was also performed on APTES coated unstructured fibres, in order to understand the surface composition of the APTES coating on fibre.

3C.2 Experimental

3C.2.1 Preparation of substrates

The preparation of silica slides, silicon wafer and lead silicate (F2) glass slides was as reported in Chapter 3B. Lead silicate (F2) glass unstructured fibre was fabricated in-house with an outer diameter of 160 μm. It was cut into ~1.8 cm long pieces and washed with HPLC grade methanol. The cleaned fibre was dried overnight in an oven at approximately 90°C.

3-Aminopropyltriethoxysilane (APTES) grafting procedure for glass slides and wafers

Each cleaned glass slide or silicon wafer was placed in an individual vial and incubated in 5% w/w APTES in anhydrous toluene (< 4 mL) for either 0.5 or 5 hours in a desiccator. The slides were washed with toluene (< 4 mL), dried under vacuum for at least 2 hours, before washing with deionized water (< 4 mL). Washing the APTES coated slides/wafers with water hydrolysed the remaining ethoxy groups attached on the APTES molecule and removed any physisorbed APTES aggregates from the glass surface [13]. The APTES coated slides were dried overnight at room temperature under vacuum before any surface analysis. Ultrasonic cleaning was avoided during all coating procedures since this cleaning step can break the SCF and therefore, is not transferable to SCFs functionalisation.

3-Aminopropyltriethoxysilane (APTES) grafting procedure for F2 fibre

F2 glass fibres (OD 160 μm) were placed in individual vials and incubated in 5 % w/w APTES in anhydrous toluene (< 4 mL) for either 0.5 or 5 hours. The fibres were washed with toluene (< 4 mL) and dried under vacuum. The coating method was identical to that used for the slides.

3C.2.2 Methods of surface analysis

X-ray photoelectron spectroscopy (XPS) measurements

This measurement procedure used is the same as described in Chapter 3B except for the calibration procedure. The bridging oxygen peak at 532.6 eV was used as the calibration standard for the APTES coated silica slides. For lead silicate (F2) glass slides, the Pb 4f 7/2 peak at 138.6 eV was used as the calibration standard.

The carbon peak was not used for calibration as the organic coating material contains an unknown quantity of carbonyl groups which could significantly alter the carbon peak.

XPS data analysis

The data analysis procedure is the same as that used in Chapter 3B except that additional constraints for the peak positions were used to perform the deconvolution of the high resolution X-ray photoelectron spectroscopy (HRXPS) carbon spectrum. Three components were fitted with fixed chemical shift differences relative to the CH peak. The chemical shift difference of CH and CN/CO was fixed at 1.5 eV; the difference of chemical shift of CH and C=O was fixed at 3 eV.

Time of flight secondary ion mass spectrometry (ToF-SIMS) measurements and analysis

ToF-SIMS experiments were performed using a Physical Electronics Inc. PHI TRIFT V nanoToF instrument (Physical Electronics Inc., Chanhassen, MN, USA) equipped with a pulsed liquid metal ^{79}Au primary ion gun (LMIG), operating at 30 kV energy. Dual charge neutralisation was provided by an electron flood gun and 10eV Ar^+ ions. Experiments were performed under a vacuum of $5x10^{-6}$ Pa or better. "Bunched" Au_1 instrumental settings were used to optimise the mass resolution for the spectra. Positive secondary mass spectrometry (+SIMS) and negative secondary mass spectrometry (-SIMS) spectra were collected from areas of 100 x 100 micron, with an acquisition time of 1 minute. For each sample, 5 different spots were measured. For all measurements the circular diaphragm (CD) was used to confine the emission angle from the samples.

Sample spectra, were processed and interrogated using WincadenceN software (Physical Electronics Inc., Chanhassen, MN, USA). The ion intensities were normalised with the total ion counts within an analysis. PCA analysis was performed using Matlab 2008.

Atomic force microscopy (AFM) measurement and data analysis

NT-MDT Ntegra Solaris AFM with a Smena head for tapping mode was used for surface roughness measurements. AFM images were taken at room temperature. Nitrogen gas was used to remove dust on the surface before the analysis. 30 x 30 μm survey images were taken and the data was then flattened by using a second-order polynomial. Only the centre 10 x 10 μm was used for the surface roughness analysis.

Spectroscopic ellipsometery (SE) measurements and data analysis

J.A. Woollam UV-Vis VASE® spectroscopic ellipsometer was used for measuring the APTES coating thickness on silicon wafers. Data from three incident angles (65°, 70° and 75°) were collected for each spot. Three spots were measured on each silicon wafer. The refractive indices (n) of the air, silicon-silica interfaces and silica in the range 187.88 – 1771.4 nm were given by the analysis software WVASE32 version 3.768. Refractive indices of the APTES coating and the native silica layer are potentially different because they have different compositions. However, the refractive index of APTES was assumed to be the same as native silica layer on silicon in previous studies [3, 4, 7]. Up to now, no direct measurement of the refractive index of APTES coating has been reported. This information is critical to modelling the impact of the APTES coating on the fibre on its optical properties. The data were fitted to a model with three layers (Figure 3C.3) with the thickness of the silicon-silica interface fixed at 1 nm and the silicon layer is fixed at 1 mm [14]. The average thickness of the APTES coating was calculated by subtracting the average thickness of the native silica on the silicon wafer.

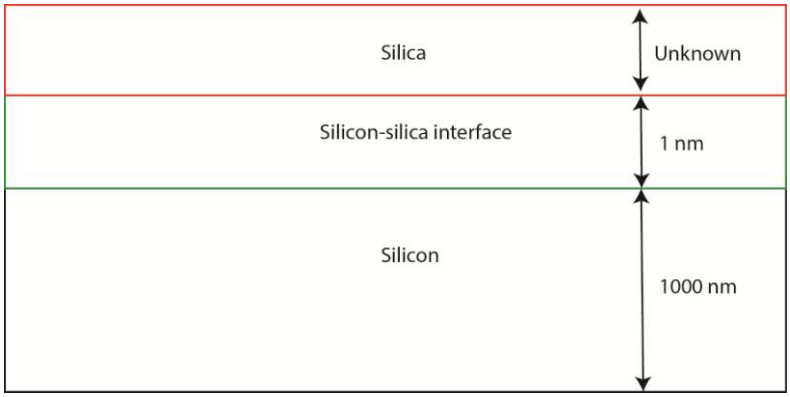

Figure 3C.3: Layers model used for the SE analysis

3C.3 Results and discussion

3C.3.1 APTES coating on silica glass slides and silicon wafers

To validate the APTES coating procedure, XPS was performed on the APTES coated silica glass slides. Figure 3C.4 shows the elemental analysis of the surface of the APTES coated silica glass slides for the two incubation times used. As shown in Chapter 3B, Section 3B.3, nitrogen does not exist on the silica glass, the presence of nitrogen shows that APTES is coated on the surface. For samples with 5 hours incubation, carbon and nitrogen atomic percentages are significantly higher than that of the samples with 0.5 hours incubation; whereas the silicon and oxygen atomic percentage of the samples with 5 hours incubation is significantly lower than that of the samples with 0.5 hours incubation. The increase of the carbon and nitrogen atomic percentages is correlated to the increase of the thickness of the APTES coating. This result agrees with previous studies [4, 7]. The increase in thickness of the APTES coating is also reflected in the decrease of silicon and oxygen atomic percentage. Due to the limited sampling depth of the XPS (the sampling depth is ~10 nm), the growth of the APTES coating masks the signal contribution from the glass substrate. After the APTES layer thickness reaches the XPS sampling depth, the Si:N should be close to 1:1. This is because the stoichiometric ratio of Si:N for an APTES molecule is 1:1.

The experimental Si:N atomic ratio of APTES with 5 hours incubation is 1.2:1, which is close to the expected stoichiometric ratio of nitrogen and silicon on an APTES molecule. The experimental Si:N ratio of APTES with 0.5 hours

incubation is 17.2:1. As expected, the APTES coating with 0.5 hours incubation is thinner than APTES coating with 5 hours incubation.

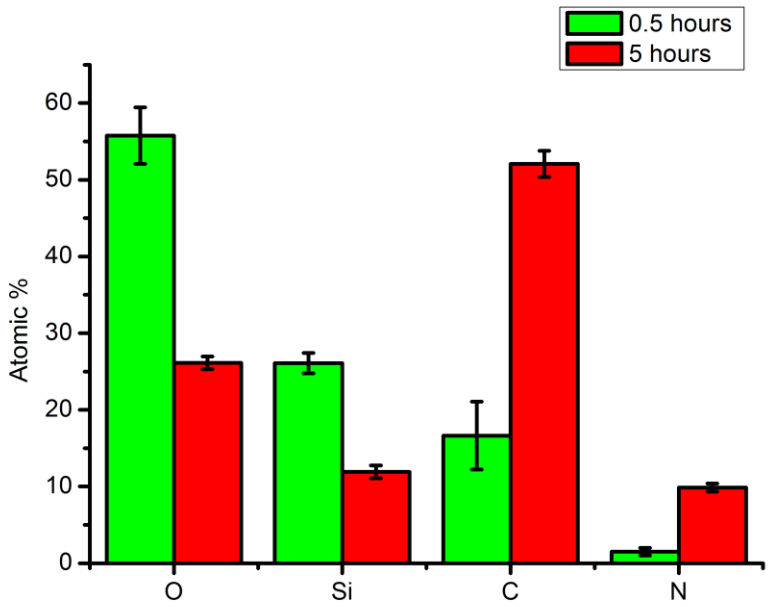

Figure 3C.4: Elemental analyses of APTES coated silica glass with 0.5 and 5 hours incubation time

An accurate thickness for an APTES coating (Table 3C.1) was determined by spectroscopic ellipsometery (SE) measurements using a silicon wafer as a model system for silica glass. The thickness of the APTES layer with 5 hours incubation is 6.26 ± 0.90 nm, whereas the APTES layer with 0.5 hours incubation is 1.06 nm. These results corroborate the observation from the Si:N atomic ratio and also suggest that the thickness of the APTES coating can be controlled by adjusting the incubation time of the coating procedure.

Table 3C.1: Average thicknesses of the APTES coating on silicon wafers with 0.5 and 5 hours incubation

	Silica + APTES/ nm	APTES /nm
No APTES	0.75 ± 0.06	N/A
0.5 hours	1.81 ± 0.11	1.06 ± 0.17
5 hours	7.01 ± 0.84	6.26 ± 0.90

Theoretically, a C:N atomic ratio represents the degree of hydrolysis of APTES on a surface (note that the C:N atomic ratio is affected by the quantity of the solvent residue remaining, as well as any adventitious hydrocarbons) [2, 7]. The theoretical C:N atomic ratio of a completely hydrolysed APTES molecule on a surface is 3:1, whereas non-hydrolysed APTES has a C:N ratio of 9:1. The experimental C:N ratio of the APTES coating with 5 hours incubation was 5.3:1, which suggests at least one ethoxy group was hydrolysed. However, multilayer APTES coatings necessitate polymerisation, which requires at least two silanol groups attached to an APTES molecule. In addition, the C:N ratio of the APTES coating with 0.5 hours incubation was 11:1, and larger than the theoretical value of the non-hydrolysed APTES molecule. The higher than expected C:N ratios for both APTES coatings are possibly due to solvent residues and adventitious hydrocarbons on the surface. Furthermore, the relative error of the average C:N ratio for the thinner coating is 77% and that of the thicker coating is 8%. The larger error in the thinner sample is due to a greater overall percentage variation of the carbon content in the thinner APTES coating where adventitious hydrocarbons has a larger effect. Thus, in this case, the C:N atomic ratio is not a reliable way to compare the degree of hydrolysis of the APTES coating.

The types of the chemical bonding for carbon, nitrogen, silicon and oxygen and their percentage contribution within for the APTES layer were determined using HRXPS analysis. Figures 3C.5a and b show HRXPS spectra of carbon 1s at 0.5 hours and 5 hours incubation (silica glass). The HR carbon 1s spectrum of APTES shows C-H, CN/CO and C=O groups, these groups are not a characteristic signal for APTES since these functional groups are also present in adventitious carbon. Table 3C.2 shows the average binding energy and the average percentage

contribution of CH, CN/CO and C=O moieties. The binding energy of the C-H component is the same as the literature value, while the binding energies of CN/CO and C=O are close to their literature values also [2]. The percentage contributions of CH, CN/CO and C=O show no significant difference in samples with 0.5 and 5 hours incubation. This is possibly due to there being a significant contribution of CH, CN/CO and C=O groups from the adventitious hydrocarbons. Therefore the variation of the CH, CN/CO and C=O groups percentage contributions due to the variation of the thickness of APTES cannot be shown.

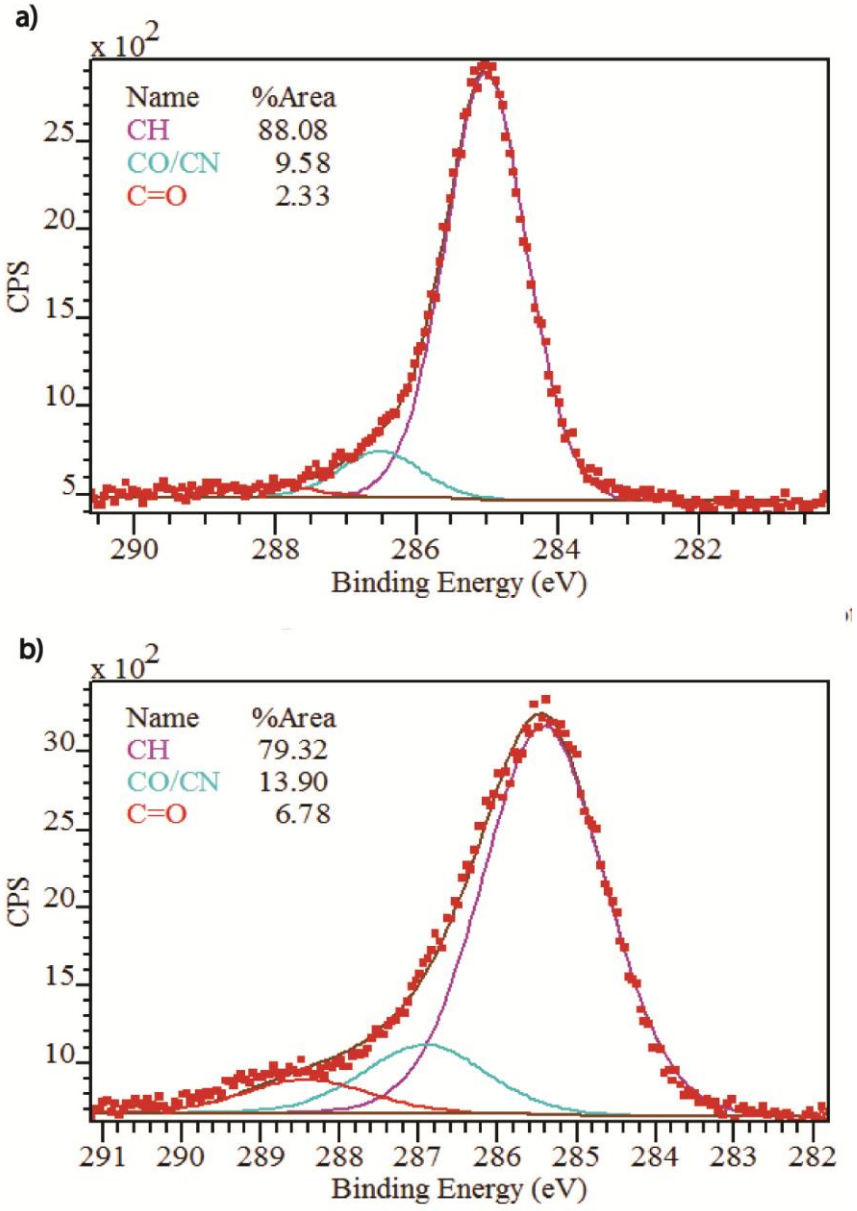

Figure 3C.5: HRXPS spectra of carbon 1s at (a) 0.5 hours and (b) 5 hours incubation

Table 3C.2: Average binding energies and average percentage contributions of CH, CO/CN and C=O groups from APTES coatings on silica glass with 0.5 hours and 5 hours incubation

	Component	Binding energy/eV (experimental)	Binding energy/eV (literature)[2]	Percentage contribution (measured)
0.5 hours	CH	285.0 ± 0.1	285.0 ± 0.0	84.1 ± 4.9
	CO/CN	286.5 ± 0.1	286.0 ± 0.2	12.2 ± 4.1
	C=O	288.0 ± 0.1	288.3 ± 0.7	3.7 ± 1.6
5 hours	CH	285.4 ± 0.0	285.0 ± 0.0	80.9 ± 3.5
	CO/CN	286.9 ± 0.1	286.0 ± 0.2	14.2 ± 2.8
	C=O	288.4 ± 0.1	288.3 ± 0.7	5.0± 1.2

Figures 3C.6a and b show the HRXPS spectra for nitrogen 1s at 0.5 hours and 5 hours incubation respectively. The nitrogen 1s spectrum is separated into two components, which are amine groups at 400 eV, and hydrogen bonded amine/ammonium group at 402 eV. These groups were reported in previous literature and the binding energy of each group is close to these literature values [1, 2]. The agreement for the binding energy of CH, CN/CO, C=O, NH_2 and NH_3^+ with the literature values further validates our APTES coating procedure.

The average binding energy and corresponding average percentage contributions are shown in Table 3C.3. The percentage contributions of the amine and ammonium groups of the APTES coating with 0.5 hours incubation are equal. However, the percentage contribution of amine groups is higher in the APTES coating with 5 hours incubation. One possible reason is that the free amine groups have a higher chance to interact with silanol groups on the surface when the APTES layer is thin. In addition, protons released from the silanol group have a higher chance of binding to the free amine groups to form ammonium ions in a thinner layer. By contrast, the protonation by or hydrogen bonding to silanol groups is more difficult as the APTES layer becomes thicker and thus, the percentage contribution of the free amine groups is higher at the APTES with 5 hours incubation.

Ammonium groups are not reactive in peptide coupling reactions [15], thus this result suggests that the thicker APTES layer may lead to a higher percentage of free amines becoming available for the peptide coupling reactions, provided that the ratio of the free amine to ammonium groups remains unchanged at the very top surface of the coating.

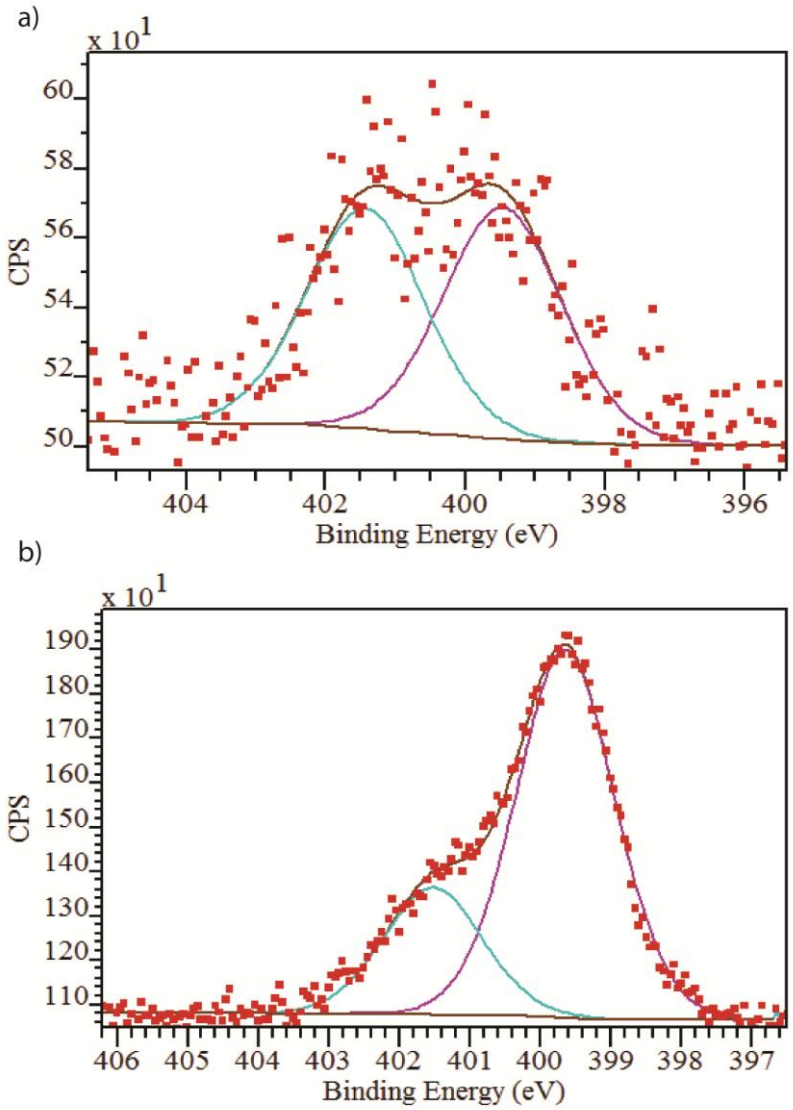

Figure 3C.6: HRXPS spectra of nitrogen 1s with (a) 0.5 hours and (b) 5 hours incubation

Table 3C.3: Average binding energies and average percentage contributions of NH_2 and NH_3^+ from APTES coatings with 0.5 hours and 5 hours incubation

	Component	Binding energy/eV (experimental)	Binding energy/eV (literature) [1, 2]	precentage contribution
0.5 hours	NH_2	399.5 ± 0.2	400.9 ± 0.2	50.6 ± 9.7
	NH_3^+	401.6 ± 0.2	402.4 ± 0.2	49.4 ± 9.7
5 hours	NH_2	399.7 ± 0.0	400.4 ± 0.2	75.5 ± 5.9
	NH_3^+	401.5 ± 0.0	401.9 ± 0.2	24.5 ± 5.9

Table 3C.4 shows that the average binding energy of Si 2p 3/2 for silica glass with an APTES coating applied with 0.5 hours incubation has the same binding energy compared with that of the uncoated silica glass. This arises because the APTES layer is thin and therefore the contribution of the silicon signal is mostly from the glass substrate. The binding energy of Si 2p 3/2 for the APTES coated glass samples with 5 hours incubation shows a significant change in the binding energy, since the major contribution from the Si 2p 3/2 is from the APTES and not the glass substrate. The decrease in the binding energy indicates that the silicon in APTES is less electropositive compared to the silicon in the silica glass; it is because silicon in APTES is bonded to one carbon atom and three oxygen atoms, whereas the silicon in the silica glass is bonded to four oxygen atoms.

Table 3C.4: Average binding energies of silicon 2p 3/2 for silica glass and APTES coated silica glass with 0.5 hours and 5 hours incubation

	Silica glass	0.5 hours incubation APTES	5 hours incubation APTES
Binding energy/eV	103.4 ± 0.1	103.3 ± 0.1	102.9 ± 0.2

In a similar manner to the treatment of the HR oxygen 1s spectrum of silica glass used in Chapter 3B, the HR oxygen 1s spectra of the APTES coated silica glass slides can be separated into three peaks. These are bridging oxygen (BO), non-bridging oxygen (NBO) and hydroxyl or carbonyl group (OH/CO). Table 3C.5 shows the average binding energy and average percentage contribution of each peak for the silica glass and APTES coated silica glass with 0.5 hours incubation and 5 hours incubation. The binding energy of each peak does not show a significant difference; however, the percentage contribution of NBOs for the APTES coated glass with 5 hours incubation has significantly increased.

Given that the HRXPS of nitrogen shows the existence of ammonium groups, the increase of NBO content is proposed to be a new evidence for the existence of an electrostatic interaction between silanate ($Si\text{-}O^-$) and ammonium (NH_3^+) groups. This interaction can be intra or inter molecular, as illustrated in Figure 3C.7. This interaction is very similar to interactions of NBOs in silica glass, which bind to positive metal ion impurities (see Chapter 3B). This interaction was proposed in previous literature, but so far the evidence for this was provided by either the nitrogen HRXPS, which only show the existence of ammonium group [1, 16], or hydrogen bonds stretch given by FT-IR spectroscopy [17, 18]. This is the first reported evidence showing the existence of such an interaction from oxygen HRXPS.

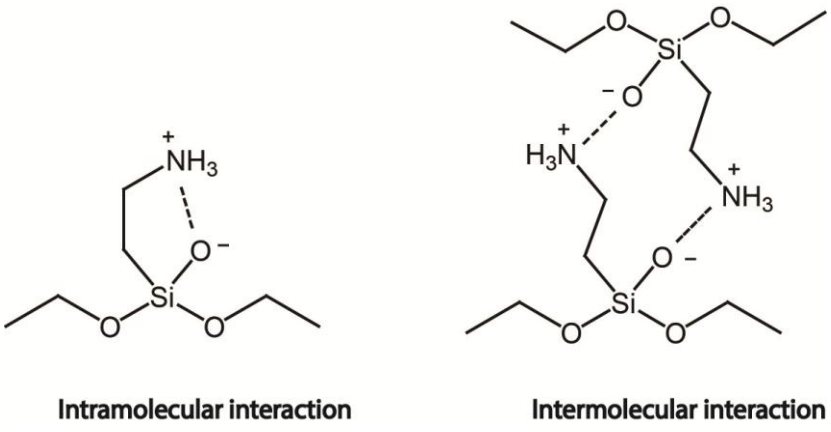

Figure 3C.7: Possible arrangements of NBOs in an APTES multilayer

Table 3C.5: Average binding energies and average percentage contributions of each component in the HRXPS oxygen 1s spectra for silica glass and APTES coated silica glass with 0.5 hours and 5 hours incubation

	Silica glass		APTES 0.5 hours		APTES 5 hours	
	Binding energy/eV	Percentage contribution	Binding energy/eV	Percentage contribution	Binding energy/eV	Percentage contribution
Non-bridging oxygen (NBO)	530.6 ± 0.1	2.5 ± 0.3	530.7 ± 0.2	4.2 ± 0.6	531.1 ± 0.1	12.2 ± 1.8
Bridging oxygen (BO)	532.6 ± 0.1	93.2 ± 0.6	532.6 ± 0.0	91.5 ± 1.8	532.6	83.6 ± 1.6
Hydroxyl/carbonyl (OH/CO)	534.2 ± 0.1	4.3 ± 0.4	534.3 ± 0.1	4.4 ± 2.0	534.3 ± 0.2	4.2 ± 0.4

To measure the surface roughness of the APTES coating, AFM measurements were performed on APTES coated silicon wafers. Figures 3C.8a and b show the AFM images of APTES coated silicon wafers with 0.5 hours and 5 hours incubation. No aggregates were found on all APTES coated silicon wafers regardless of the incubation time. The size of each image is 100 μm^2. Surface roughnesses of the APTES coating were quantified by root-mean-square deviation of the surface (Sq) (Equation 3C.1) [19].

$$Sq = \sqrt{\frac{1}{A}\iint_A (z^2(x,y)dxdy)} \qquad \text{(Equation 3C.1)}$$

A is the sampling area; z(x, y) is the function representing the height of the surface relative to the best fit plane in this case.

Table 3C.6 summarise average surface roughness (Sq) of the silicon wafers without APTES coating and with APTES coatings following 0.5 hours incubation and 5 hours incubation. The surface roughness (Sq) of the APTES coated wafer is within the variation of the uncoated wafer. These results show that the APTES

coating does not introduce extra surface roughness on the silicon wafer within 5 hours incubation time.

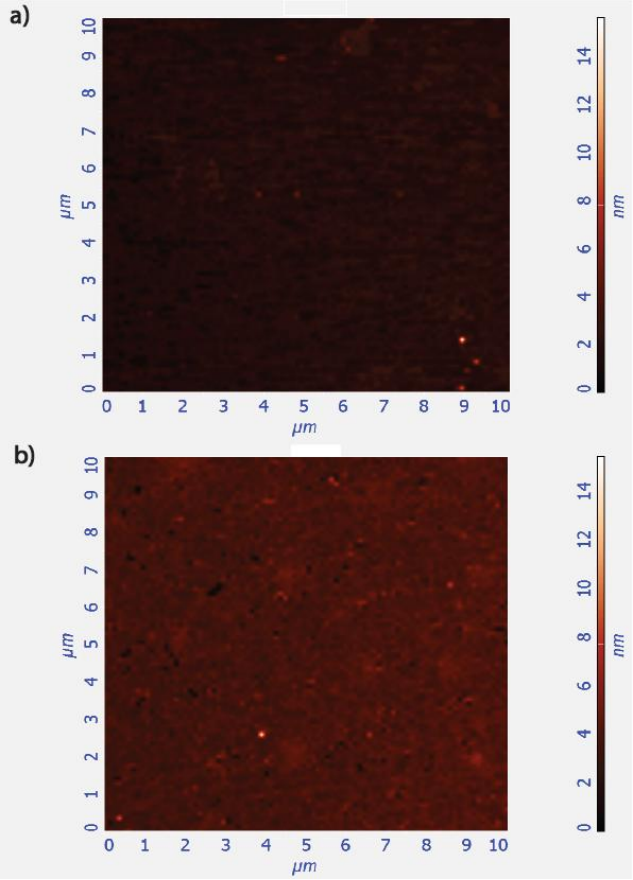

Figure 3C.8: APTES coated silicon wafers with (a) 0.5 hours incubation and (b) 5 hours incubation

Table 3C.6: Average surface roughness (Sq) for APTES coated silicon wafers

	Sq/nm
No coating	0.66 ± 0.16
0.5 hours APTES coating	0.46 ± 0.05
5 hours APTES coating	0.65 ± 0.02

3C.3.2 APTES coating on lead silicate (F2) glass

To validate the APTES coating procedure on F2 glass, XPS surface elemental analyses (Figure 3C.9a) were performed on F2 glass slides coated using the same

coating procedure as for silica glass slides. The presence of nitrogen proves APTES was coated on the F2 glass slides. Figure 3C.9b shows that the nitrogen and carbon percentage contributions of APTES coated on F2 are lower than that on silica glass, whereas the silicon and oxygen atomic percentages are higher than for silica. This suggests three possibilities, (i) the APTES coating thickness on F2 is thinner than that on silica glass, (ii) the porosity of the APTES coating on F2 glass is higher than that on silica glass, or (iii) less APTES molecules are attached on F2 glass compared with silica glass. This result suggests that the glass surface chemistry is possibly affecting the surface attachment of the APTES molecule.

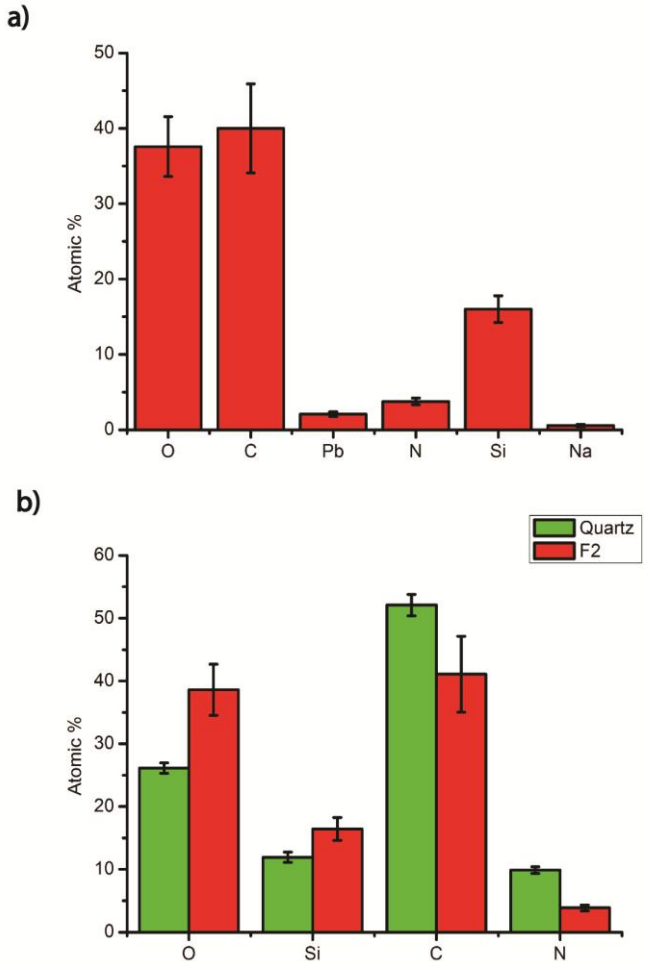

Figure 3C.9: (a) The elemental analysis of APTES coated F2 glass with 5 hours incubation. (b) A comparison of the atomic percentage of oxygen, silicon, carbon and nitrogen for APTES coated silica and F2 glass slides with 5 hours incubation

The XPS measurements show that the silanol group densities of F2 glass and silica glass are very similar. Therefore the differences in the APTES coating thickness or porosity cannot arise from the difference in the density of the silanol groups. These differences are possibly because of the higher negative charge on the F2 glass that leads to changes in the orientation of APTES molecules on the surface. In Chapter 3B, it was shown that the surface of F2 glass following exposure to aqueous solutions contains a reduced amount sodium and lead due to leaching. This causes an increase in the negative charges on the surface. Hence, APTES molecules that contain positive charge prefer to have a 'horizontal' orientation rather than 'vertical' orientation (Figure 3C.10a). 'Horizontal' APTES molecules give a thinner coating compared with 'vertically' oriented ones.

In addition, the negatively charged surface may affect the condensation reaction for covalent attachment of APTES molecule on the surface. As shown in Figure 3C.10b, orientation B is favourable for the condensation reaction on the surface, whereas the negative changed surface favours APTES in orientation A, which is not favourable for the covalent attachment of APTES molecule. Therefore, in this case, fewer APTES molecules are attached on the F2 glass surface.

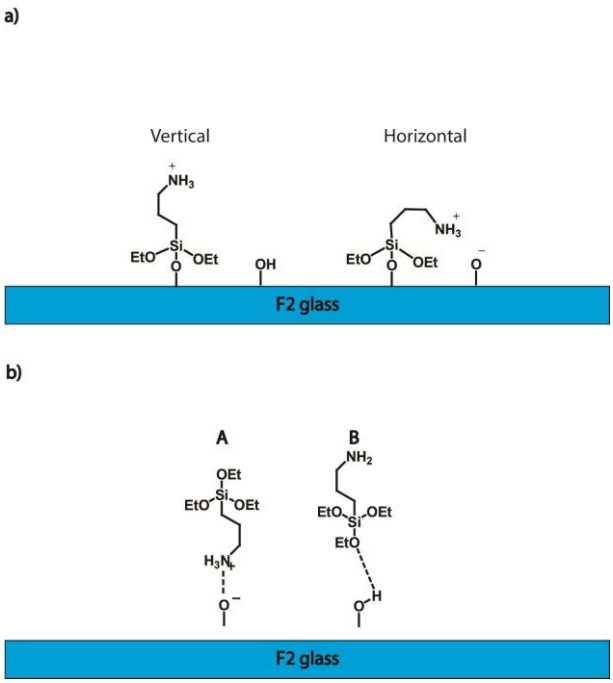

Figure 3C.10: (a) Two possible orientations of surface attached APTES molecule due to surface charge. (b)Two possible orientations of APTES before attachment on the F2 glass surface

As described in Part A, performing ellipsometery measurements on a transparent sample requires additional sample treatment to remove unwanted backside reflection that affects the fitting model [20]. To avoid these additional sample treatments, silicon wafer was used as the model system for silica glass. However, silicon wafer cannot be the model system for F2 due to the difference in the composition. In addition, the F2 slides fabricated using extrusions are not perfectly flat; this also imposes extra difficulty in the coating thickness measurements. Due to the difficulty of the measurement, the thickness of the APTES coating on F2 slide was not measured by ellipsometery and no further conclusions can be made here.

Similar to the analysis of the APTES coated silica slide, the types of the chemical bonding for carbon, nitrogen, silicon and oxygen and their percentage contributions within the APTES layer were determined by HRXPS analysis. Table 3C.7 summarises the average percentage contributions and the average binding energies of each of the separated oxygen peaks from uncoated and APTES coated F2 glass. The binding energies of the BO, NBO and OH/CO peaks of the APTES coated F2 glass are the same as the uncoated F2 glass. However, the BO percentage of the APTES layer is higher than that of the F2 glass, whereas the NBO percentage of the APTES layer is lower compared with that of the F2 glass. Lead and silicon HRXPS spectra show no significant difference in the binding energy and percentage contribution of each component before and after APTES coating; therefore the results are not shown here. The percentage contribution of the two separated peaks in the lead and silicon HRXPS spectra are constant because they are constrained based on the procedure described in Chapter 3B. The binding energy of lead is the calibration peak and therefore it is fixed. The silicon binding energy does not show a significant change after the APTES coating suggesting that the majority of the silicon signal originates from the glass substrate. This is consistent with the data presented above that indicates the APTES coating on F2 glass slides are thinner, more porous or arranged differently.

Table 3C.7: Average binding energies and average percentage contributions of BO, NBO and OH/CO from the oxygen 1s HRXPS spectra of F2 glass and APTES coated F2 glass

	F2 glass		APTES coated F2 glass	
	Binding energy / eV	percentage contribution	Binding energy / eV	precentage contribution
NBO	530.2 ± 0.1	19.6 ± 1	530.2 ± 0.1	14.7 ± 1.6
BO	532.0 ± 0.1	77.5 ± 0.9	532 ± 0.0	82.3 ± 1.6
OH/CO	533.7 ± 0.2	2.9 ± 0.7	533.8 ± 0.1	3 ± 0.7

Table 3C.8 summarises the average binding energy and the average percentage contribution of each separated peak after the deconvolution of the carbon and nitrogen 1s peaks. The binding energies and percentage contributions of the CH, CN/CO, and C=O or NH_2 and NH_3^+ peaks are either the same or very similar between APTES coated F2 and silica glass slides with 5 hours incubation. It indicates the relative composition of all of the functional groups in the APTES coating on F2 and silica glass slide are similar. However, the nitrogen atomic percentage again suggests the APTES coating on F2 slides are either thinner or more porous than it is on the silica glass slides.

Table 3C.8: Average binding energies and average percentage contributions of each component from the carbon and nitrogen 1s HR spectra for APTES coated silica and F2 glass slides with 5 hours incubation

	Silica glass		Lead silicate glass (F2)	
	Binding energy / eV	Percentage contribution	Binding energy / eV	Percentage contribution
CH	285.4 ± 0.0	80.9 ± 3.5	284.7 ± 0.0	85.5 ± 1.5
CO/CN	286.9 ± 0.1	14.2 ± 2.8	286.2 ± 0.0	10.8 ± 2.1
C=O	288.4 ± 0.1	5.0± 1.2	287.7 ± 0.0	3.7 ± 1.0
NH_2	399.7 ± 0.0	75.5 ± 5.9	399 ± 0.1	59.9 ± 9.6
NH_3^+	401.5 ± 0.0	24.5 ± 5.9	401.1 ± 0.1	40.1 ± 9.6

3C.3.3 The consistency for APTES coatings on F2 and silica glass

Variations in the thickness, roughness and functional group density of APTES coatings are major issues in SCF sensor fabrication. In order to study reproducibilities of surface roughness, thickness and nitrogen atomic percentage, these factors were analysed for 3 samples and 3 spots on each sample. Table 3C.9 summarises the percentage variation for each measurement which was calculated using Equation 3C.2.

$$\%\,\mathrm{var} = \frac{\sigma_X}{\overline{X}} \qquad \text{(Equation 3C.2)}$$

σ_X = Standard deviation of N%, Sq and Thickness(nm)

$\overline{X}$ = Mean of N%, Sq and Thickness(nm)

Table 3C.9 shows that variations of the nitrogen atomic percentage, thickness and surface roughness are less on the APTES coated silica glass with 5 hours incubation compared with only 0.5 hours. It is also worth noting that the atomic percentage of nitrogen in the APTES coating that was measured using XPS does not necessary correlate to the available 'active' amine functional group density on the top surface. Since some amine functional groups are 'buried' inside the APTES coating and not available for further attachment reactions [21]. However, the consistency of the nitrogen atomic percentages of the APTES coatings is a necessary but not sufficient condition for the consistency of the surface amine functional group density. This occurs as the XPS is sampling the entire volume of the APTES coating (the thickness of the coating with 5 hours incubation is 6.3 nm), but the 'active' amine groups are those that are located on the very top surface (i.e. first 1 nm) of the multilayer. In the multilayer, the majority of the amine groups are buried inside the APTES multilayer.[2, 8] Furthermore, the multilayer grows without restriction for the orientation of the APTES. Therefore some of the APTES molecules are in an upside-down orientation, which buries the amine groups, making them unavailable for binding.

The reduced variation in the silica sample for a 5 hours incubation time suggests that a thicker layer may be beneficial to the consistency of the amine functional group density, thickness and roughness of the coating. In fact, for SCF sensor fabrications, coating consistency is more important than the absolute value for each parameter. This concept is discussed in Chapter 5.

The percentage variation of the nitrogen atomic percentage of the APTES coated F2 glass slides with 5 hours incubation is higher than that measured for the APTES coated silica glass slides. This possibly originates from the greater variation in the surface charge for F2 slides than that of the silica glass.

Table 3C.9: Percentage variations in the nitrogen atomic percentage, coating thickness and surface roughness (Sq) extracted from XPS, AFM and SE analyses (N/A indicates data that could not be measured)

	Silica glass		Lead silicate (F2)
Incubation time/hrs	0.5	5	5
Nitrogen atomic percentage	26.9	5.3	11.8
Thickness	14.4	3.1	N/A
Surface roughness (Sq)	10.9	3.1	N/A

3C.3.4 ToF-SIMS analysis of APTES coated bare F2 fibre for different incubation times

In addition to planar model systems such as glass slides and silicon wafers, unstructured bare fibre also serves as a useful model system as the bare fibres are fabricated in the same way as SCFs; therefore they are a close model system for the internal surface of SCFs. One of the challenges with using unstructured fibre as a model system is that the fibre diameter of 150 to 200 μm is too small a surface on which to perform XPS. The curved surface shape also makes fluorescence imaging very challenging. ToF-SIMS has the ability to focus the ion beam to 100 x 100 μm area or even smaller and has high surface sensitivity owing to it sampling only the top 1 to 2 nm of a surface. Thus, ToF-SIMS analysis was

performed on APTES coated fibre, untreated F2 fibre and F2 fibre with 5 hours toluene incubation. The last two samples are controls.

Figure 3C.11a shows a principal component analysis (PCA) of the +SIMS data for the three fibres. In this PCA plot principal component 1 (PC1) and principal component 2 (PC2) cover 88.1% of the overall covariance of all the data. It shows clear cluster separations for APTES coated fibre with 1 and 5 hours incubation and controls. The clear clusters separation between untreated F2 fibre and F2 fibre with 5 hours toluene incubation indicates that ToF-SIMS can detect trace amount of solvent residue physisorbed on the fibre surface. Samples with APTES coating show positive loading in PC1. Figure 3C.11b shows the loading plot for PC1 of the +SIMS organic fragments. From the loading plot, the major positive loadings are from CH_2^+, CH_3^+, NH_4^+, CH_2N^+, CH_3N^+, CH_4N^+, CH_5N^+, $C_2H_4N^+$, $C_3H_6^+$, $C_2H_5N^+$, $C_3H_4N^+$ and $C_3H_6N^+$. Among all listed fragments CH_4N^+ has the highest positive loading for PC1 and implies this fragment is a characteristic fragment of the APTES coating. Figure 3C.12 shows that the longer the incubation time of the APTES, the higher the normalised CH_4N^+ intensity. The normalised CH_4N^+ intensity of the controls have no significant difference. On silica glass, the APTES coating thickness changes as a function of the incubation time used. Therefore, this result suggests that the normalised intensity of CH_4N^+ can be used as the measure of APTES coating thickness on unstructured F2 glass fibre surfaces.

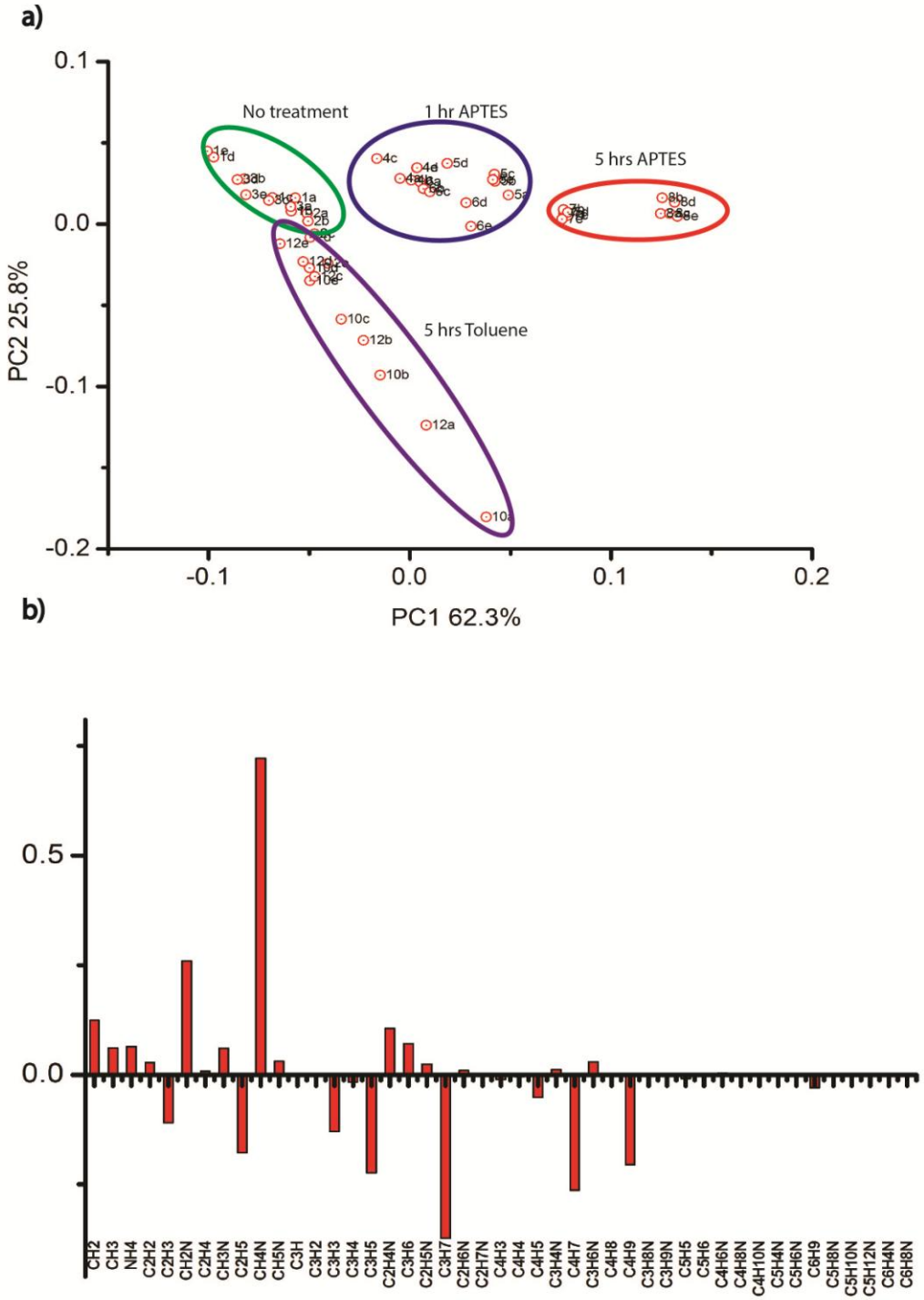

Figure 3C.11: (a) A PCA plot of the +SIMS organic fragments; PC1 contributes 62.3% and PC2 contributes 25.8% of the overall covariance among all sampling spots on F2 fibres. (b) The loading plot for PC1 in the PCA plot of the +SIMS organic fragments

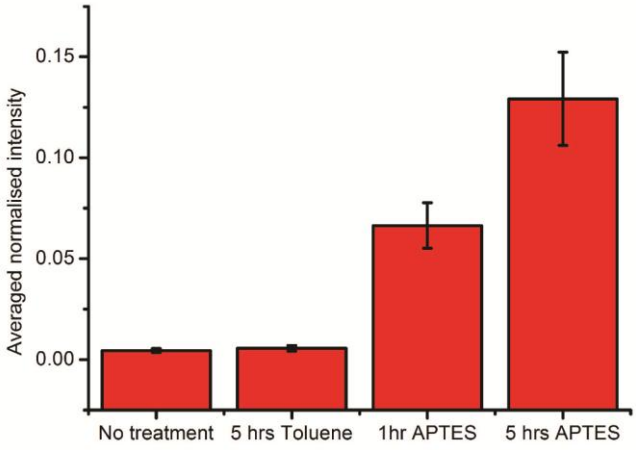

Figure 3C.12: Average normalised intensities of the CH_4N^+ fragments

-SIMS was also performed consecutively after +SIMS. Figure 3C.13a shows the PCA plot of the -SIMS. This PCA analysis covers 99.6% covariance of all data. The cluster of the APTES coated fibre and the controls are separated. However, the cluster of APTES coated F2 slides coated for 1 hour and 5 hours overlap. This indicates that the -SIMS can only separate samples with or without APTES coating, but cannot distinguish the thickness of the APTES coating. Fibres with APTES coating have a positive loading for PC1. The loading plot of PC1 (Figure 3C.13b) shows strong positive loading from CN^-. This is consistent with findings from the literature that show CN^- on APTES coated silicon wafers [22]. The average normalised intensity of CN^- (Figure 3C.14) shows insignificant difference between APTES coatings with different incubation times and hence these cannot be distinguished.

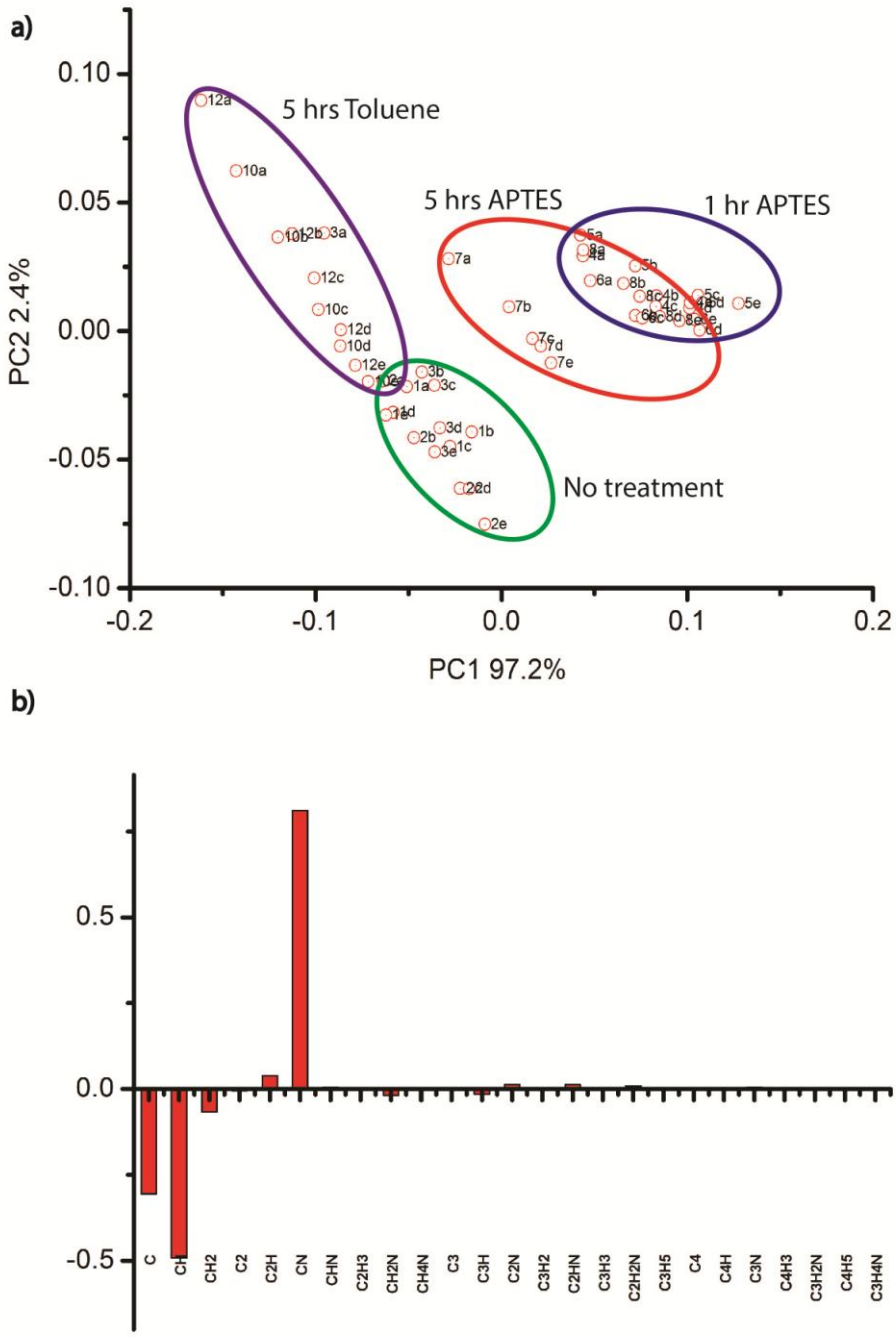

Figure 3C.13: (a) The PCA plot of the -SIMS organic fragments; PC1 contributes 97.2% and PC2 contributes 2.4% of the overall covariance among all the sampling spots on F2 fibre. (b) The loading plot for PC1 in the PCA plot of the -SIMS organic fragments

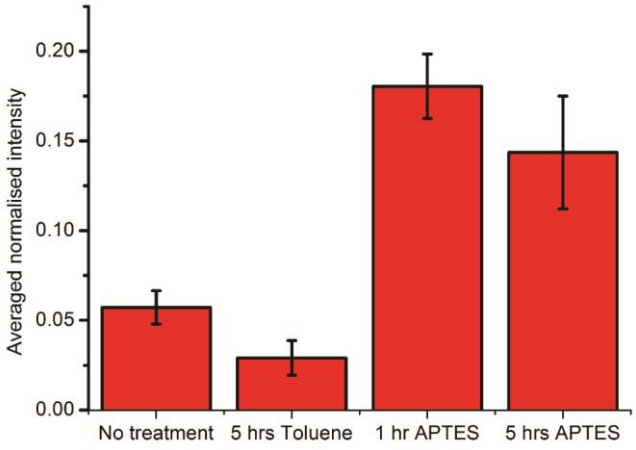

Figure 3C.14: Average normalised intensity of CN^- fragments

Figure 3C.15a shows the PCA analysis of the +SIMS data for sodium, magnesium, aluminium, silicon, potassium, calcium, iron and lead. These elements either originate in the glass or from impurities in the glass. This PCA analysis covers 95.7% total covariance of all data. The PCA analysis shows a clear separation of the data cluster of each control and APTES coated F2 fibre with 1 and 5 hours incubation time. From the PCA analysis, the APTES coated samples have a positive loading in PC1 and a negative loading from PC2. From the loading plot of PC1 (Figure 3C.15b), there are significant positive loadings from silicon and negative loadings from potassium, sodium, aluminium and lead. This is because the APTES layer has higher concentration of silicon compared with the F2 glass substrate; whereas the minor elements in the glass, such as potassium, sodium and lead are much lower in the APTES layer. Figure 3C.16 shows that average normalised ion intensity of sodium, potassium and lead display significant differences between APTES coated fibres and the controls. Moreover, the average normalised intensity of potassium and lead show significant differences for APTES coating with different incubation times and hence likely having different coating thickness.

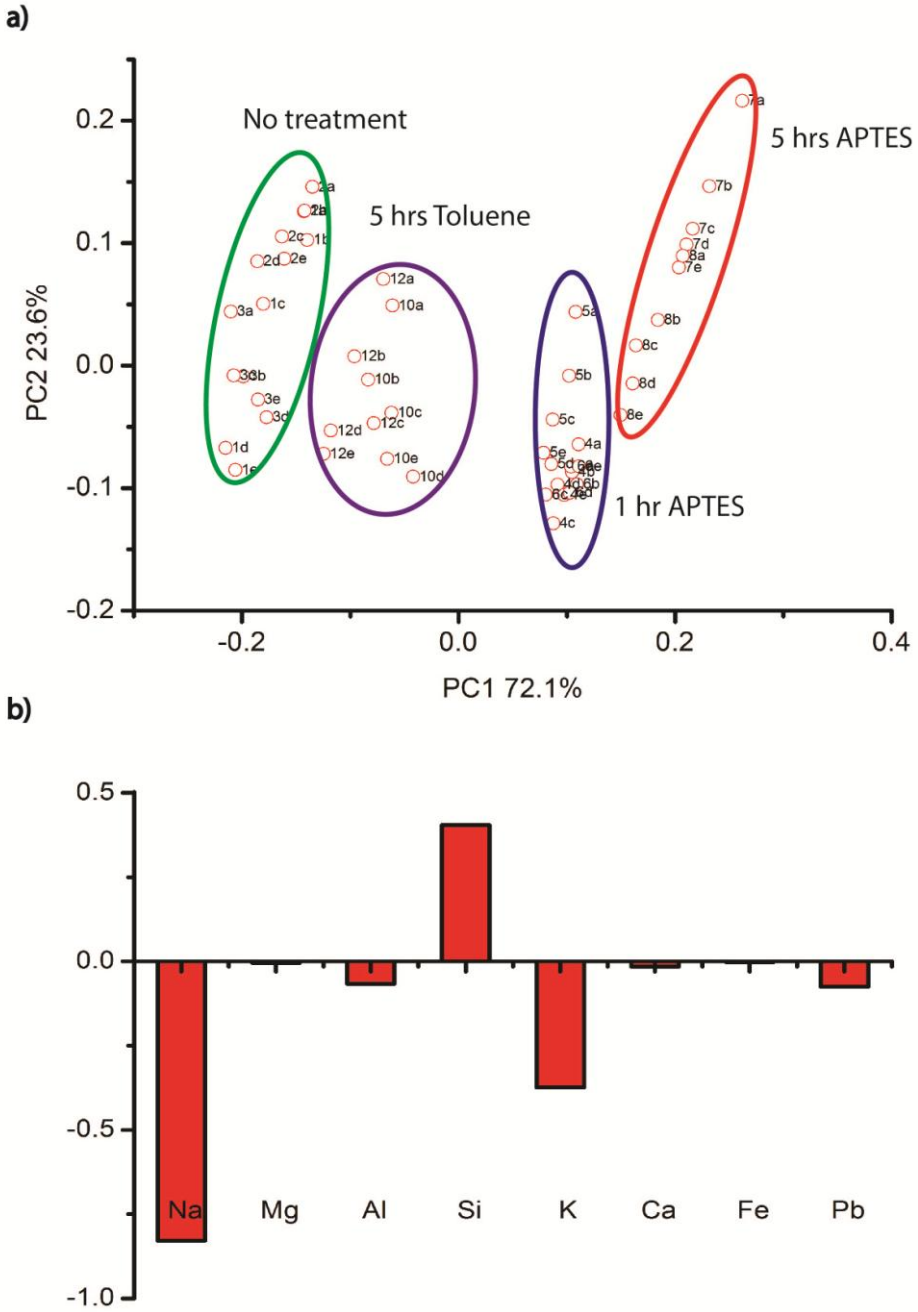

Figure 3C.15: (a) A PCA plot for +SIMS data of the inorganic elements; PC1 contributes 72.1% and PC2 contributes 23.6% of the overall covariance among all sampling spots on F2 fibre. (b) The loading plot for PC1 in the PCA plot of the +SIMS inorganic elements

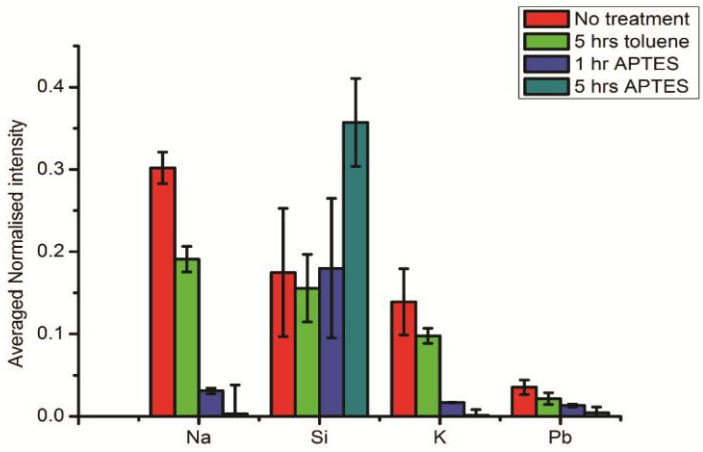

Figure 3C.16: Average normalised intensity of sodium, silicon, potassium and lead ions

3C.4 Conclusions

By applying different surface characterisation methods to APTES coated glass model systems the coating procedure using APTES in toluene was confirmed to be feasible for both silica and F2 glass. This study also showed the methods to characterise the APTES coating, and therefore the surface chemistry, metrology and coating thickness are well understood.

The detection of nitrogen on the silica and F2 glass by X-ray photoelectron spectroscopy (XPS) analysis confirmed the presence of an APTES coating on both glass materials. The nitrogen to silicon ratio measured using XPS indicated that the thickness of the APTES coating on silica glass increases, as expected, as a function of time. These findings corroborate data from the analysis using spectroscopic ellipsometery (SE) on APTES coated silicon wafers which contains an amorphous silica layer. Both findings are consistent with previous literature that shows APTES coating thickness increases with the incubation time [4, 7]. Furthermore the high resolution X-ray photoelectron spectroscopy (HRXPS) analyses showed that the binding energies for C-H, CN/CO, C=O, NH_2 and NH_3^+ on silica and F2 glass are the same as the values reported for APTES coated silica glass or silicon wafer [1, 2]. This result validated the coating procedure using APTES solution in toluene for the rest of the project.

The percentage contribution from free amine groups was higher in the samples with 5 hours APTES incubation compared with samples with 0.5 hours incubation. Since the peptide coupling step requires free amine groups, this suggests that a thicker APTES layer is better for the amide coupling reaction performed in the next step. HRXPS analysis of different thicknesses of APTES layers showed that the percentage of non-bridging oxygen (NBO) significantly increase with the thickness of APTES layer. This is the first XPS evidence for the existence of electrostatics interaction between $Si\text{-}O^-$ and NH_3^+ in the structure of an APTES multilayer.

Despite the similar silanol group density, as discussed in Chapter 3B, the nitrogen and carbon atomic percentages of APTES coated extrused F2 glass slides were significantly lower than that of the APTES coated, Piranha washed silica glass. This result suggested that the glass composition possibly affects the surface attachment of the APTES molecule.

The roughness analyses using AFM showed that an APTES coating does not increase the surface roughness (Sq) of silicon wafers over a 5 hours incubation time. The average Sq of the APTES coated (5 hours incubation) silicon wafer is 0.65 ± 0.02 nm, whereas, the average Sq of the uncoated silicon wafer is 0.66 ± 0.16 nm. This result indicated that our APTES coating procedure should be suitable for SCFs functionalisation, where the surface roughness can contribute to the attenuation of the SCFs.

The APTES coating procedure was also validated for the surface of unstructured F2 fibres. PCA analysis of the ToF-SIMS data for APTES coated F2 fibre showed that +SIMS of the organic and inorganic fragments have clear data clustering for samples with different treatments. Among all the positive fragments analysed, CH_4N^+, K^+ and Pb^+ are characteristic fragments as their average normalised ion intensities are able to distinguish different thicknesses of APTES coating on F2 fibres.

Finally, the surface analyses on the APTES coating on silica glass slides and silicon wafers at different incubation times suggested that when using 5% w/w APTES, the percentage variation of nitrogen and surface roughness with 5 hours incubation is lower than that obtained with 0.5 hours incubation. Furthermore, as

noted above, the percentage of free amine groups is higher in samples with 5 hours of APTES incubation, which is favourable for the peptide coupling reaction. Therefore, the incubation time for the APTES coating deposition in the rest of the project was fixed at 5 hours.

3C.5 References

1. Vandenberg, E.T., Bertilsson, L., Liedberg, B., Uvdal, K., Erlandsson, R., Elwing, H., and Lundstrom, I., *Structure of 3-Aminopropyl Triethoxy Silane on Silicon-Oxide.* Journal of Colloid and Interface Science, 1991. **147**(1): p. 103-118.

2. Acres, R.G., Ellis, A.V., Alvino, J., Lenahan, C.E., Khodakov, D.A., Metha, G.F., and Andersson, G.G., *Molecular Structure of 3-Aminopropyltriethoxysilane Layers Formed on Silanol-Terminated Silicon Surfaces.* Journal of Physical Chemistry C, 2012. **116**(10): p. 6289-6297.

3. Zhu, M.J., Lerum, M.Z., and Chen, W., *How To Prepare Reproducible, Homogeneous, and Hydrolytically Stable Aminosilane-Derived Layers on Silica.* Langmuir, 2012. **28**(1): p. 416-423.

4. Kim, J.Y., Seidler, P., Wan, L.S., and Fill, C., *Formation, structure, and reactivity of amino-terminated organic films on silicon substrates.* Journal of Colloid and Interface Science, 2009. **329**(1): p. 114-119.

5. Cuoq, F., Masion, A., Labille, J., Rose, J., Ziarelli, F., Prelot, B., and Bottero, J.Y., *Preparation of amino-functionalized silica in aqueous conditions.* Applied Surface Science, 2013. **266**: p. 155-160.

6. Pasternack, R.M., Amy, S.R., and Chabal, Y.J., *Attachment of 3-(Aminopropyl)triethoxysilane on Silicon Oxide Surfaces: Dependence on Solution Temperature.* Langmuir, 2008. **24**(22): p. 12963-12971.

7. Howarter, J.A. and Youngblood, J.P., *Optimization of silica silanization by 3-aminopropyltriethoxysilane.* Langmuir, 2006. **22**(26): p. 11142-11147.

8. Kim, J., Holinga, G.J., and Somorjai, G.A., *Curing Induced Structural Reorganization and Enhanced Reactivity of Amino-Terminated Organic Thin Films on Solid Substrates: Observations of Two Types of Chemically and Structurally Unique Amino Groups on the Surface.* Langmuir, 2011. **27**(9): p. 5171-5175.

9. Seitz, O., Fernandes, P.G., Tian, R.H., Karnik, N., Wen, H.C., Stiegler, H., Chapman, R.A., Vogel, E.M., and Chabal, Y.J., *Control and stability of self-assembled monolayers under biosensing conditions.* Journal of Materials Chemistry, 2011. **21**(12): p. 4384-4392.

10. Kamisetty, N.K., Pack, S.P., Nonogawa, M., Devarayapalli, K.C., Kodaki, T., and Makino, K., *Development of an efficient amine-functionalized glass platform by additional silanization treatment with alkylsilane.* Analytical and Bioanalytical Chemistry, 2006. **386**(6): p. 1649-1655.

11. Debs, J.E., Ebendorff-Heidepriem, H., Quinton, J.S., and Monro, T.M., *A Fundamental Study Into the Surface Functionalization of Soft Glass Microstructured Optical Fibers via Silane Coupling Agents.* Journal of Lightwave Technology, 2009. **27**(5-8): p. 576-582.

12. Warren-Smith, S.C., Heng, S., Ebendorff-Heidepriem, H., Abell, A.D., and Monro, T.M., *Fluorescence-Based Aluminum Ion Sensing Using a Surface-Functionalized Microstructured Optical Fiber.* Langmuir, 2011. **27**(9): p. 5680-5685.

13. Metwalli, E., Haines, D., Becker, O., Conzone, S., and Pantano, C.G., *Surface characterizations of mono-, di-, and tri-aminosilane treated glass substrates.* Journal of Colloid and Interface Science, 2006. **298**(2): p. 825-831.

14. Herzinger, C.M., Johs, B., McGahan, W.A., Woollam, J.A., and Paulson, W., *Ellipsometric determination of optical constants for silicon and thermally grown silicon dioxide via a multi-sample, multi-wavelength, multi-angle investigation.* Journal of Applied Physics, 1998. **83**(6): p. 3323-3336.

15. Montalbetti, C.A.G.N. and Falque, V., *Amide bond formation and peptide coupling.* Tetrahedron, 2005. **61**(46): p. 10827-10852.

16. Herder, P., Vagberg, L., and Stenius, P., *Esca and Contact-Angle Studies of the Adsorption of Aminosilanes on Mica.* Colloids and Surfaces, 1988. **34**(2): p. 117-132.

17. Chiang, C.H., Ishida, H., and Koenig, J.L., *The Structure of Gamma-Aminopropyltriethoxysilane on Glass Surfaces.* Journal of Colloid and Interface Science, 1980. **74**(2): p. 396-404.

18. White, L.D. and Tripp, C.P., *Reaction of (3-aminopropyl)dimethylethoxysilane with amine catalysts on silica surfaces.* Journal of Colloid and Interface Science, 2000. **232**(2): p. 400-407.

19. Leach, R., Brown, L., Jiang, X., Blunt, R., Conroy, M., and Mauger, D., *Measurement Good Practice Guide No. 108, Guide to the Measurement of Smooth Surface Topography using Coherence Scanning Interferometry*, N.P. Laboratory, Editor. 2008, : Middlesex.

20. Synowicki, R.A., *Suppression of backside reflections from transparent substrates.* Physica Status Solidi C - Current Topics in Solid State Physics, Vol 5, No 5, 2008. **5**(5): p. 1085-1088.

21. Flink, S., van Veggel, F.C.J.M., and Reinhoudt, D.N., *Functionalization of self-assembled monolayers on glass and oxidized silicon wafers by surface reactions.* Journal of Physical Organic Chemistry, 2001. **14**(7): p. 407-415.

22. Samha, H., Linford, M., Zhang, F., Davis, R., and Sautter, K., *Chemical vapor deposition of three aminosilanes on silicon dioxide: Surface characterization, stability, effects of silane concentration, and cyanine dye adsorption.* Abstracts of Papers of the American Chemical Society, 2011. **241**.

3D. Surface characterisation of 11-aminoundecyltriethoxysilane (AUTES) coated silica glass slides and silicon wafers

3D.1 Introduction

In Chapter 3C, a description of the challenges of reproducibly applying 3-aminopropyltriethoxysilane (APTES) coatings on silica and lead silicate (F2) glass materials was provided. The observed inconsistencies are due to uncontrollable multilayer formation of the APTES coating in the presence of water. This can arise either as a solvent, or in the work presented here, as an impurity introduced through the reagents or the glass surface. In addition, APTES coatings have been shown to be unstable in an aqueous environment, owing to the hydrolysis of the Si-O-Si linkage in the APTES [1-3]. The hydrolysis of the APTES coating introduces further variations and may restrict their application for surface functionalised SCF sensors.

The stability of APTES on silica has a strong pH dependency. Etienne *et al.* showed that the stability of the APTES coating on silica at pH 1 is higher than pH 5.7. APTES coatings showed the lowest stability in pure water [3]. This is because Si-O-Si bond is susceptible to nucleophilic attack by the free amine groups on APTES in the presence of water. This reaction is particularly favourable for APTES because it forms a stable five-membered cyclic intermediate. The mechanism is shown in Figure 3D.1 [3, 4]. APTES is known to have better stability in an acidic environment as the ammonium ion at the end of the APTES cannot act as a nucleophile. The coating stability is particularly important for SCF sensors that are used for continuous analyte monitoring purposes.

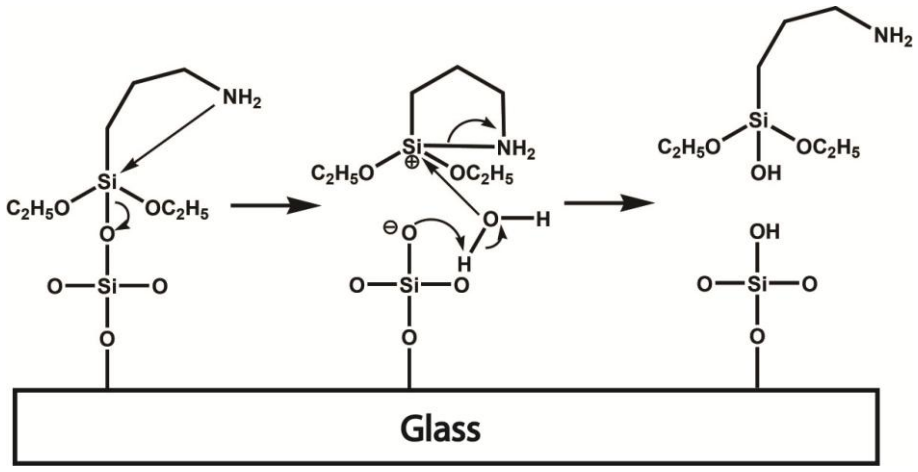

Figure 3D.1: A mechanism of APTES hydrolysis

11-Aminoundecyltriethoxysilane (AUTES) (Figure 3D.2) is an aminosilane with an 11 carbon aliphatic chain, that has potential to be a better primary coating agent for glass surface functionalisation. Using spectroscopic ellipsometery (SE) and IR absorption measurement, Seitz *et al.* showed that the variation of the composition and thickness of the APTES is higher than AUTES on a silicon wafer surface [5]. Using 3-(trimethoxysilyl)propyl aldehyde (C4-ald) and 11-(triethoxysilyl)undecanal (C11-ald) as models for APTES and AUTES respectively, Seitz *et al.* also revealed that C11-ald has a higher stability in buffer solutions compared with C4-ald. AUTES has a long hydrocarbon chain that provides steric hindrance to vertical surface polymerisation. The long hydrocarbon chain of AUTES also inhibits self polymerisation during solution attachment to a surface. In addition, the hydrophobic chain-chain interaction between grafted AUTES molecules can stabilise the layer and introduce a driving force to favour horizontally polymerised AUTES layers [5]. This ordered surface coating has a relatively lower inconsistency compared with APTES [5]. Furthermore, the long hydrocarbon chain enhances the stability of the coating by reducing the ability of water molecules to access the silica-AUTES interface [5], and the long hydrocarbon chain reduces the chance of nucleophilic attack by free amines on the Si-O-Si bonds at the interface [1, 3].

The aim of the following study is to understand the composition, chemical bonding and surface roughness of the AUTES coating on both silica glass slides and silicon wafers to explore the feasibility of using AUTES as the substitute of

APTES for the surface attachments of fluorophores. The surface elemental composition (as atomic percentages) and the chemical bonding of the AUTES coating were measured by X-ray photoelectron spectroscopy (XPS) on silica glass. The surface roughness of the AUTES coating on silicon wafers was measured by AFM.

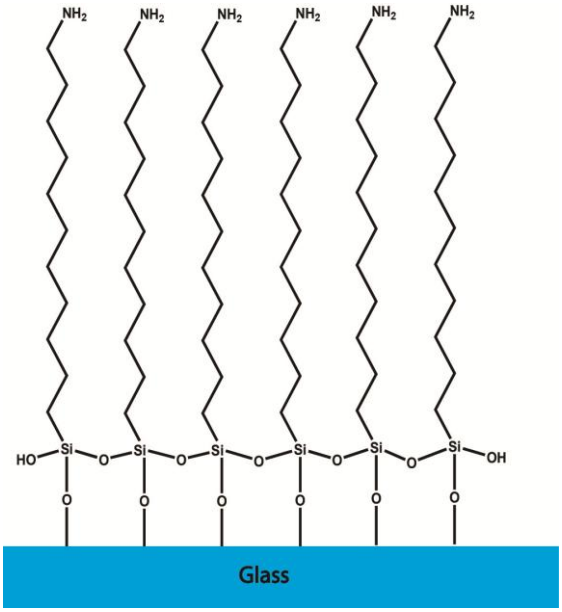

Figure 3D.2: The expected structure of AUTES on a glass surface

3D.2 Experimental

3D.2.1 Preparation of substrates

This measurement procedure used was identical to that described in Chapter 3B, Section 3B.2.1.

11-Aminoundecyltriethoxysilane (AUTES) grafting procedure for glass slides and wafers

Each cleaned glass slide or silicon wafer was placed in an individual vial and incubated in 5 % w/w AUTES in anhydrous toluene (< 4 mL) for either 0.5 or 5 hours in a desiccator. The slides were washed with toluene (< 4 mL), dried under vacuum for at least 2 hours before washing with deionized water (< 4 mL). The AUTES coated slides were dried overnight at room temperature under vacuum before any surface analysis. Ultrasonic cleaning was avoided during all coating

procedures since this cleaning step can break the SCF and, therefore, is not transferable to SCF functionalisation.

3D.2.2 Methods of surface analysis

X-ray photoelectron spectroscopy (XPS) measurements

This measurement procedure used was identical to that described in Chapter 3B, Section 3B.2.3.

Atomic force microscopy (AFM) measurement and data analysis

This measurement procedure used was identical to that described in Chapter 3C, Section 3C.2.2.

3D.3 Results and discussion

The existence of nitrogen from the XPS elemental analysis confirms that AUTES was deposited on the silica glass slides (Figure 3D.3a). Unlike APTES, the elemental composition of all the elements on AUTES did not change significantly between 0.5 and 5 hours incubation, indicating that the AUTES layer has no significant multi-layer growth at least within 5 hours for the conditions used. The Si:N ratio (Figure 3D.3b) shows no significant difference for the two incubation times, which further confirms that the thickness of the coating are similar. This is an advantage over APTES since the coating thickness is less susceptible to the incubation time variations. Using the same analysis procedure as described in Chapter 3C, the high resolution X-ray photoelectron spectroscopy (HRXPS) spectra of carbon, nitrogen, oxygen and silicon from the AUTES coated silica glass slides with 0.5 and 5 hours incubation time are separated into two to three components. They are listed as follows.

- CH, CN/CO and C=O for carbon
- BO, NBO and OH/CO for oxygen
- Si 3/2 and Si 1/2 for silicon
- NH_2 and NH_3^+ for nitrogen

The average binding energy and average percentage contribution of each component of APTES and AUTES coated silica glass slides with 0.5 and 5 hours of incubation time are summarised in Tables 1 and 2 in Chapter 3 Appendix. The binding energy of each component in APTES and AUTES for both 0.5 and 5 hours incubation time are within experimental error; either very close or the same. This is as expected because the only difference between APTES and AUTES is the length of the aliphatic carbon chain. The differences in the percentage contribution of each carbon component in APTES and AUTES for the two incubation durations are statistically insignificant. This is possibly due to the major source of carbon on APTES and AUTES coated glass slides being the adventitious hydrocarbon; such that the coating only contributes a minor content of hydrocarbon. Therefore, the difference in the percentage contribution of each carbon component (CH, CN/CO and C=O) between APTES and AUTES are masked by the variation of the composition of the adventitious hydrocarbons.

The percentage contribution of NBOs in AUTES shows no significant difference for 0.5 and 5 hours incubation time. In contrast, the percentage contribution of NBOs for the APTES coated silica glass with 5 hours incubation is significantly higher than that for the APTES with 0.5 hours incubation. The NBOs percentage for the APTES coated silica glass is also higher than the in AUTES coated silica glass with 5 hours incubation time. This result indicates that there was less multilayer formation on AUTES coated silica glass compared with APTES. As expected, the multilayer formation of AUTES is inhibited because the long hydrocarbon chain favours an aligned orientation and therefore only head-to-head or head-to-tail arrangements are favoured. However, horizontal polymerisation can only occur when they are in a head-to-head orientation; thus AUTES only polymerises in one principal orientation.

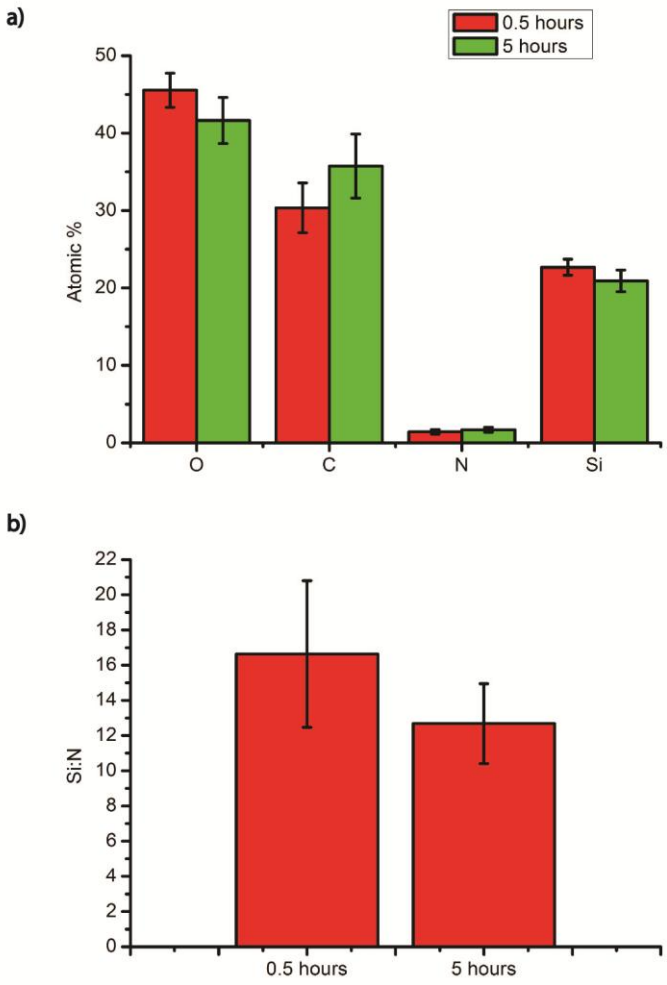

Figure 3D.3: (a) A XPS elemental analysis of AUTES coated silica glass slides. (b) The Si:N ratio of the AUTES coated silica glass slides with 0.5 and 5 hours incubation

AFM analysis shows obvious aggregates on the AUTES coated silicon wafer after 5 hours incubation (Figure 3D.4a). These micron size aggregates have a height of over 100 nm and were observed on all wafer samples with 5 hours incubation (Figure 3D.4b). It is believed that these aggregates are the AUTES residue, which cannot be washed off after the washing procedure using toluene and water. This residue cannot be detected by XPS since the sampling depth of XPS is only ~ 10 to 15 nm. Therefore the XPS data is in fact the surface of the aggregates. These aggregates were visible to the naked eye and looked like fingerprint stains on the wafer; this feature was also present on all the wafer samples with 0.5 hours incubation. Based on the literature procedure [5], AUTES coated wafers required

ultrasonic cleaning to remove the AUTES residue. However, ultrasonic cleaning is not feasible in SCFs because it is likely to damage the fibre.

The average root mean square surface roughness (Sq) of a 1 x 1 µm area, which has no aggregates, for 3 AUTES coated silicon wafers is 0.8 ± 0.1 nm. The average Sq of the AUTES coated wafer is slightly higher than that of the APTES coated wafer with 5 hours incubation (0.65 ± 0.02).

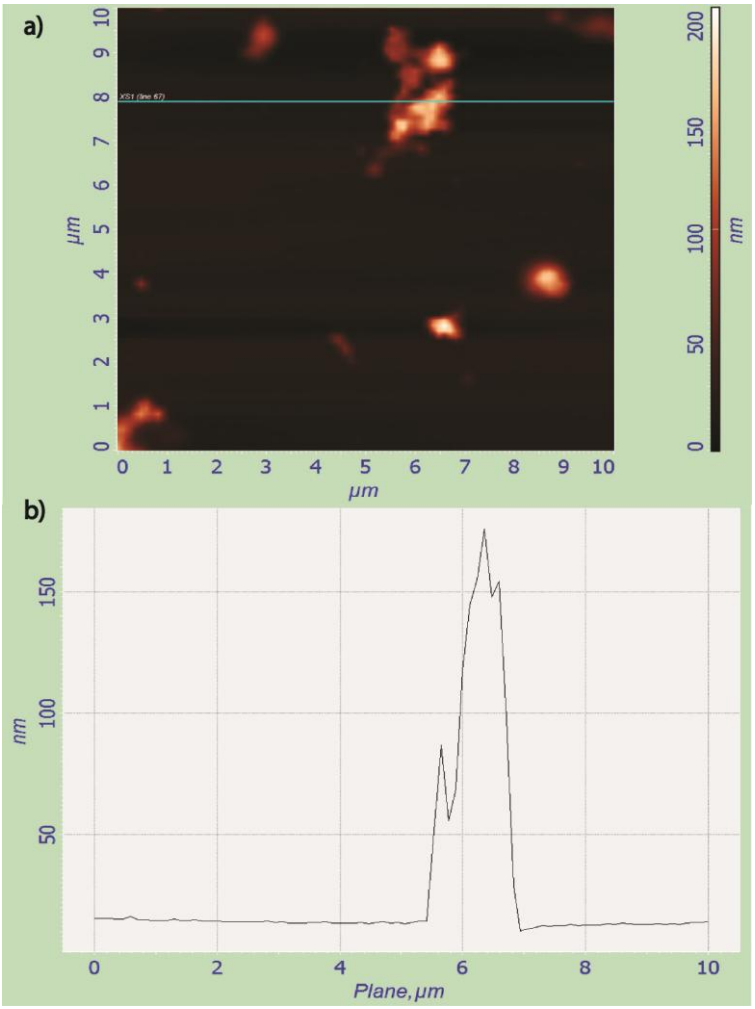

Figure 3D.4: (a) An AFM image (10 x 10 µm) of an AUTES coated silicon wafer with 5 hours incubation. (b) An example of a traverse section across a wafer showing that the maximum vertical height of this particular aggregate is 177 nm

3D.4 Conclusions

This study reported the AUTES coating of silica glass slides and silica wafers in the absence of ultrasonic cleaning. The average nitrogen atomic percentages and the average percentage contributions of NBOs showed no difference between samples with 0.5 and 5 hours incubation times. These results suggest that there is limited multilayer formation, which agrees with results from literature [5]. However, micron size aggregates were observed using AFM analysis, which are likely to be caused by AUTES residues. As the ultrasonic cleaning step typically applied when using AUTES cannot be performed for SCFs [5], a new washing procedure needs to be found before applying AUTES to the SCF functionalisation.

3D.5 References

1. Smith, E.A. and Chen, W., *How to Prevent the loss of surface functionality derived from aminosilanes.* Langmuir, 2008. **24**: p. 12405-12409.

2. Zhu, M.J., Lerum, M.Z., and Chen, W., *How To Prepare Reproducible, Homogeneous, and Hydrolytically Stable Aminosilane-Derived Layers on Silica.* Langmuir, 2012. **28**(1): p. 416-423.

3. Etienne, M. and Walcarius, A., *Analytical investigation of the chemical reactivity and stability of aminopropyl-grafted silica in aqueous medium.* Talanta, 2003. **59**(6): p. 1173-1188.

4. Cuoq, F., Masion, A., Labille, J., Rose, J., Ziarelli, F., Prelot, B., and Bottero, J.Y., *Preparation of amino-functionalized silica in aqueous conditions.* Applied Surface Science, 2013. **266**: p. 155-160.

5. Seitz, O., Fernandes, P.G., Tian, R.H., Karnik, N., Wen, H.C., Stiegler, H., Chapman, R.A., Vogel, E.M., and Chabal, Y.J., *Control and stability of self-assembled monolayers under biosensing conditions.* Journal of Materials Chemistry, 2011. **21**(12): p. 4384-4392.

Chapter 3 Appendix: Supplementary information

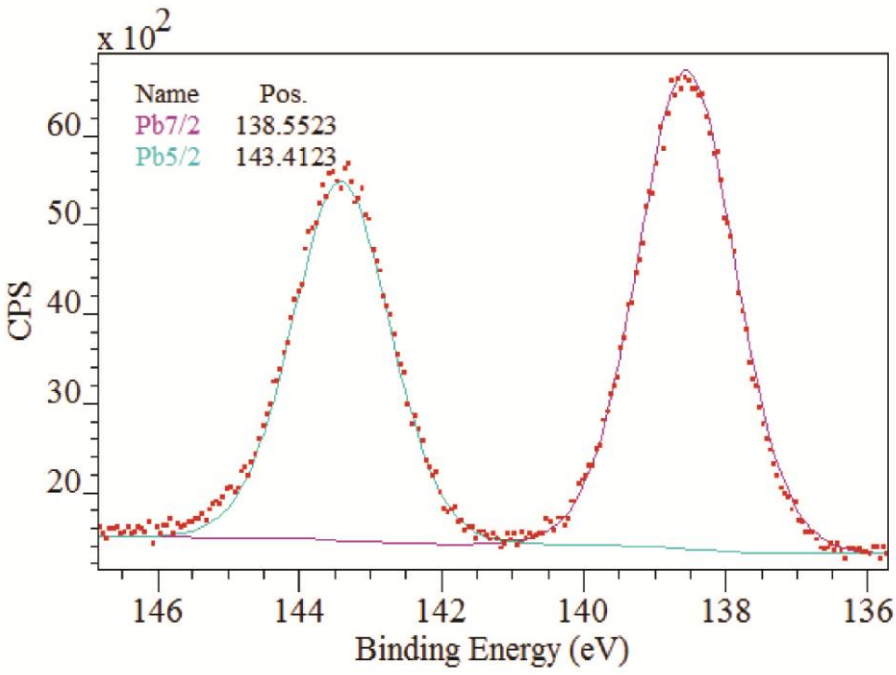

Figure 3.I: A HRXPS spectrum of the Pb 4f on F2 glass

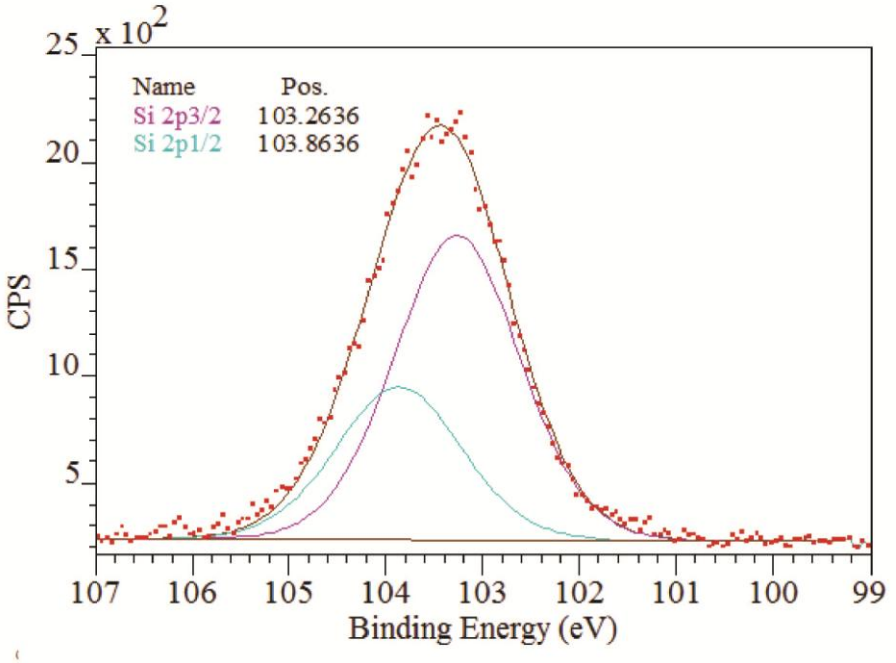

Figure 3.II: A HRXPS spectrum of Si 2p on silica glass slide

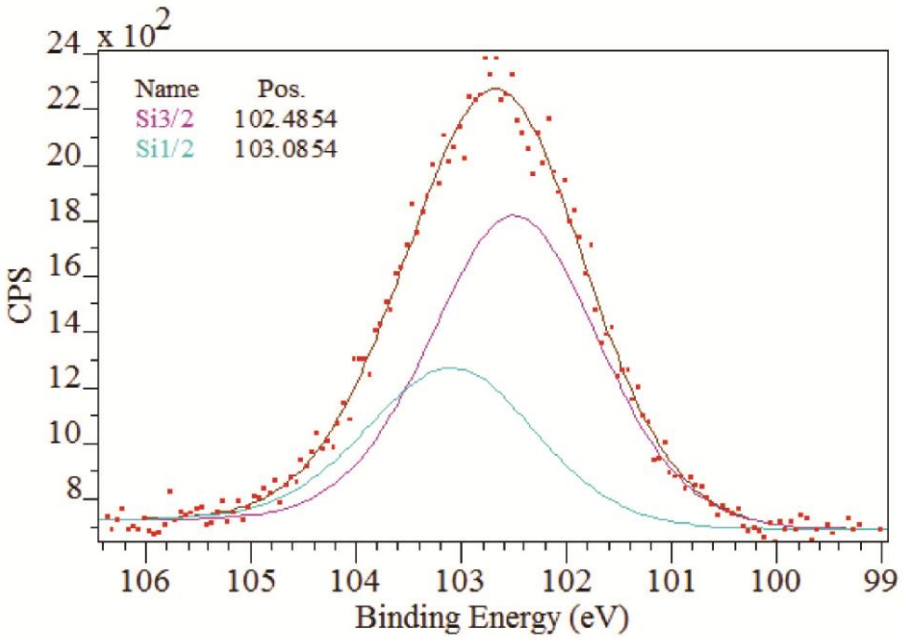

Figure 3.III: A HRXPS spectrum of Si 2p for F2 glass slide

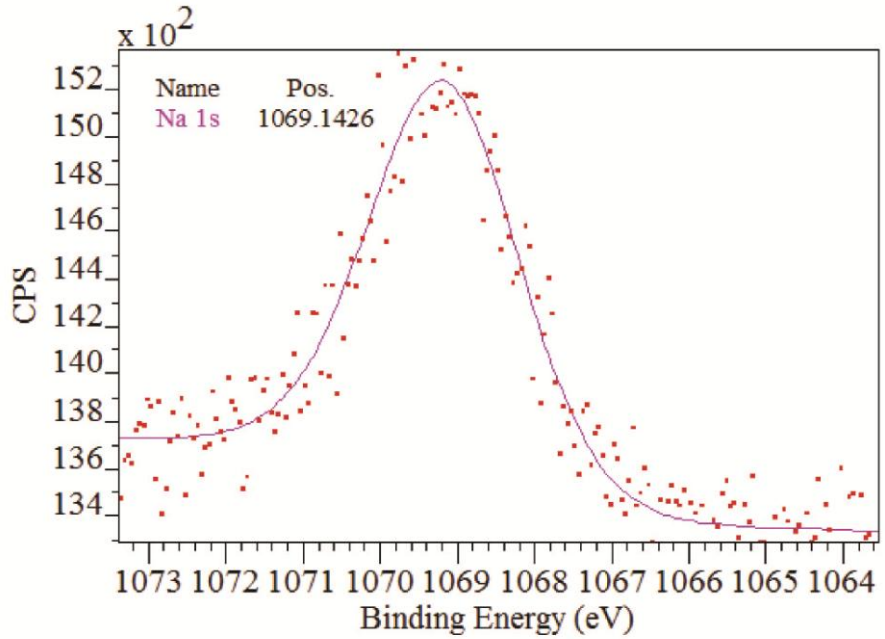

Figure 3.IV: A HRXPS spectrum of sodium 1s on F2 glass slide

Table 3.I: Average binding energies and average percentage contributions of the separated peaks from the deconvolution of the HRXPS spectra of oxygen, carbon, nitrogen and silicon of the APTES and AUTES coating with 0.5 hours incubation time

	APTES		AUTES	
	Binding energy /eV	Percentage contribution	Binding energy/eV	Percentage contribution
BO	532.6 ± 0.0	91.5 ± 1.8	532.6 ± 0.0	93.4 ± 0.6
NBO	530.7 ± 0.2	4.2 ± 0.6	530.8 ± 0.1	3.5 ± 076
OH/CO	534.3 ± 0.1	4.4 ± 2.0	534.5 ± 0.1	3.1 ± 0.3
CH	285.0 ± 0.1	84.1 ± 4.9	284.8 ± 0.0	82.2 ± 1.7
CN/CO	286.5 ± 0.1	12.2 ± 4.1	286.3 ± 0.0	13.8 ± 1.4
C=O	288.0 ± 0.1	3.7 ± 1.6	287.8 ± 0.0	3.9 ± 1.2
NH_2	399.5 ± 0.2	50.6 ± 9.7	399.3 ± 0.2	69.6 ± 6.7
NH_3^+	401.6 ± 0.2	49.4 ± 9.7	401.7 ± 0.3	30.4 ± 6.7
Si3/2	103.3 ± 0.1	N/A	103.3 ± 0.0	N/A
Si1/2	103.9 ± 0.1	N/A	103.9 ± 0.0	N/A

Chapter 4

Surface analysis of photoinduced electron transfer (PET) fluoroionophores on a lead silicate glass model system

4.1 Introduction

As discussed in Chapter 3, a major challenge in advancing the surface attachment chemistry in the voids within SCFs is the lack of characterisation techniques for quantitatively analysing the chemical homogeneity, roughness, coverage, thickness of the coating and fluorophore density. All these parameters are crucial for determining the dynamic range and sensitivity of SCF sensors as well as ensuring the reproducibility during the sensor fabrication. The quantifications of those coating parameters are also important for understanding the optimisation of the surface immobilisation procedure, which takes place in a constrained volume within the fiber. As described in Chapter 3, extruded glass slides can serve as a model glass platform that mimics the glass chemistry of the fire-polished surface of SCFs and more importantly it allows various types of surface analysis.

In this chapter, the chemistry used to attach PET fluoroionophores on APTES grafted lead silicate (F2) glass slides by standard peptide coupling reagents at room temperature (Figure 4.1) is described. The APTES coating and peptide coupling procedures developed on slides are transferrable to SCFs. The coatings of the slides were analysed by the fluorescence imaging, XPS, ToF-SIMS, ToF-SIMS imaging and ToF-SIMS depth profiling. Each analysis technique provides complementary information for semi-quantitative determinations of the surface concentration, relative coating thickness, and coating coverage of organic molecules. Information regarding the fluoroionophore surface concentration,

relative coating thickness and coating coverage on fire-polished F2 glass surfaces is discussed.

Although SCFs made from silica glass were used later to demonstrate the SCF sensing with the surface attached fluoroionophores, F2 glass was the only available option for the SCF sensing in this project. Therefore, F2 glass became the only glass substrate studied by the approach discussed in this chapter.

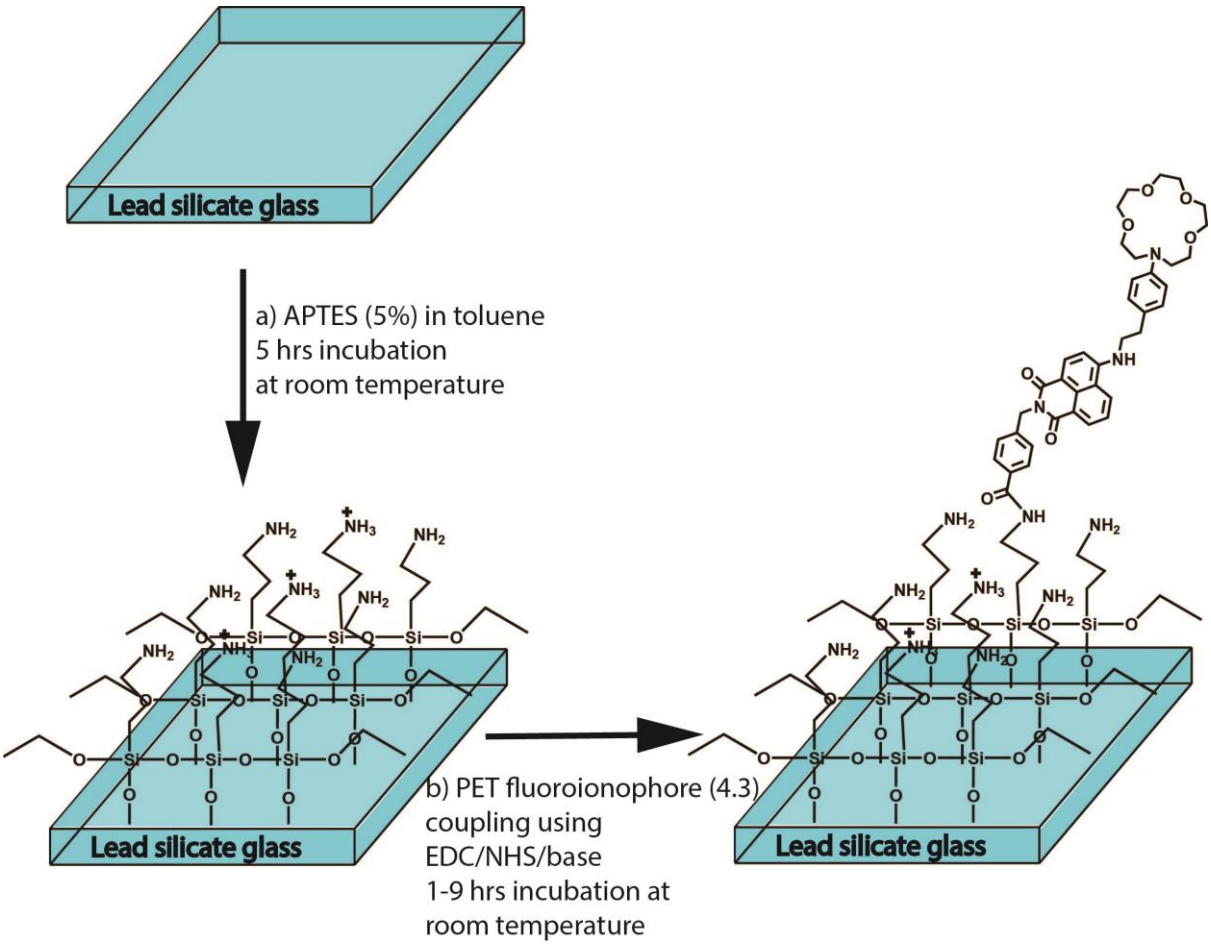

Figure 4.1: The PET fluoroionophore coating procedure in this project (a) Fire-polished glass slides were incubated in an APTES solution (5% w/w) for 5 hours at room temperature; (b) PET fluoroionophores coupling on APTES grafted glass slides for 1-9 hours at room temperature

4.2 Experimental

4.2.1 Preparation of lead silicate (F2) slides

The procedure is the same as section 3B.2.2 in Chapter 3B

4.2.2 Synthesis of the model fluoroionophore derivatives

The general experimental procedures pertaining to synthesis were described in Chapter 2. The synthesis of **2.7** was described in Chapter 2.

Synthesis of *t*-butyl-4-chloro-1,8-naphthalimidylmethyl benzoate (4.1)

4-Chloro-*N*-(4-carboxyphenylmethyl)-1,8-naphthalimide and *t*-butyl-4-chloro-1,8-naphthalimidylmethyl benzoate **4.1** were prepared by literature procedures reported by He *et. al.* [1].

4-Chloro-1,8-naphthalic anhydride (**2.1)** (10.00 g, 0.043 mol), 4-(aminomethyl)benzoic acid (6.498 g, 0.043 mol) and potassium carbonate (2.972 g, 0.0215 mol) were suspended in DMF (350 mL) and stirred at room temperature for 19 hrs and then stirred at 60°C for 7 hrs. The reaction mixture was poured into water and the pH adjusted to be in the range 2 to 4 with 1M aqueous HCl solution. The precipitate was collected via filtration and dried under high vacuum at room temperature to remove residual solvent. The resulting off-white solid (4-chloro-*N*-(4-carboxyphenylmethyl)-1,8-naphthalimide) (12.91 g, 0.0353 mol, 82%) was used in the next step without purification. m.p. over 300 °C. ^{1}H NMR (300 MHz, DMSO-d_6) δ 8.56 - 8.63 (m, 2H), 8.43 (d, *J* = 7.69 Hz, 1H), 7.96 - 8.07 (m, 2H), 7.83 - 7.91 (m, 2H), 7.41 - 7.52 (m, 2H), 5.24 - 5.32 (m, 2H).

4-Chloro-*N*-(4-carboxyphenylmethyl)-1,8-naphthalimide (5.49 g, 150 mmol) was stirred in DMF (150 mL) under nitrogen and then 1,1-carbonyldiimidazole (CDI) (9.75 g, 60.13 mmol) was added into the reaction mixture and stirred for 15 mins. *t*-butyl alcohol (29 mL, 303.2 mmol) and 1,8-diazabicyclo[5.4.0]-undec-7-ene (DBU) (9 mL, 60.18 mmol) were added into the mixture. The mixture was stirred at 60°C for 16 hrs. The reaction mixture was poured into ice-cold 1 M HCl solution (250 mL) and the precipitate was filtered. The precipitate was washed with 1 M HCl (2 x 50 mL) and dried under high vacuum at room temperature for

at least 24 hrs to yield brown solid. The crude product was purified by silica gel column with chloroform to obtain white powder of **4.1** (2.41 g, 5.71 mmol, 38%). m.p. 193 – 195°C ; ^{1}H NMR (300 MHz, $CDCl_3$) δ 8.68 (dd, *J* = 1.24, 7.28 Hz, 1H), 8.62 (dd, *J* = 1.10, 8.52 Hz, 1H), 8.52 (d, *J* = 7.97 Hz, 1H), 7.81 - 7.96 (m, 3H), 7.55 (d, *J* = 8.52 Hz, 2H), 5.41 (s, 2H), 1.54 - 1.57 (m, 9H). (Literature ^{1}H NMR (300 MHz, $CDCl_3$) δ 7.45-8.60 (m, 9H, ArH), 5.30 (s, 2H, Ar CH2), 1.50 (s, 9H, t-BuH)) [1]

Synthesis of N-(*t*-butyl-benzonate)-[4-(aza-15-crown-5)-phenylethylamino]-1,8-naphthalimide (4.2)

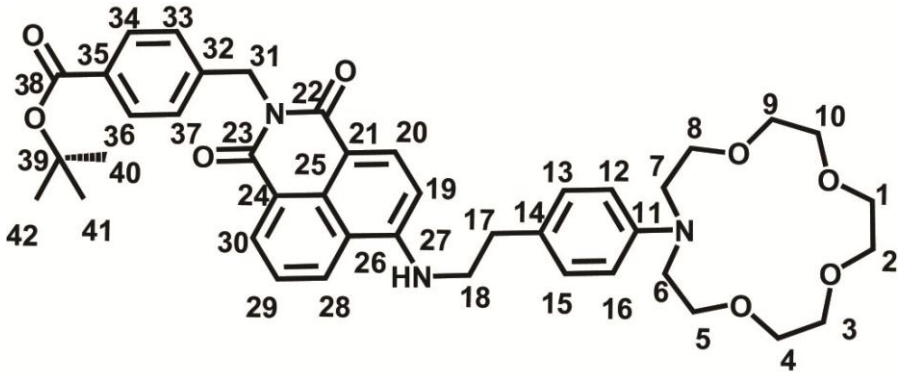

Compounds **4.1** (429 mg, 1.02 mmol), **2.7** (683 mg, 2.02 mmol) and *N*,*N*-diisopropylethylamine (DIPEA) (445 μL, 2.55 mmol) were dissolved in *N*-methyl-2-pyrrolidone (NMP) (20 mL) in a CEM ^{TM} reaction tube. The tube was sealed and heated at 100°C under microwave irradiation for 5 hours. NMP was removed by distillation under reduced pressure at 50 - 60°C and the crude product was dried at ~50°C under high vacuum. Purification on silica gel with 1:1 ethyl acetate: chloroform eluate afforded an orange yellow crude product which was triturated with ethylacetate/ hexane to yield (203 mg, 0.281 mmol, 28%) of **5** as orange-yellow crystals. m.p. 132 – 134°C. ^{1}H NMR (600 MHz, $CDCl_3$) δ 8.57 (d, *J* = 7.02 Hz, 1H, H30), 8.48 (d, *J* = 8.19 Hz, 1H, H20), 7.93 (d, *J* = 8.19 Hz, 1H, H28), 7.90 (d, *J* = 8.19 Hz, 2H, H34 and H36), 7.56 - 7.61 (m, 1H, H29), 7.54 (d, *J* = 8.19 Hz, 2H, H33 and H37), 7.10 (d, *J* = 8.19 Hz, 2H, H13 and H15), 6.77 (d, *J* = 8.78 Hz, 1H, H19), 6.65 (d, *J* = 8.78 Hz, 2H, H12 and H16), 5.39 (s, 2H, H31), 5.33 (br. s., 1H, NH), 3.55 - 3.79 (m, 23H, aza-15-crown-5 and H18), 2.99

(t, *J* = 6.73 Hz, 2H, H15), 1.55 (s, 9H, t-butyl ester). ^{13}C NMR (151 MHz, $CDCl_3$) δ 165.7 (C35), 164.6 (C22), 164.0 (C23), 149.5 (C11), 146.7 (C27), 142.5 (C32), 134.8 (C20), 131.4 (C30), 130.9 (C35) , 129.9 (C25), 129.6 (C13 and C15, C34 and C36), 128.3 (C33 and C37), 126.1 (C28), 124.7, 124.6 (C14), 123.0 (C24), 120.3 (C26), 111.8 (C12 and C16), 110.1 (C21), 104.6 (C27), 80.7 (C38), 71.3(aza-15-crown-5), 70.2(aza-15-crown-5), 70.1(aza-15-crown-5), 68.6(aza-15-crown-5), 52.5 (C18), 44.7 (aza-15-crown-5), 43.1 (C31), 33.7 (C17), 28.2 (C40-C42). UATR FTIR (Diamond/ZnSe) υ/cm^{-1} 3360, 2862, 1715, 1683, 1632, 1616, 1589, 1573, 1537, 1523. MS (ESI, +ve mode) *m/z* 724.2 ($[M + H]^+$, 100 %), 725.2 (43 %), 746.2 ($[M + Na]^+$, 28 %), 747.2 (11 %). HRMS (ESI) *m/z* found 724.35913, $[C_{42}H_{49}N_3O_8 + H]^+$ required 724.35924.

Synthesis of 4-[4'-[4''-C-(aza-15-crown-5)-phenylethylamino]-1', 8' naphthalimidylmethyl] Benzoic Acid (4.3)

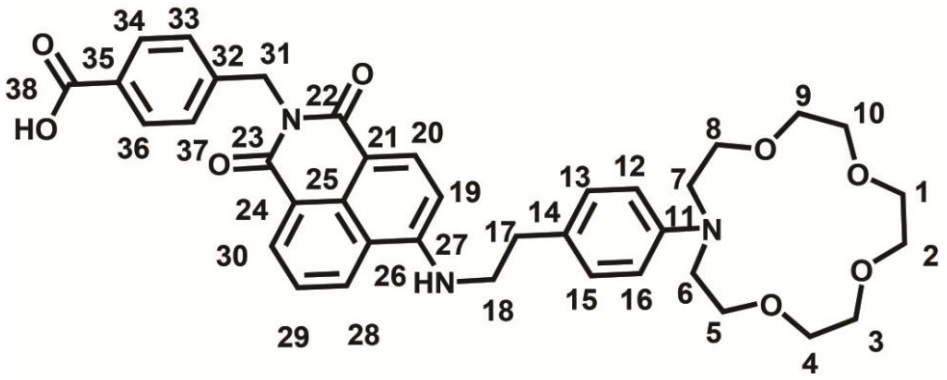

Trifluoroacetic acid (TFA) (2 mL) was added to **4.2** (80 mg, 0.11 mmol) dissolved in dichloromethane (8 mL). The mixture was stirred at room temperature for 1 hr. The solution was diluted with chloroform and the solvent was evaporated. The residue was redissolved in methanol/chloroform mixture (1:9, 50 mL) and the solvent evaporated. The process was performed three times. The residue was dissolved in methanol/chloroform mixture (1: 9) again and washed with 5% TFA solution (50 mL x 2). The organic phase was dried with $MgSO_4$ and the solvent was removed. The crude product was triturated with ethyl acetate/hexane to yield **4.3** as yellow crystals (64 mg, 0.096 mmol, 90%). m.p. 180 – 183°C. ^{1}H NMR (600 MHz, DMSO-d_6) δ 8.70 (d, *J* = 8.20 Hz, 1H, H28), 8.44 (d, *J* = 7.03 Hz, 1H, H20), 8.28 (d, *J* = 8.20 Hz, 1H, H30), 7.92 (s, 1H, NH), 7.85 (d, *J* = 8.79 Hz, 2H,

H34/36), 7.68 (t, 1H, *J* = 8.2 Hz, 1H, H29), 7.40 (d, *J* = 8.20 Hz, 2H, H33/H37), 7.08 (d, *J* = 8.20 Hz, 2H, H13/H15), 6.85 (d, *J* = 8.79 Hz, 1H, H19), 6.56 (d, *J* = 8.79 Hz, 2H, H12/H16), 5.26 (s, 2H, H31), 3.40 - 3.66 (m, 23H, aza-crown and H18), 2.86 (t, *J* = 7.62 Hz, 2H, H17). ^{13}C NMR (151 MHz, DMSO-d_6) δ 167.5 (C35), 164.3 (C21), 163.3 (C24), 151.2 (C25), 146.4 (C11), 143.4 (C32), 135.1 (C30), 131.5 (C20), 130.1, 130.0, 129.9, 129.3 (C28), 127.8 (C33/C37), 125.9 (C14), 124.8 (C29), 122.1 (C24), 120.7 (C26), 111.7 (C13/C15), 107.7, 104.6 (C19), 70.8 (aza-crown and C18), 69.9 (aza-crown and C18), 69.5 (aza-crown and C18), 68.4 (aza-crown and C18), 52.3 (C18), 45.4 (C31), 33.4 (C17). UATR FTIR (Diamond/ZnSe) υ/cm^{-1} 3359, 2971, 2948, 2885, 2646, 1737, 1718, 1682, 1635, 1616, 1570, 1544, 1521. MS (ESI, +ve mode) *m/z* 668.3 ($[M + H]^+$, 100 %), 669.3 (36 %). HRMS (ESI) *m/z* found 668.29662, $[C_{38}H_{41}N_3O_8 + H]^+$ required 668.29664.

4.2.3 Surface functionalisation procedures

3-Aminopropyltriethoxysilane (APTES) grafting procedure

Each cleaned slide was placed in an individual vial and incubated in 5% w/w APTES in anhydrous toluene (< 4 mL) for 5 hours in a desiccator. The slides were washed with toluene (< 4 mL), dried under vacuum for at least 2 hours, before washing with deionized water (< 4 mL). The APTES coated slides were dried overnight before treatment with fluorophores **4.2**, **4.3** or **2.8**.

PET fluoroionophore (4.3) amide coupling

Each cleaned APTES coated slide was placed in an individual vial and incubated in 2 mL THF/water (9:1) solution with **4.3** (0.1 mM, 1 eq.), 1-ethyl-3-(3-dimethylaminopropyl) carbodiimide (EDC) (0.5 mM, 5 eq.), N-hydroxysuccinimide (NHS) (0.5 mM, 5 eq.) and triethylamine (0.15 mM, 1.5 eq.). The incubation was performed at room temperature for 1 – 9 hours. Control experiments of slides, which have fluoroionophore **4.3** without either EDC, EDC and NHS or EDC, NHS and base, were performed at the same time. After incubation, slides were rinsed with THF (< 4 mL × 2), pH 5 potassium hydrogen phthalate buffer solution (< 4 mL × 2) and finally DI water (< 4 mL × 2). The cleaned slides were dried under vacuum overnight.

PET fluoroionophore (2.8, 4.2 and 4.3) non-covalent attachment

Each cleaned APTES coated slides was placed in an individual vial and incubated in 2 mL THF/water (9:1) solution with **2.8**, **4.2**, or **4.3** (0.1 mM) for 9 hours incubation. After incubation, slides were rinsed with THF (< 4 mL × 2), pH 5 potassium hydrogen phthalate buffer solution (< 4 mL × 2), and finally DI water (< 4 mL × 2). The cleaned slides were dried under vacuum overnight.

4.2.4 Fluorescence measurements in cuvette

Fluorescence spectra of **4.3** in CH_3CN (0.02 mM) in 700 μL quartz cuvettes with an excitation path-length of 10 mm were recorded on a Varian Cary Eclipse spectrofluorometer. The ionic strength was maintained with 100 mM tetraethylammonium perchlorate (NEt_4ClO_4), acting as an ionic buffer. The spectrofluorometer has a Xenon flash lamp as the excitation source and photomultiplier tube (PMT) as the detector. The excitation and emission slit width were set at 5 mm. The excitation wavelength was 470 nm. All measurements were recorded at 25°C.

4.2.5 Surface characterisation procedures

Scanning fluorescence imaging

Surface fluorescence from slides was measured using a Typhoon TM 8600 variable mode imager from Amersham Bioscience. Slides were excited with a 488 nm blue laser and the emission measured through a band pass filter at 520 nm with bandwidth 40 nm. It is noted that the laser choices are limited by the typhoon imager. Hence, the excitation wavelength is not the same as experiments described in previous chapters. The validity of using 488 nm for excitation is discussed in Section 4.3.2. The sensitivity setting used was medium. The resolution for each pixel was 100 μm and the PMT voltage was 500 V. The average fluorescence intensity per mm^2 of the slides was obtained by measuring 300 data points from three slides per treatment. The measurement error was 1 standard deviation (SD) of 300 data points. In order to compensate the variation of the instrument laser power between scans performed at different times, an erbium-doped phosphate glass fluorescence standard was scanned at the same time. The

composition of the standard is 68.0 P_2O_5, 2.6 MgO, 7.3 CaO, 8.0 ZnO, 7.1 BaO, 0.5 Al_2O_3, 6.4 Yb_2O_3, 0.1 Er_2O_3 (mol %).

X-ray photoelectron spectroscopy (XPS) measurements and data analysis

XPS measurements were performed in an ultra high vacuum apparatus built by SPECS (Berlin, Germany). All the measurements were performed using a non-monochromatic Mg Kα X-ray source and hemispherical Phoibo 100 energy analyser from SPECS. Charge compensation was performed by electron flood gun SPECS FG20 at 1 eV and 5 μA. The binding energy of Pb 4f 7/2 of bare lead silicate glass was calibrated by adventitious carbon (C-H = 284.8 eV) [2]. The Pb 4f 7/2 in lead silicate glass is 138.6 ± 0.1 eV, which is used as the calibration standard for all the coated glass slides. The reason for using the Pb 4f 7/2 peak in calibration is because the organic coating material contains an unknown quantity of carbonyl groups which significantly changed the carbon peak. The peak position and shape of Pb from the glass slides were assumed to be constant throughout the experiments. The aperture spot diameter was 2 mm and three spots were measurement for each slide. At each sampling spot, a survey spectra with passing energy 40 eV with 0.5 eV energy step while high resolution XPS (HRXPS) spectra were collected at each spot with passing energy 10 eV with 0.05 eV energy step. The dwell time of all spectra is 0.1 s. High resolution spectra of C 1s, N 1s, Si 2p, O 2p, Na 1s and Pb 4f were collected.

XPS data fitting was performed using commercial XPS analysis software. A Shirley background was selected to model the background signal. The relative sensitivity factors for the X-ray source at 54.7° to the detector for C, N, O, Si, Pb and Na are 0.296, 0.477, 0.711, 0.339, 8.329 and 1.685 [2]. These values were used to calculate the atomic percentage of each element from the HR spectra. A convolution of Gaussian (70%) and Lorentzian (30%) peaks were used to fit individual peaks. Peak fitting constraints were introduced in the deconvolution analysis of C and Pb HR spectrum. All synthetic components within each HR spectra were assumed to have the same full width half maximum (FWHM). In carbon HR spectra, three synthetic components were fitted with fixed chemical shift difference relative to CH peak. The chemical shift difference of CH and

CN/CO was fixed at 1.5 eV; the difference of chemical shift of CH and C=O is fixed at 3 eV.[3] In Pb HR spectra, two synthetic components were fitted with fixed chemical shift at 4.86 eV corresponding to the doublet of 4f 7/2 and 4f 5/2. The area of the 4f 5/2 was fixed at 75% of the area of 4f 7/2 [2].

Time of flight secondary ion mass spectrometry (ToF-SIMS) measurements and analysis

ToF-SIMS experiments were performed using a Physical Electronics Inc. PHI TRIFT V nanoToF instrument (Physical Electronics Inc., Chanhassen, MN, USA) equipped with a pulsed liquid metal Au primary ion gun (LMIG), operating at 30 kV energy. Dual charge neutralisation was provided by an electron flood gun and 10eV Ar^+ ions. Experiments were performed under a vacuum of $5x10^{-6}$ Pa or better. "Bunched" Au_1 instrumental settings were used to optimise mass resolution for spectra; "Unbunched" Au_1 instrumental settings were used to optimise spatial resolution for the images. +SIMS spectra were collected from areas of 200 x 200 μm^2, with an acquisition time of 1 minute. For each sample, 6 different spots were measured.

Each positive secondary ion mass spectrometry (+SIMS) images was collected from areas of 100 x 100 μm^2 with an acquisition time of 1 min. Single-gun depth profile data was also collected using the Au_1 LMIG 'Bunched' instrument settings, with an analysis raster of 100 x 100 μm^2 inside a 250 x 250 μm^2 sputter raster. The time of each sputtering cycle was 5 s and the acquisition time of the analysis was approximately 15 s raw data was collected so that depth profiles of species of interest were retrospectively produced. For each sample for depth profiling, 3 measurements were taken from different spots. Sample spectra, images and depth profiles were processed and interrogated using WincadenceN software (Physical Electronics Inc., Chanhassen, MN, USA). For all measurements, circular diaphragm (CD) was used to confine the emission angle from the sample.

ToF-SIMS principal component analysis (PCA) analysis was performed using the statistics toolbox in Matlab R2008a. Selected organic fragment ion peaks were

normalized by the total selected fragment ion peaks before the PCA analysis. ToF-SIMS images were exported from WincadenceN software. The distribution of Pb was quantified using Matlab 2008. By subdividing the 100 x 100 μm^2 image into 256 separated 16 x 16 pixel sections, the average number of pixel with Pb detected could be counted. Pixel intensity was ignored during the analysis. ToF-SIMS depth profiling data were normalised with the total ion count of that particular spectrum. The final result for each sample was the average normalised ion intensities of all measurement spots on each sample.

4.3 Results and discussion

4.3.1 Synthesis and surface attachments of the model fluoroionophore derivatives.

The syntheses of compound **2.2**, **2.7** and fluoroionophore **2.8** were described in Chapter 2. The fluoroionophore derivatives (**4.2** and **4.3**) were synthesised according to the procedures outlined in Scheme 4.1.

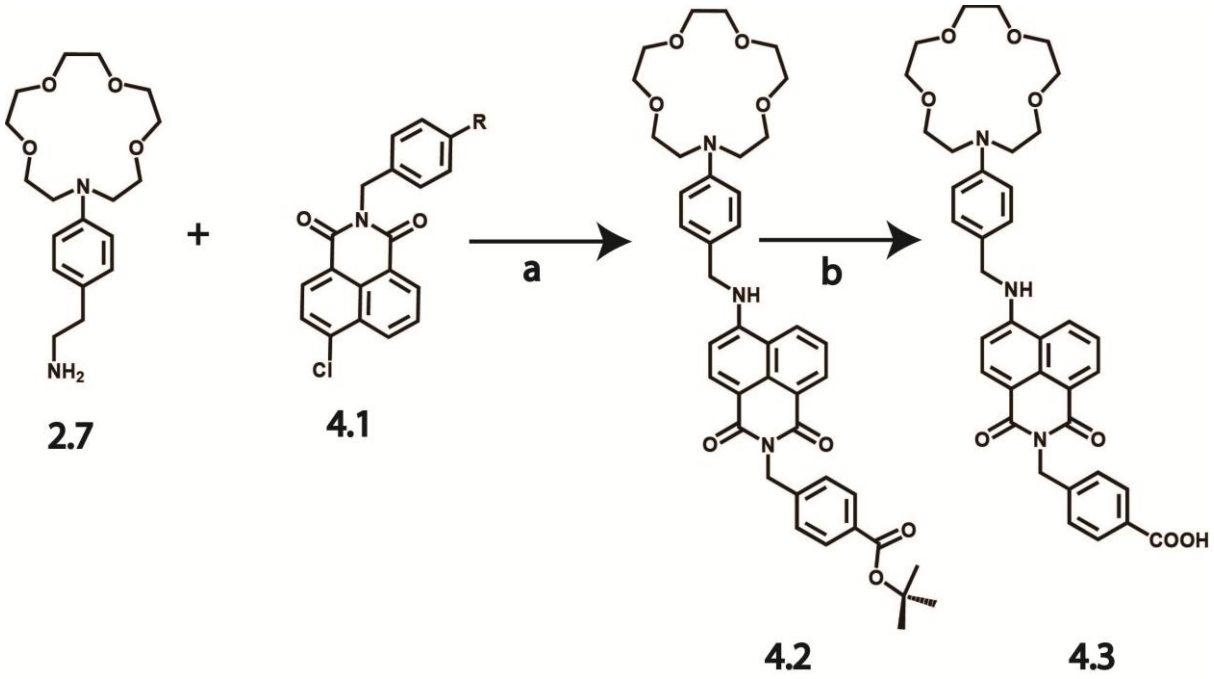

Scheme 4.1. The synthesis scheme of PET fluoroionophore derivatives (a) NMP, DIPEA, microwave 100 °C, 37%; (b) TFA, dichloromethane, room temperature, 50%

Scheme 4.1 shows the synthesis of the model PET fluoroionophore derivatives (**4.2** and **4.3**). Fluoroionophore **4.2** was synthesised by an aromatic nucleophilic substitution reaction of 4-aminoethyl-phenylaza-15-crown-5 (**2.7**) with either *t*-butyl-4-chloro-1,8-naphthalimidylmethyl benzoate (**4.1**) or *N*-benzyl-4-chloro-1,8-naphthalimide (**2.2**). The *t*-butyl ester protecting group was removed by hydrolysis using trifluoroacetic acid (TFA) to afford **4.3**, which has a carboxyl moiety for a covalently attachment to the primary amine group of the APTES grafted glass surface, in 8% overall yield. Coupling onto the APTES surface was undertaken under standard peptide coupling conditions using EDC, NHS, and triethylamine as the base. Negative controls for experiments involving the coupling of **4.3** were obtained by treatment of APTES grafted slides without all or some of the coupling reagents. Without coupling reagents, amide bond formation is not feasible at room temperature [4].

4.3.2 Scanning fluorescence imaging using the Typhoon imager

After the introduction of the carboxyl moiety on the fluorophore, the excitation spectrum of the fluoroionophore may be different. It is noted that the excitation spectrum of the fluorophore in diluted solution is generally identical to its absorption spectrum. Figure 4.2a shows the comparison of the normalised excitation spectra of fluoroionophore **2.8** and **4.3** in acetonitrile (I = 0.1 M) with emission fixed at 520 nm. Both excitation spectra overlap indicating that there is no shift in the absorption maxima after introducing the carboxyl group on the fluoroionophore for attachment. The typhoon imager has three in-build lasers at 488 nm, 532 nm and 633 nm. Figure 4.2a also shows that the 488 nm laser of the typhoon imager can be used for the excitation because it is within the absorption wavelength range, although it is at the edge of the absorption range. The normalised emission intensities of fluoroionophores **2.8** and **4.3** are 0.16 and 0.15, which suggests that their differences in molar extinction coefficient at 488 nm are within 7%. Figure 4.2b shows the excitation spectrum (350 nm to 500nm) of **4.3** in acetonitrile (I = 0.1 M) with emission fixed at 520 nm. Figure 4.2b shows the emission spectrum of **4.3** in the same solvent with excitation at 488 nm, confirming that fluoroionophore **4.3** can be excited at 488 nm.

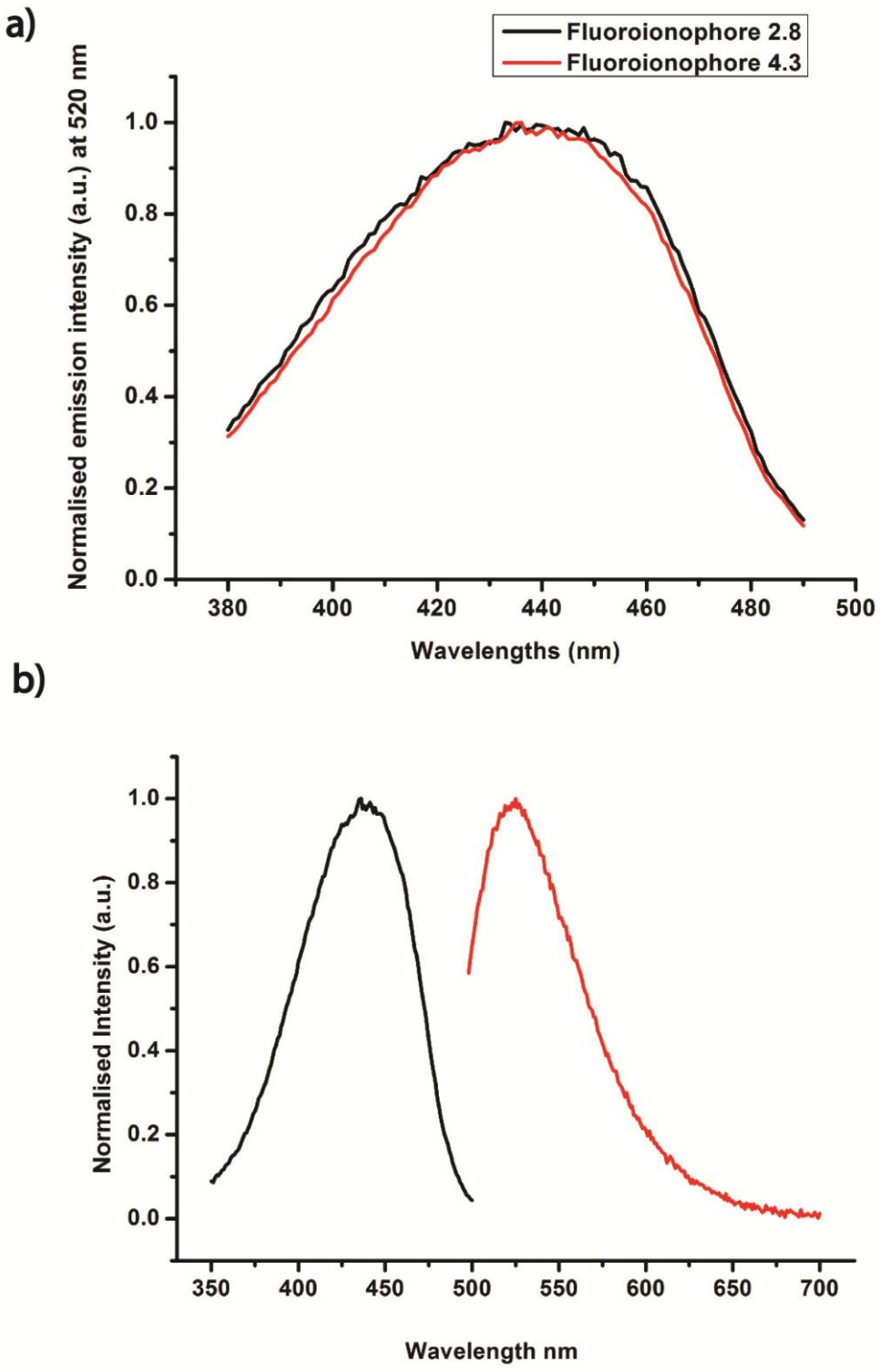

Figure 4.2: (a) Excitation spectra of fluoroionophore of **2.8** and **4.3** at 520 nm in CH_3CN (I = 0.1 M). (b) The left (black) spectrum is the normalised excitation spectrum of **4.3** with emission fixed at 520 nm, and the right spectrum is the normalised emission spectrum of **4.3** with excitation fixed at 488 nm in CH_3CN (I = 0.1 M)

Figure 4.3a shows the average fluorescence intensity per mm^2 of the coated slides (300 data points from three slides per treatment). Slides treated with fluoroionophore **4.3** and all coupling reagents show the highest fluorescence intensity compared to all the negative controls, with a statistically significant difference. Negative controls B1, B2 and B3 are samples with fluoroionophore **4.3** without EDC. The key coupling reagent for the formation of amide bond at room temperature is EDC, whereas, NHS and base only improve the yield of the coupling reaction. Hence, the fluorescence intensity of B1, B2 and B3 are similar. Negative controls E and F indicate that the APTES coating and the F2 glass have low fluorescence intensity at the emission wavelength of fluoroionophore **4.3.**

All negative controls show significantly higher fluorescence intensity compared to slides with only APTES grafting. This latter observation indicates that fluoroionophore **4.3** also adsorbs non-covalently to APTES coated slides after the washing procedure used, which involves sequential washing with THF, buffer (pH 5) and water. The slides were washed with THF in order to remove most of the THF soluble fluoroionophores. pH 5 buffer, which should not degrade the underlying APTES coating, was used to protonate the carboxylate ion and reduce the ionic attraction of the fluoroionophore and APTES. Finally water was used to remove remaining salt from the slide surfaces. Washing the slides in soxhlet glassware under reflux condition had been considered for thoroughly removing all physisorbed fluoroionophores. This method is suitable to wash slides; however, it is not feasible to apply to SCFs because the solvent cannot pass through the holes of SCF efficiently under such condition. It is important that all the sample preparation procedures used in this study are transferable to SCFs functionalisation.

The directional nature of covalent attachment introduces less variation in the orientation of the fluoroionophore on the surface, and should thereby improve the consistency of the SCF sensor performance. A non-covalent attachment is a relatively weaker binding interaction compared with a covalent attachment method and hence is more dependent on the environmental conditions such as pH or ionic strength in the analyte. Therefore the covalent attachment is more desirable over the non-covalent attachment in SCF sensors.

To probe whether the observation of non-covalent attachment of **4.3** on the APTES surface is related to the structure of the fluoroionophore, two derivatives (**4.2** and **2.8**) were incubated under the same condition for 9 hours and the slides cleaned with the standard washing procedure. Figure 4.3b shows the comparison of average fluorescence intensity per mm^2 of all three fluoroionophore derivatives incubated for 9 hours, along with the APTES-grafted and untreated glass slides. Assuming the molar extinction coefficient and quantum yield of all non-covalently attached derivatives on an APTES grafted surface are the same,[5, 6] the density of fluoroionophore **4.2** is less than **4.3** and **2.8**, whereas the difference between **4.3** and **2.8** is statistically insignificant. These experiments suggest that the structure of the fluoroionophore has a role in the non-covalent attachment to the APTES coating. Previous XPS studies on APTES grafted silicon wafers indicated that free amine (NH_2) and ammonium groups (NH_3^+) can co-exist on an APTES coated surface [3]. Thus it is likely that fluoroionophore **2.8**, **4.2** and **4.3** bind non-covalently to the APTES coated surface through a mixture of charge dipole and electrostatic interactions (Figure 4.3b). The electrostatic interaction may arise from the pH 5 buffer washing step which protonates the crown ether as well as the secondary amine. It is also possible that the positive ammonium groups of APTES are complexed by the crown ether [7]. The higher solubility of fluoroionophore **4.2** in THF/water (9:1) compared with fluoroionophore **2.8** and **4.3**, possibly due to its *t*-butyl ester group, is consistent with lower quantities on the APTES surface after washing.

Studies of fluoroionophore **2.8**, described in Chapter 2, and similar fluoroionophores show increased emission intensity from these compounds due to a change in quantum yield upon complexation of sodium or other positive ions of similar size [1, 8]. The interaction of the ionophore with positively charged ammonium ions of the APTES-grafted glass surface may also change the quantum yield of the fluoroionophores [7]. Thus, complementary measurements using XPS and ToF-SIMS, described below, were performed to corroborate the surface fluoroionophore concentrations.

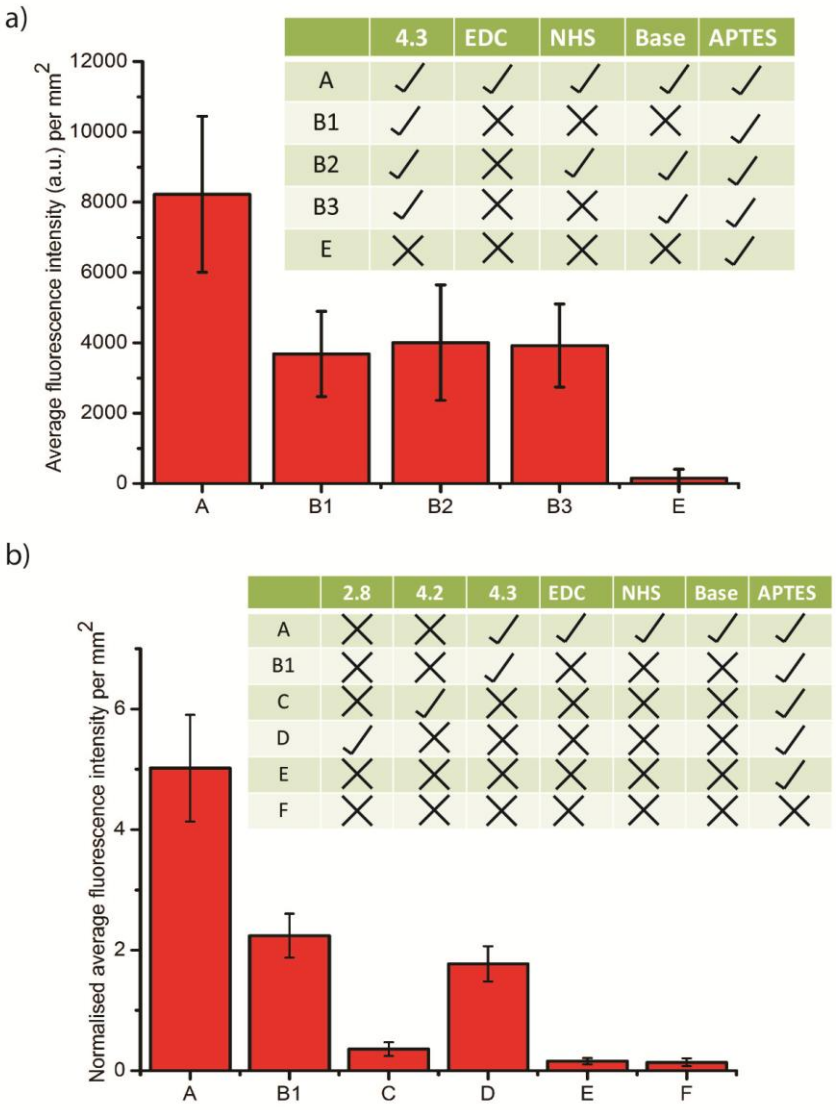

Figure 4.3: (a) Average fluorescence intensity per mm^2 for APTES grafted slides with fluoroionophore **4.3** and negative controls. A = **4.3**/EDC/NHS/base on APTES grafted F2 glass slides, B1 = **4.3** on APTES-grafted F2 glass slides, B2 = **4.3**/NHS/base on APTES-grafted F2 glass slides, B3 = **4.3**/base on APTES-grafted F2 glass slides and E = on APTES-grafted F2 glass slides (b) Normalised average fluorescence intensity per mm^2 for APTES grafted F2 glass slides with **2.8**, **4.2** and **4.3.** A = **4.3** EDC/NHS/Base on APTES-grafted F2 glass slides, B = **4.3** on APTES-grafted F2 glass slides, C = **4.2** on APTES-grafted F2 glass slides, D = **2.8** on APTES-grafted F2 glass slides, E = on APTES-grafted F2 glass slides and F = F2 glass slides. Results in Figure 4.3b are normalised with a fluorescence glass standard, because measurements were performed at different times

To establish the relationship between the surface density of fluoroionophore **4.3** with and without coupling reagents and incubation time, coupling reactions were performed for 1, 3, 5, 7, and 9 hours (data for 1, 5 and 9 hours presented). Figure 4.4 shows that samples incubated for 1 – 9 hours have no statistically significant differences in the surface fluorescence intensity; i.e. most of available amine sites were reacted within a 1 hour treatment. Nonetheless, most of the analyses described here were undertaken on samples typically treated for 9 hours to ensure maximum coverage and a consistent coupling result.

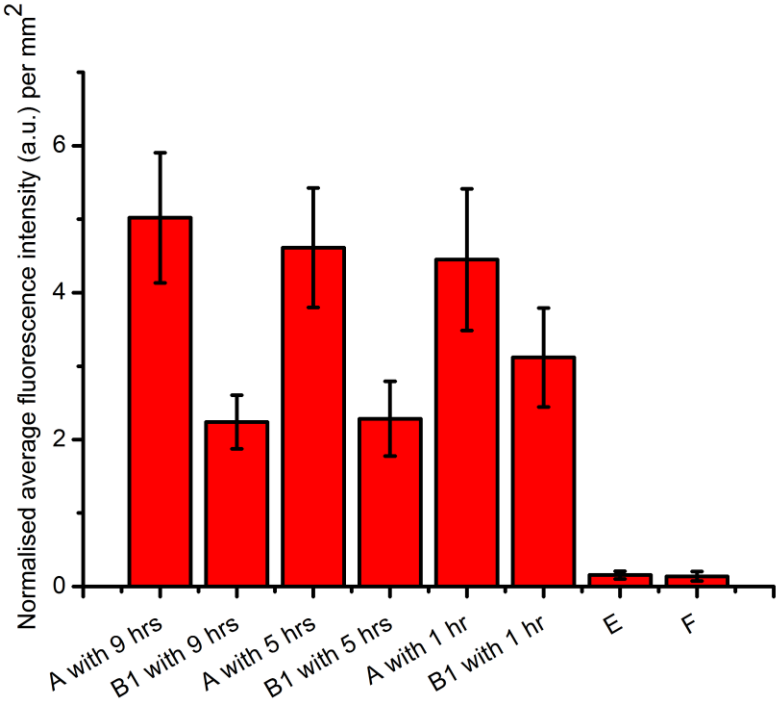

Figure 4.4: Normalised average fluorescence intensity per mm^2 for fluoroionophore **4.3** on APTES-grafted F2 glass slides after 1, 5 and 9 hours incubation and their respective negative controls. A = 4.3/EDC/NHS/base on APTES-grafted F2 glass slides, B1 = 4.3 on APTES-grafted F2 glass slide, E = on APTES-grafted F2 glass slides and F = F2 glass slides

4.3.3 X-ray photoelectron spectroscopy (XPS)

The fluorescence intensity of a surface-bound fluorophore is dependent on its molar extinction coefficient and the quantum yield of the fluorophore on the surface, which are not straightforward to measure [5, 6]. In addition, during the covalent attachment the formation of an amide bond with the APTES coated

surface may alter the molar extinction coefficient and quantum yield of the fluorophore; thus, the differing fluorescence measurements for **2.8, 4.2** and **4.3** might not be directly related to the absolute quantity/density of fluoroionophore [5, 6]. The latter source of uncertainty in the change of the molar extinction coefficient and quantum yield of **4.3** due to the amide bond formation can be understood by the model amide bond formation using a primary amine in a solution phase. In this case the structure can be confirmed by both NMR spectroscopy and mass spectrometry, and the molar extinction coefficient and quantum yield can be confirmed by both UV-Vis and fluorescence spectroscopy. However, the amide bond formation at the solid-liquid interface may have a further, different impact on the molar extinction coefficient and quantum yield of the fluoroionophore compared to the situation in solution.

In contrast to the scanning fluorescence imaging, XPS measurements are independent of the molar extinction coefficient and quantum yield. XPS provides an elemental analysis of the surface of the functionalised glass under a vacuum condition with a sampling depth of approximately 10 nm, which is ideal for investigating the composition of the chemical coatings and the glass interface [9]. Throughout these experiments, lead (Pb) 4f 7/2 peak was used as the calibration standard. Since the chemical shift of Pb 4f 7/2 in F2 has not been determined before, the C 1s peak from adventitious hydrocarbons were used to determine the binding energy of Pb 4f 7/2 of the uncoated F2 glass sides. The Pb 4f 7/2 average binding energy of F2 is 138.6 ± 0.1 eV, very close to the literature value discussed in Chapter 3B [10].

APTES-coated glass slides coupled to fluoroionophore **4.3** (with 9 hours incubation), negative control slides without coupling reagents, APTES coated slides, and uncoated F2 slides were analysed using XPS. From the survey scan, O, C, Si, Pb, Na and N were found in most of the slides. The element quantifications are based on high resolution scans. Figures 4.5a and b show the individual average atomic percentages of nitrogen and lead in all three samples from each treatment described above. Aside from two individual samples (C1 and C3), samples with fluoroionophore **4.3** coupled on the APTES coated slides were found to have a greater nitrogen atomic percentage compared to the negative

controls and slides with APTES coating only. Nitrogen is not a component of F2 glass and therefore the nitrogen content detected here probably reflects surface contamination. The variation of nitrogen content within samples that experienced the same surface treatment is possibly due to issues with the variations of the APTES coating thickness and homogeneity, issues which were discussed in Chapter 3C. However, we cannot confirm this hypothesis without ellipsometry measurements, which are difficult to perform on transparent samples as also described in Chapter 3C.

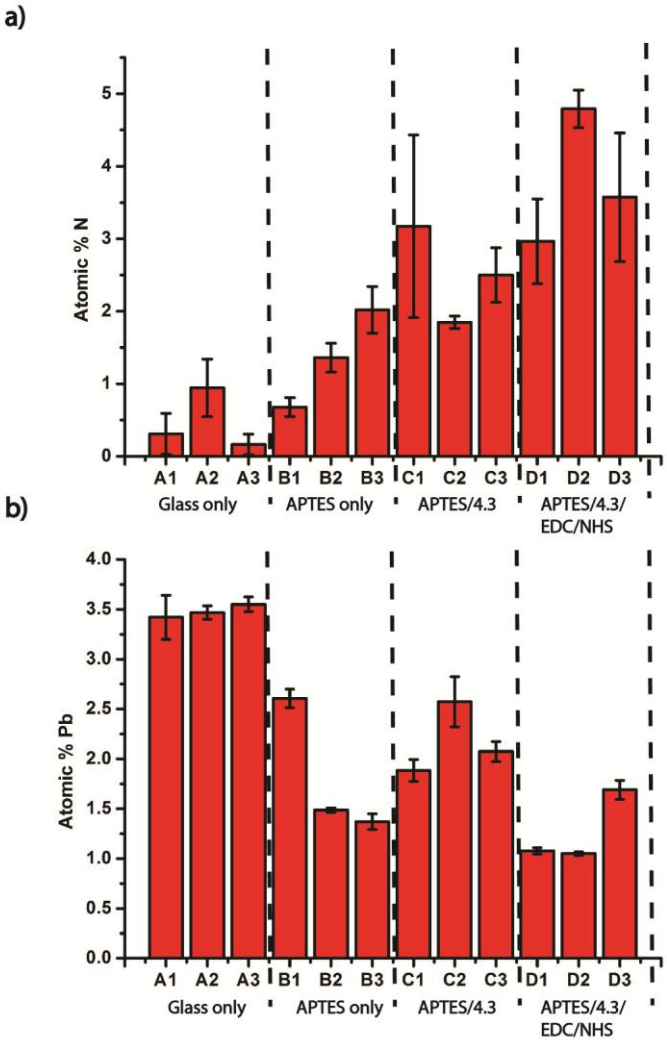

Figure 4.5: Average atomic percentages of (a) nitrogen and (b) lead on bare and coated F2 slides as measured by XPS. **A1-3** = bare glass slides, **B1-3** = APTES grafted glass slides, **C1-3** = **4.3** and APTES grafted glass slides without coupling reagents and **D1-3 = 4.3** and APTES grafted glass slides with coupling reagents

Figure 4.6a shows the linear regression between average nitrogen and lead atomic percentages ($R^2 = 0.64$) with a negative slope. Although the correlation coefficient is poor, the trend suggests that the nitrogen atomic percentages are inversely related to the lead atomic percentages. It is because the APTES coating and the fluorophores cover the glass. Similar phenomenon was discussed in Section 3C.3.4. The lead atomic percentages is consistent across uncoated F2 slides (A1, A2 and A3) as shown in Figure 4.5a, therefore the poor correlation factor is possibly due to the inconsistency of nitrogen atomic percentages from the APTES coating or the attachment of the fluoroionophores. Figure 4.6b shows that the average atomic percentages of nitrogen are correlated to the fluorescence intensities ($R^2 = 0.78$). This arises because of the attachments of fluoroionophore **4.3** (the source of fluorescence) increase the nitrogen atomic percentage on surface. However, the non-fluorescent APTES coating also contributes significantly to the overall nitrogen atomic precentage.

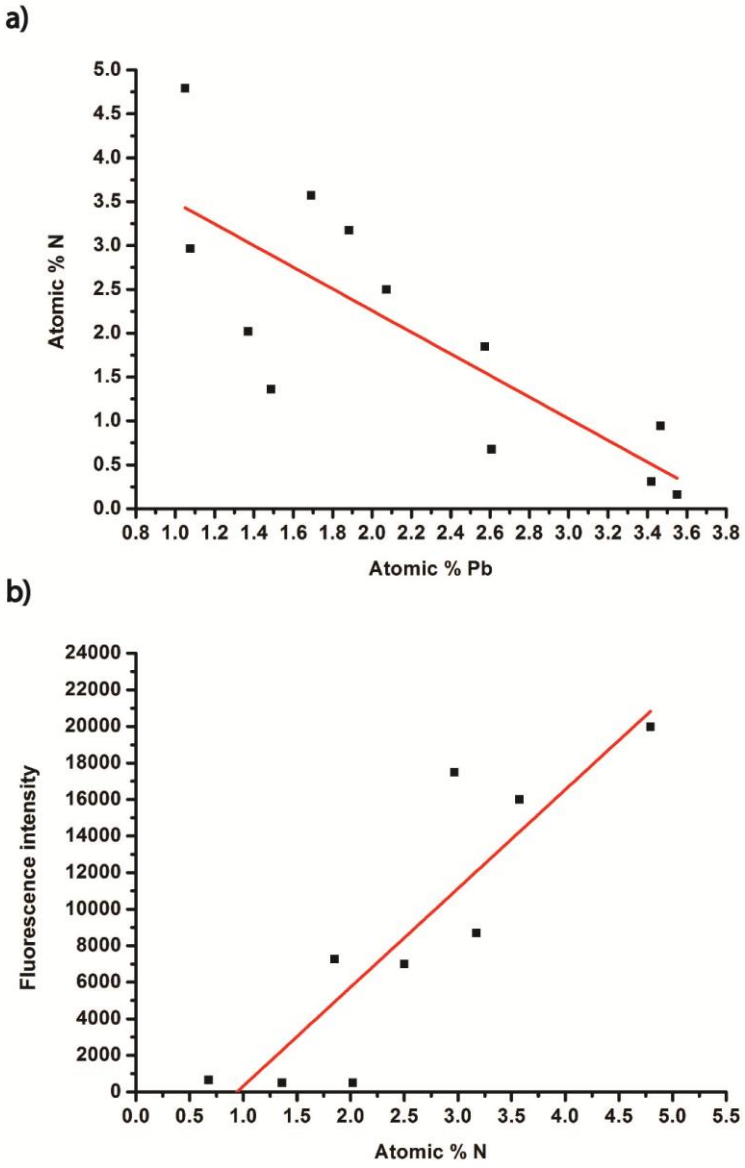

Figure 4.6: (a) Average nitrogen atomic percentages as a function of lead atomic percentages (R^2 = 0.64). (b) Average fluorescence intensities as a function of average nitrogen atomic percentages (R^2 = 0.78)

Figures 4.7a–c show the HRXPS spectra of carbon for the first position of a F2 slide, an APTES-grafted glass slide, a negative control and an APTES-grafted glass slide coupled to fluoroionophore **4.3**. Using the spectral deconvolution, the carbon peak is separated into C-H (284.5 ± 0.1 eV), CN/CO (286 ± 0.1 eV and C=O (287.5 ± 0.1 eV). The HRXPS spectra show that the samples with fluoroionophore **4.3** coupled have the highest C=O content. This is reasonable since fluoroionophore **4.3** has two C=O groups from an imide and also an amide

group when it is coupled on the surface. Figure 4.8 shows the correlation (R^2 = 0.88) between the average fluorescence intensities and the average C=O percentage contributions. The C=O atomic percentage is more specific to the PET fluoroionophore compared to the nitrogen atomic percentage, which is affected by the variation of the APTES coating. The C-N percentage contribution also increased for samples coupled with fluoroionophore **4.3**; however the APTES layer also contributes to the C-N percentage contribution. Therefore C-N percentage contribution is not a specific diagnostic signal to show the quantity of fluoroionophore **4.3**.

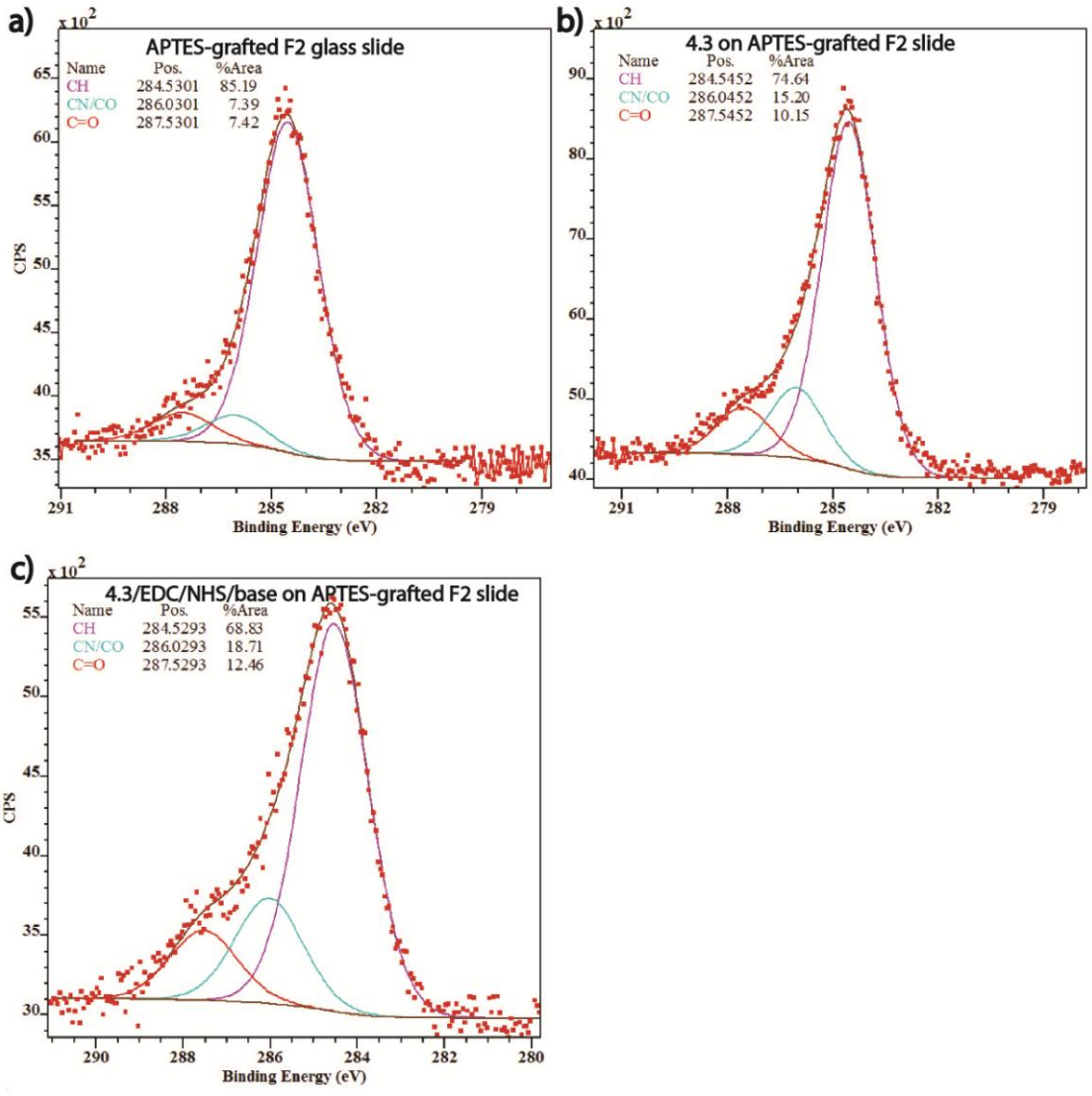

Figure 4.7: Deconvolutions of the HRXPS carbon spectra at the first sampling position of (a) an APTES-grafted F2 glass slide, (b) **4.3** on APTES-grafted F2 glass slide (c) **4.3**/EDC/NHS/base on APTES-grafted F2 glass slide

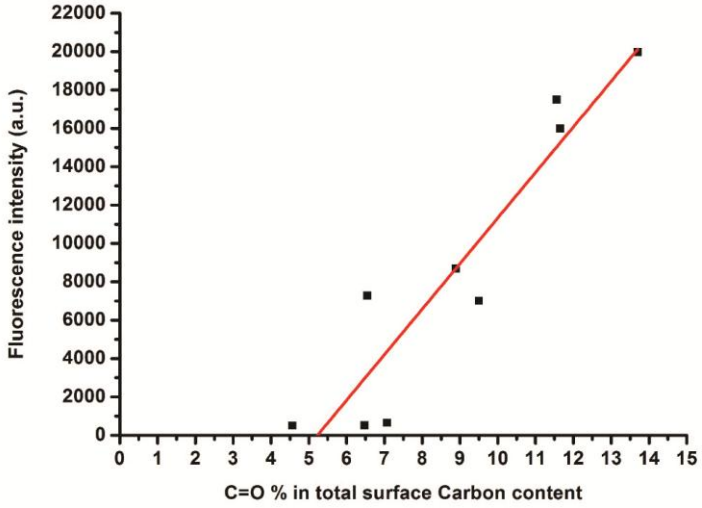

Figure 4.8: Average fluorescence intensity per mm^2 as a function of the average C=O percentage contribution (R^2 = 0.88)

4.3.4 Time-of-flight secondary ion mass spectrometry (ToF-SIMS)

ToF-SIMS is another surface sensitive technique that can provide semi-quantitative measurements of the surface density of fluoroionophores. This technique provides surface mass spectrometry information that is again independent of the optical properties of the fluoroionophore. In addition, the sampling depth of the ToF-SIMS is approximately 1-2 nm from the surface, which means it is a more surface sensitive technique compared to the XPS. However, the mass spectrometry is not usually quantitative. To establish semi-quantitative surface analyses using ToF-SIMS, multivariable statistical analyses based on principal component analysis (PCA) were performed. Since the ToF-SIMS is highly sensitive to surface contamination, samples were measured shortly after the coating process and measured for 6 spots on each slide sample. Figure 4.9a shows the results from the PCA analysis of the positive secondary mass spectrometry (+SIMS) measurements. Principle component 1 (PC1) covers 75.1 % and Principle component 2 (PC2) covers 13.9 % of the total covariance of the samples, which gives the total covariance coverage of 89 %. Samples are well clustered and separated. Samples with fluoroionophore **4.3**, as well as all necessary coupling reagents, show a negative PC1 projection score, which discriminates them from all negative control slides. The loading plot (Figure 4.10) shows all fragment peaks included in the PCA analysis. Figures 4.10 b–c show

organic fragments ($C_xH_yN_z$ and $C_xH_yN_zO$), which have a significant negative correlation to PC1. These fragments are related to the structure of the fluoroionophore and the APTES coating and most are negatively correlated to PC1 and positively correlated to PC2. Slides with **4.3**/EDC/NHS/base have negative PC1 scores and positive PC2 scores, which matches the pattern for $C_xH_yN_z$ and $C_xH_yN_zO$ organic fragments. PC1 appears correlated to the quantity of fluoroionophore **4.3** attached to the APTES grafted glass slides. Figure 4.9b shows that only slides treated with **4.3**/EDC/NHS/base have a negative PC1 score, while the rest of the treatments without the full set of coupling reagents and slides with APTES only show positive PC1 scores. The PC1 score of all slides without the full set of coupling reagents show lower PC1 scores compared to slides with APTES only. This difference is statistically significant, and shows the surface density of fluoroionophore **4.3** on an APTES grafted slides can be semi-quantitatively measured by ToF-SIMS; all slides containing fluoroionophore **4.3** show evidence for some non-covalent attachment of fluoroionophore **4.3** and thus a lower PC1 score.

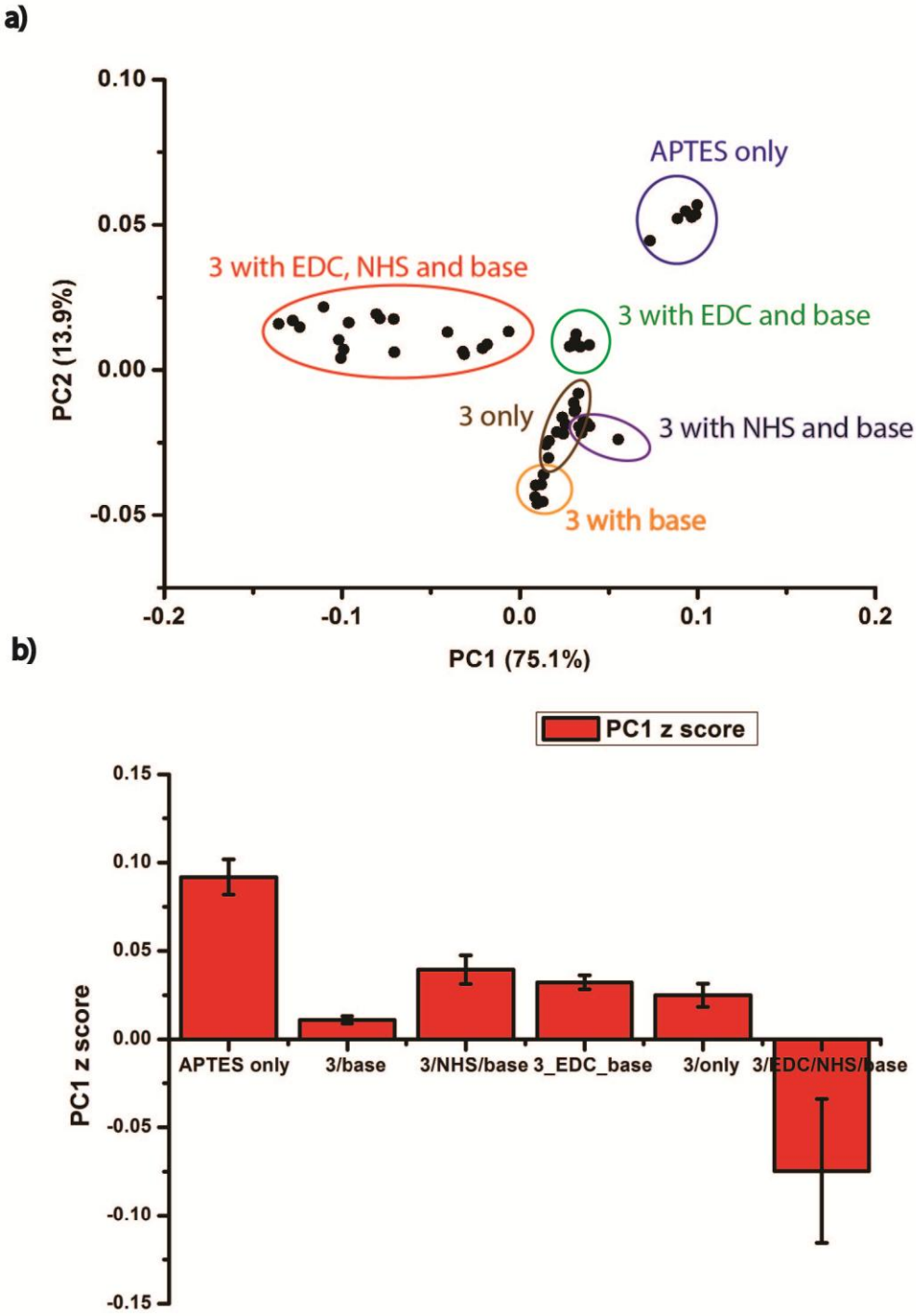

Figure 4.9: (a) The PCA analysis of the ToF-SIMS results. (b) Average PC1 projection score of all sample types

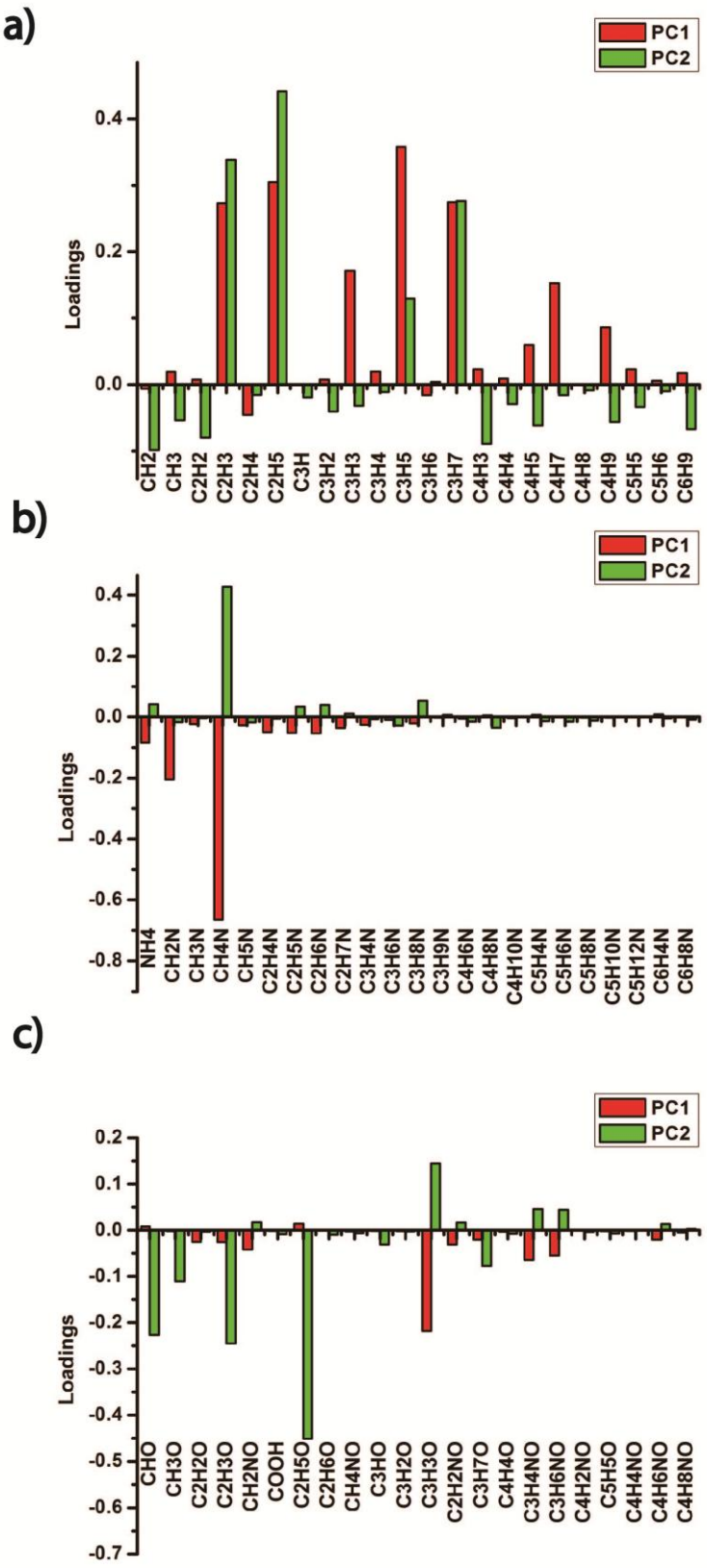

Figure 4.10: The loading plots of PC1 and PC2 for the PCA analysis of the ToF-SIMS data

Figures 4.11a–d show ToF-SIMS images of Pb ions in the samples analysed by fluorescence imaging and XPS. The size of each image is 100 μm x 100 μm and the resolution is 256 x 256 pixels; thus, each pixel represents a mass spectrum from a 391 nm x 391 nm sample area. A coloured pixel indicates that Pb was detected with intensity above the ToF-SIMS detection limit. On each slide, the Pb distribution is relatively random with no significant patchiness observed. Figure 4.12 shows the average number of Pb detected pixels in 6.3 μm x 6.3 μm area of each sample, in which the intensity was ignored in the counting of each Pb detected pixel. Thus the color of the pixel is irrelevant in this relative comparison. Grafted APTES coated slides with coupled fluoroionophore **4.3** have the minimum number of Pb detected pixels and, as expected, the Pb ion density is highest on F2 slides. However, some exceptions are observed (A1, B3 and C1), which show much lower Pb pixel count than expected. This may be due to surface contamination during sample preparation or inherited variation of the coverage of the coating. The general trend of the results shows that the Pb ion density decreases when APTES was coated on the surface, and shows a further decrease when fluoroionophore **4.3** was coupled on the surface. This observation is due to the increased coating coverage, which obscures the detection of Pb ions. This result confirms the negative correlation of the atomic percentages of N and Pb in the XPS measurements and suggests the Pb ion distribution can be used as a marker to indicate the coverage of the coating on lead silicate glass surfaces.

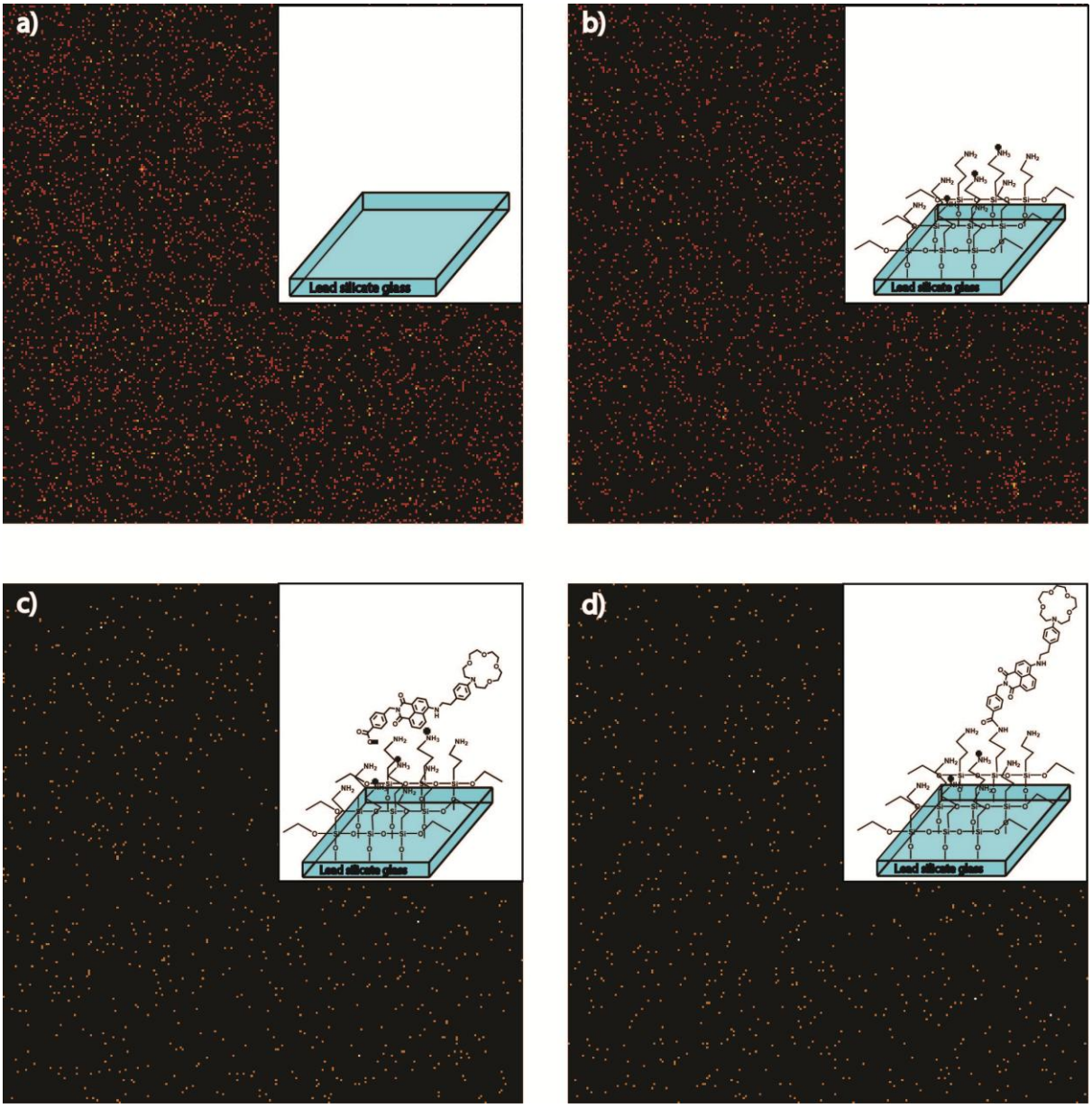

Figure 4.11: Selected Pb ion images of a (a) F2 glass slide, (b) APTES-grafted F2 glass slide, (c) **4.3** on APTES-grafted F2 glass slide, (d) **4.3**/EDC/NHS/base APTES-grafted F2 glass slide. Note that the color of the pixel is irrelevant in this relative comparison. It is the average density to show the coverage. The density of the Pb detected pixels is shown in Figure 4.12

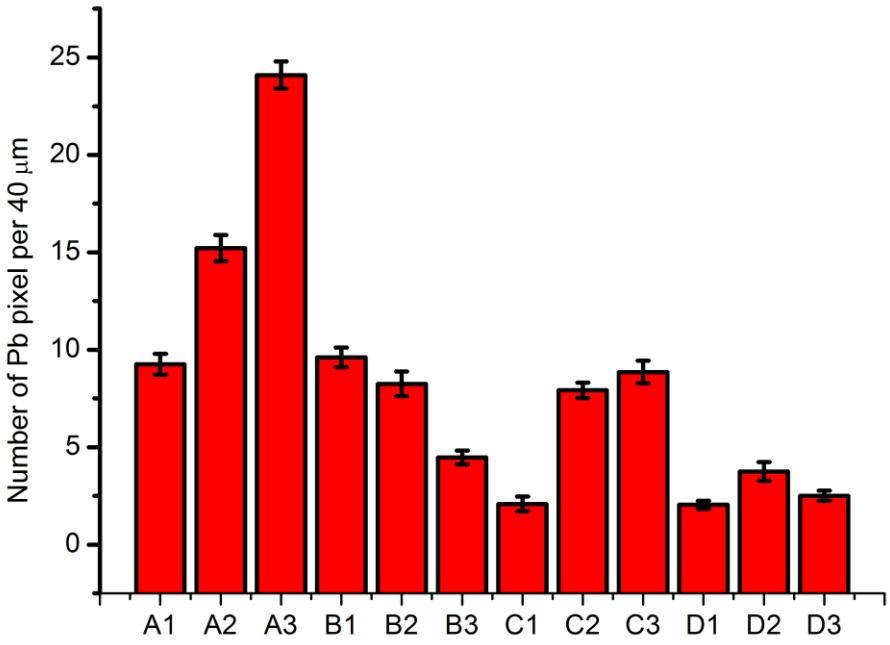

Figure 4.12: The average number of Pb detected pixels in a 6.3 µm x 6.3 µm area of the ToF-SIMs image. A1-3 = F2 slides, B1-3 = APTES grafted on F2 slides, C1-3 = **4.3** and APTES-grafted F2 slides D1-3 = **4.3**/EDC/NHS/base on APTES-grafted F2 slides

In addition to providing quantification of the surface concentration of the coupled fluoroionophores and its homogeneity on the surface, ToF-SIMS depth profiling can provide information about the relative thickness of a coating. While in this work no calibration was performed to establish the absolute thickness, as long as the sputtering beam energy is constant, the sputtering time required for the relevant organic fragment peak to reach saturation is proportional to the thickness of the coating. Similar experiments have been performed for an organic coating on hard-disk platter, and this approach enables thickness measurements on a thin film (~1 to 2 nm) on a non-reflective surface [11]. To ensure the depth profiling results are valid. Three depth profiles were performed on the same slide to establish the statistical variation of the same sample. The ion intensity of each data point was normalised to the total ion intensity in each depth profile measurement.

Figure 4.13 shows depth profiles for three identically prepared samples of fluoroionophore **4.3** coupled onto an APTES coated glass surface. It is observed that the normalised peak intensity of lead increases while CH_4N^+ decreases. Based on the loading plot (Figure 4.9) of the PCA analysis, the CH_4N^+ peak is strongly correlated to the organic coating. The depth profile shows that the relative intensity of the CH_4N^+ fragment decreased throughout sputtering, this corroborates that this fragment is related to the coating. The increase in Pb concentration is due to sputtering of the glass substrate which has a higher concentration of Pb. These measurements are consistent over the three samples.

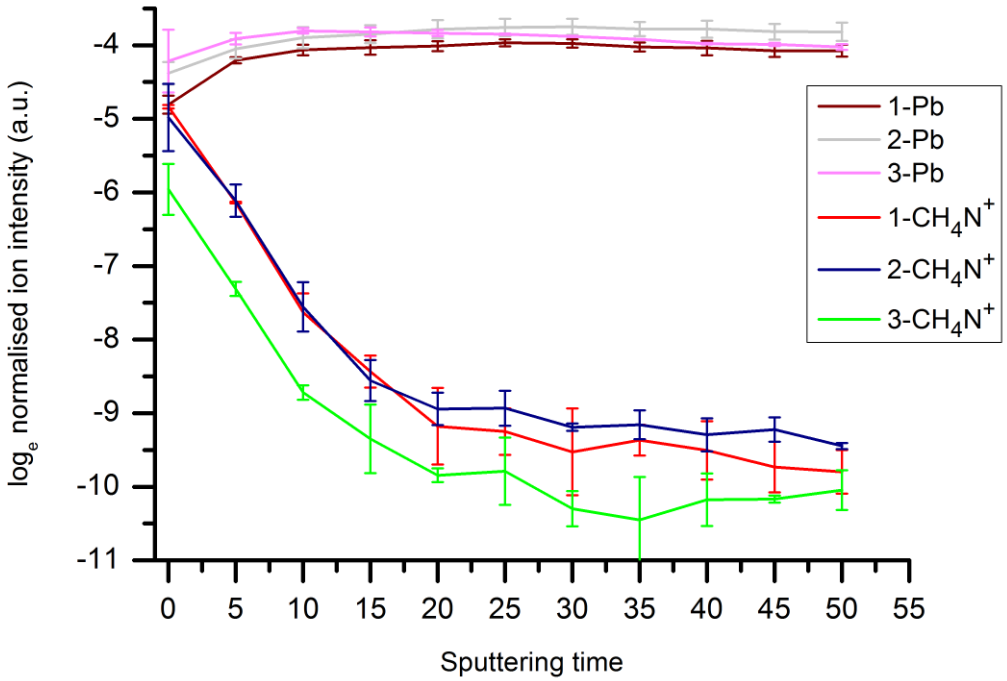

Figure 4.13: Depth profiles of glass slides with **4.3** coupled onto an APTES coated surface

Figure 4.14 shows the depth profiling of CH_4N^+ over sputtering time between 5 - 50 seconds on bare F2 slides, APTES only grafted slides, fluoroionophore **4.3** on an APTES grafted surface and fluoroionophore **4.3** coupled on an APTES grafted surface. It is observed that the relative intensity of CH_4N^+ of bare F2 slides only fluctuates within statistical error from 10 s onwards. The relative intensities of CH_4N^+ for slides with fluoroionophore **4.3** on an APTES grafted surface and fluoroionophore **4.3** coupled on an APTES grafted surface decrease over the

period of 5 – 25 seconds, with no statistical difference observed from 25 seconds onwards. In contrast, the relative intensity of CH_4N^+ on APTES only coated slides show no statistical difference from 15 seconds onwards, which indicates that the coatings with fluoroionophore **4.3** (negative control and with coupling reagents) are thicker than just the APTES only coating, regardless of the nature of attachment (non-covalent vs covalent). These results also suggest that the coating thickness of fluoroionophore **4.3** on slides with and without amide coupling are similar.

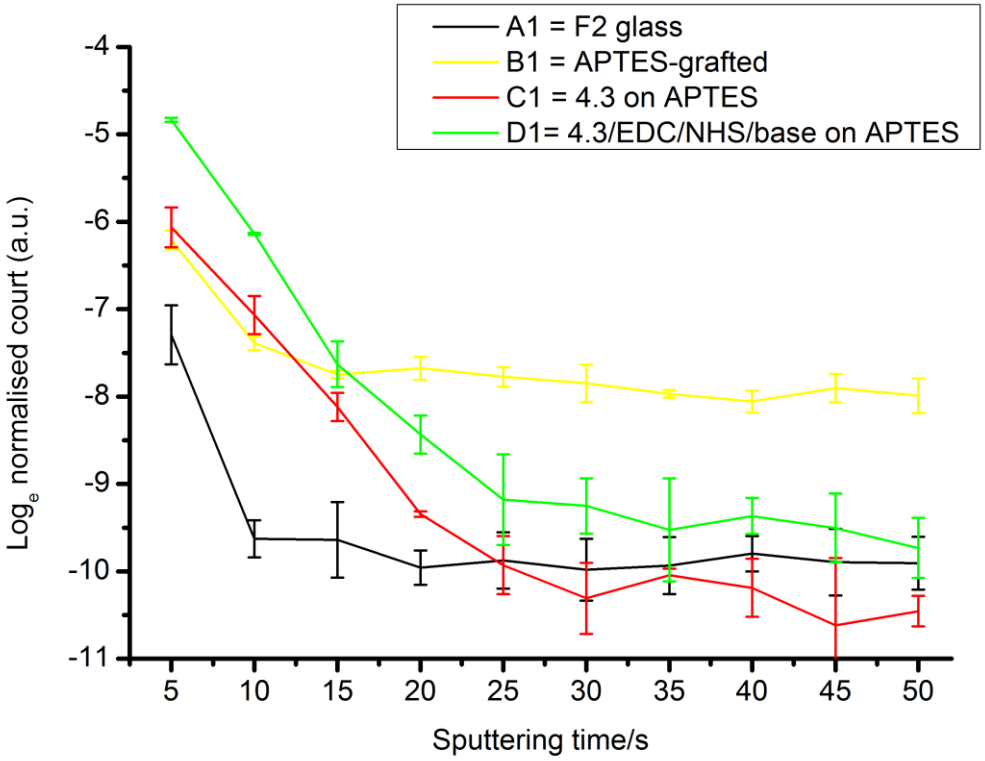

Figure 4.14: CH_4N^+ depth profiles for a (a) A1 = F2 slide, (b) B1 = APTES-grafted F2 slide, (c) C1 = the 4.3 on APTES-grafted F2 slide and (d) D1 = **4.3**/EDC/NHS/base on APTES-grafted F2 glass slide

4.4 Conclusions

This chapter described the feasibility of performing comprehensive surface analyses of surface attachment of fluoroionophores on extruded lead silicate (F2) glass slides. Importantly, these slides were fabricated from the same material of F2 suspended-core fibres (SCFs) and the surface was fire-polished; therefore it is a good model system of the internal surface of SCFs. Surface attachment reactions of fluoroionophores were performed using a functionalisation conditions feasible for SCFs meaning that the observations here are transferable to a glass structure (e.g. SCFs) that are traditionally extremely difficult to characterise. The development of this model system and methods to characterise these surfaces enable optimisation of established attachment strategies to suit glasses and surfaces of interest and the performance of different surface attachment methods to be systematically examined. These include using other silane reagents with different functional groups or polyelectrolytes as the first functional layer, or a single step functionisation using pre-coupled fluoroionophore and silane reagent to be directly grafted onto the glass surface. Furthermore, these characterisation methods are versatile and can be transferred to other glass types which can be extruded to form slides.

The relative quantification of the surface density, surface coverage, nature of attachment and the coating thickness of the specific naphthalimide fluoroionophores were analysed by the fluorescence imaging, XPS and ToF-SIMS, ToF-SIMS imaging and depth profiling. Using the fluorescence imaging, it was found that the attachment of the model fluoroionophore **4.3** could occur with or without coupling reagents. This was confirmed by XPS measurements that showed a strong correlation of the C=O percentage contributions in the high resolution carbon spectrum to fluorescence intensities. Through measurement of the C=O percentage contribution, XPS data was able to identify a difference in surface density between covalent and non-covalent fluoroionophore attachment on APTES coated slides.

The principle component analysis (PCA) of the ToF-SIMS data was shown to be able to distinguish the nature of different coatings; in particular, samples with

fluoroionophore **4.3** covalently coupled on the glass surface showed markedly different PC1 projection scores compared to non-covalent attachment or APTES-only coated slides. ToF-SIMS imaging also revealed that the lead ion distribution could be used as a marker of surface coverage of the coating; the lead distribution is inversely related to the coverage of coating on the glass slide. Furthermore, relative thickness measurements were also performed via depth profiling using ToF-SIMS. It was found that slides with model PET sensor moieties attached show no difference in thickness regardless of the mode of binding used and would thus interact with the evanescent field to the same extent.

4.5 References

1. He, H.R., Mortellaro, M.A., Leiner, M.J.P., Young, S.T., Fraatz, R.J., and Tusa, J.K., *A fluorescent chemosensor for sodium based on photoinduced electron transfer.* Analytical Chemistry, 2003. **75**(3): p. 549-555.

2. Moulder, J.F., Stickle, W.F., Sobol, P.E., and Bomben, K.D., *Handbook of X-ray Photoelectron Spectroscopy*, ed. J. Chastain and J. Roger C. King. 1995, Minnesota: Physical Electronics, Inc.

3. Acres, R.G., Ellis, A.V., Alvino, J., Lenahan, C.E., Khodakov, D.A., Metha, G.F., and Andersson, G.G., *Molecular Structure of 3-Aminopropyltriethoxysilane Layers Formed on Silanol-Terminated Silicon Surfaces.* Journal of Physical Chemistry C, 2012. **116**(10): p. 6289-6297.

4. Valeur, E. and Bradley, M., *Amide bond formation: beyond the myth of coupling reagents.* Chemical Society Reviews, 2009. **38**(2): p. 606-631.

5. Hennig, A., Borcherding, H., Jaeger, C., Hatami, S., Würth, C., Hoffmann, K., Thiele, T., Schedler, U., and Resch-Genger, U., *Scope and Limitations of Surface Functional Group Quantification Methods: Exploratory Study with Poly(acrylic acid)-Grafted Microand Nanoparticles.* Journal of the American Chemical Society, 2012. **134**(19): p. 8268-8276.

6. Wang, L.L., Gaigalas, A.K., and Reipa, V., *Optical properties of Alexa (TM) 488 and Cy (TM) 5 immobilized on a glass surface.* Biotechniques, 2005. **38**(1): p. 127-132.

7. Spath, A. and Konig, B., *Molecular recognition of organic ammonium ions in solution using synthetic receptors.* Beilstein Journal of Organic Chemistry, 2010. **6**.

8. Englich, F.V., Foo, T.C., Richardson, A.C., Ebendorff-Heidepriem, H., Sumby, C.J., and Monro, T.M., *Photoinduced Electron Transfer Based Ion Sensing within an Optical Fiber.* Sensors, 2011. **11**(10): p. 9560-9572.

9. Ratner, B.D. and Castner, D.G., *Electron Spectroscopy for Chemical Analysis*, in *Surface Analysis The principal techniques*, J.C. Vickerman and I.S. Gilmore, Editors. 2009, Wiley: West Sussex. p. 47-109.

10. Wang, P.W., Zhang, L.P., Lu, L., Lemone, D.V., and Kinser, D.L., *Surface Modification of Lead Silicate Glass under X-Ray-Irradiation.* Applied Surface Science, 1995. **84**(1): p. 75-83.

11. Zhu, L., Liew, T., and Chong, T.C., *A novel method for film thickness measurement of perfluoropolyether lubricant by secondary ion mass spectroscopy.* Applied Surface Science, 2002. **189**(1-2): p. 53-58.

Chapter 5

Sodium sensing in SCFs with surface functionalised PET fluoroionophores

5.1 Introduction

As described in Chapter 1, a SCF with surface attached PET fluoroionophores is the more desirable sensor architecture (Operating Scenario B) as it does not require the mixing of fluoroionophores and analytes prior to sensing.

There are two major technical challenges in the fabrication of this sensor architecture. The first challenge is the additional optical attenuation caused by the surface functionalisation. The attenuation in an optical fibre is due to combined effects of surface scattering, glass material absorption, bending, and confinement loss [1]. For all SCF sensors discussed in this chapter, the main sources of attenuation are surface scattering and absorption due to the surface functionalisation [2]. In the context used, there is an negligible attenuation caused by fibre bending or confinement loss due to the high refractive index contrast between the silica glass (1.458 at 589 nm) and analytes (acetonitrile = 1.344 at 589 nm and water = 1.332 at 589 nm). The surface functionalisation procedure can impose extra surface roughness owing to the formation of uneven coatings. In addition, residual coupling reagents or salt from the buffer solution left on the fibre surface after the washing procedure also introduce surface scattering and additional absorption [3]. The increased surface roughness arising from the coating or deposition of other compounds on the surface causes the scattering loss, while the attenuation caused by an absorption is dependent on both the molar extinction of APTES coating and fluoroionophores or fluorophores. Furthermore, the quantities of the fluoroionophore or fluorophore on the SCF surface also contribute to the attenuation. If the attenuation is too high, the SCF cannot deliver light for excitation and the emitted light also cannot transmit back to the detector, thus significantly reducing the available signal.

The second challenge is the photobleaching of the surface attached PET fluoroionophores. The mechanism of photobleaching was described in Chapter 1. In Chapter 2, no photobleaching of fluoroionophores (**2.8**) was observed after optimisation of the excitation power and exposure time. However, the photostability of PET fluoroionophores after immobilisation is unknown.

In the study described in this chapter, the aims were to demonstrate the feasibility of using the surface attached PET fluoroionophore **4.3** in SCFs for sodium sensing and to establish an understanding of the attenuation caused by surface functionalisation. The model fluorophore **5.3** was used instead of fluoroionophore **4.3** in the experiments for understanding attenuation because this approach allows us to separate out any attenuation and variation caused by the ionophore.

Note that while the surface attachment analyses in Chapter 4 were on APTES grafted F2 glass slides; the demonstration of surface attached PET fluoroionophore SCF sensing was conducted on silica glass. The motivation for this change was driven by the results discussed in Chapter 3C, which revealed a higher consistency of the APTES coating on the Piranha solution washed silica glass slides compared with that on unwashed F2 slides. Furthermore, silica glass is more chemically robust compared with lead silicate glass [4, 5].

5.2 Experimental

5.2.1 Silica SCF fabrication

Figure 5.1a shows an SEM image of the silica SCF used in all experiments in this chapter. It is made from LWQ glass produced by Hereaus. The detailed fabrication method was described in Chapter 1. The outer diameter (OD) of the silica SCF is 206 μm and the average hole diameter is 39.5 μm. Figure 5.1b shows the core diameter was measured as 2.8 μm, as defined by a circle that maximally fits within the core [2]. The measurement was performed using Adobe Illustrator CS6.

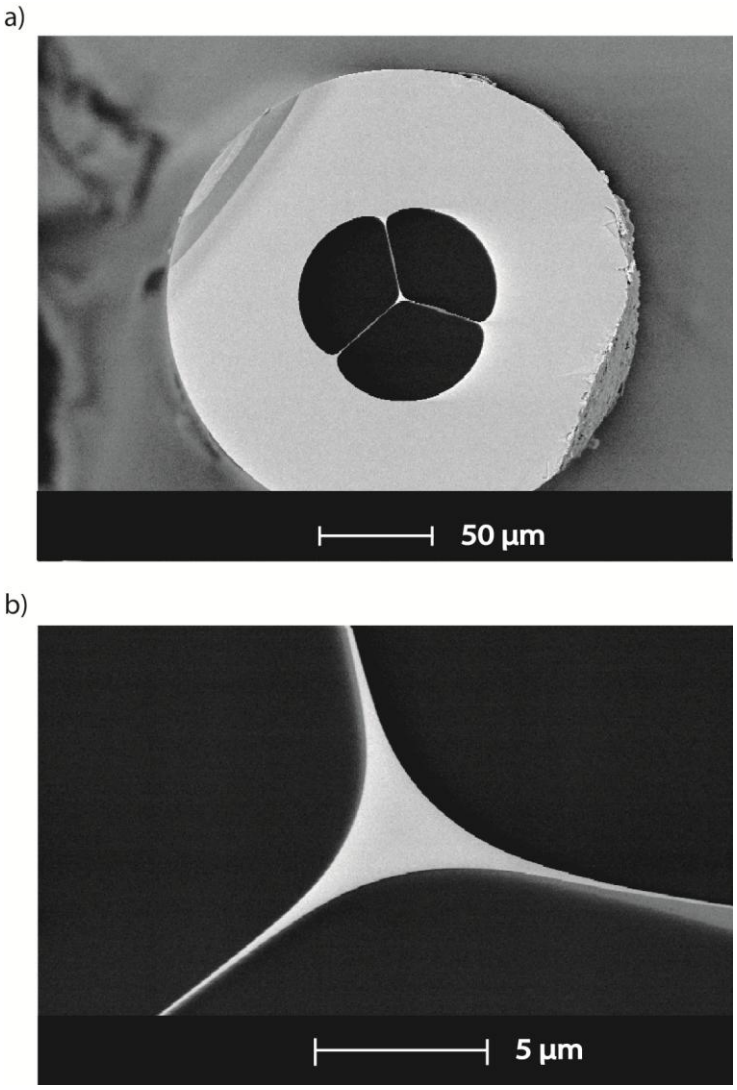

Figure 5.1: (a) A SEM image of a silica SCF. (b) A SEM image of the core of a silica SCF

5.2.2 Synthesis for the surface attachable fluorophore and PET fluoroionophore

The synthesis of surface attachable fluoroionophore **4.3** was described in Chapter 4.

***N*-(*t*-Butyl-benzonate)-4-propylamino-1,8-naphthalimide (5.2)**

Compound **5.1** (595 mg, 1.41 mmol), propylamine (240 µL, 2.92 mmol) and *N*,*N*-diisopropylethylamine (DIPEA) (620 µL, 3.56 mmol) were dissolved in *N*-methyl-2-pyrrolidone (NMP) (15 mL) in a CEM ^{TM} reaction tube. The tube was

sealed and heated at 100°C under microwave irradiation for 5 hours. NMP was removed by distillation under reduced pressure at ~ 65°C and the crude product was dried at ~50°C under high vacuum. The crude product was dissolved in a small amount of chloroform and the ammonium salt was precipitated by an addition of ethyl acetate. The salt was filtered and then purified on silica gel with 1: 3 ethyl acetate:hexane eluate to afford an orange yellow crude product which was triturated with ethyl acetate/ hexane to yield (354 mg, 0.84 mmol, 59%) of **5.2** as orange-yellow crystals. m.p. 140 – 141°C. ^{1}H NMR (300 MHz,$CDCl_3$) δ 8.58 (dd, *J* = 0.96, 7.28 Hz, 1H), 8.47 (d, *J* = 8.24 Hz, 1H), 8.08 (dd, *J* = 1.10, 8.52 Hz, 1H), 7.86 - 7.95 (m, 2H), 7.49 - 7.65 (m, 3H), 6.73 (d, *J* = 8.52 Hz, 1H), 5.40 (s, 2H), 5.24 - 5.34 (m, 1H), 3.38 (dd, *J* = 1.92, 7.14 Hz, 2H), 1.74 - 1.94 (m, 2H), 1.11 (t, *J* = 7.42 Hz, 3H); ^{13}C NMR (75 MHz,$CDCl_3$) δ 165.9, 164.8, 164.2, 149.9, 142.7, 135.0, 131.6, 131.1, 130.1, 129.7, 128.6, 126.2, 124.9, 123.2, 120.3, 110.1, 104.6, 81.0, 45.7, 43.3, 28.4, 22.4, 11.9; UATR FTIR (Diamond/ZnSe) υ/cm^{-1} 3380, 2971, 1996, 1713, 1686, 1638, 1573, 1541, 1479; MS (ESI) *m/z* 467.1 (M^+ + Na, 100%), 468.1 (40%)

4-Propylamino-1,8-naphthalimidylmethyl benzoic acid (5.3)

Trifluoroacetic acid (TFA) (1 mL) and **5.2** (194 mg, 0.46 mmol) were dissolved in dichloromethane (4 mL). The mixture was stirred at room temperature for 1 hr. The solution was diluted with chloroform (25 mL) and the solvent was evaporated. The residue was redissolved in methanol/chloroform mixture (1:9, 50 mL) and the solvent evaporated. The process was repeated three times. The residue was dissolved in methanol/chloroform mixture (1: 9) (60 ml) again and washed with 5% TFA solution (60 mL). The organic phase was dried with $MgSO_4$ and the solvent was removed. The crude product was triturated with ethyl acetate/hexane to yield **5.3** (85 mg, 0.22 mmol, 48%) as yellow crystals. ^{1}H NMR (300 MHz, DMSO-d_6) δ 8.75 (d, *J* = 7.69 Hz, 1H), 8.46 (d, *J* = 6.59 Hz, 1H), 8.29 (d, *J* = 8.79 Hz, 1H), 7.87 (d, *J* = 8.24 Hz, 3H), 7.70 (s, 1H), 7.40 (d, *J* = 8.24 Hz, 2H), 6.81 (d, *J* = 8.79 Hz, 1H), 5.28 (s, 2H), 1.72 (d, *J* = 7.14 Hz, 2H), 0.99 (t, *J* = 7.42 Hz, 3H); ^{13}C NMR (75 MHz, DMSO-d_6) δ 164.4, 163.5, 151.6, 135.2, 131.5, 130.0, 129.9, 129.3, 127.6, 124.9, 121.9, 120.5, 107.3, 104.5, 53.7, 45.0, 42.9,

21.6, 12.0; UATR FTIR (Diamond/ZnSe) υ/cm^{-1} 3382, 1706, 1682, 1630, 1613, 1583, 1550; MS (ESI) *m/z* 433.2 (M^+ + 2Na –H, 100), 434.3 (32).

5.2.3 SCFs functionalisation process

To surface functionalise the surfaces within the confined holes of a suspended-core fibre, fluids containing coating materials must be passed through the fibre and following this the surfaces must be rinsed. This was achieved using a positive pressure filling technique, which not only allows faster fibre filling than a capillary action alone, but also allows the continuous flow of solution. Figures 5.2a shows the positive pressure filling setup, with four individual chambers into which pre-mixed liquids can be placed. Figure 5.2b shows the internal structure of the pressure chamber. The mechanism of the filling setup is illustrated in Figure 5.3. Nitrogen gas was used to increase the pressure of the chamber and force solutions into the holes of SCFs. Also, the concentrations of the solutions in the vials are maintained in the filling process because evaporation of the solvent is minimised under higher pressure and the use of nitrogen ensures that the solutions are stored under an inert atmosphere during the filling process. The SCFs are sealed into the chambers through the use of needles to pierce a rubber stopper. The needle is then removed and the stopper contracts around the fibre re-creating a seal. Before adding any new coating reagents, the pressure chamber lid is removed and a new vial is inserted before again closing the lid; this breaks the pressure seal temporarily.

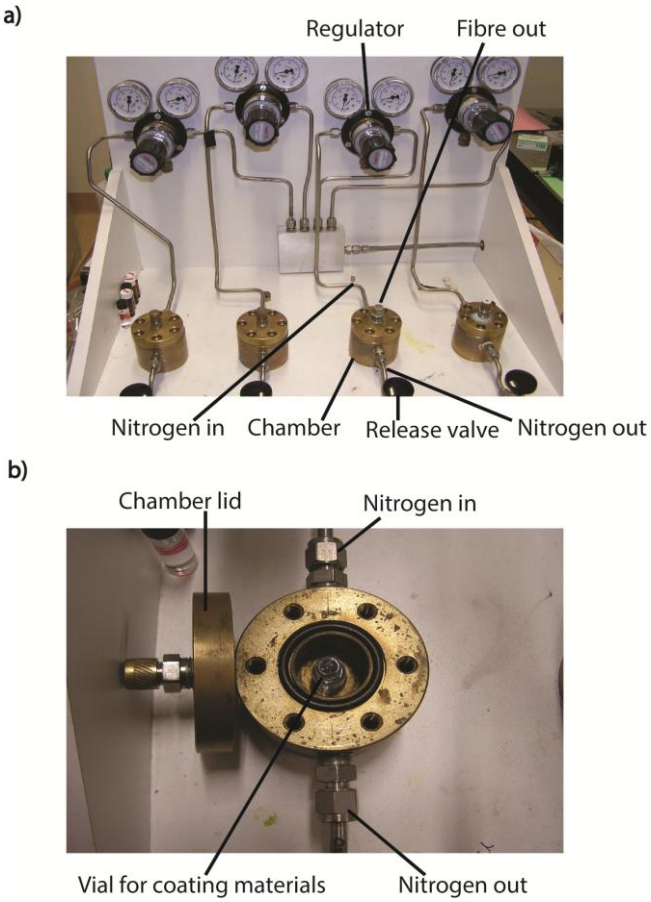

Figure 5.2: (a) The positive pressure filling setup for SCFs. (b) The internal structure of pressure chamber and the vial for coating materials

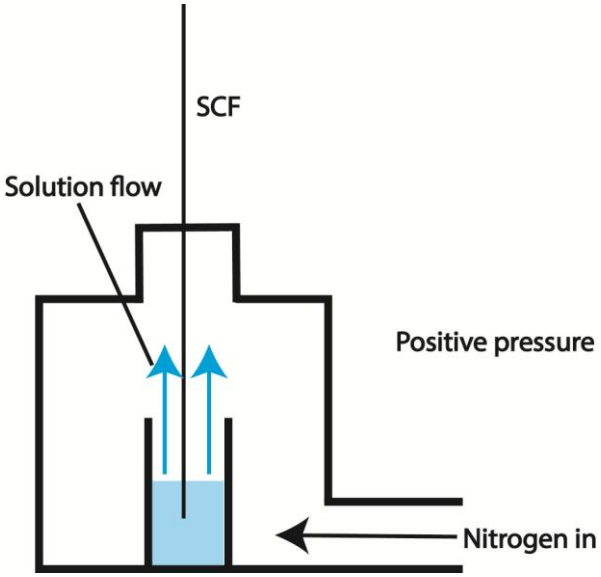

Figure 5.3: The mechanism of the positive pressure filling setup

The functionalisation procedures were as follows. All flushing and drying procedures were performed under a < 20 psi chamber pressure.

1. 5% w/w APTES in anhydrous toluene flush for 5 hours
2. Toluene flush for 20 mins
3. Dry with nitrogen for 20 mins
4. Deionized H_2O flush for 20 mins
5. Air dry overnight
6. (a) Surface attachable fluoroionophore (**4.3**) 0.1 mM /EDC 0.5 mM /NHS 0.5 mM /triethylamine 0.15 mM flush for 3 hours
   (b) Surface attachable fluorophore (**5.3**) 0.1 mM /EDC 0.49 mM/ triethylamine 0.15 mM flush for 3 hours
7. THF flush for 30 mins
8. pH5 buffer (0.7 mM potassium hydrogen phthalate and 0.3 mM sodium hydroxide) flush for 30 mins
9. Deionized H_2O flush for 30 mins
10. Dry with nitrogen gas for at least 1 hour

Note that the Piranha solution wash in silica was not performed due to the safety concern for pressurising hot Piranha solution in an enclosed chamber. This may increase the variation of the APTES coating within silica SCFs.

5.2.4 SCF attenuation measurements

To determine the attenuation of the SCF after surface functionalisation, a cut-back measurement was performed using the setup shown in Figure 5.4. For all functionalised fibres, a 633 nm He-Ne laser from JDS Uniphase was used and attenuated to 140 – 146 μW. The light source was first aligned to illuminate the cladding of the SCF. The light was then aligned to the core so that when the output light from the other end of the fibre was imaged onto a white card the fraction of the power launched into the central triangular core was maximised and light in the cladding minimised. Conductive carbon paint, which is known as DAG, was coated onto the outside of SCF to remove any residual cladding light. The power was subsequently maximised by fine tuning the nanostage with the output of the fibre directly coupled into the integrating sphere. At the completion

of the optimisation the final coupled power was recorded. The SCF was then cleaved at the output end of the fibre and then the power was measured after each cleave. Note that particular care was taken to ensure that the alignment of the light into the input end of the fibre was not disturbed when the cleaves were made. The slope of the power change as the function of length is the optical loss of the SCF. Three loss measurements were performed on the fluorophore **5.3** functionalised SCF. The error was calculated by the least squares method.

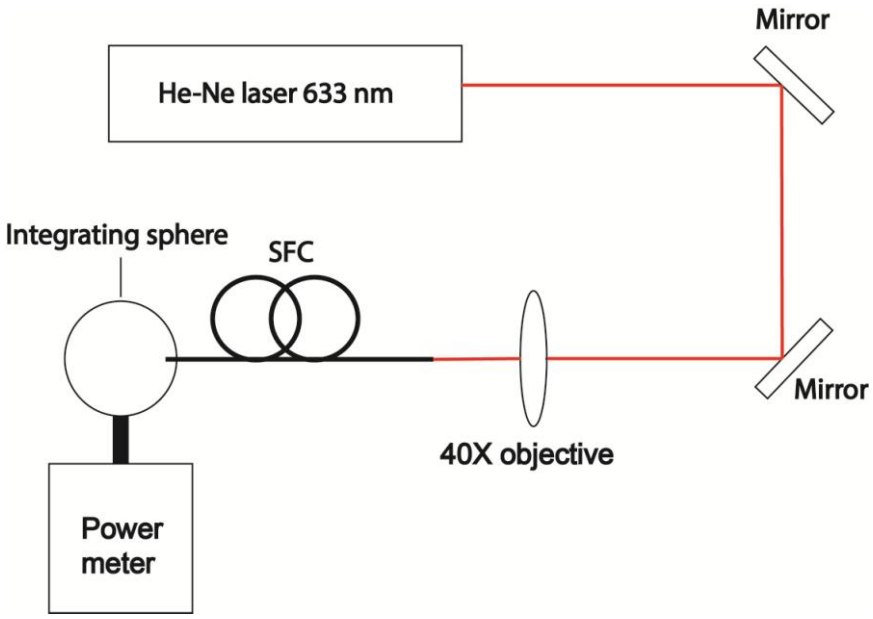

Figure 5.4: Set-up for functionalised SCF loss measurements

5.2.5 Sodium ions sensing with a surface attached PET fluoroionophore (4.3) in SCF

Sodium sensing experiments were performed using functionalised SCFs. 24 cm of SCF was used for each measurement. Figure 5.5 shows a diagram of the optics setup of the experiment as shown in Chapter 2 (3rd generation optics setup); the blue line shows the laser beam path and the green line is the back fluorescence beam path. The excitation source was a Toptica iBeam Smart-S 473S. A shutter was used to control the exposure of fluorophores in order to minimise photobleaching of fluorophores. The neutral density filter wheel provides a quick way to coarsely control the laser power coupled into the SCF. The 40x objective is to focus the beam into the core of the SCF. The measured power at the 40x lens

before the fibre was 14.7 µW using a neutral density filter with an optical density (OD) of 2 (1 % transmission) and 1.535 µW at for OD = 3 (0.1 % transmission). A backward collection mode was used in this experiment, where the emission light was collected at the input end of the SCF [6]. The dichroic mirror and long pass filter were used to isolate the excitation wavelength from the emission.

Light was launched into the core of the SCF using the method described in Chapter 2. 10 spectra were taken with a 16 ms exposure time for each spectrum. Spectra of the unfilled SCFs were taken first. Then acetonitrile with tetrabutyl ammonium perchlorate (0.1 M) and sodium was then filled into the SCF for 1 min by a capillary action. This filling duration approximately half fills the 24 cm fibre (the average hole diameter is 39.5 ± 1 µm). Full filling was avoided to prevent deposition of salt at the laser input end, which can adversely affect the optical coupling [3]. Immediately after the filling process, 10 spectra were taken with 16 ms exposure time for each spectrum.

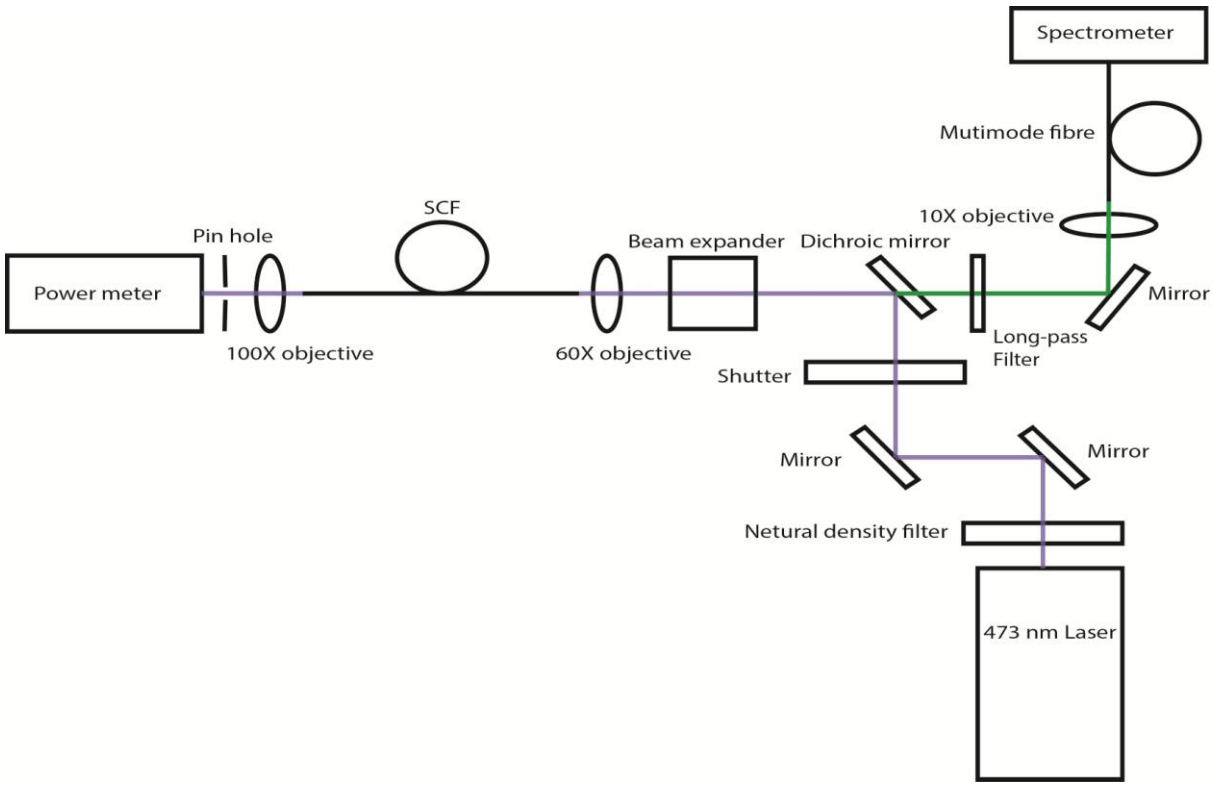

Figure 5.5: Schematic diagram of the optical set-up for the fluorescence measurements

5.2.6 Data analyses for the sodium ions sensing experiments

The percentage fluorescence enhancement, which is, the increase in fluorescence when filled with analyte in solution, of each piece of SCF was calculated by Equation 5.1. Each average spectrum was integrated from 480 nm to 700 nm.

$$\%FE = \left(\frac{I_{Filled} - I_{Empty}}{I_{Empty}}\right)100\%$$

(Equation 5.1)

%FE = Fluorescence enhancement relative to a coated but unfilled SCF.

I_{Filled} = Integrated fluorescence intensity of the average spectra of the SCF filled with sodium solution

I_{Empty} = Integrated fluorescence intensity of the average spectra of the SCF without sodium solution

5.2.7 Sample preparation and measurement procedures for using the spectrofluorometer

This measurement procedure was identical to that described in Chapter 2, Section 2.2.1.

5.3 The theory behind fluorescence enhancement and sodium ion concentration

As shown in Chapter 4, the absolute quantity of the surface attached fluoroionophore within a SCF is difficult to quantify and it is also unlikely to be consistent between SCFs. Therefore, normalisation methods are necessary. Since no reference signal is available in the SCF, the only feasible method is to normalise the difference of emission intensity of the sodium-loaded and unloaded functionalised SCF with the emission intensity of the unloaded functionalised SCF. This is assumed in this work that the quantity of the surface attached fluoroionophore is constant before and after filling of analyte. This is because the filling of the analyte is just by capillary action and no flushing was performed.

To understand the theory of using fluorescence enhancement (FE) to quantify the concentrations of sodium ions, we first note the equation (Equation 5.2) that describes the relationship between a fluorescence intensity and a fluorophore concentration measured in cuvette by fluorescence spectroscopy, where $I(l)$ is a fluorescence intensity generated from a cell of length l, k is a geometric instrument factor, Φ is the fluorophore quantum efficiency, I_o is a incident excitation intensity at a different wavelength than fluorescence, ε is a molar extinction coefficient and c is a concentration of the fluorophore in cuvette [7].

$$I(l) = k\Phi I_o(1 - e^{-\varepsilon lc}) \qquad \text{(Equation 5.2)}$$

Expanding Equation 5.2 as a Maclaurin series (Equation 5.3) yields:

$$I(l) = k\Phi I_o\left[\varepsilon lc - \frac{\varepsilon lc}{2!} + \frac{\varepsilon lc}{3!} + ...\right] \qquad \text{(Equation 5.3)}$$

If the absorbance (εlc) is <0.05 the relative error caused by only keeping the first term is 0.13 %.

$$I(l) = k\Phi I_o \varepsilon lc \qquad \text{(Equation 5.4)}$$

Therefore, for low concentrations of fluorophore the fluorescence intensity has a linear relationship to concentration. Equation 5.4 also assumes that the fluorophore concentration is sufficiently low such that reabsorption is negligible [7].

Equation 5.4 is also applicable to fluorophore functionalised SCFs after including a fluorescence capturing fraction (*FCF*) and a power fraction of guided light outside the glass (*PF*) into the equation. A SCF specific parameter K_{fibre} is represented by Equation 5.5.

$$K_{fibre} = k(FCF)(PF) \qquad \text{(Equation 5.5)}$$

where K_{fibre} represents the capacity of a SCF to transmit the excitation light and to capture the emission light. k is the geometric instrument factor . *FCF* is the fraction of photons which are captured into the guided mode of SCF and *PF* is the fraction of the guided light which propagates in the evanescent field [8]. The *FCF*

and *PF* are mainly determined by the SCFs geometry and the refractive index difference between the glass and solvent of the analyte [9].

Equation 5.6 represents the relationship between the fluorescence intensity and surface fluorophore density where the path length (*l*) is equal to the fibre length (*L*), I_o is the excitation intensity through the fibre and *c* is replaced by a surface fluorophore concentration (σ). σ is given in terms of number of moles of fluorophores/fluoroionophores per unit volume on top of the APTES layer on SCF. It is assumed that the fluorophore/fluoroionophore layer on top of APTES is not a monolayer; therefore there is a certain thickness, which was not measured in this project. The fluorophore concentration in the coating (σ) can be calculated from the surface fluorophore density (mol per unit area) if the thickness of the fluorophore/fluoroionophore is known.

$$I(L) = K_{fibre}\Phi I_o \varepsilon L \sigma \qquad \text{(Equation 5.6)}$$

The fluorescence intensity (*I*) emitted from the fluorophores and captured by the SCF is reduced by fibre attenuation factors α_{sc} and α_{ab}. α_{ab} is associated with the surface fluorophore density and its effects have been included in the calculation of the *PF* and *FCF*. α_{sc} is closely related to the surface roughness, and can also include inherent fibre loss due to glass impurities and Rayleigh scattering [1]. After considering the additional factors of attenuation, a new SCF specific parameter, K_{eff}, is given as Equation 5.7. Note that this term should be multiplied by a factor of two, due to the return trip of the excitation-fluorescence along the fibre, but then divided by two as, on average, the fluorescence is generated at the mid-point of the fibre assuming low loss and low absorption.

$$K_{eff}(L) = k(FCF)(PF)e^{-\alpha_{sc}L} \qquad \text{(Equation 5.7)}$$

By combining Equations 5.6 and 5.7, the fluorescence intensity (*I*) detected from the functionalised SCF by the spectrometer is described by Equation 5.8

$$I(L) = k(PF)(FCF)\Phi I_o \varepsilon L \sigma e^{-\alpha_{sc}L} \qquad \text{(Equation 5.8)}$$

Within the SCF, the binding of the sodium ion and fluoroionophore **4.3** is represented by the Equation 5.9:

$$[H] + [G] \underset{}{\overset{K_{binding}}{\rightleftharpoons}} [H\text{-}G] \quad \text{(Equation 5.9)}$$

where [H] is the concentration of the host which in this case is the surface concentration of fluoroionophore **4.3**; [G] is the concentration of the guest, in this case it is sodium ion in solution; [H-G] is the concentration of the complex of fluoroionophore **4.3** and sodium ions; and $K_{binding}$ is the binding constant. The fluorescence emissions are from both fluoroionophore **4.3** -sodium complexes and fluoroionophore **4.3**. The binding constant determines the contribution ratio of both fluorescent compounds. The overall fluorescence intensity captured from the filled (superscript F) SCF and empty (superscript E) SCF are represented by Equation 5.10 and Equation 5.11.

$$I^F = I^F_{[H-G]} + I^F_{[H]} \quad \text{(Equation5.10)}$$

$$I^E = I^E_{[H]} \quad \text{(Equation 5.11)}$$

Equation 5.1 is rewritten by combining Equation 5.10 and 5.11 to yield Equation 5.12

$$FE = \frac{I^F_{[H-G]} + I^F_{[H]} - I^E_{[H]}}{I^E_{[H]}}$$

(Equation5.12)

Substitution of Equation 5.8 into 5.12 and rearrangement of the equation yields Equation 5.13.

$$FE = \frac{(PF^F)(FCF^F)(\Phi^F_{[H-G]}\sigma^F_{[H-G]} + \Phi^F_{[H]}\sigma^F_{[H]})\varepsilon^F e^{-\alpha^F_{sc}L}}{(PF^E)(FCF^E)\Phi^E_{[H]}\sigma^E_{[H]}\varepsilon^E e^{-\alpha^E_{sc}L}} - 1 \quad \text{(Equation 5.13)}$$

The molar extinction coefficients (ε) and quantum efficiencies (Φ) of fluoroionophore **4.3** in air and in solution are not the same; therefore two independent constants are required in Equation 5.14 to describe ε and Φ in filled and empty conditions respectively. Likewise, the scattering loss, power fraction, fluorescence capturing fraction are different for filled fibre and empty fibre cases. This is due to the difference in refractive indices. The molar extinction coefficient

(ε) of an ideal PET fluoroionophore is independent to the ion (e.g. sodium) concentration, therefore $\varepsilon_{[H\text{-}G]Filled}$ and $\varepsilon_{[H]Filled}$ are the same [10].

To simplify Equation 5.14 we can define an efficiency term, β, which represents the difference in performance of the fibre comparing filled and unfilled scenarios and is effectively constant between different experiments if the fibre geometry is constant. The ratio of extinction coefficients is also included as this is also constant. This is defined as given in Equation 5.15.

$$\beta = \frac{(PF^F)(FCF^F)\varepsilon^F e^{-\alpha_{sc}^F L}}{(PF^E)(FCF^E)\varepsilon^E e^{-\alpha_{sc}^E L}} \qquad \text{(Equation 5.15)}$$

Substituting Equation 5.15 into Equation 5.14 gives:

$$FE = \beta \frac{(\Phi_{[H-G]}^F \sigma_{[H-G]}^F + \Phi_{[H]}^F \sigma_{[H]}^F)}{\Phi_{[H]}^E \sigma_{[H]}^E} - 1 \qquad \text{(Equation 5.16)}$$

We also assume that the surface densities of the fluoroionophores of the load and unloaded SCF are constant for the same SCF.

$$\sigma_{[H]}^E = \sigma_{[H]}^F + \sigma_{[H-G]}^F \qquad \text{(Equation 5.17)}$$

Substituting Equation 5.17 into Equation 5.16 and rearranging gives the following expression for the fluorescence enhancement.

$$FE = \frac{\sigma_{[H-G]}^F}{\sigma_{[H]}^E}\left[\frac{\beta(\Phi_{[H-G]}^F - \Phi_{[H]}^F)}{\Phi_{[H]}^E}\right] + \left[\frac{\beta\Phi_{[H]}^F}{\Phi_{[H]}^E} - 1\right] \qquad \text{(Equation 5.18)}$$

Equation 5.18 shows that there is a linear relation between the fluorescence enhancement (FE) and the ratio between the concentration of H-G complexes ($\sigma^F_{[H\text{-}G]}$) in a filled SCF and fluoroionophores ($\sigma^E_{[H]}$) in an empty SCF. The concentration of H-G is correlated to the concentration of sodium ions according Equation 5.9. However, the FE is not always correlated to sodium ions concentration. Figures 5.6a to 5.6d show four different hypothetical scenarios with two different surface densities of fluoroionophores. Figures 5.6a and b show the scenarios with the concentration of fluoroionophores in excess to sodium ions. The ratio of $\sigma^F_{[H\text{-}G]}$ to $\sigma^E_{[H]}$ in Figure 5.6a is 0.6, whereas in Figure 5.6b the ratio is 0.75, despite the overall sodium ion concentration being the same.

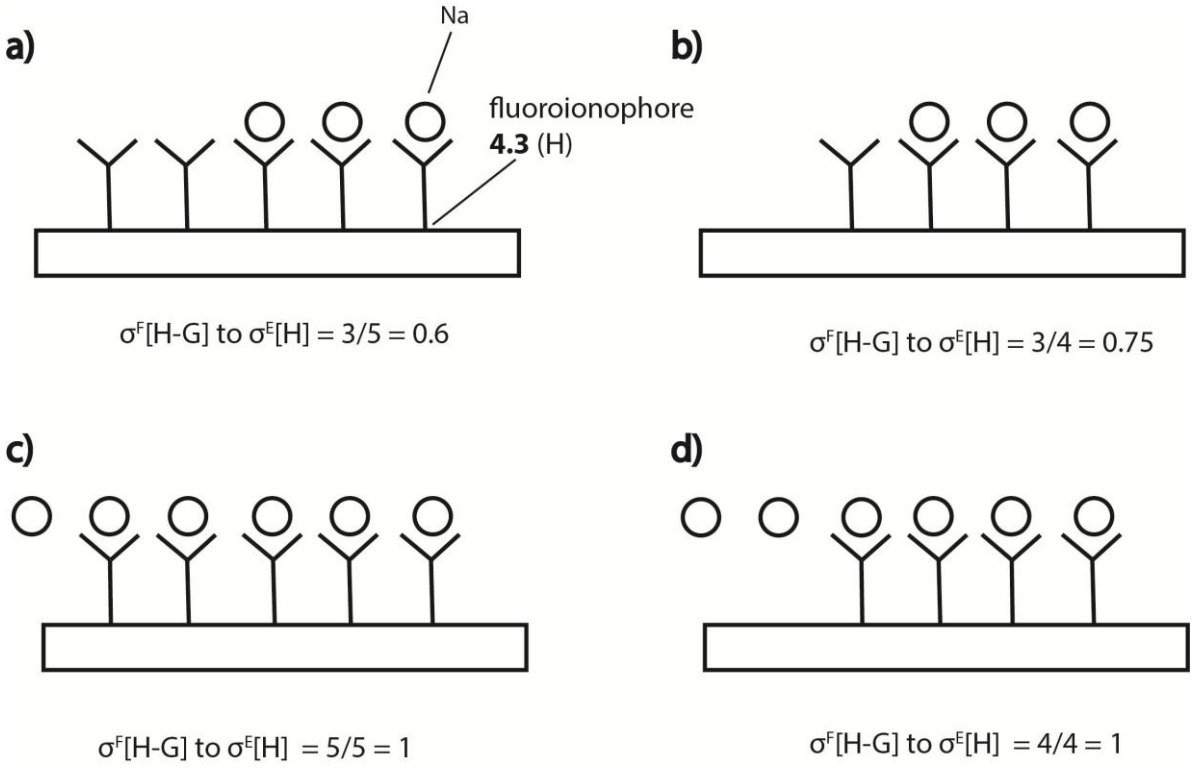

Figure 5.6: Hypothetical scenarios of fluoroionophore **4.3** (host = H) binding with the same concentration of sodium ions (Na, guest = G)

Based on previously reported data, the surface amine group concentration from APTES coated on silica glass using toluene as the solvent is ~2.5 pmolmm^{-2} [11]. Based on Figure 5.1b, the surface area on the core of a 12 cm length of SCF (half filled) is ~ 2.1 mm^2 and thus the quantity of the maximum number of attached fluoroionophores is ~4.5 pmol. The minimum concentration of the sodium ions in the experiment is 2.3 ppm and the summation volume of three holes in SCF shown in Figure 5.1a is ~4.4 x 10^{-7} L, the number of mole of sodium ion is ~44 pmol. Therefore, the number of moles of sodium ion is considerably higher than the maximum number of fluoroionophore moieties that can be attached to the surface of the core by approximately a factor of 10; thus in this case the quantity of fluoroionophore is the limiting factor.

Figures 5.6c and 5.6d show scenarios in which the quantity of fluoroionophore is the limiting factor, the ratio of $\sigma^F_{[H\text{-}G]}$ to $\sigma^E_{[H]}$ is independent to the variation of surface concentration of fluoroionophores. Nevertheless, it also means that the FE is independent to the change in sodium ion concentration because all the fluoroionophores is saturated. A calibration curve can still be established because

the filling time was fixed at 1 min and the measurement time was 0.144 s, the time lag between removing the solution and starting the spectrometer was within 10 to 15 s. This time lag is the main source of variation. The sodium ion concentration differences result in differences for the initial rate of binding. Figure 5.7 shows a hypothetical graph of the normalised concentrations of H-G complexes as a function of time. It shows that as long as the times of the measurements are constant and the fluoroionophores were not yet saturated, different sodium ion concentrations can generate different concentrations of the H-G complexes.

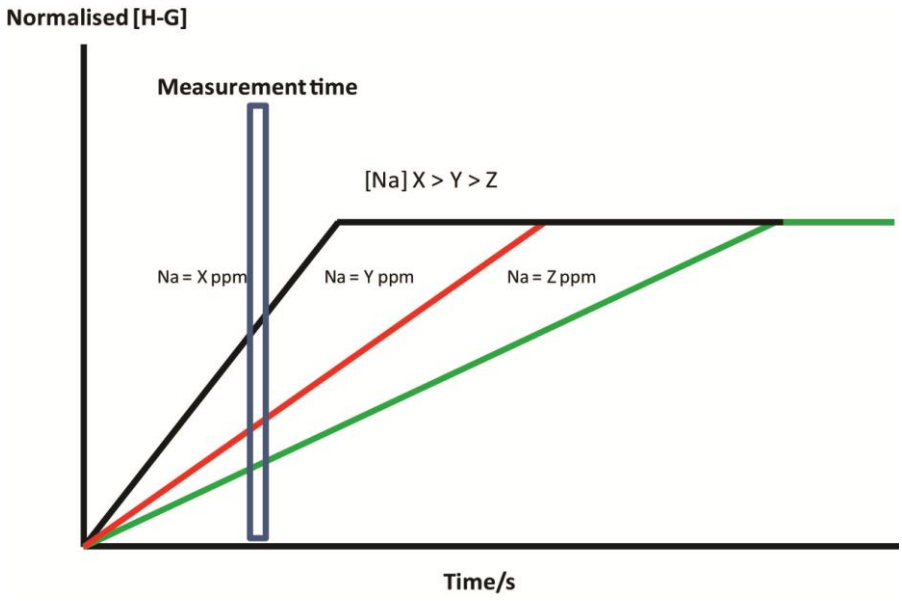

Figure 5.7: A hypothetical graph showing the normalised concentration of an H-G complex as a function of time (s)

5.4 Results and discussion

5.4.1 Synthesis of 4-propylamino-1,8-naphthalimidylmethyl benzoic acid (5.3)

To measure the attenuation caused by the immobilisation of fluorophores without interference from the scattering attenuation caused by sodium ions, model fluorophore **5.3** was synthesised. The synthesis of **5.3** is outlined in Scheme 5.1. The synthesis of **5.1** was described in Chapter 4. A microwave heated nucleophilic aromatic substitution reaction was used to efficiently couple propylamine to compound **5.1,** which was then deprotected to afford model fluorophore **5.3**. Figure 5.8 shows the absorption spectrum of fluorophore **5.3** in CH_3CN with 1% MeOH (0.03 mM) to aid solubility, which shows that the wavelength of the excitation laser (473 nm) used for experiments in Chapter 2 is within the absorption peak.

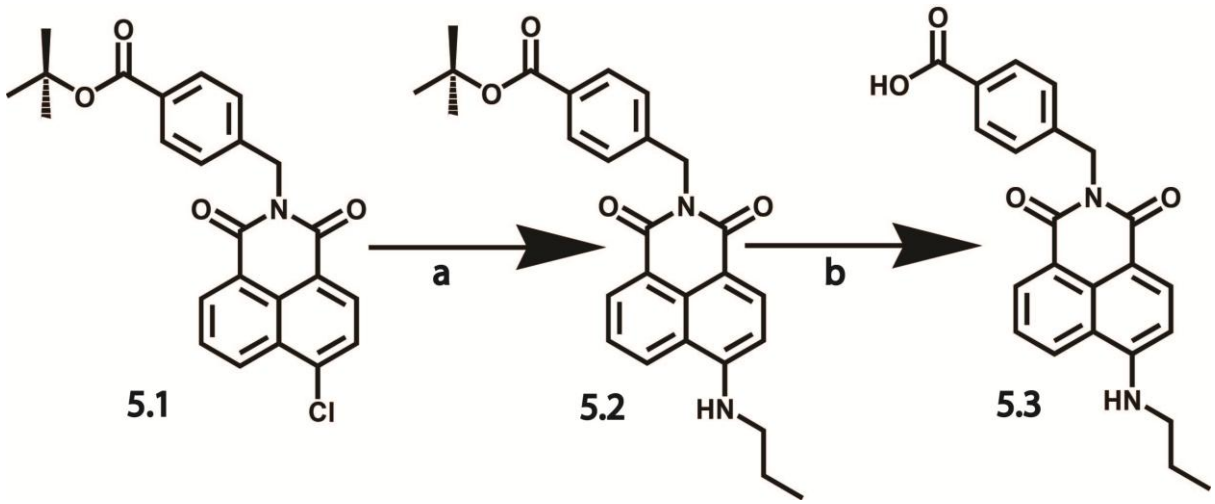

Scheme 5.1: Synthesis of 4-propylamino-1,8-naphthalimidylmethyl benzoic acid (**5.3**). a) propylamine, NMP, DIPEA, 5 hrs in microwave at 100 °C, 59%. b) TFA, DCM, 1.5 hours at room temperature, 48%

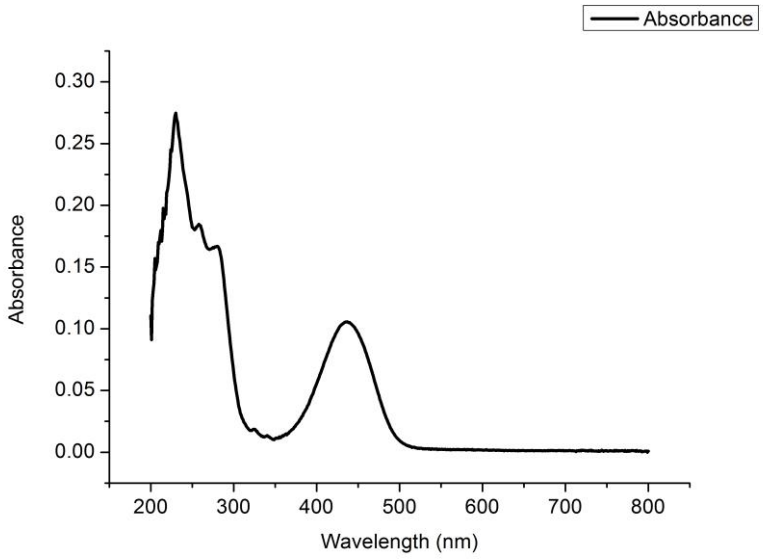

Figure 5.8: An absorption spectrum of fluorophore **5.3** in CH_3CN with 1% MeOH

5.4.2 Quantification of the scattering attenuation caused by surface functionalisation

To quantify the attenuation caused by the surface roughness introduced from the surface functionalisation procedure, fluorophore **5.3** was attached onto the SCF surface using a similar attachment procedure to fluoroionophore **4.3**.

The attenuation was measured using a 633 nm He-Ne laser source, which allowed the scattering attenuation to be mostly separated from the attenuation caused by the absorption of the coating. Figure 5.8 shows the absorption spectrum of fluorophore **5.3** in CH_3CN with 1% MeOH, which is measured by Cary spectrofluorometer. It shows that 633 nm is outside the absorption spectrum of the fluorophore.

Table 5.1 shows the result of all three loss measurements of SCF functionalised with fluorophore **5.3** at 633 nm. The average attenuation of functionalised SCFs was 0.76 dBm^{-1}. The attenuation of the silica SCF without functionalisation was 0.43 dBm^{-1}. The attenuation after the functionalisation is higher because the surface coating is rougher than the initial fire polished glass surface.

Despite the attenuation increases of a factor of 1.8, the increase in the attenuation was less than the previously reported value for a 3-mercaptopropyltrimethoxysilane functionalised F2 SCF [12]. This may be because the functional coating on silica SCF is more homogeneous compared with F2 SCF, therefore it introduce less surface roughness.

Table 5.1: Fibre loss measurements for **5.3** functionalised SCFs at 633 nm

	Loss dBm^{-1}
SCF 1	0.95 ± 0.08
SCF 2	0.63 ± 0.08
SCF 3	0.71 ± 0.04
Uncoated SCF	0.43 ± 0.03

5.4.3 Sodium sensing using SCFs with surface functionalised PET fluoroionophore

Figure 5.9a shows the average integrated fluorescence intensity of five 24 cm long SCFs functionalised with PET floroionophore. The intensity varied from 19772 a.u. to 51264 a.u.. It reveals that the fluorescence intensity was inconsistent between SCFs functionalised under the same condition.

While the inconsistency of the fluorescence intensity between different SCFs is due to the inconsistency of the APTES coating and the amide coupling reaction to attach the fluoroionophores, it can also be attributed to the change in the concentration of fluoroionophores during the pressure filling process. Figure 5.9b shows the trend of averaged integrated fluorescence intensity of three 14 cm sections (B1–B3) of SCF cut from a ~ 60 cm SCF functionalised with model fluorophore **5.3**. The section which was the closest to the vial of the solution in the filling setup showed the highest fluorescence intensity. The intensity decreased when the section was further away from the vial. This result suggests there was a concentration gradient of the fluorophore during the SCF filling process. This concentration gradient is possibly due to the physisorption and coupling of the fluorophore to the APTES coated surface within a small volume tube (the volume of one SCF hole is ~5.1×10^{-8} L).

The inconsistency of the fluoroionophores attachment caused a different baseline fluorescence level for each piece of fibre; therefore the sodium ions sensing cannot be demonstrated by comparing different pieces of functionalised fibre produced by a standard protocol used in Chapter 2. Instead it would be necessary to compare pieces of fibre taken from the same location relative to the filling set up.

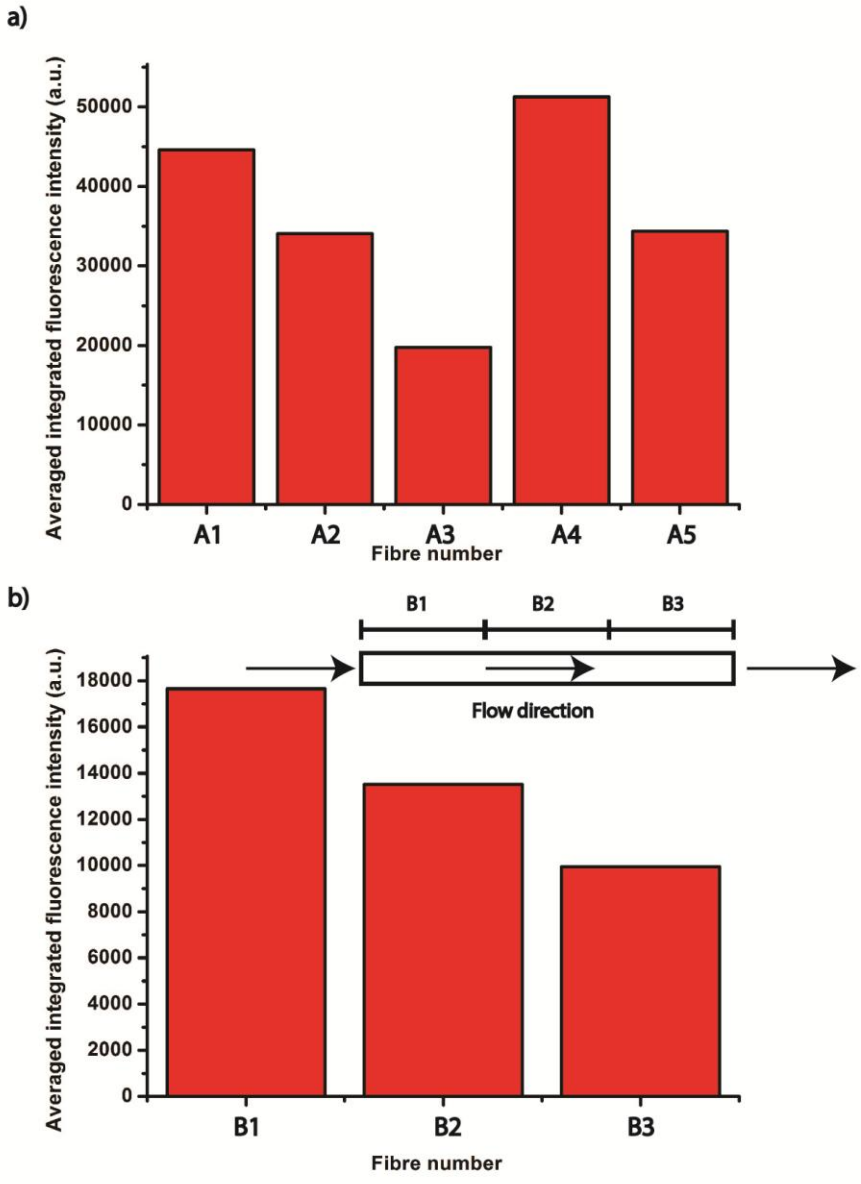

Figure 5.9: (a) Unfilled fluoroionophore **4.3** functionalised SCFs used in the first sodium ions sensing experiment. (b) Average integrated fluorescence intensity of fluorophore **5.3** functionalised SCFs. The insert shows the position of SCF section B1–B3 and the solution flow direction in the pressure filling setup

The inconsistency of the baseline fluorescence between functionalised fibres is due to a combination of the following factors:

1. Surface fluoroionophore concentration (σ)

   The fluoroionophore concentration attached to the surface is not consistent in each fibre.

2. Attenuation caused by surface scattering (α_{sc})

   The surface roughness after functionalisation is different for each fibre, which causes different scattering loss.

3. Optical coupling stability

   Any variation of the coupling position of the excitation light into the core of the SCF affect the excitation intensity (I_o) (Equation 5.8) propagating along the core, which attributes to the change in the emission intensity.

4. Laser beam power

   Power fluctuations of the excitation light directly affect the the excitation intensity (I_o) (Equation 5.8) which attributes to the change in emission intensity.

5. Photostability of the fluoroionophore

   Photobleaching of the fluoroionophore diminishes the emission intensity of the fluoroionophore. However, fluoroionophore **4.3** did not show any photobleaching during the experiment based on the results shown and therefore this parameter is considered irrelevant in considering the inconsistency of the baseline fluorescence.

Since the baseline fluorescence intensity is variable, all results presented are expressed as a percentage fluorescence enhancement (%FE) (Equation 5.1), which is the ratio of the fluorescence intensity of fluoroionophore **4.3** with sodium ions to the fluorescence intensity of fluoroionophore **4.3** in an empty SCF. Note that the FE is also related to the incubation time as discussed in Section 5.3, each measurement was immediately started after 1 min solution filling. Figures 5.10a

to 5.10e show the pairs of average fluorescence spectrum for unfilled and analyte solution filled SCFs. Fluorescence enhancement was observed in each measurement. Figure 5.11a and 5.11b show the fluorescence enhancement calculated from Equation 5.1. The background measurement (0 ppm of sodium ions) shows higher fluorescence enhancements compared with samples with 2.3 and 6.9 ppm of sodium ions. If the 0 ppm sample is excluded in the linear regression, the correlation coefficient (R^2) is 0.996. This result indicates a linear calibration curve can be established using fluoroionophore **4.3** functionalised SCFs.

The over 40% fluorescence enhancement observed for the 0 ppm sample can be attributed to the interaction of the fluoroionophore with surface ammonium groups from the APTES layer. In Chapter 3C, we have discussed the presence of ammonium ions on APTES coated surfaces. Ammonium ions on the surface are the only possible cations which can bind to the fluoroionophore in the 0 ppm sample; there are no added sodium ions in solution. The fluorescence enhancement of the 0 ppm sample suggests that the interaction of the fluoroionophore with surface ammonium groups is more favourable in acetonitrile than that in the absence of solvent. Nevertheless, the measured fluorescence enhancements of the samples with 2.3 and 6.9 ppm sodium ions have lower values than the 0 ppm sample. This may be related to the presence of sodium ions in acetonitrile decreasing the extent of the interaction of the fluoroionophores with the surface ammonium ions by changing the orientation of the surface attached fluoroionophores (perhaps through changes in the polarity of the solution). When the fluoroionophores are directed away from the surface, the fluorescence enhancement is only dependent on the sodium ion concentration.

.

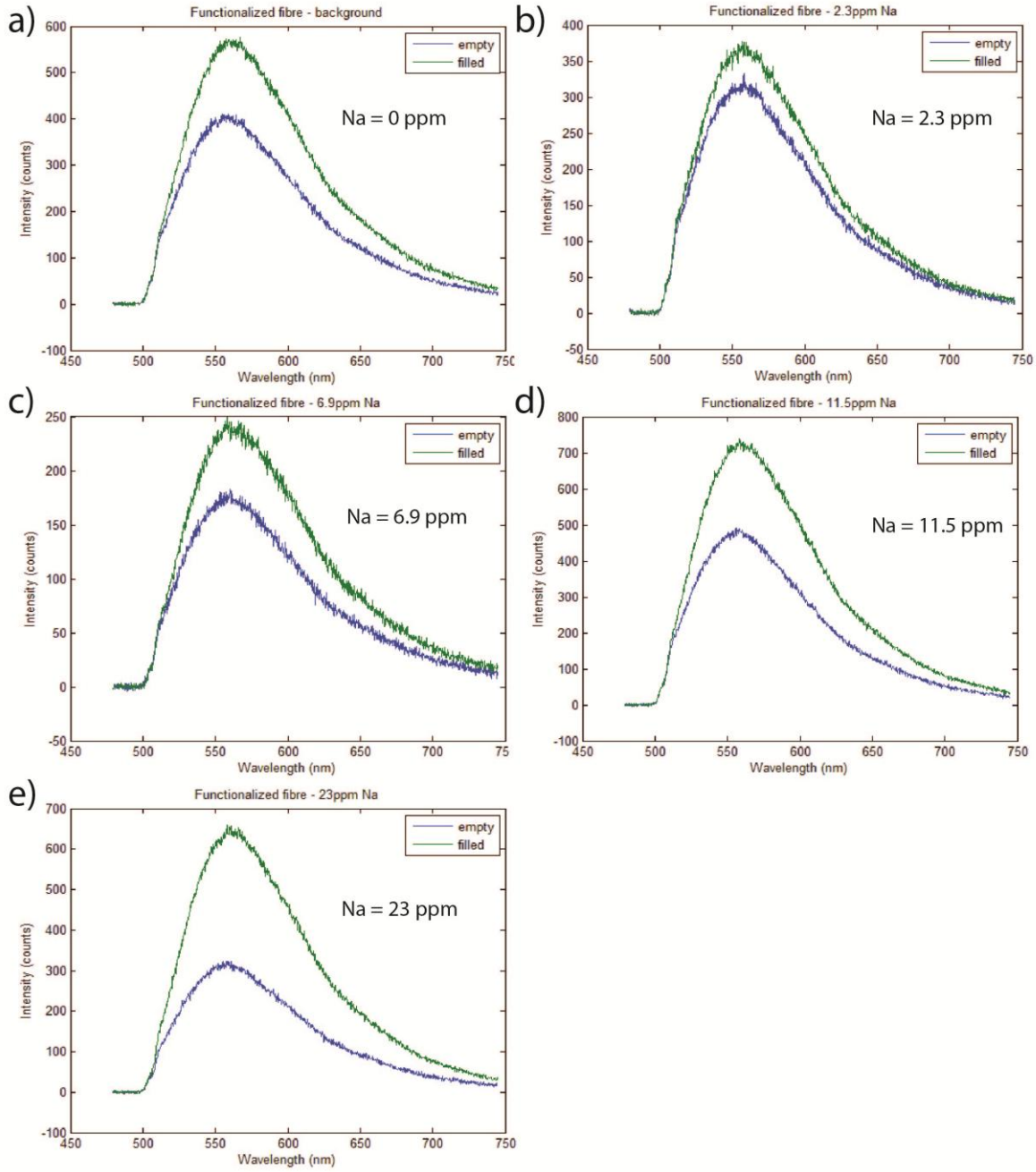

Figure 5.10: Average fluorescence spectra of the empty and filled SCF with 0 ppm of Na (a), 2.3 ppm of Na (b), 6.9 ppm of Na (c), 11.5 ppm of Na (d) and 23 ppm of Na (e) (Figures prepared by Mai-Chi Nguyen)

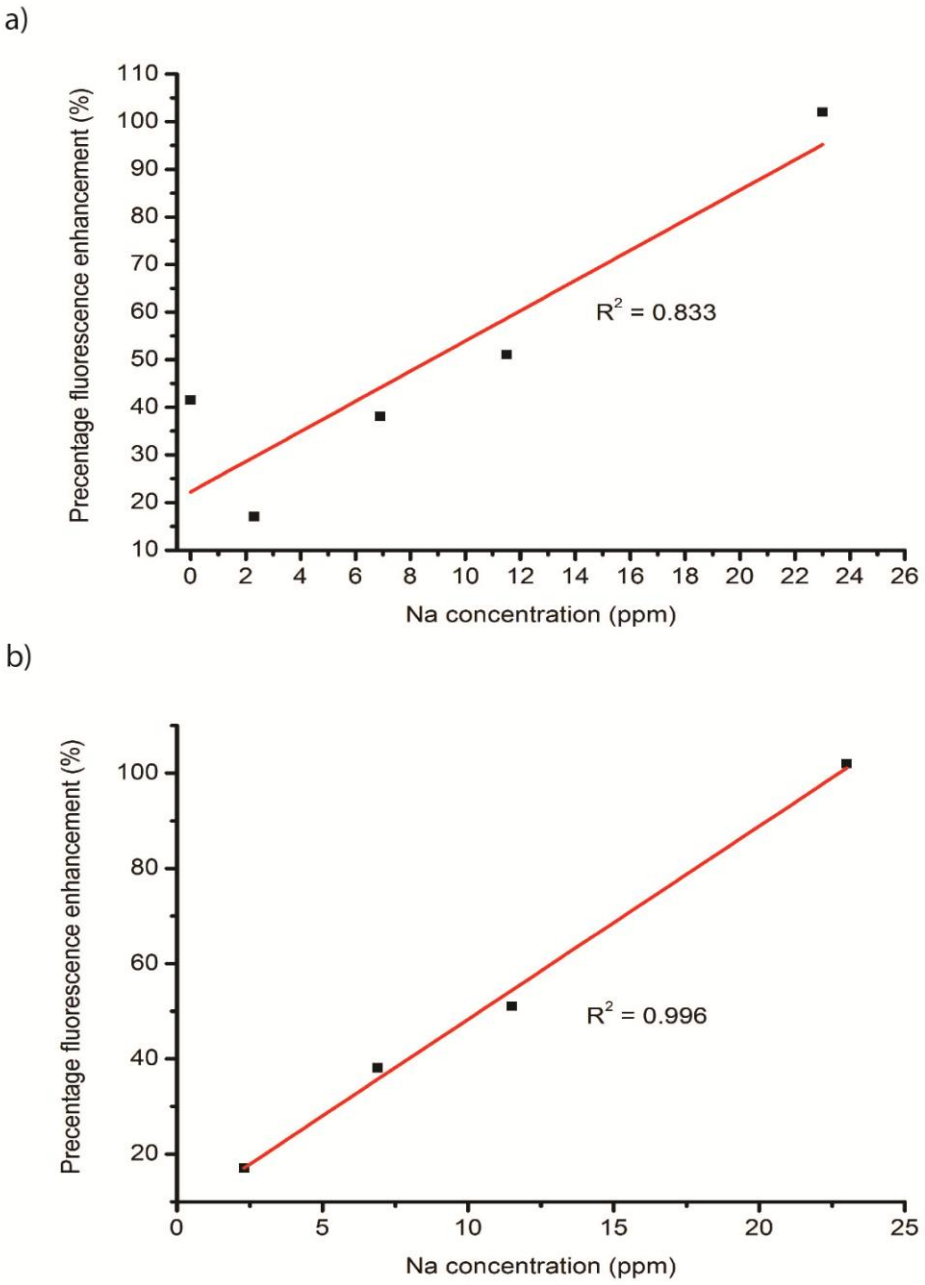

Figure 5.11: Linear regression of percentage fluorescence enhancement against sodium ion concentrations (a) including the 0 ppm Na ions measurement and (b) excluding the 0 ppm Na ions measurement

In addition to demonstrating the response to Na ions by the surface attached fluoroionophore, the photostability of the fluoroionophore over a typical measurement time (144 ms, as shown in Chapter 2) is also an important criterion. Figures 5.12a, 5.12c, 5.12e, 5.13a and 5.13c show all fluorescence spectra of the unfilled functionalised SCFs and Figures 5.12b, 5.12d, 5.12f, 5.13b and 5.13d are

spectra for SCFs with 0, 2.3, 6.9, 11.5 and 23 ppm sodium ions in acetonitrile (I =0.1 M). The bottom section of each figure shows the percentage fluctuation of each measurement (all spectra normalised to the first spectrum taken at 0 s). The maximum fluorescence intensity decrease for the empty functionalised SCFs was only 1.5% at Figure 5.12e, but other than this there were no signs of photobleaching. Progressive fluorescence intensity increases (Figures 5.12b, 5.12f, 5.13b and 5.13d) were found in all filled functionalised SCFs except the sample with 2.3 ppm Na (Figure 5.12d). This suggests that the fluoroionophores attached within the SCFs were not saturated during the experiment and hence show a progressive fluorescence intensity increase with the measurement time.

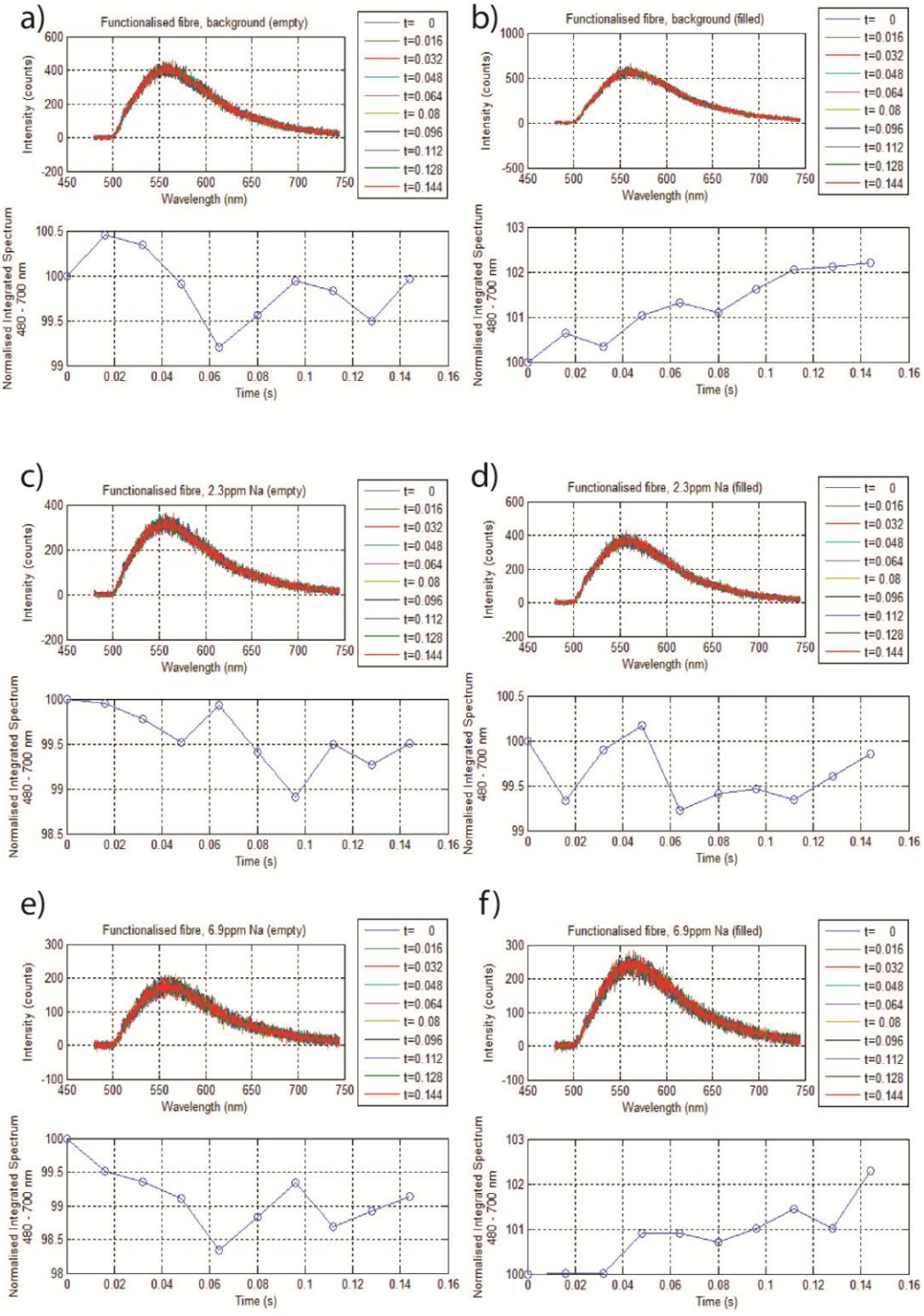

Figure 5.12: Fluorescence spectra and normalised integrated spectra from 480 – 700 nm for the empty and filled SCFs with 0 ppm of Na (a, b), 2.3 ppm of Na (c, d), 6.9 ppm of Na (e, f)

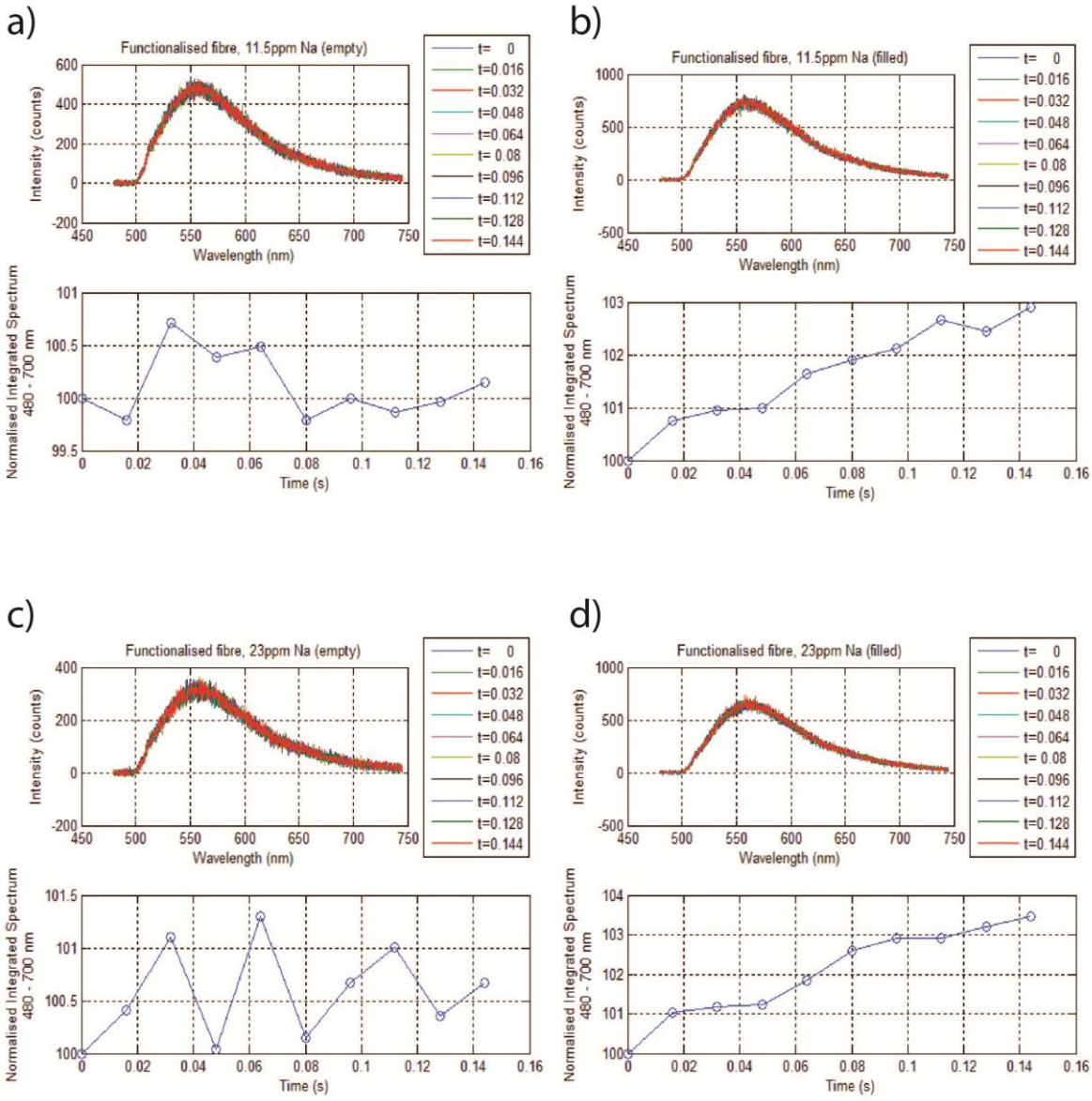

Figure 5.13: Fluorescence spectra and normalised integrated spectra from 480 – 700 nm for the empty and filled SCFs with 11.5 ppm of Na (a, b) and 23 ppm of Na (c, d)

5.5 Conclusions

In this chapter, quantitative sodium ion measurements using functionalised SCFs with surface attached PET fluoroionophore **4.3** were demonstrated. No photobleaching of fluoroionophore **4.3** was observed within the measurement time; therefore surface attachments of fluoroionophore **4.3** inside SCF does not increase the photobleaching rate within the parameters of the experiment. The average scattering attenuation of a SCF after the functionalisation procedure was 0.76 dBm^{-1}. The increase of the scattering attenuation was being less than previously reported data of functionalised F2 SCFs. This may be because the functional coating on silica SCF is more homogeneous compared with F2 SCFs, therefore it introduces less surface roughness.

While the fluorescence intensity of each functionalised SCF was inconsistent due to the inconsistency of the surface functionalisation, this inconsistency can be normalised by the comparison of the loaded and unloaded SCF. By doing this normalisation, a linear calibration curve of the percentage fluorescence enhancement (FE) as a function of sodium concentrations was observed.

5.6 References

1. Snyder, A.W. and Love, J.D., *Optical waveguide theory*. Science paperbacks. 1983, London ; New York: Chapman and Hall.

2. Ebendorff-Heidepriem, H., Warren-Smith, S.C., and Monro, T.M., *Suspended nanowires: Fabrication, design and characterization of fibers with nanoscale cores.* Optics Express, 2009. **17**(4): p. 2646-2657.

3. Schartner, E.P., *Hydrogen peroxide sensing with microstructured optical fibres*, in *School of Chemistry and Physics*. 2011, The University of Adelaide.

4. Paul, A., *Chemical Durability of Glasses - Thermodynamic Approach.* Journal of Materials Science, 1977. **12**(11): p. 2246-2268.

5. Bunker, B.C., *Molecular Mechanisms for Corrosion of Silica and Silicate-Glasses.* Journal of Non-Crystalline Solids, 1994. **179**: p. 300-308.

6. Afshar, S.V., Ruan, Y.L., Warren-Smith, S.C., and Monro, T.M., *Enhanced fluorescence sensing using microstructured optical fibers: a comparison of*

forward and backward collection modes. Optics Letters, 2008. **33**(13): p. 1473-1475.

7. Skoog, D.A., Holler, E.J., and Crouch, A.R., *Principles of Instrumental Analysis*. 6th ed. 2007, Canada: Brooks/Cole.

8. Warren-Smith, S.C., *Fluorescence-based chemical sensing using suspended-core microstructured optical fibres*, in *School of Chemistry and Physics*. 2010, The University of Adelaide.

9. Afshar, S., Warren-Smith, S., and Monro, T., *Enhancement of fluorescence-based sensing using microstructured optical fibres.* Optics Express, 2007. **15**(26): p. 17891-17901.

10. De Silva, A.P., Moody, T.S., and Wright, G.D., *Fluorescent PET (Photoinduced Electron Transfer) sensors as potent analytical tools.* Analyst, 2009. **134**(12): p. 2385-2393.

11. Moon, J.H., Kim, J.H., Kim, K., Kang, T.H., Kim, B., Kim, C.H., Hahn, J.H., and Park, J.W., *Absolute surface density of the amine group of the aminosilylated thin layers: Ultraviolet-visible spectroscopy, second harmonic generation, and synchrotron-radiation photoelectron spectroscopy study.* Langmuir, 1997. **13**(16): p. 4305-4310.

12. François, A., Ebendorff-Heidepriem, H., and Monro, T., *Comparison of surface functionalization processes for optical fibre biosensing applications*, in *20th international conference of optical fibre sensors*. 2009.

Chapter 6

Conclusions

This thesis described fluorescence-based ion sensing using suspended core fibres (SCFs) as the optical platform and photoinduced electron transfer (PET) fluoroionophores as the molecular sensors. The motivation of this work was to develop a fibre optic ionic soil nutrient sensor using SCFs for an advanced agricultural management, in particular for a site-specific crop management (SSCM). Compared with a traditional optical fibre sensor, SCF has much longer pathlength for light-matter interaction and require only nanoliters of analyte for an analysis. The long interaction path length has potential to significantly enhance the sensitivity of the optical fibre sensor.

There are two possible operating scenarios (A and B as described in Chapter 1) for performing sensing with PET fluoroionophores and SCFs. Operating scenario A requires mixing of the PET fluoroionophores with the analyte before injecting it into the SCF. Operating scenario B necessitates having the PET fluoroionophores attached on a 3-aminopropyltriethyoxysilane (APTES) terminated SCF internal surface, which requires a detailed understanding of the surface functionalisation of the silica and lead silicate glass materials used for SCF fabrications.

In Chapter 2, suspended core fibres (SCFs) filled with 4 amino-1,8-naphthalimide based PET model fluoroionophores, which have either a phenylaza-15-crown-5 as the ionophore for sodium ions or thiourea moities as the ionophore for fluoride ions (Operating Scenario A), demonstrated their capability for measuring sodium and fluoride ion concentrations in acetonitrile. Concentration measurements were demonstrated for sodium ions (0 – 9.2 ppm) and fluoride ions (0 – 19 ppm). After an optimisation of the excitation power and exposure time, no photobleaching was observed to occur within the measurement time, which demonstrates the possibility of using 4 amino-1,8-naphthalimide based PET fluoroionophores without photobleaching issues in SCFs. The sensitivity and dynamic linear range for fluoride ions sensing in cuvette and SCF showed no significant difference. For cations sensing, SCF showed a lower sensitivity and a shorter dynamic range

compared with cuvettes because of the interference from the lead silicate glass material. It is also suggesting other factors such as attenuation and preparation mode are possibly affecting the performance of the SCF sensors. Future work should focus on understanding how does the attenuation and the preparation methods affect the dynamic range and the sensitivity of the SCF sensor. Despite the sensitive and the dynamic range of SCF sensors are not better than curvettes, these sensors can perform sensing with smaller volume and more localised measurement compared with curvettes.

Operating scenario B requires understanding of the surface chemistry of the glass substrate and the coating. Chapter 3 demonstrated the use of glass model systems such as silicon wafers, extruded slides, capillaries and bare fibres for studying the surface functionalisation of glass material used for SCFs fabrication. In this project, all glass materials were functionalised using a two-step procedure that firstly coated the glass surface with 3-aminopropyltriethoxysilane (APTES). This provides an amine functional group terminated surface for further functionalisation. The fluoroionophores were then attached on the APTES layer via peptide coupling chemistry. Three parameters are important in the surface functionalisation of the glass materials towards SCF sensors. They are (i) surface density of amine groups of the APTES coating and surface density of sensor molecule attached to APTES (ii) thickness of the coating and (iii) roughness of the coating. The consistency of each parameter is important in the SCF sensor reproducibility.

Before analysing the APTES coated glass slides, the surface chemistry of silica and lead silicate glass (F2) slides were studied by the X-ray photoelectron spectroscopy (XPS) in order to understand the compositions and structure of the glass substrate surfaces. It was found that the surface composition of F2 glass measured by XPS is not the same as the bulk composition measured by energy dispersive X-ray (EDX) analysis. Sodium and lead atomic percentages were less on the surface compared with the bulk composition, which possibly introduces negative charges to the surface. In addition, no statistical difference was found between the percentages of silanol groups on piranha washed silica and F2 glass surfaces, which suggests the density of binding sites for APTES molecules on F2 and piranha washed silica glass surfaces may be the same.

For the study of the APTES functionalised glass slides, the nitrogen to silicon ratio measured using XPS and spectroscopic ellipsometery indicated that the thickness of the APTES coating on silica glass increases as a function of time. These findings corroborate data reported by others on the APTES coating thickness increases with the incubation time. Although this multilayer formation is not a new discovery, the HRXPS studies of different thicknesses of APTES layers show that the percentage of non-bridging oxygen (NBO) significantly increases with the thickness of APTES layer. It is the first XPS evidence for the existence of electrostatic interactions between $Si\text{-}O^-$ and NH_3^+ in the structure of the APTES multilayer.

The percentage contribution of free amine groups was higher in the samples with 5 hours APTES incubation compared with the samples with 0.5 hours incubation. Since the peptide coupling requires free amine groups, it suggested the thicker APTES layer is better for the next peptide coupling step to provide for sensor molecule attachments. In addition, the nitrogen and carbon percentages of APTES coated extruded F2 glass was significantly less than that of the APTES coated Piranha washed silica glass, despite the similar silanol group density found from the XPS analysis. This result suggests that the glass composition possibly affects the surface attachment of the APTES molecule.

The surface chemistry of the APTES coating was also analysed on bare F2 fibres. Principal component analysis (PCA) of the time of flight secondary ion mass spectrometry (TOF-SIMS) data for APTES coated F2 fibres showed a clear data clustering in positive secondary ion mass spectrometry (+SIMS) of the organic and inorganic fragments for samples with different treatments. Among all the positive fragments analysed, CH_4N^+, K^+ and Pb^+ are characteristic fragments. Their average normalised ion intensities were used to distinguish different thicknesses of APTES coating on F2 fibre. In terms of the surface roughness of the APTES layer, measured byatomic force microscopy (AFM) showed that an APTES coating did not increase the surface roughness of silicon wafers over a 5 hours incubation period. This result suggests that the APTES coating itself does not increase scattering loss for the SCF.

XPS surface analysis showed that the nitrogen surface content has at least 5% nitrogen atomic percentage variation for silica glass and 11% for F2 glass. The nitrogen percentage variation suggests variation of amine group density. This discovery motivated a study of the use of 11-aminoundecyltriethoxysilane (AUTES), which was expected to enhance the coating consistency. This study investigated AUTES coating on silica glass slides and silica wafers in the absence of ultrasonic cleaning. The nitrogen atomic percentages and the percentage contribution of NBOs show no difference between samples with 0.5 and 5 hours incubation times. These results suggest that there is limited multilayer formation, which corroborate results from literatures. However, micron size aggregates were observed using AFM analyses, which are possibly caused by AUTES residues. As the ultrasonic cleaning step typically applied in AUTES deposition reactions cannot be performed for SCFs, a new washing procedure needs to be found before applying AUTES to SCF functionalisations.

Chapter 3 included a comparative study of two different surface functionalisation methods, specifically APTES and polyelectrolyte multilayer (PEM) primary coatings. In this part of the work, surface functionalisation experiments were performed in F2, silica, tellurite, bismuth and ZBLAN glass capillary. The demonstration of functionalisation of tellurite, bismuth and ZBLAN glass suggested the possibility of using those glass materials for near to mid-infrared sensing applications.

The functionalisation study suggests that PEM has relatively more active amine groups on the surface compared to APTES on all of the different oxide glass surfaces. Therefore, it is a better surface functionalisation strategy if the surface density of sensor molecules is important and the sensor molecules are not sensitive to the ions existing on the coating. PEM is particularly suitable for biological sensing applications. This study also showed that the minimum 'active' amine groups surface density of the APTES coated on untreated silica and F2 glass are 0.9 ± 0.6 and 4.5 ± 0.6 fmolmm^{-2}. These data are important in estimating the quantity of fluoroionophores attached on the internal surface of a SCF.

Chapter 4 demonstrated the feasibility of performing comprehensive surface analyses on extruded lead silicate (F2) glass slides. The relative quantifications of

the surface density, the surface coverage, the nature of attachment and the coating thickness of the fluoroionophores were analysed by fluorescence imaging, XPS and ToF-SIMS, ToF-SIMS imaging and depth profiling. Using fluorescence imaging, it was found that attachments of model fluoroionophores could occur with or without coupling reagents, although the nature of the attachment differs. The fluorescence intensity was correlated with the quantity of the fluorophore on the surface. This was confirmed by XPS measurements that showed high correlations of the C=O percentage contributions in the high resolution carbon spectrum to fluorescence intensities. A principal component analysis (PCA) of the ToF-SIMS data was shown to be able to distinguish the nature of different coatings; in particular, samples with fluoroionophores covalently coupled on the glass surfaces showed a markedly different PC1 projection score. ToF-SIMS imaging also revealed that the lead ion distribution could be used as a marker of surface coverage of the coating; the lead ions distribution is inversely related to the coverage of coating on the glass slide. Furthermore, relative thickness measurements were also performed via depth profiling using ToF-SIMS. It was found that slides with model PET sensor attachments exhibit no difference in thickness regardless of the mode of binding used and thus interacts with the evanescent field to the same extent.

In Chapter 5, quantitative sodium ion measurements using functionalised SCFs with surface attached PET fluoroionophores were demonstrated. No photobleaching of fluoroionophores was found within the measurement time; therefore surface attachment of fluoroionophores inside SCFs do not increase the photobleaching rate of the fluoroionphores. A linear calibration curve of the percentage fluorescence enhancement (FE) as a function of the sodium ion concentrations can be established. However, fluorescence intensity of each functionalised fibre was inconsistent due to the inconsistency of surface functionalisation. To improve the consistency of the surface functionalisation, it is necessary to improve the consistency of the surface attachment of the amine functional groups. Chemical vapour deposition (CVD) of APTES is one of the possible ways to improve the consistency of the coating [1]. Furthermore, AUTES deposition is promising if the suitable cleaning method to remove aggregates is identified.

This thesis has shown that sodium and fluoride ion sensing are feasible in SCFs using operating scenario A. This discovery provides the foundation towards the development of a selective SCF ions sensor for aqueous samples for agricultural applications. Operating scenario B also demonstrates the feasibility of sodium ions sensing via measuring percentage fluorescence enhancement, however, the inconsistency of the surface functionalisation in the SCF limits the practical use of the functionalised SCF sensor. The future research targets should be centred on understanding the causes of the inconsistency of surface functionalisation, and hence improving the consistency of the surface functionalisation.

This thesis has also demonstrated a versatile approach of using different glass model systems and surface analysis techniques for measuring parameters such as the surface density of amine groups and sensor molecules, coating coverage, surface roughness and coating thickness that represent the surface chemistry of SCF. This provides a promising route for improving the consistency of the surface functionalisation in SCFs.

References

1. Samha, H., Linford, M., Zhang, F., Davis, R., and Sautter, K., *Chemical vapor deposition of three aminosilanes on silicon dioxide: Surface characterization, stability, effects of silane concentration, and cyanine dye adsorption.* Abstracts of Papers of the American Chemical Society, 2011. **241**.

Appendix A

Towards normalisation methods using signals from references

A.1 Introduction

The consistency of the emission intensity of the fluorophores is highly dependent on the consistency of the power of the excitation. For suspended core fibres (SCFs), the consistency of the excitation power is dependent on the stability of the excitation source i.e. laser and the optical alignment. Figure A.1 shows a pictorial representation of the target alignment and misalignment position of a SCF. Since the core of a SCF is small (~ 1 μm), maintaining constant alignments at a position is difficult. The instability of the alignment is caused by the combined effect of vibrations of optical components (eg mirrors, lenses, mounts) or drift in the laser beam or the changes in environmental conditions such as temperature. This is a significant issue when the measurement must be taken over a long time. Note also that for the relatively small core sizes of the optical fibres used here, sub-micron accuracy is required in terms of the positional accuracy with which the focused light is located onto the triangular glass core. In this project, the alignment stability was not a concern because the data from each fibre was collected within a short time (144 ms).

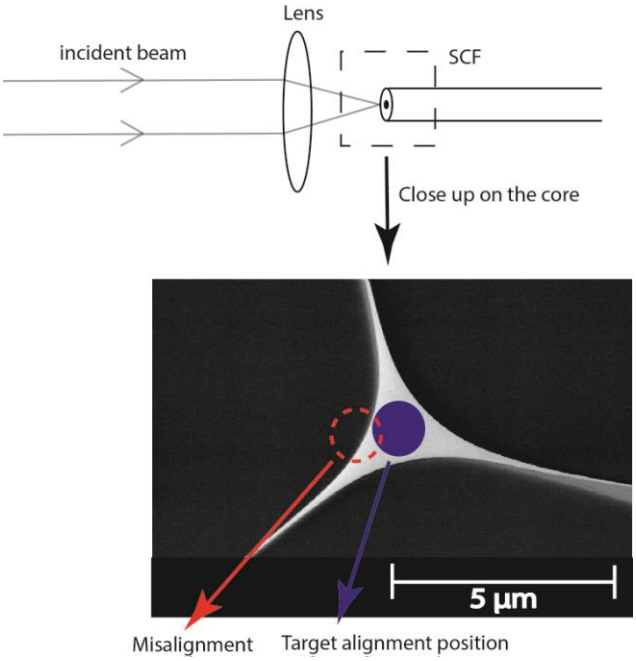

Figure A.1: A schematic diagram of the target alignment and misalignment positions

The main concern in this project is the reproducibility of the same alignment between different SCF. This is particularly important because a reproducible alignment is required in order to be able to compare the fluorescence intensity between SCFs.

The procedure described in the Chapter 2 and 5 use the maximum transmitted power as an indicator of optimised optical alignment to the core and assuming if maximum transmitted power is achieved in another fibre, the alignment position on the core is approximately the same. A variation in the optical alignment causes a variation in the power coupled into the core of SCF, which changes the power in the evanescent field that is available to interact with the sample to be sensed. In addition, the instability and inconsistency in the alignment changes the coupling efficiency to all guided modes coupled into the core of SCF if the SCF is not a single mode fibre. Different guided modes have different power fraction of evanescent field. The fundamental mode has the smallest power fraction in the evanescent field relative to the higher order mode (Figure A.2) [1]. Hence the alignment eventually affects the overall power fraction in the evanescent field and then influence the emission intensity of the fluorophores in the solution. None of

the SCF used in this project is a single mode fibre; therefore the consistence of an alignment was important in this project.

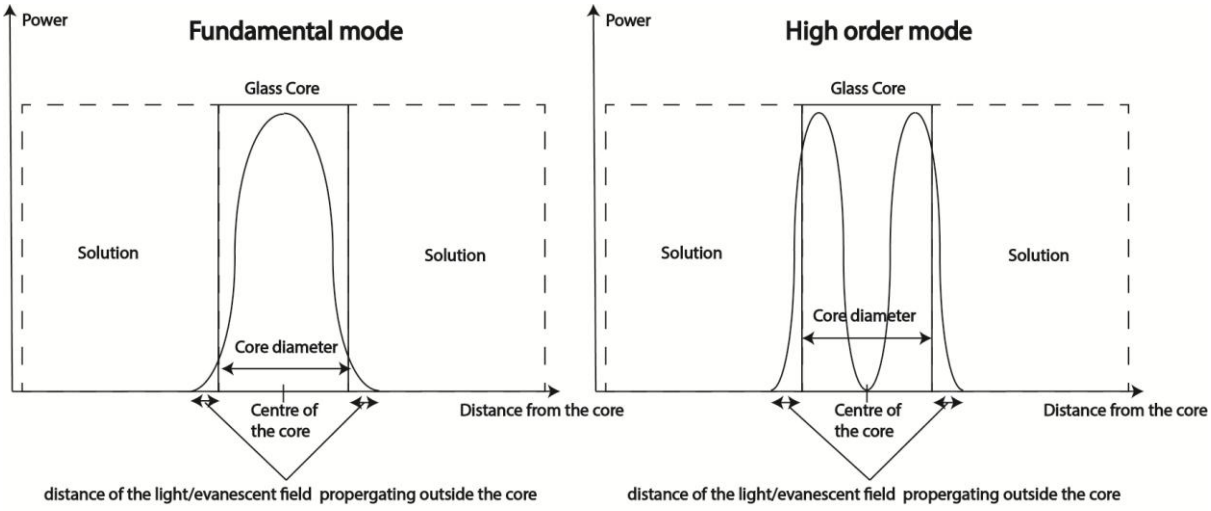

Figure A.2: Power distribution of fundamental mode and high order mode

Recently, Warren-Smith *et al.* has demonstrated that the issue of the optical alignment variation during the measurement can be compensated by reflection-based automated alignment system; however, this device was based on piezo-control stages with a feedback loop, which is an expensive and bulky set-up for environmental motoring applications [2].

An ideal standard is the one impacted by the optical alignment to the same degree as the sensor molecules, thus allowing variations in the optical alignment to be cancelled out by the normalisation. We have identified two possible approaches to this calibration. The first approach is to use the emission peak at 502 nm, which arises from the Raman shift of the excitation wavelength caused by the vibration of Si-O bond in the glass, as the reference peak. The second approach is to use an external fluorescence standard such as quantum dots, which need to be pre-mixed with the analyte. All reference materials must be sufficiently photostable to enable use within the high intensity light fields found in the SCF.

The aim of this study is to explore the feasibility of both normalisation methods, experiments were performed by measuring the emission peak of the model fluorophore(4-propylamino-1,8-naphthalimide fluorophore (**2.3**)) and the reference after intentional misalignments were made. The ratio of the intensity of

the model fluorophores to the reference signal's intensity was expected to be constant if they were equally affected by the variation of the optical alignment.

A.2 Experimental

A.2.1 Normalisation using Si-O Raman peak and fluorophore 2.3

Using the setup described in Chapter 5, the F2 SCF was filled with 2 μM fluorophore **2.3** in acetonitrile. The laser beam was aligned into the core to the optimum position, which is the position gives the maximum transmission power. After an optimisation, 10 fluorescence spectra were acquired. Emission spectra were then acquired after the fibre was translated a step in the z direction (Figure A.3). The movement along z axis was unidirectional. The spectra acquisition setting was the same as described in Chapter 5.

The same procedure was performed for translations in the x and y direction respectively after the fibre was moved back to the optimal alignment position. The emission peak of the fluorophore and the reference were determined after fitting the average fluorescence spectrum with Gaussian model using Matlab. Only F2 SCF was used in the measurement to demonstrate the normalisation concept.

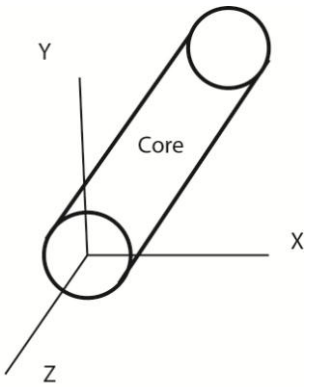

Figure A.3: Directions of the movement of a SCF in the experiment

A.2.2 Normalisation using Qdot800 and fluorophore 2.3

The Qdot800 ITK^{TM} used in the experiment was flocculated using the standard procedure suggested by Invitrogen [3]. THF solution with fluorophore **2.3** (21 μM) and Qdot (22 nM) was filled into silica SCFs by capillary action. The experimental set-up was the same as A.2.1. The optical alignment was optimised and 10 fluorescence spectra were acquired. Another 10 fluorescence spectra were acquired after the fibre was translated a step in the x direction (Figure A.3); this step was performed 6 times in total and the movement was assumed to be unidirectional.

A.3 Results and discussion

A.3.1 Normalisation using emission peak from Si-O Raman shift and fluorophore (2.3)

Emission spectra of unfilled SCF excited at 473 nm was measured using the same setup as described in Chapter 5. Figure A.4 shows the emission spectra of lead silicate glass (F2) (Figure A.4a) and silica glass (Figure A.2b). For F2 glass, there are 2 sharp peaks at 478 nm and 502 nm, one broad peak at 770 nm and 5 peaks at 913 nm, 921 nm, 931 nm, 949 nm, 996 nm. The sharp peak at 478 nm originates from the residual light from the excitation laser which cannot be completely removed because the cut-off edge of the dichroic mirror is at 478 nm. The peak at 502 nm originates from the Raman shift of the excitation wavelength caused by the vibration of Si-O bond [4]. The broad peak at 770 nm arises from impurities such as iron, zinc and vanadium [5]. For silica glass, the origin of peaks at 478 nm and 502 nm is the same as F2, but the broad peak at 567 nm came from different impurities or from the defect of the silica glass that exhibited fluorescence. The origin of peaks for both F2 and silica glass above 900 nm is likely to be glass fluorescence arising from the impurites.

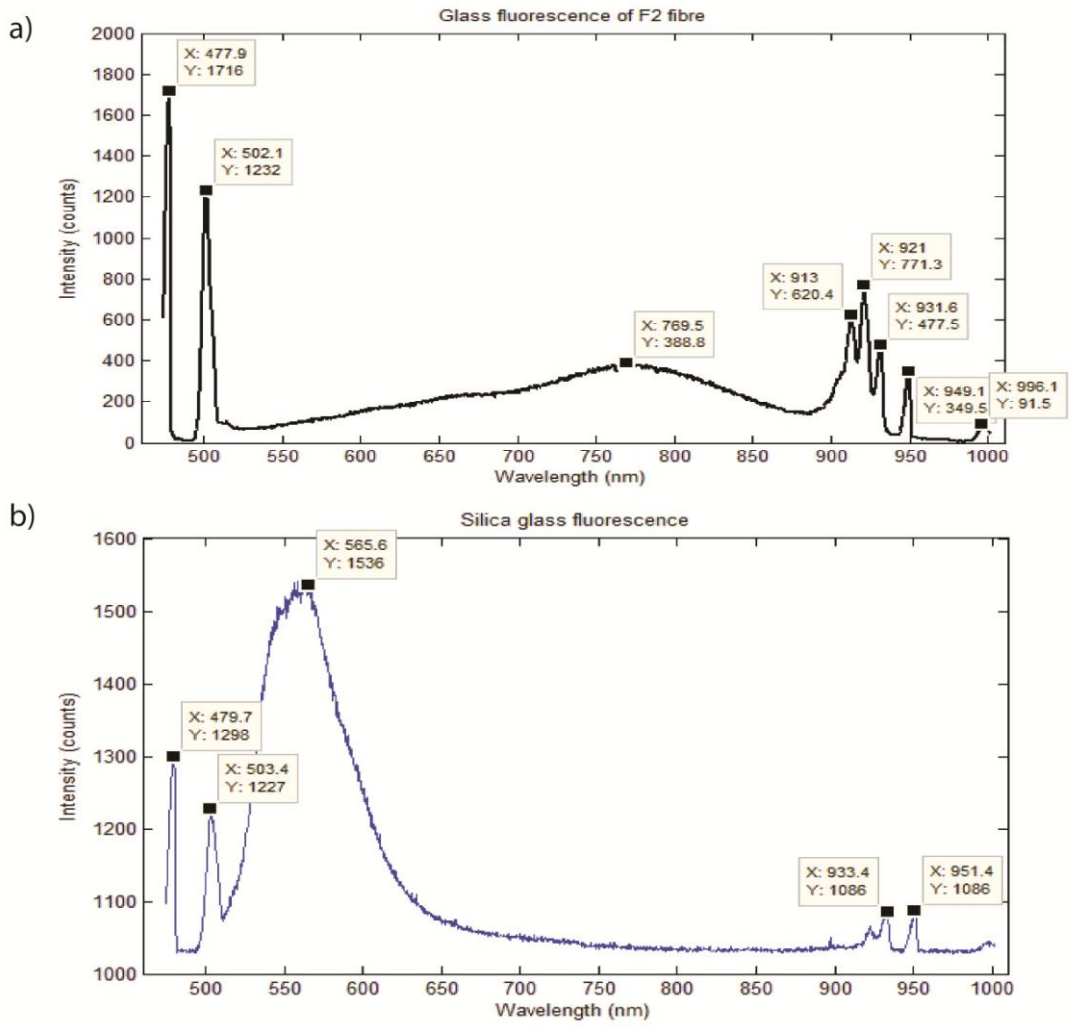

Figure A.4: Emission spectra of (a) Lead silicate SCF (F2) and (b) silica glass SCF excited at 473 nm

Figure A.5a shows emission spectrum of 2 μM fluorophore **2.3** in acetonitrile in a F2 SCF at the optimised position and Figure 5b shows emission spectrum of the same fibre after 5 steps towards the Z direction. It shows that, as expected, the relative intensity of fluorophore **2.3** decreased for z-axis positions corresponding to non-optimised coupling. The ratios of the maximum count of the Si-O Raman peak at 502 nm to maximum count of fluorophore **2.3** at 555 – 558 nm at different positions are shown at Figure A.6. The ratio increase when the fibre is moved away from the optimal point to the z direction, while this ratio decreases when the fibre is moved away from the optimal point in either the x or y direction. The ratio does not remain constant while the position of coupling changes. It is because the misalignment of the excitation beam has different amplitude of impact on the

Raman signal, which arises from the core of SCF, and the fluorophores, which arise from the hole of SCF. The Raman signal is proportional to the transmitted power though the core of SCF, the misalignment only changes the power of the excitation so as to the Raman emission intensity. However, the misalignment of the excitation beam also causes changes in modal distributions, which change the power fraction in the evanescent field. In certain occasions, misalignment can increase the power fraction in the evanescent field; therefore it behaves in an opposite direction as the Raman emission intensity when a misalignment happened. In conclusion, this result suggests that this method is not suitable for normalisation.

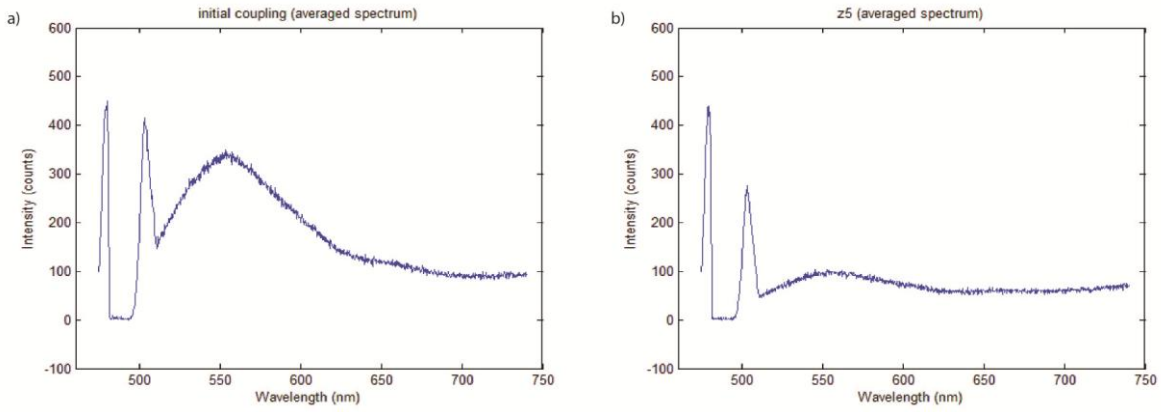

Figure A.5: Emission spectrum of F2 SCF filled with 2 μM fluorophore **2.3** in acetonitrile at (a) optimum position and (b) z5 position

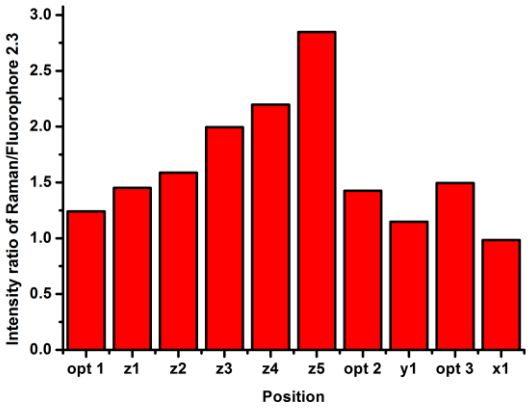

Figure A.6: Intensity ratios of emission peak at 502 nm to emission peak of fluorophore **2.3** at different positions on x, y and z dimensions

A.3.2 Quantum dot 800 as the external standard

Quantum dots (Qdots) are engineered fluorescence nanoparticles that exhibit high photostability and can exhibit a variety of emission wavelengths. Also, Qdots have a broad spectral range that can be used for an excitation and have a large Stokes' shift. In order to avoid the Qdot emission spectrum overlapping with the fluorophore **2.3** emission, Qdot800 ITK^{TM} with an emission peak close to 800 nm was chosen in the following experiment. When Qdots were mixed with fluoroionophores, theoretically they are exposed to the same evanescent field within the SCF, regardless of the optical alignment instability. In principle, this should circumvent the issue that was identified in the first calibration approach trialled above associated with variations in coupling to the different modes guided by the fibre. To demonstrate the concept, both fluorophore **2.3** and Qdot 800 ITK^{TM} organic quantum dots were dissolved in THF and their emission intensities were measured after intentional misalignments.

Figure A.7a shows the fluorescence spectrum at the position in which optimised alignment is obtained. The peak at 550 nm is the emission from fluorophore **2.3** and the peak at 790 nm is the emission from Qdot. Figure A.7b shows the fluorescence intensity after translating the fibre in the x-direction. The relative intensity of both peaks changed after the fibre was moved. Figure 8 shows the decrease of intensity ratio of Qdot 800 to fluorophore **2.3** along the movement of the fibre to x-direction. It shows that the change in an optical alignment did not affect both emission peaks equally; therefore the ratio is not constant. This result suggests that fluorophore **2.3** and Qdot are not evenly distributed inside the holes of a SCF. It is possibly due to the surface charges of the glass attract the small molecule such as fluorophore **2.3** to the core surface. Hence, the Qdot and fluorophore **2.3** are not affected in the same degree when the modal distributions change. This result shows that this approach does not work.

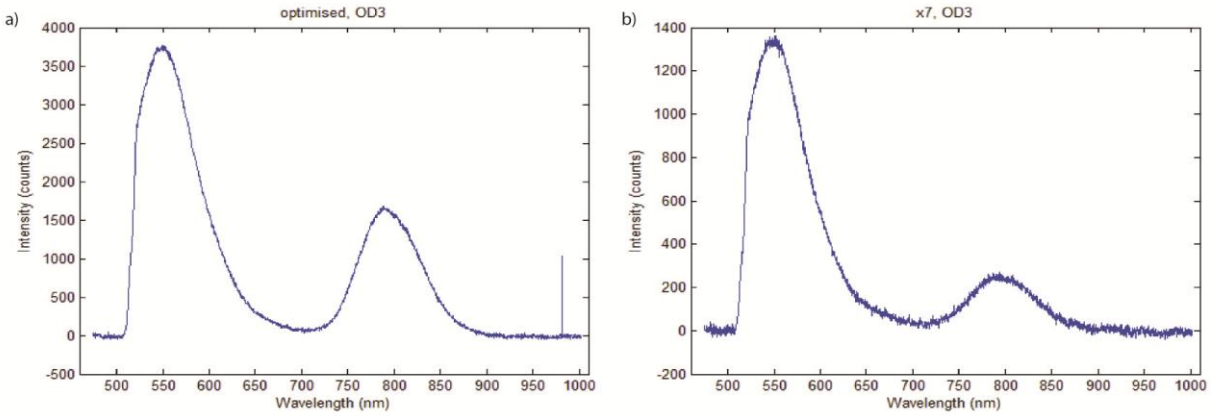

Figure A.7: Emission spectra of silica SCF filled with fluorophore **2.3** (21 μM) and Qdot (22 nM) in THF at optimum position (5a) and x5 position (5b)

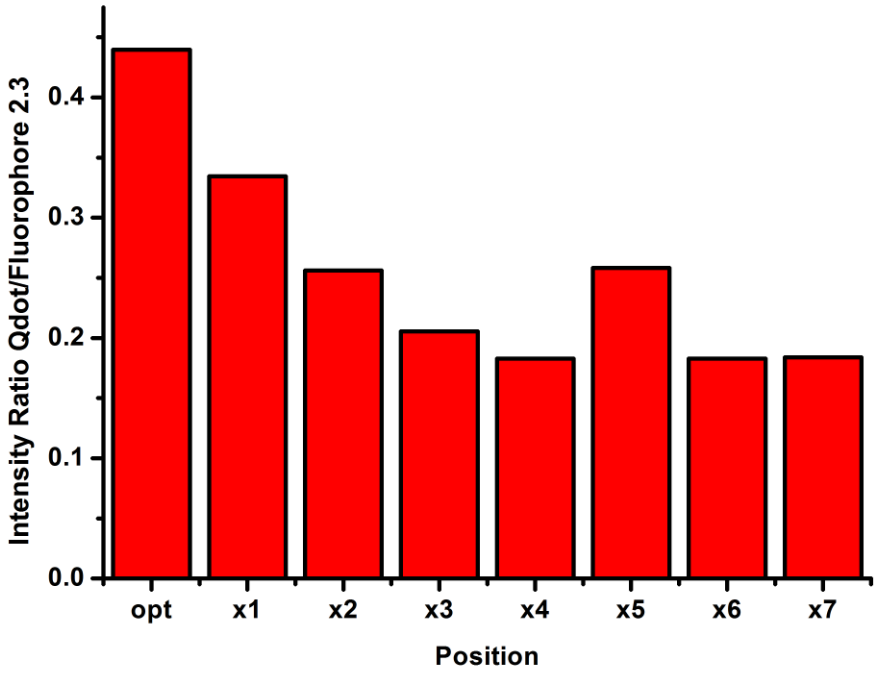

Figure A.8: Intensity ratios of Qdot to fluorophore **2.3** at different positions along the x-dimension

A.4 Conclusions

The attempts of using intrinsic Raman signals from the glass and extrinsic emission from Qdots were found to be unsuitable for normalisation regarding an optical alignment variation. Thus, the future work for developing field deployable environmental monitoring sensor will be focusing on identifying other suitable intrinsic or extrinsic reference materials in order to compensate the optical alignment variation. One of the possible future approaches will be to use strictly single-mode fibres to avoid the impact of higher order modes on the evanescent field. Hence, the variation of the emission intensity due to an alignment variation will be removed.

A.5 References

1. Snyder, A.W. and Love, J.D., *Optical waveguide theory*. Science paperbacks. 1983, London ; New York: Chapman and Hall.

2. Warren-Smith, S.C., Nie, G., Schartner, E.P., Salamonsen, L.A., and Monro1, T.M., *Enzyme activity assays within microstructured optical fibers enabled by automated alignment.* BIOMEDICAL OPTICS EXPRESS, 2012. **3**(12).

3. Invitrogen (2005) *Flocculation of Qdot® ITK™ Organic Quantum Dots from Decane.*

4. Robinet, L., Bouquillon, A., and Hartwig, J., *Correlations between Raman parameters and elemental composition in lead and lead alkali silicate glasses.* Journal of Raman Spectroscopy, 2008. **39**(5): p. 618-626.

5. SCHOTT (2012) *Fluorescence of optical glass.*

Appendix B

Attempted syntheses of potassium ion-selective PET fluoroionophores for use in aqueous solution

B.1 Introduction

Previous chapters demonstrated that ion sensing using PET fluoroionophores in suspended core fibres (SCFs) is feasible. Therefore, the next step for developing SCF ions sensors for agricultural applications is to make the fluoroionophore selective to a particular ion. The selectivity of the SCF sensor is controlled by the selectivity of the fluoroionophore. As discussed in Chapter 1, target ions for this project are potassium (K), nitrate (NO_3^-) and phosphate (PO_4^{3-}). The development of ionophores or fluoroionophores selective for polyatomic anions (e.g. NO_3^- and PO_4^{3-}) is more challenging than developing cation (K^+) selective entities because of the following factors [1].

1. Anions are generally larger than cations and have many different shapes other than spherical. Hence the design of the ionophore to capture an anions is difficult.
2. Anions have higher free energy of solvation compared with that of similar size cations; thus ionophores for anions experience more competition from the solvent.
3. Many anions are coordinatively saturated and the binding between an ionophore and the anion is by relatively weak interactions such as hydrogen bonds or van der Waals interactions.

On the basis of these observations, fluoroionophores for sensing monoatomic potassium ions are a more feasible target within this project. He *et. al.* reported a potassium selective fluoroionophore in 2003 (**He.2,** as shown in Figure B.1) [2]. This fluoroionophore consists of a cryptand derivative as the ionophore and 4-aminonaphthalimide as the fluorophore, which is identical to the fluorophore used

in this project. In terms of potassium ion selectivity, the cryptand displays higher selectivity than the crown ether; the binding constant of the cryptand for potassium in methanol is 10^4 times higher than that of the crown ether [1]. However, the synthesis of the cryptand moiety of the fluoroionophore reported by He *et. al.* involves 10 linear steps, and thus constitutes a relatively labour intensive and time-consuming process. Carpenter *et.al.* reported the synthesis of another potassium selective fluoroionophore (**Carpenter.1**, as shown in Figure B.1). In this synthesis, the first ring of the cryptand is synthesized by Buchwald-Hartwig amination, a palladium-catalyzed cross-coupling of the diaza-18-crown-6- ether with chloroimidazole. [3] The second ring of the cryptand is incorporated by monoalkylation of chloroimidazole with 3-(4-(bis(2-chloroethyl)amino)phenyl)ethylamine. Using this approach, the synthesis of cryptand requires only 3 steps.

The aim of this section of work is to synthesise three potassium ion selective fluoroionophores **B12** and **B23a** and **B23b (**Figure B.1) for use as the SCF ions sensor in operating scenario A (as discussed in Chapter 1). Fluoroionophore **B12** was synthesised using the same procedure reported by He *et.al* except that the fluoroionophore **B12** does not possess a carboxyl group for surface attachment [2]. Fluoroionophores **B23a** and **B23b** were to be synthesised using the streamlined approach reported by Carpenter *et.al.* [4]. However, **B23a** and **B23b** were designed to have aminonaphthalimide entities as the fluorophore. Since the size of the cryptands for **B23a** and **B23b** are similar, it was expected that the binding affinity for potassium would be similar. The motivation of having two different structures was to explore the feasibility of two different synthetic pathways.

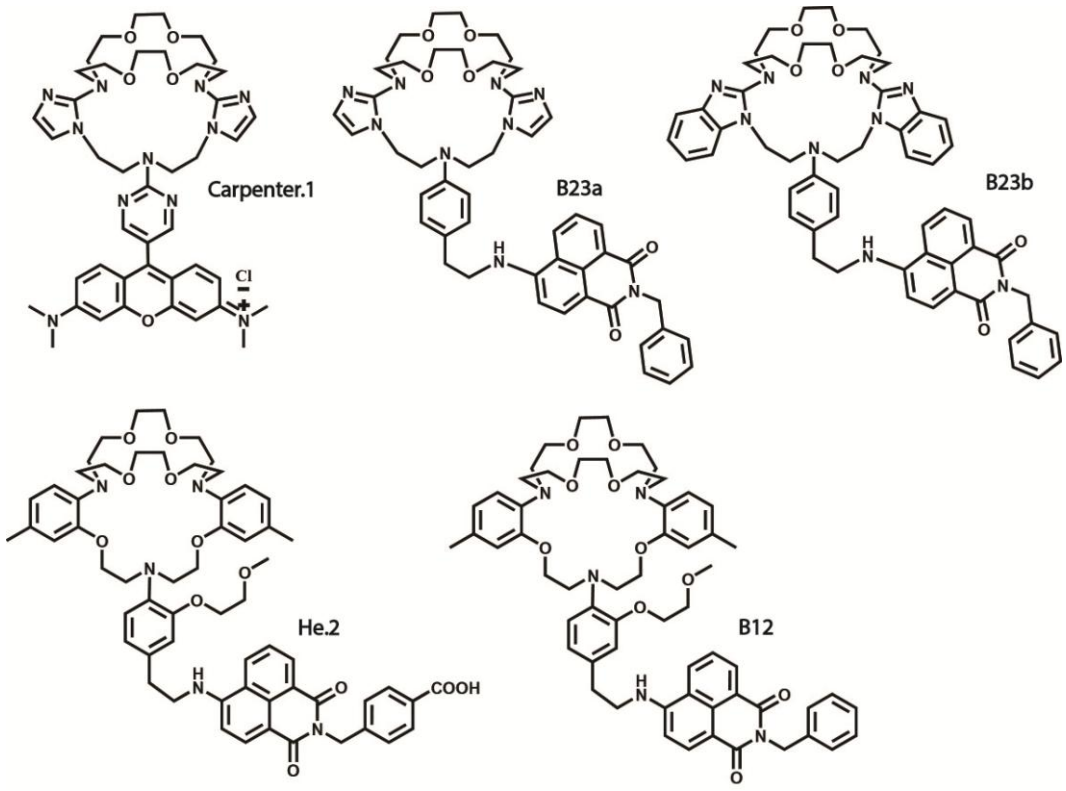

Figure B.1: Structures of fluoroionophores **He.2**, **B12**, **Carpenter.1**, **B23a** and **B23b**

B.2 Experimental

General procedures were reported in Chapter 2.

Attempted synthesis of potassium selective fluoroionophore (B12)

The synthesis procedures (steps a - l) of **B12** were reported in the supplementary information by He *et.al.* [2].

Attempted synthesis of 7,16-bis(1*H*-imidazol-2-yl)-1,4,10,13-tetraoxa-7,16-diazacyclooctadecane (B15a)

The general procedure used for the Buchwald-Hartwig amination to give **B15a** was reported in the supplementary information by Carpenter *et.al.[4]*. Table B1 shows the experimental conditions used in the synthesis of **B3a**. The reaction mixture was heated at 95°C by microwave irradiation for 30 minutes.

Table B1: Experimental conditions used in the synthesis of **B3a**

Trail	Catalyst	Ligand	Base	Solvent	Heating method
1	$PdCl_3$	QuinaPhos*	K_2CO_3	DMF	Microwave
2		PPh_3		Dioxane	

*QuinaPhos (((2S)-1-((11bR)-dinaphtho[2,1-d:1',2'-f][1,3,2]dioxaphosphepin-4-yl)-8-(diphenylphosphino)-2-(naphthal-en-1-yl)-1,2,3,4-tetrahydroquinoline) was purchased from Stream Chemicals, Inc.

Attempted synthesis of 7,16-Bis(1*H*-benzimidazol-2-yl)-1,4,10,13-tetraoxa-7,16-diazacyclooctadecane (B15b)

Method 1

1,4,10,13-Tetraoxa-7,16-diazacyclooctadecane(diaza-18-crown-6- ether) (**B14**) (222 mg, 0.85 mmol), 2-chlorobenzimidazole (**B13b**) (325 mg,3.17 mmol) and *N*,*N*-diisopropylethyl amine (DIPEA) (590 μL) were stirred in dioxane (10 mL) at 130°C for 4 days. The reaction mixture was cooled down to room temperature and then poured into saturated a sodium bicarbonate solution (25 mL). The aqueous layer was extracted with chloroform (2 x 25 mL). The combined organic layer was then washed with water (2 x 25 mL). The combined organic layer was dried with magnesium sulphate. The solvent was removed to afford the crude product.

Method 2

1,4,10,13-Tetraoxa-7,16-diazacyclooctadecane (**B14**), 2-chlorobenzimidazole (**B13b**), sodium *t*-butoxide and Buchwald palladcycle precatalysts were stirred in DMF (5 mL) and heated at 100°C under microwave irradiation for 1 hour. Five different types of pre-catalyst were used in five individual trials. Table B2 shows the experiment conditions used in the synthesis. The pre-catalysts were purchased from Strem Chemicals, Inc.

Table B2: Experimental conditions used in the synthesis of B.3b using Buchwald palladcycle pre-catalysts

Pre-catalyst	Pre-catalyst	B.1b	B.2	Base
Type	mg/mmol	mg/mmol	mg/mmol	mg/mmol
Chloro(2-di-t-butylphosphino-2',4',6'-tri-i-propyl-1,1'-biphenyl)[2-(2-aminoethyl)phenyl] palladium(II) (t-BuXPhos Palladacycle)	4/0.0058	74/ 0.48	50/ 0.19	30/0.31
Chloro(2-dicyclohexylphosphino-2',6'-dimethoxy-1,1'-biphenyl)[2-(2-aminoethylphenyl)] palladium(II) (SPhos Palladacycle)	5/0.0074	75/ 0.49	50/ 0.19	28/0.29
Chloro[2-(dicyclohexylphosphino)-3,6-dimethoxy-2'-4'-6'-tri-i-propyl-1,1'-biphenyl] [2-(2-aminoethyl)phenyl]palladium(II) (BrettPhos Palladacycle)	5/0.0063	73/ 0.48	50/0.19	28/0.29
Chloro(2-dicyclohexylphosphino-2',6'-di-i-propoxy-1,1'-biphenyl)[2-(2-aminoethylphenyl)] palladium(II) (RuPhos Palladacycle)	4/0.0055	75/ 0.49	50/0.19	28/0.29
Chloro(2-dicyclohexylphosphino-2',4',6'-tri-i-propyl-1,1'-biphenyl)[2-(2-aminoethyl)phenyl] palladium(II) (XPhos Palladacycle)	4/0.0054	74/ 0.48	49/0.19	28/0.29

B.3 Results and discussion

B.3.1 Attempted synthesis of fluoroionophore (B12)

Scheme B.1 shows the synthetic pathway used in the attempted synthesis of fluoroionophore **B12**. In our hands, the literature procedures were successfully repeated up until the synthesis of **B11**. A NMR spectrum of **B10** shows dialogistic doublets at 7.5 and 7.92 ppm originating from the ethylene moiety next to the nitro group. However, this step introduces significant loss of material because as during purification most of the crude product was lost on the silica gel [2]. The synthesis of **B11** involves reduction of the ethylene and nitro group of the ionophore. This step was performed twice and no evidence was found to show the reduction of **B10** was successful. Due of the significant loss of the product in this step, there was lack of material to continue the synthesis of fluoroionophore **B12** and, due to other avenues of investigation, this aspect of the project was discontinued.

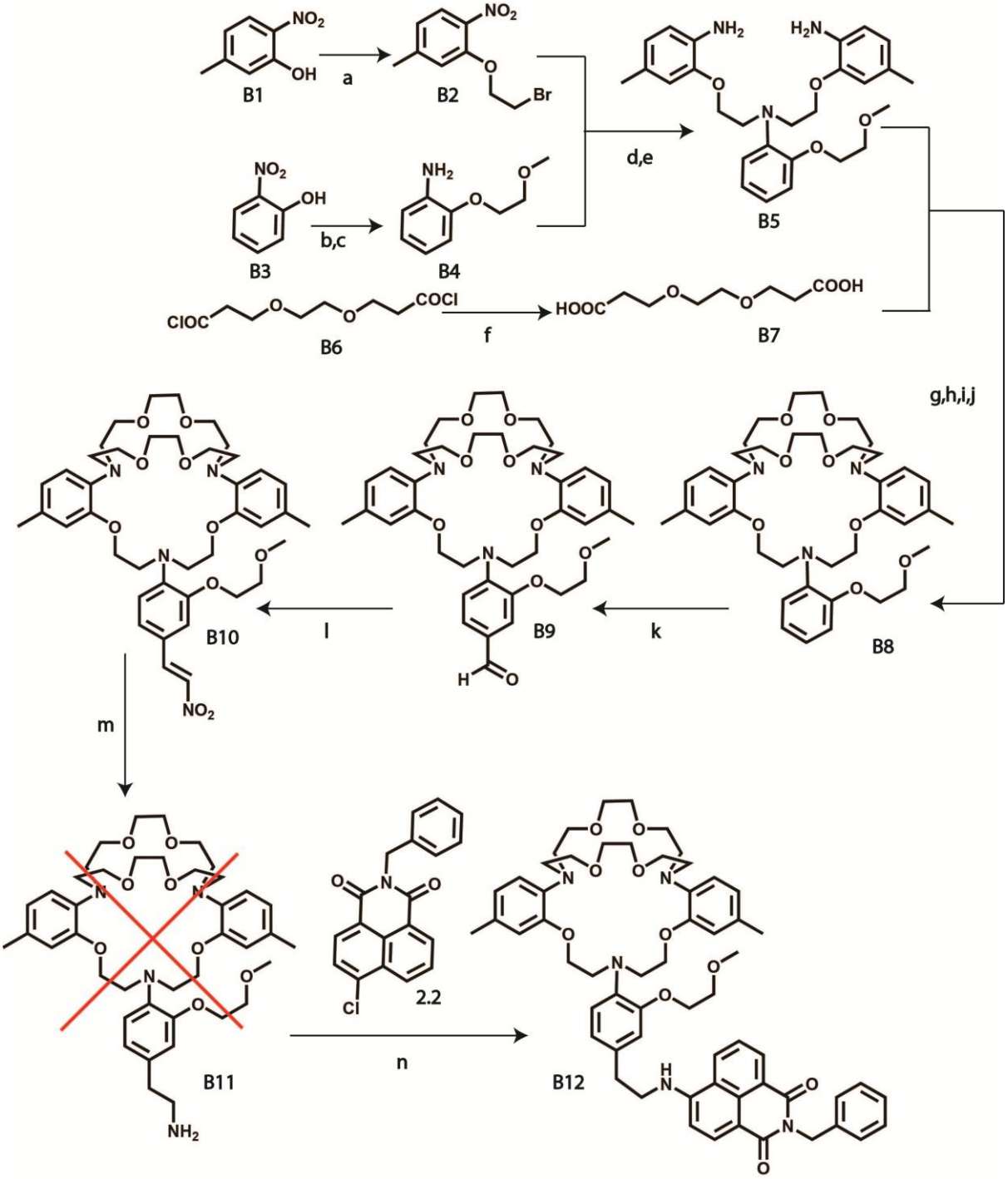

Scheme B.1: Synthesis of fluoroionophore (**B12**) after He *et al.* [2]: (a) $BrCH_2CH_2Br$, K_2CO_3, DMF, 100 ^oC, (b) $CH_3OCH_2CH_2Cl$, K_2CO_3, DMF, 100^oC, (c) H_2, 5% Pb/C, ethanol, (d) K_2CO_3, KI, CH_3CN, reflux, 3 days, (e) H_2, 5% Pb/C, DMF, (f) oxalyl chloride, $CHCl_3$, (g) DODC, triethylamine, CH_2Cl_2, (h) BH_3, THF, (i) DODC, pyridine, CH_2Cl_2, (j) BH_3, THF, (k) $POCl_3$, DMF, 0–25°C, (l) nitromethane, ammonium acetate, acetic acid 18 hours, (m) $LiAlH_4$, THF, 5 hours, (n) NMP, DIPEA, 80°C, 18 hours

B.3.2 Attempted synthesis of fluoroionophores (B23a and b)

The most time consuming part of synthesising fluoroionophores **He.2 and B12** is the synthesis of the cryptand. This synthesis can be streamlined by direct conversion of diaza crown ether into the cryptand; Carpenter *et. al.* demonstrated that a diaza-18-crown-6-ether can be coupled with a chloroimidazole under Buchwald-Hartwig amination conditions and cyclised with 3-(4-(bis(2-chloroethyl)amino)phenyl)ethylamine to complete the second ring of the cryptand.[4] Scheme B2 shows the route used for the attempted synthesis of fluoroionophores **B15a** and **B15b**. The first step involves a Buchwald-Hartwig amination reaction of diaza-18-crown-6- ether and 2-chloroimidazole or 2-chlorobenzimidazole. Two reported procedures for the synthesis of **B15a** were unable to be reproduced, with no evidence of the product found from a thin layer chromatography (TLC) or a NMR spectroscopy. Two methods were also attempted for the synthesis of **B15b**. In the first method 2-chlorobenzimidazole was reacted with diaza-18-crown-6-ether in the presence of a base (DIPEA) in dioxane at 130^{o}C. Similar reaction conditions had been reported by Pizze *et al*. for coupling 2-chlorobenzimidazole with a cyclic secondary amine. [5] However, unfortunately TLC showed that no product was formed. The second method was to couple 2-chlorobenzimidazole to diaza-18-crown-6-ether using Buchwald palladcycle pre-catalysts, which are more air- and moisture-stable compared with active phosphine-ligated Pd(0) complexes used traditionally in this type of reaction[3, 6]. Five different types of palladcycle precatalysts (t-BuXPhos, SPhos, BrettPhos, RuPhos and XPhos) were used in five individual reactions; however, TLC showed no products were formed in any of those reactions. The lack of success with the Buchwald-Hartwig amination reactions is possibly due to the use of non-optimised reaction conditions and the future work could focus on finding suitable conditions for these reaction [7].

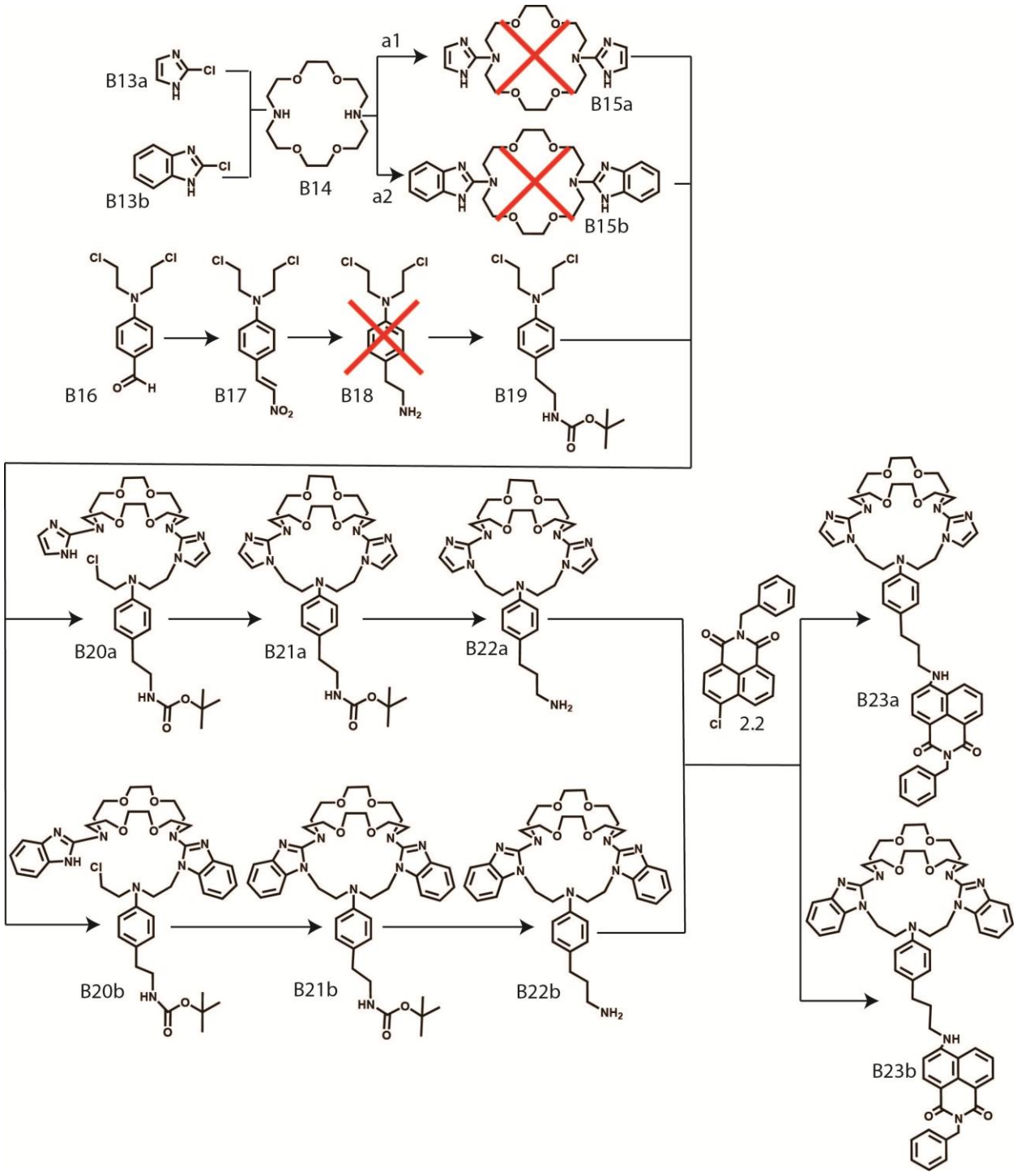

Scheme B2: Synthesis of fluoroionophores (**B23a** and **B23b**): (a1) Quinaphos/PPh_3, $PdCl_3$, K_2CO_3, DMF/dioxane, microwave 100°C for 1 hour (a2) Method 1: DIPEA, dioxane, 130°C for 4 days. Method 2: Buchwald palladcycle pre-catalysts, sodium *t*-butoxide, DMF, 100°C microwave

In addition to challenges encountered in the synthesis of **B15a** and **B15b**, the identification of a suitable reductant to prepare the mustard **18** (i.e. capable of reducing the ethylene and nitro groups but without substituting the chloro groups) was a further roadblock in this section. Given the synthesis of **B15a** and **B15b** were not successful, no further work was performed on the synthesis of **B18**.

A future direction for the synthesis of **B23a** or **B23b** would be to use the natural product chlorambucil (4-(4-(bis(2-chloroethyl)amino)phenyl)butanoic acid)(**B24**) as the starting material of the second ring of the cryptand [8]. This introduces an additional methylene group to the spacer but will provide access to a compound (**B25**) that is structurally similar to **B18**. Min *et. al* demonstrated that **B25** can be synthesied in a 3-step reaction (Scheme B3) that involves formation of an isocyanate intermediate under basic conditions and then conversion to its ammonium chloride salt under acidic conditions. Although, **B25** has one extra carbon compared with **B18**, the selectivity of the fluoroionophore is unlikely to be affected since the structure of the cryptand is the same, although the PET process may be modulated by the change in the spacer moiety.

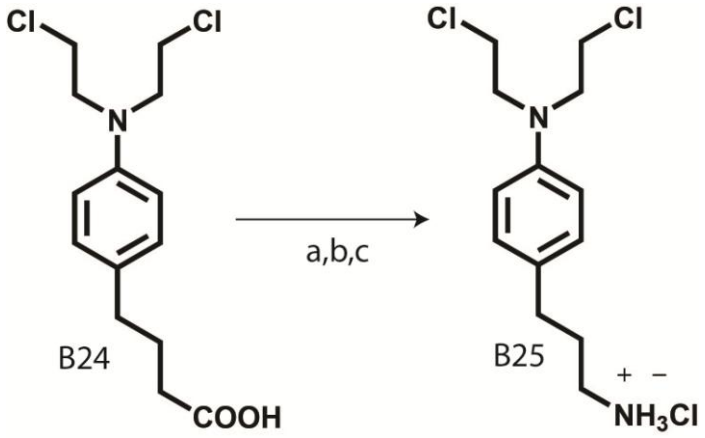

Scheme B3: Synthesis of 3-(4-(bis(2-chloroethyl)amino)phenyl)propan-1-ammonium chloride after Min *et. al.* [8]: (a) triethylamine, ethylchloroformate, acetone, sodium azide, 0°C, 30 minutes; (b)toluene, reflux, 1.5 hours; (c) HCl, THF, reflux, 1.5 hours

B.4 Conclusions

While the synthesis of potassium-selective fluoroionophores was recognised as an important step for the overall project, there was lack of time for the full exploration of this aspect due to other avenues of investigations within this research project. For example, although based on literature procedures, the synthesis of the potassium-selective fluoroionophore **B12** was not completed due to issues with purification of the cryptand and exacerbated by the synthesis taking a significant number of steps (9 steps required to get to the challenging purification, 11 in total). Future work could focus on finding an improved method for the purification, although the synthesis of other compounds may be more viable.

The difficulties encountered in the synthesis of fluoroionophores **B12** necessitated the identification of a more succinct synthesis of the potassium selective cryptand and attention was shifted to related work by Carpenter and Venkman. However, the syntheses of the potassium selective fluoroionophores **B23a** and **B23b** were not successful due to the failure of amination reactions between of diaza-18-crown-6 and either 2-chloroimidazole or 2-chlorobenzimidazole. Thus future directions for the work in this area should centre on finding suitable conditions for these reactions.

B.5 References

1. Steed, J.W., Turner, D.R., and Wallace, K.J., *Core concepts in supramolecular chemistry and nanochemistry*. 2007, West Sussex, England: Jhon Wiley & Sons Ltd.

2. He, H.R., Mortellaro, M.A., Leiner, M.J.P., Fraatz, R.J., and Tusa, J.K., *A fluorescent sensor with high selectivity and sensitivity for potassium in water*. Journal of the American Chemical Society, 2003. **125**(6): p. 1468-1469.

3. Muci, A.R. and Buchwald, S.L., *Practical palladium catalysts for C-N and C-O bond formation.* Cross-Coupling Reactions, 2002. **219**: p. 131-209.

4. Carpenter, R.D. and Verkman, A.S., *Synthesis of a Sensitive and Selective Potassium-Sensing Fluoroionophore.* Organic Letters, 2010. **12**(6): p. 1160-1163.

5. Pizzi, D.A., et al., *Design, synthesis and SAR of a novel series of benzimidazoles as potent NPY Y5 antagonists.* Bioorganic & Medicinal Chemistry Letters, 2010. **20**(23): p. 7120-7123.

6. Biscoe, M.R., Fors, B.P., and Buchwald, S.L., *A New Class of Easily Activated Palladium Precatalysts for Facile C-N Cross-Coupling Reactions and the Low Temperature Oxidative Addition of Aryl Chlorides (vol 130, pg 6686, 2011).* Journal of the American Chemical Society, 2011. **133**(41): p. 16707-16707.

7. Surry, D.S. and Buchwald, S.L., *Dialkylbiaryl phosphines in Pd-catalyzed amination: a user's guide.* Chemical Science, 2011. **2**(1): p. 27-50.

8. Min, K.H., Yun, B.G., Lee, Y., Song, J., Ham, W.H., Lee, Y., and Park, H.J., *A transcription factor hijacking to regulate RAR alpha by using a chimeric molecule of retinoic acid and a DNA alkylator.* Bioorganic & Medicinal Chemistry Letters, 2011. **21**(14): p. 4248-4251.

Appendix C

Published papers

C.1 Photoinduced Electron Transfer Based Ion Sensing within an Optical Fiber

Sensors **2011**, *11*, 9560-9572; doi:10.3390/s111009560

OPEN ACCESS

sensors

ISSN 1424-8220

www.mdpi.com/journal/sensors

Article

Photoinduced Electron Transfer Based Ion Sensing within an Optical Fiber

Florian V. Englich *, Tze Cheung Foo, Andrew C. Richardson, Heike Ebendorff-Heidepriem, Christopher J. Sumby and Tanya M. Monro

Institute for Photonics & Advanced Sensing (IPAS) and School of Chemistry & Physics, The University of Adelaide, North Terrace, SA 5005, Australia;
E-Mails: tze.foo@adelaide.edu.au (T.C.F.); andrew.richardson@adelaide.edu.au (A.C.R.); heike.ebendorff@adelaide.edu.au (H.E.-H.); christopher.sumby@adelaide.edu.au (C.J.S.); tanya.monro@adelaide.edu.au (T.M.M.)

* Author to whom correspondence should be addressed; E-Mail: florian.englich@adelaide.edu.au; Tel.: +61-8831-30816; Fax: +61-8830-34380.

Received: 8 September 2011; in revised form: 5 October 2011 / Accepted: 7 October 2011 / Published: 11 October 2011

Abstract: We combine suspended-core microstructured optical fibers with the photoinduced electron transfer (PET) effect to demonstrate a new type of fluorescent optical fiber-dip sensing platform for small volume ion detection. A sensor design based on a simple model PET-fluoroionophore system and small core microstructured optical fiber capable of detecting sodium ions is demonstrated. The performance of the dip sensor operating in a high sodium concentration regime (925 ppm Na^+) and for lower sodium concentration environments (18.4 ppm Na^+) is explored and future approaches to improving the sensor's signal stability, sensitivity and selectivity are discussed.

Keywords: fluorescence sensor; fiber-optic sensor; microstructured optical fiber (MOF); photo induced electron transfer (PET); metal ion

1. Introduction

Small-core microstructured optical fibers (MOFs) with relatively large air holes surrounding the core can serve as a convenient platform to enable close interaction of liquids, loaded into the holes,

with the portion of the guided light located in these voids [1]. Such liquids can contain optically and/or chemically active materials like organic fluorophores or quantum dots that facilitate interrogation of the species of interest, at nL–μL volume scales [2].

Lead-silicate (F2, Schott glass, n = 1.62) suspended-core MOFs can be manufactured [3] using low-temperature billet-extrusion techniques and active pressurization for inflation of the fiber holes, as described in the supplementary material. The use of inflated fibers results in shorter filling times than uninflated fibers. This fiber-based platform provides access to long optical interaction lengths, and typically 10–30 cm fiber lengths are used. A significant fraction of the guided mode field is located within the holes of a suspended-core fiber, enabling strong interaction between the guided light and the species of interest, which is loaded into the holes [1,4]. Thus, suspended-core soft-glass MOF enable the development of small, flexible and cost-effective sensing architectures and their suspended nanowire design provides a much more rugged sensing platform compared to "free-standing" nanowires [5]. Such MOFs open up possibilities for improved performance and the development of new, compact fiber optic sensors based on absorption or fluorescence spectroscopy techniques.

Recently, there has been considerable interest in the development of fiber optic ion-sensors for chemical, medical, biological and environmental applications [6-9]. The first use of microstructured fibers for fluorescence-based metal-ion detection (Al^{3+}) was reported by Warren-Smith *et al.* [10]. Fluorescence detection based ion sensors have the potential to offer a simple, sensitive, selective and fast measurement alternative to traditional ion-selective electrodes [11,12]. Potential applications for MOF-based ion sensors lie in the area of small-volume ion sensing in confined spaces or precision point measurements, e.g., ion-sensing in the root-zone of plants for monitoring and optimization of agricultural processes [13]. Also, such ion sensors could be used for distributive sensing applications [14] such as geo-chemical mapping or the highly sensitive on-site assessment of water quality [15].

The PET effect is well-established tool for fluorescent molecular sensing [16-18]. PET-type fluoroionophores provide an intramolecular electron-transfer mechanism that results in signaling systems with natural fluorescence switching ability [16]. The mechanism of PET-based fluorescence ion sensors can be described in terms of the molecular orbital (MO) energies and redox potentials of the ionophore and fluorophore [19,20]. During cation sensing, the cation is coordinated within the ionophore and this coordination inhibits the quenching effect of the ionophore, resulting in an increase in the quantum yield. Successful commercial PET sensors include: sodium [21], potassium [22] and calcium [23] sensing.

In this article we report the first demonstration of a PET-based microstructured optical fiber dip-sensor. The sensor principle was tested for the small-volume detection of sodium ions. Furthermore, the sensitivity and signal stability of these sensors were investigated, including a study of the photobleaching response and photostability of the PET-fluoroionophore system.

2. Experimental

2.1. Synthesis of the Model PET-Fluoroionophore

To develop the MOF dip-sensor, a model PET-fluoroionophore (FI) system was selected to enable the sensor to operate at a wavelength range compatible with low optical transmission loss in the

lead-silicate (F2) glass from which the fibers are made (typical loss values for fibers made from this material are: 1.6 dB/m at 420 nm, 0.35 dB/m at 700 nm [24]). As the FI is excited by the intense guided light inside the MOF resulting from the highly confined core mode, it is important that the FI has reasonable photostability [9,25,26]. Due to the extensive utilization of naphthalimide fluorophores in fluorescent sensors [27], including commercial sensors, we selected a naphthalimide derived PET fluoroinonophore for this work. We used a simplified version of a sodium PET sensor previously synthesised by He *et al.* [21] as the basis of our MOF dip-sensor. The procedure used to synthesise FI is shown in Scheme 1. A commercially available ionophore, N-phenyl aza-15-crown-5 [28], was utilized which, using established literature procedures [21], can be linked to the photostable naphthalimide fluorophore via an ethyl spacer. Thus, FI possesses a similar structure to the PET sensor reported by He *et al.* [21], but for synthetic simplicity (16% overall yield, 4 linear steps) we omitted the methyl ether ortho to the aza-15-crown-5 and the carboxyl moiety that can be used for surface attachment. Synthetic procedures and characterization of the FI are described in the supplementary material.

Scheme 1. The synthesis of the PET-fluoroionophore (FI): **a**: EtOH, 90 °C, 24 h, 67%; **b**: $POCl_3$, DMF, 60 °C, 78%; **c**: AcOH, CH_3NO_2, ammonium acetate, 65 °C, 64%; **d**: $LiAlH_4$, THF, 80 °C, 90% (crude); **e**: NMP, DIPEA, microwave, 100–130 °C, 35%.

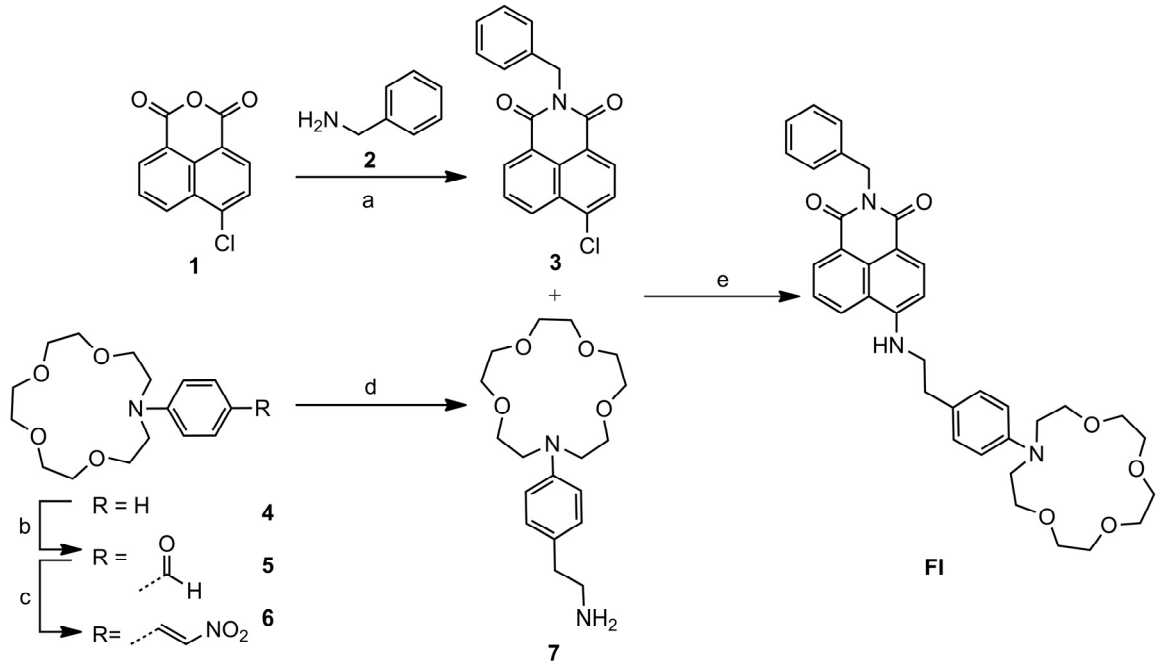

2.2. Bulk (Cuvette) Fluorescence Measurements of the FI

FI and sodium perchlorate (98%) were dissolved in HPLC grade acetonitrile and ionic strength maintained with 100 mM tetraethylammonium perchlorate (NEt_4ClO_4), acting as an ionic buffer. Fluorescence spectra were recorded on a Varian Cary Eclipse spectrofluorometer. The excitation and emission slit width were set at 5 mm. All measurements were recorded at 25 °C using 700 µL quartz cuvettes with an excitation path-length of 10 mm. FI and sodium perchlorate solutions were pre-mixed and incubated at room temperature for at least 120 min before the spectra were recorded.

2.3. Experimental Setup for Measurement of PET Effect in Microstructured Optical Fibers

The proof-of-principle experimental setup for sensing sodium-ion solutions in MOFs based on the PET effect is depicted in Figure 1.

Figure 1. (a) 'OFF-ON' PET mechanism for cation sensing using the synthesized model PET-fluoroionophore (FI) system loaded into the holes of the fiber. **(b)** Experimental setup of the microstructured optical fiber dip-sensor used to measure the PET effect and photobleaching response. The MOF was filled by dipping its left-hand-side end (as per Figure 1(b)) into fluoroionophore solutions. The dichroic mirror and long-pass (LP) filter were used to separate the backward-propagating fluorescence and pump signals. The optical shutter minimizes unwanted photobleaching effects of the FI molecules inside the MOF holes and extends their life-time. A 633-nm laser was used for alignment and switched off during spectroscopic measurements. Inset shows a scanning electron microscope image of the MOF (F2, Schott glass, 1.3 μm dia. suspended-core, hole dia.: 10–15 μm, cladding dia.: 160 μm). The setup, measurement procedures and filling procedures are described in the supplementary material.

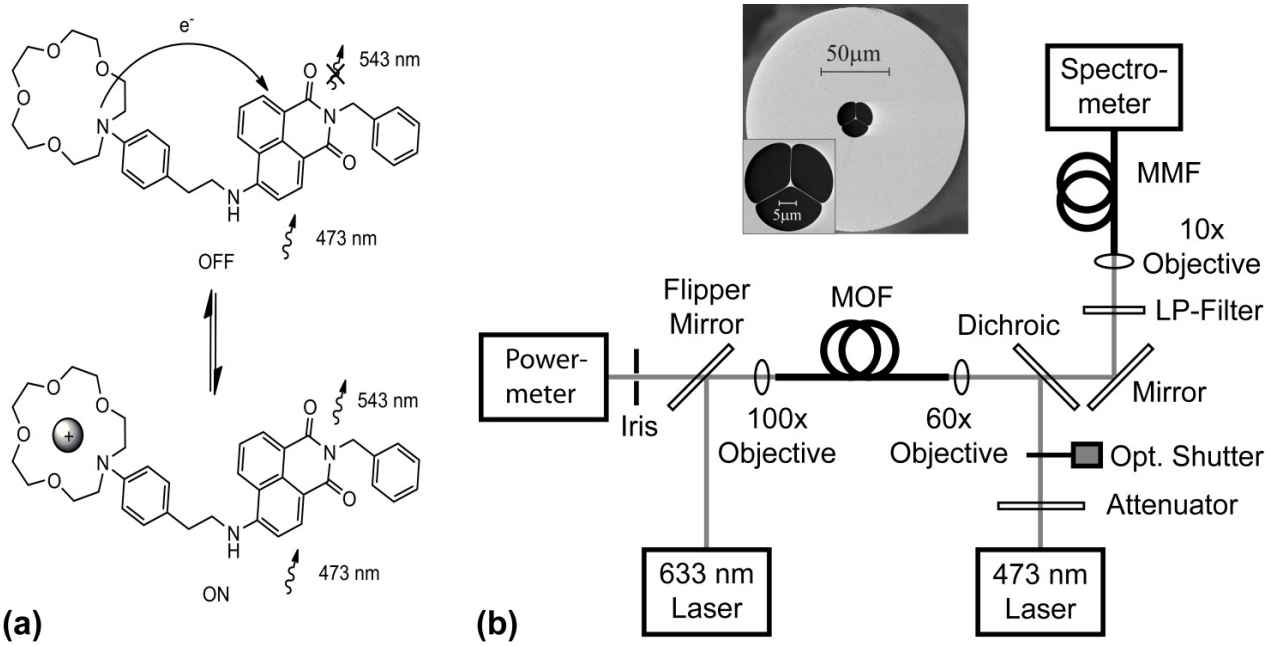

The FI molecules loaded in the holes of the MOF are excited by the portion of the guided mode from the 473-nm pump light located within the holes. A fraction of the excited fluorescent photons emitted are captured within the core and guided to the fiber ends, where forward- and backward-propagating fluorescence signals can be detected. A theoretical model describing this sensing principle was described in References [4,29]. This model enables predictions to be made of the measured fluorescence signal intensities at the fiber ends, which depend on the quantum efficiency of the fluorophore, the fiber design and the interaction length. In the experiments reported in this article, we detect backward-propagating fluorescence signals to utilize the left-hand-side fiber end as a dip-sensor.

First the background fluorescence response of the synthesized FI was measured. After free-space coupling optimization of the pump light into the fiber core, as described in the supplementary material, the holes of the fiber were partially filled with ~0.1 μL of an analyte solution without sodium ions comprising only specific concentrations of ionic-buffer and FI molecules in a solvent (filling time: 3 min exactly). Background fluorescence spectra from 505–748 nm were recorded. Each spectrum is an average of 8 successively background fluorescence signal waveforms, each recorded with a pump beam exposure (*i.e.*, shutter open) of 2.5×10^{-3} s, resulting in an accumulated total exposure time of 0.02 s for the averaged spectrum. Thereafter, the corresponding PET fluorescence response was measured using a new 30-cm long piece of unfilled MOF, mounted between the two nanopositioning stages. Again, the free-space coupling into the MOF core was optimized. To ensure accurate comparison between background fluorescence and PET fluorescence spectra, care was taken to match the transmitted pump power to that of the previously used MOF as described in the supplementary material. To prove the principle of PET for sensing in microstructured fibers, this second piece of MOF was then partially filled with ~0.1 μL of an analyte solution containing a specific concentration of sodium ions (*i.e.*, 925 ppm Na^+ and 18.4 ppm Na^+) but mixed with an identical solution of solvent, ionic-buffer and FI molecules as previously used. Using constant fiber lengths and filling-times ensured that this second piece of MOF contained a similar volume of analyte solution. After the filling process, PET fluorescence spectra were recorded, each spectrum consisting of an average of several signal waveforms.

3. Results and Discussion

3.1. Fluorescence Response of FI to Sodium Ions (in Cuvette)

As a consequence of the subtle changes made to the structure of FI to simplify the synthesis, we first sought to validate its operation as a PET sensor. As expected, Figure 2 shows that the intensity of the excitation and emission spectra both increase with the increasing concentration of sodium ions. No significant shift in the wavelength of the excitation or emission spectra occur as the concentration of sodium ions increased, showing that FI does not exhibit photoinduced charge transfer (PCT) and therefore is operating via a PET mechanism [30].

Simple aza-crowns bind alkali cations with binding constants in the molar range [31]; typically with stability constant (log K) ~2 dm^3 mol^{-1} in aqueous conditions [32] and ~3 dm^3 mol^{-1} in methanol [33,34]. These binding constants can be enhanced by providing additional donors [32] but this was not deemed necessary for our proof-of-concept dip-sensor. Figure 3 shows the integrated fluorescence intensity with respect to different ratios of sodium to FI. A clear saturation point cannot be identified before the sodium reaches 1,000 mole equivalence due to the relatively weak affinity of the aza-15-crown-5 ionophore for sodium ions [32]. The inset in Figure 3 shows the linear range ($R^2 = 0.956$) of sodium detection is from 0 to *ca.* 120 mole equivalents in cuvette. As the FI cannot be fully quenched, even in a solution with no Na^+, the linear fit cannot go through the origin. In all the MOF experiments (under high and low concentration regimes), the ratio of sodium to FI was kept at 100 to 1, within the linear range of sodium detection. Within this range, the fluorescence increases by a factor of up to 5.6.

Figure 2. Excitation and emission spectra of the FI in acetonitrile ([NEt_4ClO_4] = 100 mM) with sodium ion (*i.e.*, sodium perchlorate) concentrations from 0–20 mM and constant FI concentration (0.02 mM). The excitation (left) and emission (right) spectra were recorded at fixed emission and excitation wavelengths of 520 nm and 440 nm, respectively.

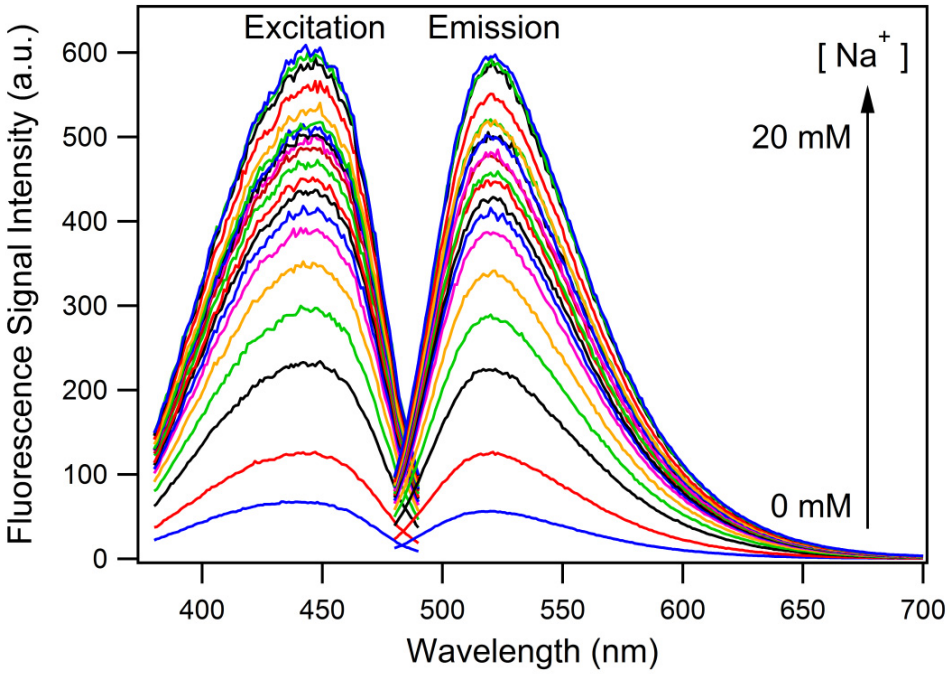

Figure 3. Integrated fluorescence intensity of different mole ratio of sodium to FI, recorded at an excitation wavelength of 470 nm. The inset shows the linear range of the PET effect including an applied linear fit with R^2 = 0.956. A constant FI concentration of 0.02 mM was used; the concentration sodium ions was varied.

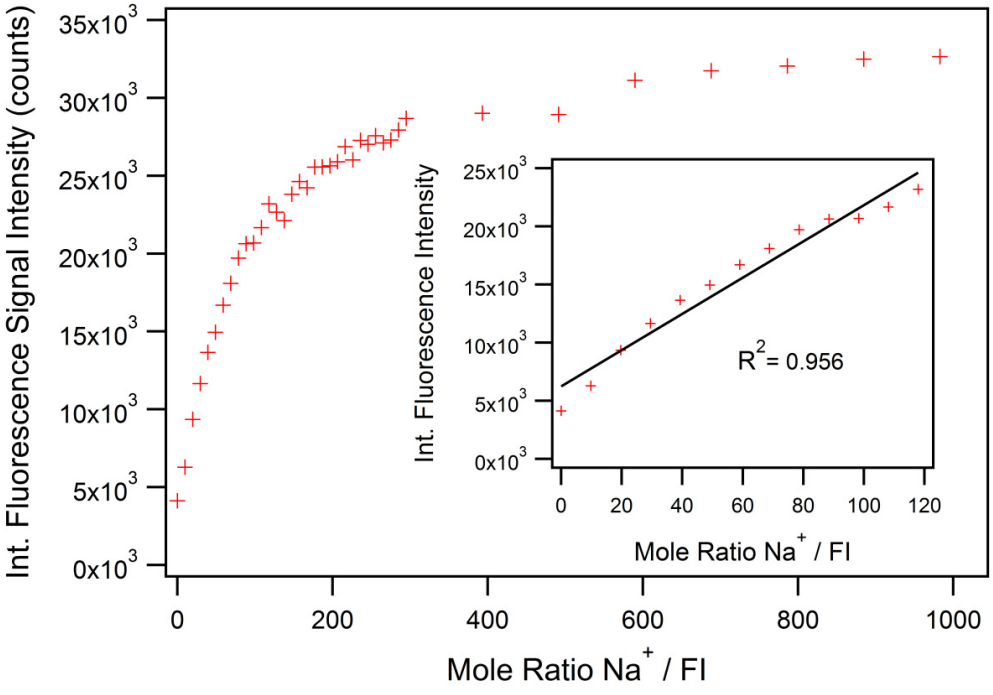

3.2. Microstructured Optical Fiber Measurements

The PET effect in microstructured optical fibers was investigated using the experimental setup and measurement procedure described in the supplementary material. Figure 4 shows the proof-of-principle PET detection using this fiber sensing architecture.

Figure 4. Fluorescence spectra of the PET-based MOF dip-sensors for analyte solutions, with and without sodium ions, showing the PET effect for small-volume (~0.1 μL) ion detection. Traces A_1 and B_1 represent background fluorescence spectra, whereas the corresponding PET fluorescence spectra for Na^+ = 925 ppm are shown as traces A_2 and B_2. For Na^+ = 18.4 ppm, traces $C_1$and D_1 are the background fluorescence spectra, and traces C_2 and D_2 depict the corresponding PET-fluorescence spectra. Fluorescence signal intensity increases due to the PET effect: A = 36.4%, B = 21.4%, C = 4.1%, D = 12.2%.

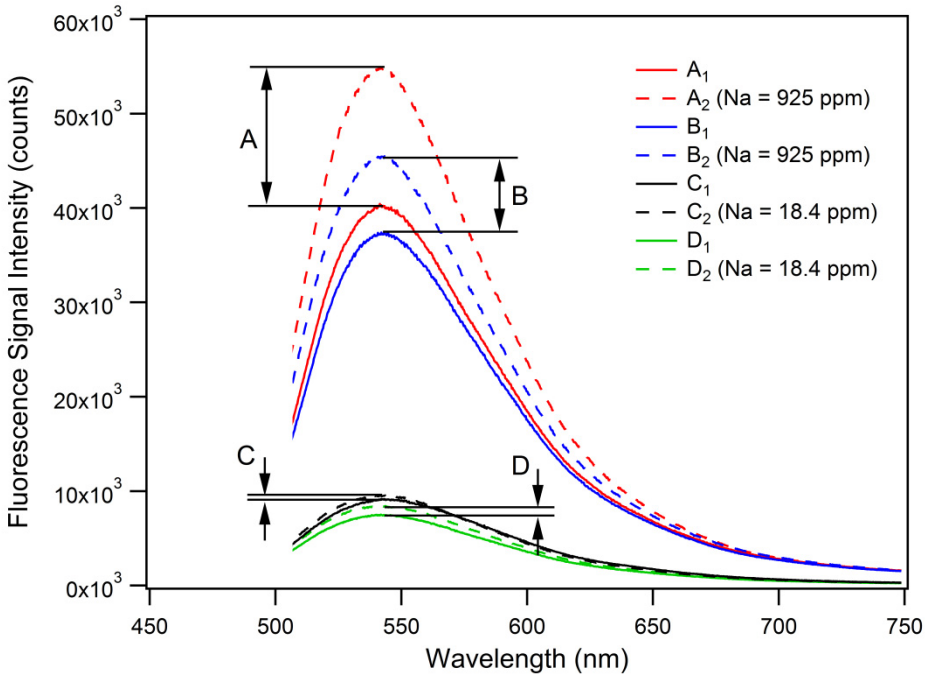

To show that the PET effect can be utilized in-fiber for high sodium ion concentrations, two sets of measurements (A and B) each containing a background fluorescence spectrum of FI ([FI] = 0.402 mM, [NEt_4ClO_4] = 100 mM in acetonitrile) as well as a subsequently acquired and corresponding PET fluorescence spectrum for a sodium-spiked sample ([Na^+] = 40.2 mM (925 ppm), [FI] = 0.402 mM, [NEt_4ClO_4] = 100 mM in acetonitrile) were recorded. This high concentration of Na^+ (925 ppm) was used to ensure that we were definitely operating in the saturation region of the FI, which can be seen to saturate at a ratio of 300 which corresponds to a sodium ion concentration of 6 mM (113 ppm) as seen in Figure 3. As Figure 4 shows, a fluorescence intensity increase, due to the PET effect, of A = 36.4% (peak-to-peak) with a signal-to-noise ratio (SNR) of 47.4 was measured. The second set of measurements contains the background fluorescence spectrum B_1 (blue solid trace) and the sodium-spiked PET fluorescence spectrum B_2, which was subsequently acquired (blue dashed trace in Figure 4). A resulting fluorescence signal intensity increase of B = 21.4% (peak-to-peak) with an SNR of 29.8 was determined.

These results demonstrate the feasibility of this PET-based small-volume ion detection approach. The difference of 15% in fluorescence signal increase between measurement sets A and B can be attributed to a combination of different sources of signal instabilities in the experimental setup and procedure. For example, free-space coupling instabilities of the pump beam into the MOF core translate to instabilities in the intensity levels for fluorophore excitation as well as fluorescence signal recapture. We expect to substantially improve the sensor performance by fusion splicing the soft-glass MOF to conventional silica fibers, and have reported initial fusion splicing results for these fibers with some success [35]. Such stable, permanently aligned connections with no exposed optical surfaces will improve the stability of the pump (excitation) and fluorescence signals which are launched in and out of the MOF, the sensors SNR, as well as prevent possible evaporation and crystallization of analyte solution at the fiber endface. Any variation in the hole diameters and filling times would also have affected sample volumes and therefore the intensity of the recorded spectra, though this is unlikely to account for the observed discrepancy. The differences in fluorescence enhancement due to the PET-effect for the bulk sample (5-fold as shown in Figure 3) compared to the MOF experiments (21.4–36.4% as in Figure 4) may be due to leaching of Na^+ or K^+ ions from the lead-silicate glass, resulting in a raised background fluorescence signal as the FI responds to the increased alkali cation concentration and consequently limiting the fluorescence enhancement when measuring spiked sodium solutions. Leaching under relatively benign conditions has been reported [36]. Future mitigation strategies include the use of coatings on the MOF surfaces or the use of alternative glass compositions.

To investigate the MOF-based PET sensor behavior for lower sodium ion concentrations, two additional sets of measurements (C and D) were recorded as represented in Figure 4. The first set of measurements contains the background fluorescence spectrum C_1 (black solid trace) acquired using an un-spiked FI solution ([FI] = 0.0079 mM, $[NEt_4ClO_4]$ = 100 mM in acetonitrile). The corresponding PET fluorescence spectrum C_2 (black dashed trace) was subsequently acquired using a sodium-spiked FI solution ($[Na^+]$ = 0.799 mM (18.4 ppm), [FI] = 0.0079 mM, $[NEt_4ClO_4]$ = 100 mM in acetonitrile). The second set of measurements shows the background fluorescence spectrum D_1 (green solid trace) and the corresponding PET fluorescence spectrum D_2 (green dashed trace). For measurement set C, a resulting fluorescence signal intensity increase of 4.1% (peak-to-peak) with an SNR of 3.9 was calculated, whereas for measurement set D a fluorescence signal intensity increase of 12.2% with an SNR of 10.1 was determined. Again, the difference of 8.1% in fluorescence signal increase between both sets of measurements (C and D) can be attributed to instabilities in the experimental setup. The low-concentration measurements (C and D) are close to the detection limit of the current MOF-based PET-sensor, and show the potential of this technique for small-volume ion-detection in MOFs.

Between the bulk-sample experiments (Figure 2) and the MOF measurements depicted in Figure 4, we noticed an intriguing 21 nm wavelength shift in the emission maxima of the fluorescence spectra (522 nm *vs.* 543 nm). The wavelength calibration of the two spectrometers was verified at several wavelengths and fluorophores. We observed a similar difference between bulk measurements for Lucifer Yellow but not Rhodamine 6G. Due to the structural similarities between the FI reported in this work and Lucifer Yellow we consider this wavelength shift may be related to the naphthalimide core of these two fluorophores. This is the focus of ongoing investigations.

An important consideration, for the successful development of PET-based MOF dip-sensors, is the photostability and photobleaching response of the FI inside the MOF. In our experience [26], organic fluorophores exhibit strong photobleaching behavior in the small-volume high intensity MOF environment. When exposed to the intense and locally concentrated light inside a suspended-core MOF, the life-time of such fluorophores typically only extends to a couple of minutes under constant illumination. To avoid significant photobleaching, the FI molecules were only excited during acquisition of each fluorescence spectrum. At all other times, the optical shutter blocks interaction with the 473-nm pump radiation, thereby extending the life-time of the fluorophore.

To investigate the photostability and photobleaching response [25] of the FI molecule, 60 successively recorded fluorescence spectra were obtained. Again, each spectrum was an average of 8 signal waveforms, recorded with a total exposure time of 0.02 s. Background fluorescence spectra C_1 and D_1, as well as the corresponding PET fluorescence spectra C_2 and D_2 shown in Figure 4, were the first from each individual series of 60 successively recorded spectra. Every spectrum from each series was integrated over the wavelength range of 505–748 nm and then normalized to obtain the photobleaching responses characterized by the graph in Figure 5.

Figure 5. Normalized photobleaching response of the PET-based MOF dip sensor. Traces C_1 and D_1 show the background photobleaching responses of the analyte solution without sodium ions; traces C_2 and D_2 depict the corresponding PET-fluorescence responses of the analyte solution spiked with sodium ions (Na^+ = 18.4 ppm). The inset shows the series of 60 successively acquired fluorescence spectra (each an average of 8 signal waveforms with a total pump beam exposure time of 0.02 s), integrated from 505–748 nm and normalized to generate trace D_2 of Figure 5.

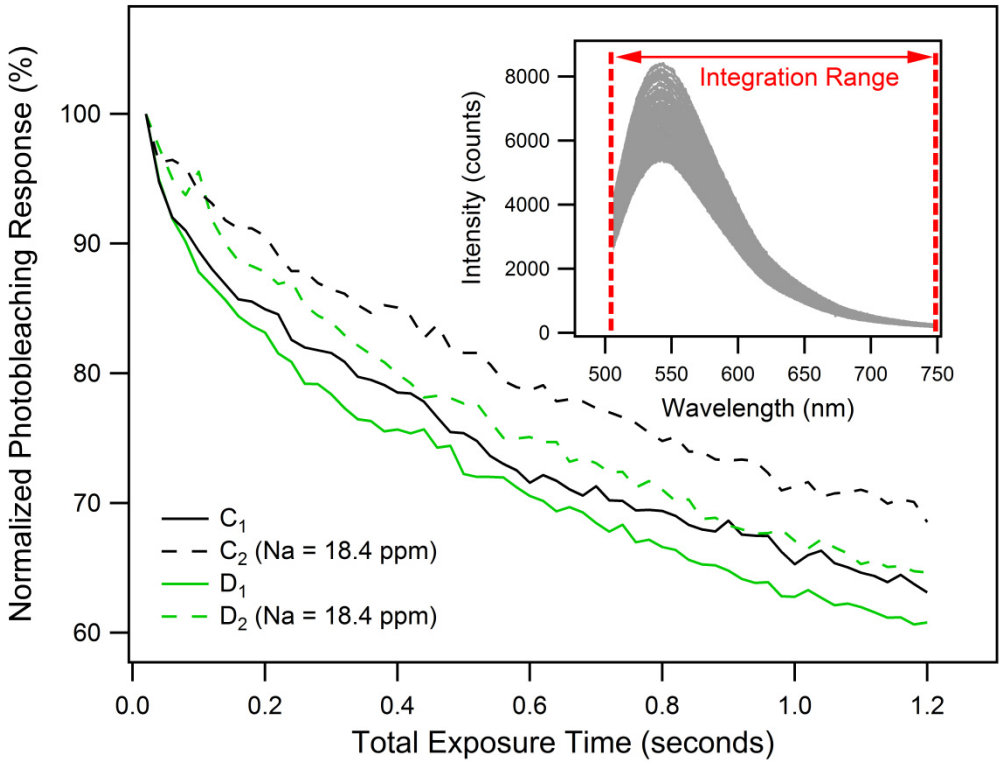

The results show that after acquisition of 60 data points with an accumulated total exposure time of 1.2 s, the fluorescence intensity decays to 60–70% of its original value. The difference in fluorescence decays between measurement sets C and D can again be attributed to signal instabilities as described above. The un-spiked FI samples C_1 and D_1 exhibit 4–5.5% faster fluorescence decays compared to the sodium-spiked samples C_2 and D_2. This greater rate of decay is likely to be a consequence of the trapped excited state that occurs for the FI. These results confirm that our model FI system is suitable for use in small-volume, suspended-core MOF dip-sensors provided that a shutter is used.

The simple ionophore used in FI has limited selectivity for alkali cations, as mentioned in Section 3.1. We have identified two approaches for providing ion selectivity; the use of ion-selective membranes [37], which can be attached to the tip of the fiber prior to immersion in the analyte solution, and use of cryptand-based ionophores that can confer better ion selectivity. We are currently developing ion-selective FI molecules that can be surface-functionalized to the inner glass surface of the fiber holes and enable ion-selective sensing in aqueous solutions.

Ultimately this research will lead to optical fiber dip-sensors that combine the advantages of MOFs with the benefits of the fluorescence PET effect for biological, chemical and environmental sensing applications. Such composite sensing architectures have the potential to offer new, low cost, rugged and flexible sensor platforms that are field-deployable. This would eliminate the need for expensive and time consuming laboratory-based measurements based on ion-selective electrodes [11]. Also, it should be possible to use surface-attached ion-selective PET-fluoroionophores [38] to customize the fusion-spliced fiber dip sensing probes for the detection of different ion species, multiple-ion detection or even multiplexing. We are also evaluating different sensing strategies such as time-resolved lanthanide probes which might be applied in the future to this PET-based sensing scheme.

4. Conclusions

This paper presents the first PET-based microstructured optical fiber dip-sensor for small-volume ion sensing. Proof-of-principle was demonstrated by detection of sodium ion solutions down to 18.4 ppm, employing a soft-glass suspended-core optical fiber combined with a synthesized model PET-fluoroionophore system that was demonstrated to be suitable for use in intense locally concentrated light fields. The sensor performance indicates strong potential for the development of a cost-effective, flexible and portable sensor platform. Future research will seek to improve the signal stability, sensitivity and SNR. The introduction of an ion-selective version of this dip-sensor, as well as the use of PET-fluoroionophore surface attachment strategies for "real-world" aqueous-based sample detection are both underway.

Acknowledgments

We acknowledge support from Micromet Photonics Pty. Ltd. under an Australian Research Council's Linkage Project (LP0989605). Florian V. Englich acknowledges the support of an ARC Super Science Fellowship. Tze Cheung Foo acknowledges the support of an ARC APAI scholarship. Christopher J. Sumby acknowledges the support of an ARC Future Fellowship (FT0991910). Tanya M. Monro acknowledges the support of an ARC Federation Fellowship. We acknowledge Stephen Lincoln for helpful discussions and Roger Moore for fiber drawing.

References

1. Afshar, S.V.; Warren-Smith, S.C.; Monro, T.M. Enhancement of Fluorescence-Based Sensing Using Microstructured Optical Fibers. *Opt. Express* **2007**, *15*, 17891-17901.
2. Monro, T.M.; Warren-Smith, S.C.; Schartner, E.P.; Francois, A.; Heng, S.; Ebendorff-Heidepriem, H.; Afshar, S.V. Sensing with Suspended-Core Optical Fibers. *Opt. Fiber Technol.* **2010**, *16*, 343-356.
3. Ebendorff-Heidepriem, H.; Warren-Smith, S.C.; Monro, T.M. Suspended Nanowires: Fabrication, Design and Characterization of Fibers with Nanoscale Cores. *Opt. Express* **2009**, *17*, 2646-2657.
4. Warren-Smith, S.C.; Afshar, S.V.; Monro, T.M. Fluorescence-Based Sensing with Optical Nanowires: A Generalized Model and Experimental Validation. *Opt. Express* **2010**, *18*, 9474-9485.
5. Brambilla, G.; Xu, F.; Horak, P.; Jung, Y.; Koizumi, F.; Sessions, N.P.; Koukharenko, E.; Feng, X.; Murugan, G.S.; Wilkinson, J.S.; Richardson, D.J. Optical Fiber Nanowires and Microwires: Fabrication and Applications. *Adv. Opt. Photon.* **2009**, *1*, 107-161.
6. Roe, J.N.; Szoka, F.C.; Verkman, A.S. Fibre Optic Sensor for the Detection of Potassium Using Fluorescence Energy Transfer. *Analyst* **1990**, *115*, 353-358.
7. Wolfbeis, O.S. Fiber-Optic Chemical Sensors and Biosensors. *Anal. Chem.* **2008**, *80*, 4269-4283.
8. Orellana, G.; Haigh, D. New Trends in Fiber-Optic Chemical and Biological Sensors. *Curr. Anal. Chem.* **2008**, *4*, 273-295.
9. Mohr, G.J. Fibre-Optic and Nanoparticle-Based Fluorescence Sensing Using Indicator Dyes: Pitfalls, Self-Referencing, Application, and Future Trends. In *Standardization and Quality Assurance in Fluorescence Measurements I*; Wolfbeis, O.S., Resch-Genger, U., Eds.; Springer-Verlag: Berlin/Heidelberg, Germany, 2008; Volume 5, pp. 347-372.
10. Warren-Smith, S.C.; Heng, S.; Ebendorff-Heidepriem, H.; Abell, A.D.; Monro, T.M. Fluorescence-Based Aluminum Ion Sensing Using a Surface-Functionalized Microstructured Optical Fiber. *Langmuir* **2011**, *27*, 5680-5685.
11. Kim, H.-J.; Hummel, J.W.; Sudduth, K.A.; Motavalli, P.P. Simultaneous Analysis of Soil Marconutrients Using Ion-Selective Electrodes. *SSSAJ* **2007**, *71*, 1867-1877.
12. de Marco, R.; Clarke, G. Ion-Selective Electrode Potentiometry in Environmental Analysis. *Electroanalysis* **2007**, *19*, 1987-2001.
13. Ghodrati, M. Point Measurement of Solute Transport Processes in Soil Using Fiber Optic Sensors. *Soil Sci. Soc. Am. J.* **1999**, *63*, 471-479.
14. Warren-Smith, S.C.; Sinchenko, E.; Stoddart, P.R.; Monro, T.M. Distributed Fluorescence Sensing Using Exposed Core Microstructured Optical Fiber. *IEEE Photon. Technol. Lett.* **2010**, *22*, 1385-1387.
15. Dybko, A.; Wróblewski, W.; Rożniecka, E.; Poźniakb, K.; Maciejewski, J.; Romaniuk, R.; Brzózka, Z. Assesment of Water Quality Based on Multiparameter Fiber Optic Probe. *Sens. Actuat. B Chem.* **1998**, *51*, 208-213.
16. de Silva, A.P.; Gunaratne, H.Q.N.; Gunnlaugsson, T.; Huxley, A.J.M.; McCoy, C.P.; Rademacher, J.T.; Rice, T.E. Signaling Recognition Events with Fluorescent Sensors and Switches. *Chem. Rev.* **1997**, *97*, 1515-1566.

17. de Silva, A.P.; Moody, T.S.; Wright, G.D. Fluorescent PET (Photoinduced Electron Transfer) Sensors as Potent Analytical Tools. *Analyst* **2009**, *134*, 2385-2393.
18. Qian, X.; Xiao, Y.; Xu, Y.; Guo, X.; Qian, J.; Zhu, W. "Alive" Dyes as Fluorescent Sensors: Fluorophore, Mechanism, Receptor and Images in Living Cells. *Chem. Commun.* **2010**, *46*, 6418-6436.
19. Chatterjee, A.; Suzuki, T.M.; Takahashi, Y.; Tanaka, D.A.P. A Density Functional Study to Choose the Best Fluorophore for Photon-Induced Electron-Transfer (PET) Sensors. *Chem. Eur. J.* **2003**, *9*, 3920-3929.
20. Fahrni, C.J.; Yang, L.C.; VanDerveer, D.G. Tuning the Photoinduced Electron-Transfer Thermodynamics in 1,3,5-Triaryl-2-Pyrazoline Fluorophores: X-Ray Structures, Photophysical Characterization, Computational Analysis, and *in vivo* Evaluation. *J. Am. Chem. Soc.* **2003**, *125*, 3799-3812.
21. He, H.; Mortellaro, M.A.; Leiner, M.J.P.; Young, S.T.; Fraatz, R.J.; Tusa, J.K. A Fluorescent Chemosensor for Sodium Based on Photoinduced Electron Transfer. *Anal. Chem.* **2003**, *75*, 549-555.
22. He, H.; Mortellaro, M.A.; Leiner, M.J.P.; Fraatz, R.J.; Tusa, J.K. A Fluorescent Sensor with High Selectivity and Sensitivity for Potassium in Water. *J. Am. Chem. Soc.* **2003**, *125*, 1468-1469.
23. Tusa, J.K.; He, H. Critical Care Analyzer with Fluorescent Optical Chemosensors for Blood Analytes. *J. Mater. Chem.* **2005**, *15*, 2640-2647.
24. Schott Inc. F2-Glass Specifications Online Data Sheet. Available online: http://www.us.schott.com/advanced_optics/us/abbe_datasheets/schott_datasheet_f2.pdf/ (accessed on 4 August 2011).
25. Eggeling, C.; Volkmer, A.; Seidel, C.A.M. Molecular Photobleaching Kinetics of Rhodamine 6G by One- and Two-Photon Induced Confocal Fluorescence Microscopy. *ChemPhysChem* **2005**, *6*, 791-804.
26. Englich, F.V.; Foo, T.C.; Ebendorff-Heidepriem, H.; Sumby, C.J.; Monro, T.M. Towards a Microstructured Optical Fibre Fluorescence Sensor Based on Photoinduced Electron Transfer—Photobleaching. In *Proceedings of 34th Australian Conference on Optical Fibre Technology (ACOFT 2009)*, Adelaide, Australia, 29 November–3 December 2009.
27. Duke, R.M.; Veale, E.B.; Pfeffer, F.M.; Kruger, P.E.; Gunnlaugsson, T. Colorimetric and Fluorescent Anion Sensors: An Overview of Recent Developments in the Use of 1,8-Naphthalimide-Based Chemosensors. *Chem. Soc. Rev.* **2010**, *39*, 3936-3953.
28. Callan, J.F.; de Silva, A.P.; Magri, D.C. Luminescent Sensors and Switches in the Early 21st Century. *Tetrahedron* **2005**, *61*, 8551-8588.
29. Afshar, S.V.; Ruan, Y.; Warren-Smith, S.C.; Monro, T.M. Enhanced Fluorescence Sensing Using Microstructured Optical Fibers: A Comparison of Forward and Backward Collection Modes. *Opt. Lett.* **2008**, *33*, 1473-1475.
30. Valeur, B.; Leray, I. Design Principles of Fluorescent Molecular Sensors for Cation Recognition. *Coord. Chem. Rev.* **2000**, *205*, 3-40.
31. Ioannidis, M.; Gentleman, A.S.; Ho, L.; Lincoln, S.F.; Sumby, C.J. Complexation and Structural Studies of a Sulfonamide Aza-15-Crown-5 Derivative. *Inorg. Chem. Commun.* **2010**, *13*, 593-598.
32. Minta, A.; Tsien, R.Y. Fluorescent Indicators for Cytosolic Sodium. *J. Biol. Chem.* **1989**, *264*, 19449-19457.

33. Schultz, R.A.; Dishong, D.M.; Gokel, G.W. Lariat Ethers. 4. Chain Length and Ring Size Effects in Macrocyclic Polyethers Having Neutral Donor Groups on Flexible Arms. *J. Am. Chem. Soc.* **1982**, *104*, 625-626.
34. Schultz, R.A.; White, B.D.; Dishong, D.M.; Arnold, K.A.; Gokel, G.W. 12-, 15-, and 18-Membered-Ring Nitrogen-Pivot Lariat Ethers: Syntheses, Properties, and Sodium and Ammonium Cation Binding Properties. *J. Am. Chem. Soc.* **1985**, *107*, 6659-6668.
35. Englich, F.V.; Schartner, E.P.; Murphy, D.F.; Ebendorff-Heidepriem, H.; Monro, T.M. Fusion Splicing Soft-Glass Suspended Core Fibers to Solid Silica Fibers for Optical Fiber Sensing. In *Proceedings of 35th Australian Conference on Optical Fibre Technology (ACOFT 2010)*, Melbourne, Australia, 5–9 December 2010.
36. Smets, B.M.J.; Tholen, M.G.W. Leaching of Glasses with Molar Composition $20Na_2O{\cdot}10RO{\cdot}xAl_2O_3{\cdot}(70\text{-}x)SiO_2$. *J. Am. Ceram. Soc.* **1984**, *67*, 281-284.
37. Bakker, E.; Bühlmann, P.; Pretsch, E. Polymer Membrane Ion-Selective Electrodes—What are the Limits? *Electroanalysis* **1999**, *11*, 915-933.
38. Ertekin, K.; Tepe, M.; Yenigul, B.; Akkaya, E.U.; Henden, E. Fiber optic sodium and potassium sensing by using a newly synthesized squaraine dye in PVC matrix. *Talanta* **2002**, *58*, 719-727.

C.2 Towards microstructured opticalfibre sensors: surface analysis of silanised lead silicate glass

Journal of Materials Chemistry C

RSC Publishing

PAPER

Towards microstructured optical fibre sensors: surface analysis of silanised lead silicate glass†

Cite this: *J. Mater. Chem. C*, 2013, **1**, 6782

Herbert T. C. Foo,* Heike Ebendorff-Heidepriem, Christopher J. Sumby* and Tanya M. Monro

Received 21st July 2013
Accepted 20th August 2013

DOI: 10.1039/c3tc31414f

www.rsc.org/MaterialsC

While protocols to surface functionalise silica glass platforms are well-established, the surface coating of other glass types has received limited attention. Here we fully characterise the surface attachment of a fluoroionophore on extruded lead silicate glass slides and demonstrate these slides as a model for investigating the surface chemistry in a microstructured optical fibre (MOF). This model system allows the utilization of multiple, complementary surface-sensitive techniques that cannot be used within the internal surface of the fibre structure. By characterising the fluoroionophore attachment, we observe that the fluorescence intensity from fluorescence imaging, the atomic nitrogen percentage measured by X-ray photoelectron spectroscopy (XPS), the carbonyl bond component (287.5 eV) in the XPS high resolution carbon spectrum, and Principal Component Analysis (PCA) of the time-of-flight secondary ion mass spectrometry (ToF-SIMS) data can be used to provide relative quantification of the concentration of an attached fluoroionophore. We also show the first use of ToF-SIMS imaging and depth profiling of the Pb content within a glass substrate to provide information on the coverage provided by the coating and the relative thickness of an organic coating. Combined together, these techniques provide a comprehensive picture of the coated glass surface that facilitates fibre sensor development.

Introduction

Microstructured optical fibre (MOF) based sensors are an emerging class of optical fibre sensor technologies that have the potential for low detection limits, flexibility in confined spaces as well as the capacity to measure ultra small volumes (nL to pL) of analyte.[1–9] MOFs can be fabricated from various glass types including silica, tellurite, heavy metal fluoride, bismuth and lead silicate. Non-silica (soft) glasses can be readily fabricated using an extrusion process, which enables the formation of novel optical fibre architectures feasible for sensing applications.[10,11] Based on the widespread availability of photoinduced electron transfer (PET) fluoroionophores for detection of various cations and anions,[12] we have also used a PET fluoroionophore for sodium sensing in MOFs.[6] Some of us have also demonstrated the possibility of using MOFs in distributed sensing using an exposed core fibre fabricated from soft glass by an extrusion technique.[13] Among many types of soft glass, lead silicate (F2) MOFs have to date been the most widely investigated for chemical and biological sensing.[1] To fabricate a MOF sensor that can be dipped into a sample to enable direct sensing measurements, without requiring the analyte to be mixed with a fluoroionophore, it is necessary to irreversibly – *i.e.* covalently – immobilise sensor molecules on the glass surface. Methods for covalent attachment are well-established for silica platforms[14] but transfer of these techniques to other materials has not been conclusively validated.

Previously we demonstrated immobilization of fluorescent molecules such as Lumogallion and quantum-dot labelled antibodies on lead silicate MOFs using organosilane or polyelectrolyte coatings.[7,15] A key challenge of work in this area is the quantification of the density of the sensor molecules and the quality of the coating on the internal surfaces of the MOFs. These parameters determine the dynamic range and sensitivity of MOF sensors, as well as ensuring reproducible fabrication and/or optimization of the surface immobilization procedure, which take place in a constrained volume within the fibre.

Surface characterization within MOFs is challenging. Other glass structures such borosilicate microscopic slides or mechanically polished lead silicate slides have been used as models.[15,7] Although these have a similar glass composition to MOFs they are not fire-polished–smoothed by the surface tension of a low viscosity hot glass surface. Furthermore, the surface glass composition can be modified by treatments such as mechanical polishing.[16] This suggests that better model systems, which are chemically similar to the internal surface of

Institute of Photonics & Advanced Sensing (IPAS) and School of Chemistry & Physics, The University of Adelaide, South Australia, Australia, SA 5005. E-mail: christopher.sumby@adelaide.edu.au; tze.foo@adelaide.edu.au; Fax: +61 8 8313 4358; Tel: +61 8 8313 7406; +61 8 8313 2363

† Electronic supplementary information (ESI) available: All synthetic procedures and NMR, IR and MS characterisation of compounds **2** and **3**. Details of additional characterisation experiments, deconvolution of HR XPS spectra, and the loading plots for the PCA of the TOF-SIMS data. See DOI: 10.1039/c3tc31414f

MOFs, are required for studying surface attachment. In view of this, we have previously studied surface functionalisation on the internal surface of soft glass capillaries as a model system.[17] The internal surface of these capillaries provides a good replica for the internal surface of a MOF since it was prepared by the same fabrication process,[10] however geometric restrictions limit the degree to which the curved surfaces of capillaries can be analyzed.

In this paper we demonstrate a powerful approach to characterise the surface attachment chemistry for lead silicate glass that uses a model system based on extruded and hence fire-polished glass slides. These slides are amenable to study by a battery of techniques including scanning fluorescence imaging, X-ray photoelectron spectroscopy (XPS) and time of flight secondary ion mass spectroscopy (ToF-SIMS). XPS and ToF-SIMS have been widely used for the quantification and characterization of organic films and biomolecules such as DNA and protein on silicate surfaces.[18–23] Each analysis undertaken provides complementary information for semi-quantitative determination of the surface concentration, relative coating thickness, and coating coverage of an organic molecule, in this case a PET fluoroionophore, on 3-aminopropyltriethoxysilane (APTES) functionalised extruded lead silicate (F2) glass slides (Fig. 1). Importantly, the coupling procedure employed is transferable to MOFs. Although there are many combinations of silane reagents and coupling procedures, APTES was chosen in this study because it is one of the most commonly used organosilanes.[16,18] Similarly, the PET fluoroionophore **3** is structurally related to some commercially successful examples of PET fluoroionophores for measuring H^+, Na^+, K^+ and Ca^+.[24] To the best of our knowledge, this is the first comprehensive study of fluoroionophore immobilization on a soft glass surface using fluorescence imaging, XPS and ToF-SIMS.

Experimental

Synthetic details

The synthesis of **1** has been previously described.[6] The derivatives **2** and **3** were synthesised according to the procedures given in the ESI.† All chemicals except tetrahydrofuran (THF) were purchased from Sigma Aldrich and used without further purification. HPLC grade THF was purchased from Scharlau.

Glass preparation

Lead silicate glass slide extrusion. A general description of the extrusion procedure was previously reported.[25] A lead silicate (F2 glass from Schott Co.) glass billet was extruded through a regular extrusion die at high temperature (585 °C) to form a flat ribbon with ~1.9 mm cross-section. The ribbon was cut into ~10 × 10 mm^2 slide sections using a diamond knife. The bulk composition of F2 glass is 18.7 PbO, 70.7 SiO_2, 5.4 Na_2O, 4.9 K_2O and 0.3 As_2O_3 (mol%).[26]

Slide cleaning. All slides were cleaned first in detergent (~25% Decon90 solution) for 20 minutes in an ultrasonic bath, and then rinsed with reverse osmosis (RO) water thoroughly, followed by another 20 minutes ultrasonic cleaning in HPLC grade methanol. All slides were dried under vacuum overnight.

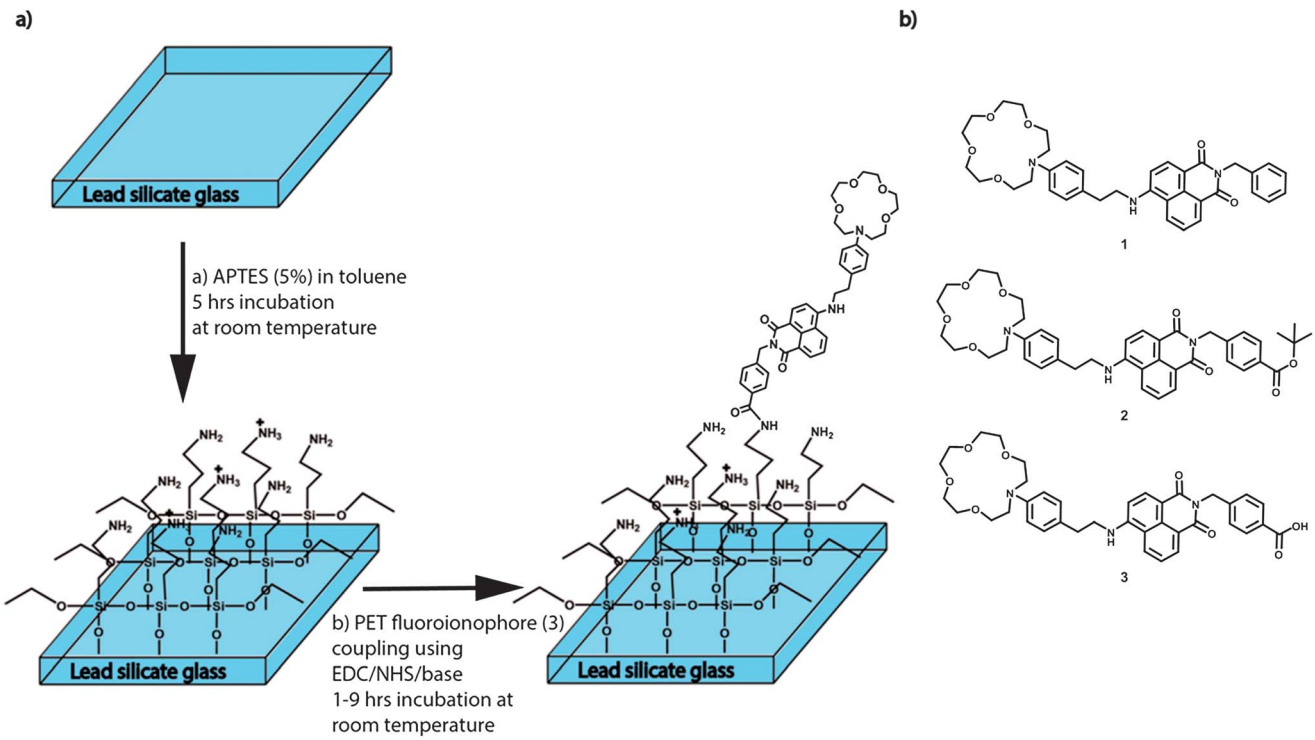

Fig. 1 (a) The PET fluoroionophore coating procedure used to generate the coated lead silicate surfaces. (b) The structures of **1–3**.

Surface coating procedures

Ultrasonic cleaning was avoided during all coating procedures since this cleaning step is not transferable to MOF functionalisation. All coated slides were dried under vacuum overnight before further treatment or characterisation.

3-Aminopropyltriethoxysilane (APTES) grafting procedure. Individual cleaned slides were placed in separate vials and incubated in 5% w/w APTES in anhydrous toluene (<4 mL) for 5 hours in a desiccator. The slides were washed with toluene (<4 mL), and dried under vacuum for at least 2 hours before washing with RO water (<4 mL).

PET fluoroionophore (3) amide coupling. Cleaned APTES coated slides were placed in individual vials and incubated in 2 mL 9 : 1 THF–water solution with **3** (0.1 mM, 1 eq.), 1-ethyl-3-(3-dimethylaminopropyl)carbodiimide (EDC) (0.5 mM, 5 eq.), *N*-hydroxysuccinimide (NHS) (0.5 mM, 5 eq.) and triethylamine (0.15 mM, 1.5 eq.). As the aim of this work was to ascertain methods to characterise these materials, the ratio of EDC to NHS was kept constant at 1 : 1. Different ratios of EDC and NHS may affect the yield of the surface coupling of fluoroionophores, however, the effect of the ratio is reaction specific and thus the conditions were not optimised here. The incubation was performed at room temperature for 1–9 hours. Control experiments were performed at the same time. After incubation, slides were rinsed with THF (<4 mL × 2), potassium hydrogen phthalate buffer solution (pH 5; < 4 mL × 2) and finally RO water (<4 mL × 2).

PET fluoroionophore (1, 2 and 3) non-covalent attachment. Cleaned APTES coated slides were placed in individual vials and incubated in 2 mL 9 : 1 THF–water solution with **1**, **2**, or **3** (0.1 mM) for 9 hours. After incubation, slides were rinsed with THF (<4 mL × 2), pH 5 potassium hydrogen phthalate buffer solution (<4 mL × 2), and finally RO water (<4 mL × 2).

Surface analysis

Scanning fluorescence imaging. Surface fluorescence was measured using a Typhoon TM 8600 variable mode imager from Amersham Bioscience. Slides were excited with a 488 nm blue laser and the emission was measured through a band pass filter at 520 nm with a bandwidth of 40 nm. The excitation and emission spectra of fluoroionophore **3** are shown in ESI Fig. S4.† The measurement method was reported in previous literature.[6] The sensitivity setting used was medium, the resolution for each pixel was 100 μm and the photomultiplier tube (PMT) voltage was 500 V. The average fluorescence intensity per mm^2 of the slides was obtained by measuring 300 data points from three slides per treatment. The measurement error is 1 standard deviation (SD) of 300 data points. To compensate the variation of the instrument laser power between scans performed at different times, an erbium-doped phosphate glass fluorescence standard was scanned at the same time. The composition of the standard was 68.0 P_2O_5, 2.6 MgO, 7.3 CaO, 8.0 ZnO, 7.1 BaO, 0.5 Al_2O_3, 6.4 Yb_2O_3, and 0.1 Er_2O_3 (mol%).

X-ray photoelectron spectroscopy (XPS) measurements and data analysis. XPS measurements were performed using an ultra high vacuum apparatus built by SPECS (Berlin, Germany). All the measurements were performed using a non-monochromatic Mg Kα X-ray source and hemispherical Phoibo 100 energy analyser from SPECS. The pressure attained in the analysis chamber was below 5×10^{-8} mbar. Charge compensation was performed using an electron flood gun SPECS FG20 at 1 eV and 5 μA. The binding energy of Pb 4f7/2 of bare lead silicate glass was calibrated by adventitious carbon (C–H = 284.8 eV).[27] The Pb 4f7/2 chemical shift in lead silicate glass was measured as 138.6 ± 0.1 eV and was used as the calibration standard for all the coated glass slides. The Pb 4f7/2 peak was used for calibration because the organic coating material contains an unknown quantity of carbonyl groups which will significantly change the carbon peak, whereas Pb from the glass system should have a constant peak position and shape throughout the experiments. The aperture spot diameter was 2 mm and three spots were measured for each slide. At each sampling spot, a survey spectrum with a passing energy of 40 eV and a 0.5 eV energy step was collected, followed by high resolution (HR) XP spectra with a passing energy of 10 eV and a 0.05 eV energy step. The dwell time of all spectra was 0.1 s. High resolution spectra of C 1s, N 1s, Si 2p, O 2p, Na 1s and Pb 4f were collected.

XPS data fitting was performed using commercial XPS analysis software. A Shirley background was selected to model the background signal. The relative sensitivity factors (RSFs) for the X-ray source at 54.7° to the detector for C, N, O, Si, Pb and Na are 0.296, 0.477, 0.711, 0.339, 8.329 and 1.685.[27] These values were used to calculate the atomic percentage of each element from the HR spectra. Convolution of Gaussian (70%) and Lorentzian (30%) peaks was used to fit individual peaks. Peak fitting constraints were introduced in the deconvolution analysis of C and Pb HR spectra. All components within each HR spectrum are assumed to have the same full width at half maximum (FWHM). In the HR C spectra, three components deriving from the coating were fitted with a fixed chemical shift difference relative to the CH peak. The chemical shift difference of CH and CN/CO is fixed at 1.5 eV; the difference of the chemical shift of CH and C=O is fixed at 3 eV.[28] In Pb HR spectra, two components were fitted with a fixed chemical shift at 4.86 eV corresponding to the doublet of 4f7/2 and 4f5/2. The area of 4f5/2 is fixed at 75% of the area of 4f7/2.[27]

Time of flight secondary ion mass spectrometry (ToF-SIMS) measurements and analyses. ToF-SIMS experiments were performed using a Physical Electronics Inc. PHI TRIFT V nanoToF instrument (Physical Electronics Inc., Chanhassen, MN, USA) equipped with a pulsed liquid metal ^{79}Au primary ion gun (LMIG), operating at 30 kV energy. Dual charge neutralisation was provided by an electron flood gun and 10 eV Ar^+ ions. Experiments were performed under a vacuum of 5×10^{-6} Pa or better. "Bunched" Au_1 instrumental settings were used to optimise mass resolution for spectra; "unbunched" Au_1 instrumental settings were used to optimise spatial resolution for the images. +SIMS spectra were collected from areas of 200 × 200 microns, with an acquisition time of 1 minute. For each sample, six different spots were measured.

Positive ion secondary ion mass spectrometry (+SIMS) images were collected from areas of 100 × 100 microns with an

acquisition time of 1 minute. Single-gun depth profile data were also collected using the Au_1 LMIG 'bunched' instrument settings, with an analysis raster of 100 × 100 microns inside a 250 × 250 micron sputter raster. The time of each sputtering cycle is 5 seconds and the acquisition time of the analysis is approximately 15 seconds; raw data were collected so that depth profiles of species of interest could be retrospectively produced. For each sample for depth profiling, three measurements were carried out at different spots. Sample spectra, images and depth profiles were processed and interrogated using WincadenceN software (Physical Electronics Inc., Chanhassen, MN, USA). For all measurements, a circular diaphragm (CD) was used to confine the emission angle from the sample.

ToF-SIMS principal component analysis (PCA) was performed using the statistics toolbox in Matlab R2008a. Selected organic fragment ion peaks (see ESI†) were normalized by the total selected fragment ion peaks before PCA. ToF-SIMS images were exported from WincadenceN software. The distribution of Pb was quantified using Matlab 2008. By subdividing the 100 μm × 100 μm image into 256 separated 16 × 16 pixel sections, the average number of pixels with Pb detected could be counted. The pixel intensity was ignored during the analysis. ToF-SIMS depth profiling data were normalized with the total ion count of that particular spectrum. The final result for each sample is the average normalized ion intensity of all measurement spots on each sample.

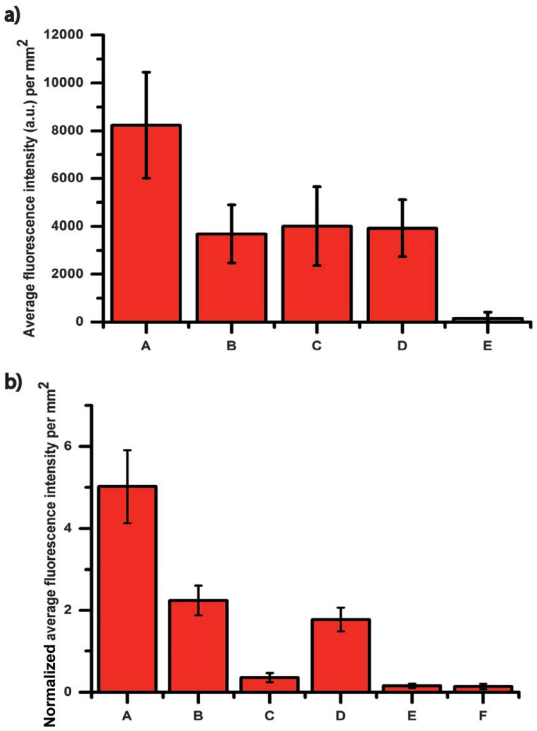

Fig. 2 (a) Average fluorescence intensity per mm^2 for slides grafted with APTES and **3** and negative controls. A = **3**/EDC/NHS/base, B = **3** only, C = **3**/NHS/base, D = **3**/base and E = APTES only. (b) Normalized average fluorescence intensity per mm^2 grafted with APTES and **1**, **2** and **3**. A = **3** EDC/NHS/base, B = **3** only, C = **2** only, D = **1** only, E = APTES only and F = glass.

Results and discussion

Synthesis and surface attachment

Model PET fluoroionophores **1** and **2** were synthesized by reactions of 4-aminoethyl-phenylaza-15-crown-5 with either *N*-benzyl-4-chloro-1,8-naphthalimide or *t*-butyl-4-chloro-1,8-naphthalimidylmethyl benzoate. The *t*-butyl ester protecting group was removed by hydrolysis using trifluoroacetic acid to afford **3**, which has a carboxyl moiety for covalent attachment to the APTES grafted glass surface, in 8% overall yield. Coupling onto the APTES surface was undertaken under standard peptide coupling conditions using EDC, NHS and triethylamine as the base. Negative controls for the coupling of **3** were obtained by treatment of APTES grafted slides without all or some of the coupling reagents. Without coupling reagents, amide bond formation is not feasible at room temperature.[29]

Surface analysis

Fig. 2(a) shows the average fluorescence intensity per mm^2 of the coated slides. As expected, slides treated with **3** and all coupling reagents show the highest fluorescence intensity compared to the negative controls, with a statistically significant difference. However, all negative controls show significantly higher fluorescence intensity compared to slides with only APTES grafting. This latter observation indicates that **3** also adsorbs non-covalently onto APTES coated surfaces after a soft-glass fibre compatible washing procedure, which involves sequential washing with THF, buffer (pH 5) and water. To establish the relationship between the surface density of **3** with or without coupling reagents and incubation time, coupling reactions were performed for 1, 5, and 9 hours (ESI Fig. S1†). No statistically significant difference for samples incubated for 1–9 hours was observed, but to ensure that the maximum level of coupling was obtained, most analyses were undertaken on samples treated for 9 hours.

To probe whether the non-covalent attachment of **3** on the APTES surface is related to the chemical structure of the fluoroionophore, derivatives **1** and **2** were incubated under the same conditions. Fig. 2(b) shows the comparison of fluorescence intensity per mm^2 of all three fluoroionophore derivatives incubated for 9 hours, along with the APTES-grafted and untreated glass slides. Assuming the molar extinction coefficient and the quantum yield of all non-covalently attached derivatives on an APTES grafted surface are the same,[30,31] the quantity of **2** is less than those of **1** and **3**, while the difference between **1** and **3** is statistically insignificant. These experiments suggest that the fluorophore attachment point has some role in non-covalent binding to the APTES coating. Previous XPS studies on APTES grafted silicon wafers indicated that free primary amine and ammonium groups can co-exist on an APTES coated surface.[28] Thus it is likely that **1** and **3** bind non-covalently to the APTES coated surface through a mixture of charge dipole and electrostatic interactions. It is also possible that the positive ammonium groups are complexed by the crown ether.[32] A difference in solubility of **2** due to the *t*-butyl ester group is consistent with the significantly lower quantities on the APTES surface after washing.

As compounds **1–3** are fluoroionophores, they show increased emission intensity upon complexation with sodium or other positive ions of similar size.[6,33] As a consequence, the interaction of the ionophore with positively charged ammonium ions of the APTES-grafted glass may also change the emission of the fluoroionophore[31] and affect the measurements by scanning fluorescence imaging. Thus, complementary measurements using XPS and ToF-SIMS were performed to corroborate the scanning fluorescence imaging. Importantly, XPS measurements are independent of the molar extinction coefficient and quantum yield and furthermore, the sampling depth of XPS is approximately 10 nm from the surface, thus it is ideal for investigating the composition of the chemical coatings and the glass interface.[34]

The Pb 4f7/2 peak was used as the calibration standard throughout these experiments. Since the binding energy of Pb 4f7/2 in this glass composition has not been determined before, the adventitious carbon shift was used to determine the chemical shift Pb 4f7/2 of the uncoated glass. The Pb 4f7/2 chemical shift of F2 was 138.6 ± 0.1 eV, which is very close to the literature value for a similar glass composition.[35] APTES-grafted slides coupled to **3**, the negative control without coupling reagents, APTES only coated slides, and bare F2 slides were analysed using XPS. From survey scans, O, C, Si, Pb, Na and N were found in most of the slides. The element quantifications are based on high resolution scans and the summary of the surface elemental analysis can be found in the ESI.† Previous studies have shown that the reproducibility of grafting for the APTES reagent is highly dependent on experimental conditions including humidity, temperature, and water content in the solvent and water that is surface-bound on the glass.[36,37]

Fig. 3(a) shows the individual atomic percentages of nitrogen in all three samples from each treatment described above. Apart from two individual samples, samples with **3** coupled to the APTES surface were found to have a greater nitrogen content compared to the negative controls and samples with APTES only. Nitrogen is not a component of F2 glass and therefore the nitrogen detected in samples of F2 glass probably reflects surface contamination. The variation of the nitrogen content within samples that experienced the same surface treatment may be related to the APTES coating thickness and homogeneity; however, we cannot confirm this hypothesis without ellipsometry and atomic force microscopy that is not possible for these substrates. Fig. 3(b) shows the linear correlation between nitrogen and lead content (R^2 = 0.64). The low R^2 is due to the variation of APTES coating, which gives a large variation of nitrogen atomic %, while the atomic % of lead among all samples is relatively constant. Despite this, Fig. 3(b) shows a trend of the negative correlation between lead and nitrogen, because the APTES coating is obscuring the lead silicate glass substrate. Fig. 3(c) shows that the XPS-measured nitrogen content correlates with the fluorescence intensity (R^2 = 0.78). This correlation arises because the attachment of **3** increases the nitrogen content on the surface, but is partly affected by variation of the APTES coating which also increases the nitrogen content but does not contribute to fluorescence.

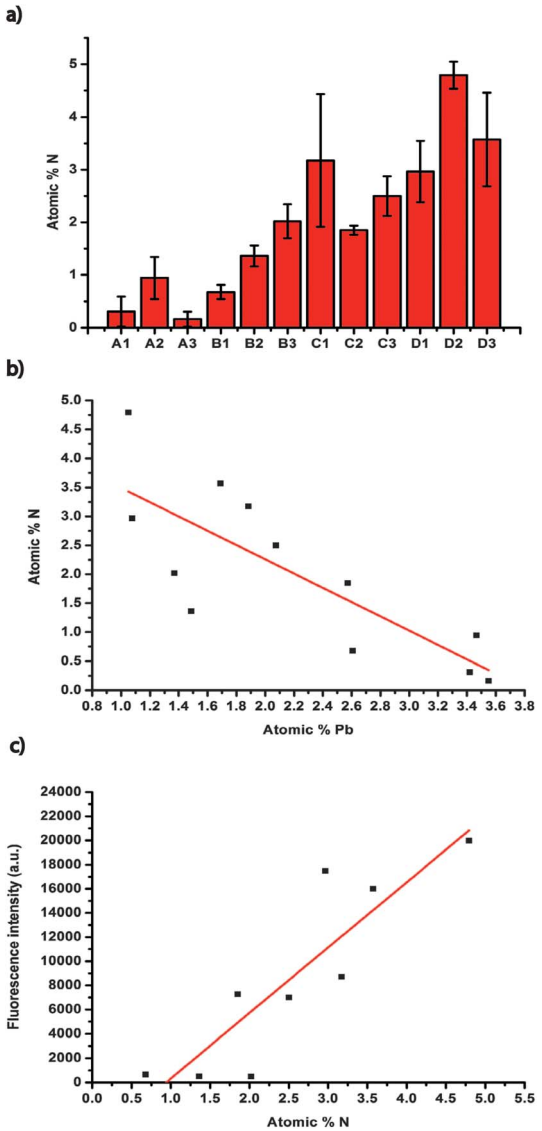

Fig. 3 Atomic percentages of (a) nitrogen on bare and coated F2 slides as measured by XPS. A1–A3 = bare glass samples, B1–B3 = APTES grafted glass samples, C1–C3 = **3** and APTES grafted glass without coupling reagents and D1–D3 = **3** and APTES grafted glass with coupling reagents. (b) Nitrogen atomic percentage as a function of lead atomic percentage (R^2 = 0.64). (c) Average fluorescence intensity as a function of nitrogen atomic percentage (R^2 = 0.78).

To establish a characteristic XPS signal strongly correlated with **3**, we investigated the high resolution (HR) spectrum of carbon in all samples. Using spectral deconvolution, the carbon peak was separated into C–H (284.5 ± 0.1 eV), CN/CO (286 ± 0.1 eV) and C=O (287.5 ± 0.1 eV), see ESI, Fig. S2(a)–(c).† The HR spectra show that samples with **3** coupled to the surface have the highest C=O content. This is reasonable since **3** has three C=O groups, two from the imide and a third from an amide group when **3** is coupled onto the surface. Fig. 4 shows the correlation (R^2 = 0.88) between the fluorescence intensity and the average C=O content on each sample.

ToF-SIMS is another surface sensitive technique that can provide non-optical quantification – by mass spectrometry – of the surface density of a chemical. Notably, the sampling depth

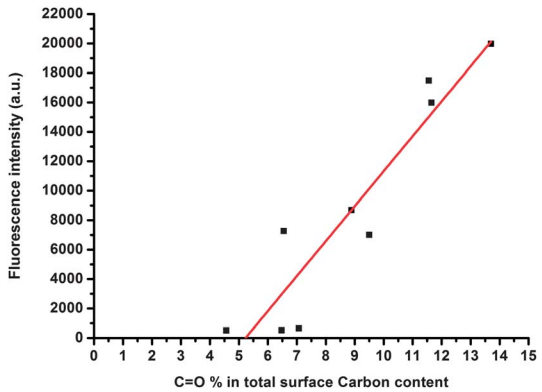

Fig. 4 Average fluorescence intensity per mm^2 as a function of the C=O percentage from the deconvolution of the high resolution carbon spectra (R^2 = 0.88).

of the ToF-SIMS is approximately 1–2 nm from the surface, which means that it is a more surface-sensitive technique than XPS. However, mass spectrometry is not usually quantitative so as to establish semi-quantitative surface analysis using ToF-SIMS, multivariable statistical analysis based on Principal Component Analysis (PCA) was performed. Fig. 5(a) shows the results from the PCA of the +SIMS measurements. PC1 covers 75.1% and PC2 covers 13.9% of the covariance of the samples, which gives the total covariance coverage of 89%. Samples are well clustered and separated. Samples with **3**, as well as all necessary coupling reagents, show a negative PC1 projection score, which discriminates samples from all negative controls. A loading plot (ESI†) shows all fragment peaks included in the PCA (also see Table S3a and b† for a list of all $C_xH_yN_z$ and $C_xH_yN_zO$ organic fragments which have a significant negative correlation with PC1). These $C_xH_yN_z$ and $C_xH_yN_zO$ organic fragments are related to the structure of **3** and the APTES coating and most of the $C_xH_yN_z$ and $C_xH_yN_zO$ organic fragments are negatively correlated with PC1 and positively correlated with PC2. Samples with **3**/EDC/NHS/base have negative PC1 scores and positive PC2 scores, which matches the pattern for $C_xH_yN_z$ and $C_xH_yN_zO$ organic fragments. Furthermore, PC1 appears to be correlated with the quantity of **3** attached to the APTES grafted glass surface. Fig. 5(b) shows that only samples treated with **3**/EDC/NHS/base have a negative PC1 score, while the rest of the treatments without the full set of coupling reagents and samples with APTES only show positive PC1 scores. All samples without the full set of coupling reagents show lower PC1 scores compared to samples with APTES only. This difference is statistically significant, showing that the non-covalent attachment of **3** on an APTES grafted surface can be characterised by ToF-SIMS.

Fig. 6(a)–(d) show ToF-SIMS images for Pb ions in four different samples. The size of each image is 100 μm × 100 μm and the resolution is 256 × 256 pixels; thus, each pixel represents a mass spectrum from a 391 nm × 391 nm sample area. A coloured pixel indicates that Pb was detected with intensity above the ToF-SIMS detection limit. This can be quantified to show the average number of Pb detected pixels in each 6.3 μm × 6.3 μm area of each sample. Thus APTES grafted slides coupled to **3** have the minimum number of Pb detected pixels and, as expected, the Pb ion density is the highest in F2 glass. The Pb

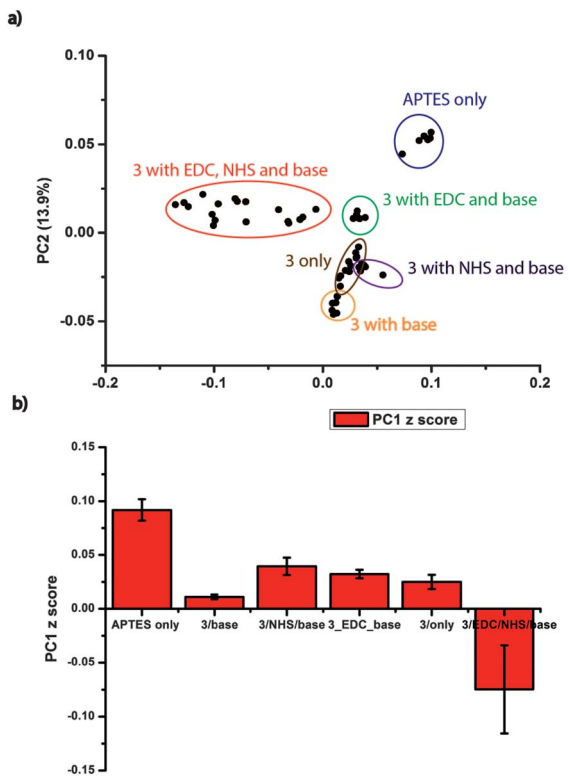

Fig. 5 (a) PCA of the ToF-SIMS results. (b) PC1 projection score of all sample types.

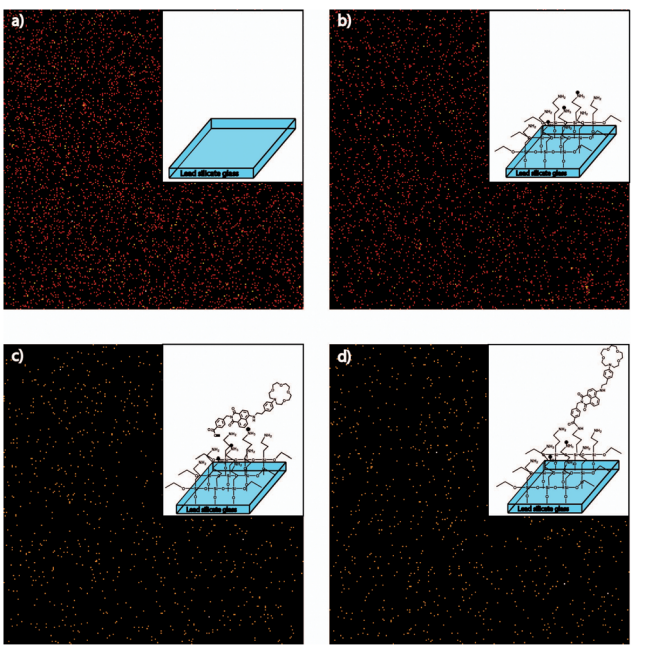

Fig. 6 Selected Pb ion images of lead silicate slides with (a) F2 glass, (b) APTES-grafted F2 glass, (c) the negative control and (d) APTES-grafted F2 glass coupled to **3**.

ion density decreases when APTES was coated on the surface, and shows a further decrease when **3** was coupled onto the surface. This result corroborates the negative correlation of N and Pb in the XPS measurements and suggests that the Pb ion distribution could be used as a marker to indicate coating coverage on lead silicate glass. Notably, on each slide Pb distribution is relatively random with no significant patchiness observed.

In addition to the quantification of the surface concentration of the coupled fluorophore and the homogeneity of the surface, ToF-SIMS depth profiling can provide information about the relative thickness of a coating. Although in this paper, no calibration was performed to establish the absolute thickness, as long as the sputtering beam energy is constant, the sputtering time required for the relevant organic fragment peak to reach saturation is proportional to the thickness of the coating. Similar experiments have been previously performed for an organic coating on a hard-disk platter, and this approach enables thickness measurements on a thin film (~1 to 2 nm) on a non-reflective surface.[38]

To ensure that the depth profiling results are consistent, three depth profiles were obtained on the same slide to establish the statistical variation within the same sample. The ion intensity was normalized with the total ion intensity from each depth profile. Fig. 7(a) shows the depth profile for three identically prepared samples of **3** coupled onto an APTES coated glass surface. It is observed that the normalized peak intensity of Pb increases while that of CH_4N^+ decreases. Based on the loading plot (see ESI†) of the PCA, it was identified that the CH_4N^+ peak is strongly correlated with the organic coating. These measurements are consistent over the three samples.

Fig. 7(b) shows the depth profiles of CH_4N^+ over sputtering time between 5 and 25 seconds on bare F2 slides (A1), APTES only grafted slides (B1), **3** on an APTES grafted surface (C1) and **3** coupled onto an APTES grafted surface (D1) as previously studied by XPS. It was observed that the relative intensity of CH_4N^+ for bare F2 slides only fluctuates within statistical error throughout this sputtering time range. The relative intensity of CH_4N^+ for slides with **3** on an APTES grafted surface and **3** coupled onto an APTES grafted surface decreased over the period of 5–15 seconds, with no statistical difference observed from 15 seconds onwards. In contrast, the relative intensity of CH_4N^+ on APTES only coated samples shows no statistical difference from 10 seconds onwards, which indicates that the coatings with **3** (negative control and with coupling reagents) are thicker than just the APTES only coating, regardless of the nature of attachment (non-covalent *vs.* covalent). These results also indicate that the coating thickness of **3** (negative control and with coupling reagents) is similar.

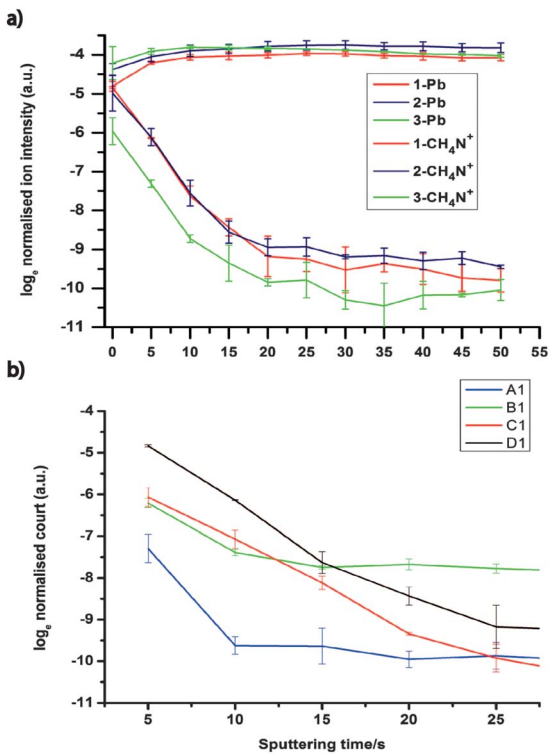

Fig. 7 (a) Depth profiles for samples of **3** coupled onto an APTES coated glass surface. (b) CH_4N^+ depth profiling for F2 glass (A1), APTES-grafted F2 glass (B1), the negative control (C1) and APTES-grafted F2 glass coupled to **3** (D1).

Conclusion

This work has demonstrated the feasibility of performing surface analysis of extruded glass slides as a model system for the internal surfaces of microstructured optical fibres (MOFs) or indeed for any sensing platform based on surface functionalized glass. Surface attachment reactions of **3** were performed under functionalisation conditions feasible for MOFs, meaning that the observations here are transferable to a fibre structure which is traditionally extremely difficult to characterize. Fluorescence imaging identified that attachment of fluoroionophore **3** could occur with or without coupling reagents. This was confirmed by XPS measurements that showed strong correlations of the C=O content in the high resolution carbon spectrum with fluorescence intensity. Through measurement of the C=O content, XPS data were able to identify a difference between covalent and non-covalent fluoroionophore attachment.

PCA of the ToF-SIMS data was able to distinguish the nature of different coatings; in particular, samples with **3** covalently coupled onto the glass surface showed markedly different PC1 projection scores. ToF-SIMS imaging also revealed that the Pb ion distribution could be used as a marker of surface coverage for the coating; the lead distribution is inversely related to the coverage of the glass slide. Furthermore, relative thickness measurements were also performed *via* depth profiling using ToF-SIMS which identified that slides with model PET sensor attachments show no difference in thickness regardless of the mode of binding used.

The development of a model extruded glass structure and our validation of methods to characterise these surfaces will enable reaction optimisation of established strategies and the performance of different surface attachment methods to be systematically examined. These include the use of other silane reagents with different functional groups or polyelectrolytes as the first functional layer, or a single step functionalisation using

pre-coupled fluoroionophore and silane reagent that can be directly grafted onto the glass surface. Furthermore, these glass fabrication and characterisation methods are versatile and can be transferred to other glass types capable of being extruded.

Acknowledgements

We acknowledge support from Micromet Pty. Ltd. under the Australian Research Council's Linkage Projects funding scheme (project LP0989605). The surface functionalisation facility within the Adelaide of the Optofab node of the Australian National Fabrication Facility (ANFF) was used. ANFF provides nano and microfabrication facilities for Australian researchers. Dr Gunther Andersson and Ms Natalya Schmerl are thanked for helpful discussions and technical assistance with the XPS measurements. XPS measurements were performed at the Flinders University in South Australia. We also acknowledge the facilities, and scientific and technical assistance of the Australian Microscopy & Microanalysis Research Facility at the South Australian Regional Facility (SARF), University of South Australia. Dr John Daman is thanked for running the ToF-SIMS measurements and for discussion of the ToF-SIMS data analysis. T.M.M. acknowledges an ARC Federation Fellowship and C.J.S. acknowledges an ARC Future Fellowship (FT0991910).

Notes and references

1 T. M. Monro, S. Warren-Smith, E. P. Schartner, A. Francois, S. Heng, H. Ebendorff-Heidepriem and S. Afshar, *Opt. Fiber Technol.*, 2010, **16**, 343–356.
2 T. M. Monro, W. Belardi, K. Furusawa, J. C. Baggett, N. G. R. Broderick and D. J. Richardson, *Meas. Sci. Technol.*, 2001, **12**, 854–858.
3 E. P. Schartner, H. Ebendorff-Heidepriem, S. C. Warren-Smith, R. T. White and T. M. Monro, *Sensors*, 2011, **11**, 2961–2971.
4 L. Rindorf, P. E. Hoiby, J. B. Jensen, L. H. Pedersen, O. Bang and O. Geschke, *Anal. Bioanal. Chem.*, 2006, **385**, 1370–1375.
5 V. P. Minkovich, D. Monzon-Hernandez, J. Villatoro and G. Badenes, *Opt. Express*, 2006, **14**, 8413–8418.
6 F. V. Englich, T. C. Foo, A. C. Richardson, H. Ebendorff-Heidepriem, C. J. Sumby and T. M. Monro, *Sensors*, 2011, **11**, 9560–9572.
7 S. C. Warren-Smith, S. Heng, H. Ebendorff-Heidepriem, A. D. Abell and T. M. Monro, *Langmuir*, 2011, **27**, 5680–5685.
8 S. V. Afshar, Y. L. Ruan, S. C. Warren-Smith and T. M. Monro, *Opt. Lett.*, 2008, **33**, 1473–1475.
9 C. Sonnenfeld, S. Sulejmani, T. Geernaert, S. Eve, N. Lammens, G. Luyckx, E. Voet, J. Degrieck, W. Urbanczyk, P. Mergo, M. Becker, H. Bartelt, F. Berghmans and H. Thienpont, *Sensors*, 2011, **11**, 2566–2579.
10 H. Ebendorff-Heidepriem, S. C. Warren-Smith and T. M. Monro, *Opt. Express*, 2009, **17**, 2646–2657.
11 H. Ebendorff-Heidepriem and T. M. Monro, *Opt. Express*, 2007, **15**, 15086–15092.
12 A. P. de Silva, T. S. Moody and G. D. Wright, *Analyst*, 2009, **134**, 2385–2393.
13 S. C. Warren-Smith, E. Sinchenko, P. R. Stoddart and T. M. Monro, *IEEE Photonics Technol. Lett.*, 2010, **22**, 1385–1387.
14 K. Hoffmann, R. Mix, J. F. Friedrich and U. Resch-Genger, in *Reviews in Fluorescence 2008*, ed. C. D. Geddes, Springer, New York, 2010, pp. 139–160.
15 Y. Ruan, T. C. Foo, S. Warren-Smith, P. Hoffmann, R. C. Moore, H. Ebendorff-Heidepriem and T. M. Monro, *Opt. Express*, 2008, **16**, 18514–18523.
16 N. P. Mellott, S. L. Brantley, J. P. Hamilton and C. G. Pantano, *Surf. Interface Anal.*, 2001, **31**, 362–368.
17 T. C. Foo, A. François, H. Ebendorff-Heidepriem, C. J. Sumby and T. M. Monro, in *Australian Conference on Optical Fibre Technology (ACOFT)*, Adelaide, Australia, 2009.
18 J. A. Howarter and J. P. Youngblood, *Langmuir*, 2006, **22**, 11142–11147.
19 H. S. Kim, Y. P. Kim, M. Y. Hong, H. K. Shon, D. W. Moon and T. G. Lee, *Appl. Surf. Sci.*, 2006, **252**, 6801–6804.
20 S. Libertino, F. Giannazzo, V. Aiello, A. Scandurra, F. Sinatra, M. Renis and M. Fichera, *Langmuir*, 2008, **24**, 1965–1972.
21 H. Min, D. W. Moon and T. G. Lee, *Surf. Interface Anal.*, 2011, **43**, 393–396.
22 D. Y. Petrovykh, H. Kimura-Suda, M. J. Tarlov and L. J. Whitman, *Langmuir*, 2004, **20**, 429–440.
23 D. Y. Petrovykh, H. Kimura-Suda, L. J. Whitman and M. J. Tarlov, *J. Am. Chem. Soc.*, 2003, **125**, 5219–5226.
24 J. K. Tusa and H. R. He, *J. Mater. Chem.*, 2005, **15**, 2640–2647.
25 H. Ebendorff-Heidepriem and T. M. Monro, *Opt. Mater. Express*, 2012, **2**, 304–320.
26 X. C. Long and S. R. J. Brueck, *Opt. Lett.*, 1999, **24**, 1136–1138.
27 J. F. Moulder, W. F. Stickle, P. E. Sobol and K. D. Bomben, *Handbook of X-ray Photoelectron Spectroscopy*, Physical Electronics, Inc., Minnesota, 1995.
28 R. G. Acres, A. V. Ellis, J. Alvino, C. E. Lenahan, D. A. Khodakov, G. F. Metha and G. G. Andersson, *J. Phys. Chem. C*, 2012, **116**, 6289–6297.
29 E. Valeur and M. Bradley, *Chem. Soc. Rev.*, 2009, **38**, 606–631.
30 A. Hennig, H. Borcherding, C. Jaeger, S. Hatami, C. Würth, K. Hoffmann, T. Thiele, U. Schedler and U. Resch-Genger, *J. Am. Chem. Soc.*, 2012, **134**, 8268–8276.
31 L. L. Wang, A. K. Gaigalas and V. Reipa, *BioTechniques*, 2005, **38**, 127–132.
32 A. Spath and B. Konig, *Beilstein J. Org. Chem.*, 2010, **6**, 32.
33 H. R. He, M. A. Mortellaro, M. J. P. Leiner, S. T. Young, R. J. Fraatz and J. K. Tusa, *Anal. Chem.*, 2003, **75**, 549–555.
34 B. D. Ratner and D. G. Castner, in *Surface Analysis: The Principal Techniques*, ed. J. C. Vickerman and I. S. Gilmore, Wiley, West Sussex, 2009, pp. 47–109.
35 P. W. Wang, L. P. Zhang, L. Lu, D. V. Lemone and D. L. Kinser, *Appl. Surf. Sci.*, 1995, **84**, 75–83.
36 E. Metwalli, D. Haines, O. Becker, S. Conzone and C. G. Pantano, *J. Colloid Interface Sci.*, 2006, **298**, 825–831.
37 R. M. Pasternack, S. R. Amy and Y. J. Chabal, *Langmuir*, 2008, **24**, 12963–12971.
38 L. Zhu, T. Liew and T. C. Chong, *Appl. Surf. Sci.*, 2002, **189**, 53–58.